DEUTSCHES ELEKTRONEN-SYNCHROTRON

DESY-THESIS-1999-008
February 1999

The Production of Leading Protons at HERA

A Measurement of Its Properties Using the LPS of ZEUS

by

Yu. E. Zamora Garcia

ISSN 1435-8085

NOTKESTRASSE 85 - 22607 HAMBURG

To be sure that your reports and preprints are promptly included in the HEP literature database
send them to (if possible by air mail):

DESY
Zentralbibliothek
Notkestraße 85
22603 Hamburg
Germany

DESY
Bibliothek
Platanenallee 6
15738 Zeuthen
Germany

The Production of Leading Protons at HERA

A measurement of its properties using the LPS of ZEUS

Yuri E. ZAMORA GARCIA

Université de Genève, Genève
Suisse

December, 1998

UNIVERSITÉ DE GENÈVE

FACULTÉ DES SCIENCES

Département de physique
nucléaire et corpusculaire

Professeur Allan G. Clark

The Production of Leading Protons at HERA

A measurement of its properties using the LPS of ZEUS

THÈSE

présentée à la Faculté des sciences de l'Université de Genève pour l'obtention du titre de Docteur ès sciences, mention physique

par

Yuri E. ZAMORA GARCIA

de

Lima, Peru

Thèse N° 3061

GENÈVE

Atelier de reproduction de la Section de Physique

1999

La Faculté des sciences, sur le préavis de Messieurs A. CLARK, professeur ordinaire et directeur de thèse (Département de physique nucléaire et corpusculaire), J. FIELD, docteur (Département de physique nucléaire et corpusculaire), M. ARNEODO, professeur (Università del Piemonte Orientale, Dipartimento di Scienze Mediche – Novara, Italia) et T. MASSAM, docteur (CERN, World Laboratory - Genève) autorise l'impression de la présente thèse, sans exprimer d'opinion sur les propositions qui y sont énoncées.

Genève, le 19 février 1999

Thèse - 3061 -

Le Doyen, Jacques WEBER

To my parents and family for their encouragement and concern since the very beginning of my scientific career.

To Kathrin for her moral support, collaboration, enormous patience, continuous encouragement and confidence in me. I will always be there for her!

The Production of Leading Protons at HERA

A measurement of its properties using the LPS of ZEUS

Abstract

This thesis presents the measurement of the momentum distribution and the analysis of the mechanisms by which the leading protons are produced at HERA. Leading protons are detected at HERA using the Leading Proton Spectrometer (LPS) of ZEUS with an overall r.m.s. momentum resolution of 0.4% at 820 GeV. The events belonging to the process $e + p \to e' + p' + X$ are selected in two kinematical regions defined by the virtuality of the exchanged boson, Q^2, with $Q^2 > 4$ GeV (DIS) and $Q^2 < 0.02$ GeV (PHP). Additionally, a constraint of $x_L > 0.6$, where x_L is the fraction of the proton beam momentum carried by the leading proton is also required. The fraction of the events with a leading proton and the shape of their P_t^2 distribution are determined as functions of x_L. It is found that the shapes of the acceptance-corrected x_L spectra for DIS and PHP are flat within the experimental errors and are similar at values of $0.6 < x_L < 0.95$. The P_t^2 distributions of the leading proton in both DIS and PHP samples can be fitted with a simple exponential at x_L value. Comparison of the exponential slope-parameter for the two cases reveals no difference within 80% statistical confidence level. The results are compared to different theoretical models and measurements obtained for leading neutrons at ZEUS and leading protons at the former ISR of CERN. A preliminary study of the properties of events with a leading protons in the final state is also presented and compared to expectations from different models.

Submitted in partial fulfilment of the requirements for the degree of Docteur ès sciences in physics at the University of Geneva

Abstract

Cette thèse présente les mesures de la distribution d'impulsions des "Leading Protons" , ainsi que l'analyse des mécanismes par lesquels ces protons sont produits dans le collisioneur HERA. Ils sont détectés dans le LPS (Leading Proton Spectrometer) de l'expérience ZEUS avec une résolution en impulsion de 0,4% à 820 GeV. Les évènements issus du processus $e+p \to e'+p'+X$ sont selectionnés dans deux régions cinématiques définies par la virtualité du boson échangé, Q^2, avec $Q^2 > 4$ GeV (DIS) et $Q^2 < 0,02$ GeV (PHP). De plus, nous avons appliquée une contrainte $x_L > 0,6$ ou x_L est la fraction de l'impulsion du proton incident emportée par le Leading Proton.

La fraction des évènements avec un Leading Proton et la forme de leur distribution en P_t^2 sont déterminées comme des fonctions de x_L. Il se trouve que la forme des spectres en x_L corrigés en acceptance pour DIS et PHP sont plats dans les limites des erreurs expérimentales et sont identiques pour $0,6 < x_L < 0,95$. Les distributions en P_t^2 du Leading Proton dans les échantillons DIS et PHP peuvent etre ajustées avec une simple exponentielle en x_L. La comparaison des paramètres de pente dans les deux cas se révèlent identiques dans la limite de 80% de niveau de confiance.

Les résultats sont comparés avec différents modèles théoriques et des mesures obtenues avec le Leading Neutron à ZEUS et aussi les expériences de Leading Proton aux ISR du CERN. Une étude préliminaire des propriétés des évènements avec un Leading Proton dans l'état final est aussi présentée et comparée avec les prévisions de différents modèles.

Acknowledgements

I would like to thank very much my thesis advisor Prof. Allan Clark for his support and guidance during my doctoral studies and research. I am also deeply grateful to Dr. John Field for innumerable discussions and guidance in the interpretation of the physics associated with the leading proton production as well as for his support of my thesis. Their comments and suggestions were a source of motivation towards the conclusion of my doctoral thesis.

This thesis would never been possible without the support of the World Laboratory which introduced me to the field of high energy physics. I am grateful to Prof. A. Zichichi for enabling me to collaborate in the LPS group. I have also very much appreciated his support and that of all members of the former CERN-LAA/LPS project with whom I worked in the first steps of the experimental program. I would like to thank specially to C. Nemoz, H. Larsen, J. Schipper, P. Ford, M. Hourican, M. Chiarini and G. Anzivino for their friendship and help during my start in the group. In particular I am indebted to my professor, friend and intellectual father Dr. Thomas Massam for his dedicated teaching, patience, encouragement, guidance, advice and insight. This thesis is a humble tribute to him.

Likewise, many thanks to my ZEUS-LPS colleagues and friends at DESY. Their friendship, commitment and expertise during our many discussions helped me to pursue and enhance my research work. Particularly, I would like to thank to Michele Arneodo for his suggestions and advice and for his support of my thesis. Special thanks to I. Gialas, N. Cartiglia, A. Garfagnini and R. Sacchi for their support and advice whilst implementing my analysis work.

At CERN, I would like to thank very much Dr. Jim Allaby for his support and trust in the final stages of the writing of my thesis. Special thanks to F. Anselmo and F. Rivera for encouragement and support and to all my colleagues and friends who helped me to face the challenges which I have found during my stay in Geneva.

In the analysis and presentation of my results during the writing stage of my thesis I had the pleasure to learn from discussions with Profess. L. Lipatov and V. Petrov on special aspects of the physics behind the leading proton production. Special thanks to D. de Florian for teaching me the QCD fracture functions and providing me valuable numerical calculations for comparisons with our data.

During all this time, whilst working and doing research for my thesis, I have enjoyed the support, help, trust and friendship of many people, both at CERN or DESY. I am indebted to all of them, and regret that I have not been able to mention everyone here.

Contents

1 Résumé

1.1 Introduction générale

Après les premières collisions fortement inélastiques réalisées au SLAC[1], il y a à peu près trois décennies, où des électrons accélérés à 20 GeV étaient dirigés vers une cible fixe afin d'étudier les structures du nucléon, la compréhension de la matière hadronique a contribué à l'élaboration de l'actuelle Chromodynamique Quantique (QCD).

Afin de continuer l'étude de la matière hadronique et tester la validité des modèles théoriques, plusieurs expériences ont été proposées et réalisées partout dans le monde. Ainsi, HERA, un accélérateur ep fut construit à DESY, Hambourg en Allemagne. Cet accélérateur nous permet d'explorer les constituants de la matière hadronique par le biais d'une sonde ponctuelle (boson) dont le transfert d'impulsion invariante quadridimensionnelle, Q^2, permet de mesurer les composants de protons qui amènent une fraction de leur impulsion x aussi faible que 10^{-5}. HERA augmente les champs de mesure des variables x et Q^2 de plus de deux ordres de grandeur par rapport à ceux mesurés par les expériences à cible fixe.

Deux expériences principales à HERA, ZEUS et H1, sont utilisées pour étudier des collisions ep. En Particulier, ZEUS est équipé d'un spectromètre à silicium à haute résolution, le "Leading Proton Spectrometer" (LPS). Il permet la détection de protons diffusés (leading protons) qui fournit d'une part, une contrainte cinématique supplémentaire en x, et d'autre part la forme de la distribution en impulsion longitudinale et transversale. Le sujet de ce travail de recherche porte sur la mesure et l'analyse de cette distribution de l'impulsion longitudinale et transversale, ainsi que sur l'analyse du mécanisme de production du "leading" proton.

Cette thèse est organisée de la façon suivante: dans un premier chapitre, une description de la cinématique et de la classification des événements produits à HERA est présentée, ainsi que les modèles théoriques censés expliquer la production de ces événements, et plus particulièrement la génération du "leading" proton.
Les descriptions de l'accélérateur HERA, de l'expérience ZEUS et du spectromètre à "leading" proton, ainsi que le système d'acquisition de données seront présentées respectivement au deuxième, troisième et quatrième chapitres. Le LPS est décrit en détail au troisième chapitre.
L'analyse des "leading" protons enregistrés par le LPS, ainsi que la méthode développée pour le calcul d'acceptation géométrique feront l'objet du cinquième chapitre, laissant au sixième chapitre les diverses corrections qui sont nécessaires pour la mesure finale d'impulsion transversale et longitudinale du "leading" proton.
La discussion et la comparaison des résultats de mesures avec les prévisions théoriques, basées sur la QCD perturbative et celle développée par Regge, feront l'objet du septième chapitre. Dans ce même chapitre, une comparaison avec des résultats obtenus à ZEUS pour le "leading" neutron et à l'ISR[2] sera présentée.
Le huitième chapitre aura pour objet l'étude préliminaire des événements associés à la production du "leading" proton en mettant l'accent sur la similarité des configurations présentés par ces événements dans différents régimes cinématiques (DIS et PHP).

[1] Collisionneur à cible fixe aux Etats-Unis
[2] Collisionneur pp dans les années 1970 au Laboratoire européen pour la Physique des Particules (CERN)

Finalement, au neuvième chapitre, des conclusions générales seront synthétisées et les futurs travaux seront mis en perspective.

1.2 Description de la physique et classification des interactions ep

De nos jours, plusieurs modèles théoriques sont utilisés pour expliquer les interactions ep. Parmi eux, on peut distinguer ceux qui sont développés dans le cadre de la QCD perturbative et ceux qui, en l'absence de modèles QCD cohérents avec les résultats expérimentaux, s'inspirent de la théorie développée par Regge. A HERA, ces modèles, qui sont expliqués avec certains détails au premier chapitre, sont testés quotidiennement et leurs champs de validité cinématique sont définis.

En général, à HERA, les débris produits lors des collisions ep sont détectés. Dans une fraction de ces collisions, le proton peut, soit survivre, soit se régénérer après la collision, résultant un proton à l'état final. Ce processus, peut être décrit par l'équation suivante:

$$e + p \rightarrow e' + p' + X \tag{1.1}$$

où e' est l'électron diffusé, p' le proton à l'état final et X les débris de la collision (hadronisation). Ce type de processus peut être généré dans un domaine cinématique tres étendu en x et Q^2. Généralement, un processus ep est classifié comme collision fortement inélastique, DIS (*deep inelastic scattering*), si $Q^2 > m_p^2$ ou comme photo-production, PHP (*photo-production*), si $Q^2 = 0$. Cette classification nous permet de tester les modèles théoriques dans des régions cinématiques très bien définies. Particulièrement, des processus ep qui donnent un proton à l'état final ne sont pas très bien expliqués par la théorie, d'où l'intérêt de l'étude systématique de la production de ce proton. La figure 1.2.1 montre le diagramme de Feynman d'ordre inférieur pour la réaction de l'équation [1.1] et qeulques unes des contributions de physique pour la production du "leading" proton.

Parmi plusieurs modèles théoriques proposés pour expliquer la production du "leading" proton, à HERA, on distingue un modèle basé sur la théorie de Regge et un autre sur la QCD perturbative qui propose la nécessité de l'introduction d'une quantité appelée "fonction de fracture".

Dans la cadre de la théorie de Regge les échanges de trajectoires (objets ou pôles de Regge) sont le mécanisme dominant pour la production du "leading" proton. Ces trajectoires peuvent correspondre à un *pomeron*, ou pion ou plus généralement un *reggeon*. En ce qui concerne le trajectoire ou l'objet échangé le spectre de l'impulsion du "leading" proton aura une configuration caractéristique.

Les fonctions de fracture QCD ont été introduites pour élargir la description QCD usuelle des partons des processus semi-inclusifs dans les collisions fortement inélastiques à la région de l'espace des phases correspondant aux basses impulsions tranversales, où la contribution de la fragmentation de la cible devient importante. Cette fonction de fracture mesurable est une nouvelle quantité incalculable similaire à celle de la fonction de structure qui mesure la distribution des partons de l'objet échangé entre la cible et le hadron final, sans faire d'hypothèse au sujet de l'objet en question.

Ces deux approches, fondamentalement très différentes, sont décrites en détail au premier chapitre. En outre, elles sont comparées avec nos résultats expérimentaux (chapitre 7) en donnant des accords remarquables.

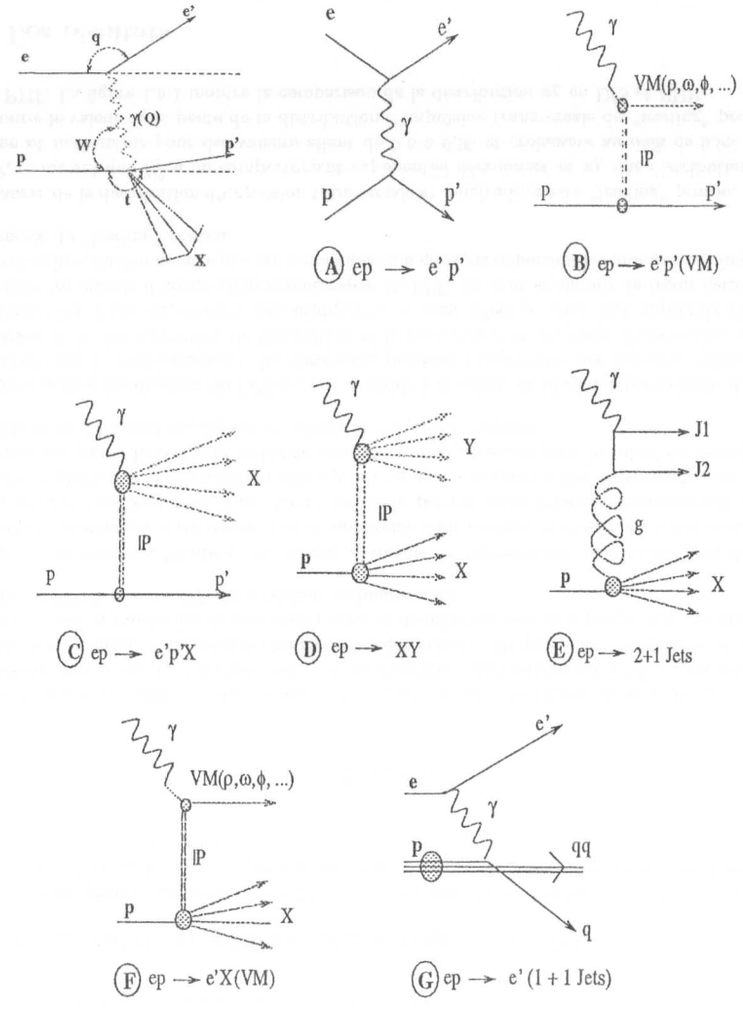

Figure 1.2.1: En haut, gauche: diagramme de Feynman d'ordre inférieur pour la réaction $e + p \rightarrow e' + p' + X$. Les quantités q, et t sont le transfert d'impulsions aux vertex de l'electron et du proton respectivement. W est l'énerie du centre de masse du système γp. Les diagrammes de (A) à (G) montrent quelques unes des contributions de la physique pour la production du "leading" proton.

1.3 L'appareil expérimental

Le détecteur à collisionneur de DESY, ZEUS, utilise le faisceau de HERA, collisionneur ep, dont l'énergie dans le centre de masse ($\sqrt{s} = 314$ GeV) est l'équivalent de celui d'un collisionneur à cible fixe utilisant un faisceau d'électron à 52 TeV. L'analyse présentée dans cette thèse est basée sur les données collectés pendant l'année 1994, correspondant à une luminosité intégrée de $\approx 3{,}7\ pb^{-1}$. L'accélérateur HERA, le détecteur ZEUS ainsi que les composants utilisés dans notre analyse seront brièvement décrits au deuxième chapitre.

Le spectromètre à "leading" proton, composant de ZEUS, consistait principalement en 1994 en trois stations de détecteurs à silicium (S4 → S6) distribuées autour du faisceau de protons sur les 90 premiers mètres au sortir du lieu d'intéraction. Fig 1.3.1 montre un plan schématique del emplacement du LPS et ZEUS.

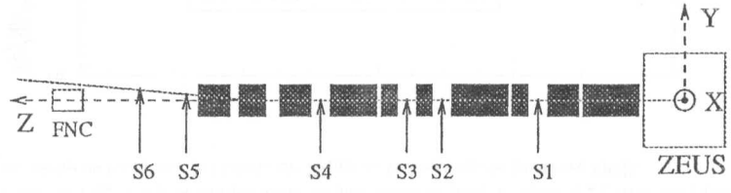

Figure 1.3.1: Plan schématique du positionnement du LPS, ZEUS el de la ligne du faisceau de protons. Il montre aussi l'endroit où le détecteur à "leading" neutrons (FNC)est placé.

Les détecteurs du LPS sont fixés près du faisceau à l'aide des stations moviles (*roman pots*). Chaque station contient jusqu'à six plans de strips de silicium, orientés verticalement ou à un angle de $\pm 45°$, avec un pas d'environ $100\mu m$ et est positionnée pendant la prise des données à dix déviations standards de la dimension transversale du faisceau par rapport à sa position nominale.

Le LPS a une résolution moyenne d'impulsion de 0,4% à 820 GeV et peut atteindre 0,16% dans des régions cinématiques spécialement sélectionnées. Les détails du LPS sont décrits au troisième chapitre, mettant l'accent sur les aspects techniques de sa construction ainsi que la méthode utilisée pour la reconstruction du "leading" proton et le calibrage du spectromètre.

1.4 La sélection de données

Dans nos analyses de données, nous utilisons deux différentes classes d'événements ep, chacune définie dans des régions cinématiques très distinctes. Ce sont des événements appartenant aux classifications DIS et PHP. Dû á l'acceptation et efficience du detecteur ZEUS, les evenements correspondent aux classification DIS sont definies comme celles où $Q^2 > 4$ (GeV/c)^2 et l'énergie de l'électron diffusee $E_e > 8$ GeV, pendant que des événements appartenant aux classifications PHP comme celle avec $Q^2 < 0.02$ (GeV/c)^2 et $12 < E_e < 18$ GeV.

Ces événements, malgré un processus de sélection très rigoureux, ne sont pas complètement à l'abri des contaminations par les bruits de fond. Ces derniers peuvent être des interactions ep

en coïncidence avec des faisceaux "halo" (commun à DIS et PHP) ou des interactions provenant des réactions Bremsstrahlung (principalement présent en PHP). Ces bruits de fond sont identifiés et prélevés statistiquement dans nos données. La sélection finale des événements est contrainte par des régions cinématiques à acceptation raisonnable du LPS.

1.5 Le calcul d'acceptation géométrique du LPS

Le calcul d'acceptation géométrique du LPS a été fait avec l'aide d'événements Monte Carlo. Ces événements ont été spécialement générés avec une distribution linéaire en x_L et une distribution exponentielle en P_t^2 en accord avec:

$$\frac{dN}{dP_t^2} \propto e^{-6P_t^2} \tag{1.2}$$

Comme le positionnement des détecteurs du LPS par rapport aux faisceaux de protons a un effet appréciable dans le calcul d'acceptation, une configuration particulière du LPS, où les détecteurs sont placés en position d'acceptation maximale, a été utilisée. De plus, cette configuration du LPS a été choisie car la simulation de plusieurs positions de détecteurs dans le programme de simulation générale du ZEUS est très difficile à réaliser techniquement.

Puisque les événements Monte Carlo décrits ci-dessus ne reproduisent pas les données du LPS, une méthode statistique a été développée et appliquée pour corriger la distribution des événements générés donnée par l'équation [1.2]. Cette méthode permet aussi d'inclure correctement dans le calcul d'acceptation et d'efficacité les effets produits par la migration des événements lors de leur reconstruction par le LPS. Cette méthode ainsi que son application pour le calcul de l'acceptation géométrique du LPS sont expliquées en détail au cinquième chapitre.

La reconstruction des données du LPS est très sensible à la valeur de plusieurs paramètres. Les plus significatifs sont le positionnement des détecteurs pendant l'acquisition des données, l'efficacité et la précision de la reconstruction de l'impulsion et la reconstruction du point d'interaction *ep*. Ces paramètres sont d'une importance non négligeable et leurs effets peuvent être appréciés s'ils sont inclus dans les calculs d'acceptation géométrique du LPS. Ils sont expliqués de façon détaillée au sixième chapitre, où l'on montre que ces corrections changent certainement les mesures de l'impulsion transversale du "leading" proton.

Les mesures de la distribution d'impulsion transversale et longitudinale du "leading" proton, en DIS et PHP, montrent que P_t^2 a un comportement exponentiel décroissant et x_L une distribution quasi uniforme et horizontale pour des valeurs allant de 0,6 à 0,95 et croissante au delà de 0,95. Table 1.5.1 donne le valeur de la pente de la distribution d'impulsion transversale du "leading" proton en DIS et PHP. La figure 1.5.1 montre la comparison de la distribution x_L en DIS et PHP.

1.6 Les résultats

La comparaison de la mesure d'impulsion du "leading" proton en DIS et PHP montre, que les distributions d'impulsion peuvent avoir la même forme dans la limite des fluctuations statistiques. Cette constatation suggère que les processus physiques, mis en jeu lors de la production du "leading" proton dans deux régimes cinématiques très différents, peuvent avoir une certaine similarité.

x_L bin	ZEUS-LPS PHP Data		ZEUS-LPS DIS Data	
	-b	χ^2	-b	χ^2
0.60 – 0.63	6.64 ± 2.18	1.58	6.66 ± 2.08	3.70
0.63 – 0.67	8.23 ± 2.38	1.13	6.72 ± 1.10	1.19
0.67 – 0.73	5.57 ± 0.82	0.48	7.48 ± 0.88	3.14
0.73 – 0.79	7.27 ± 1.28	0.91	8.46 ± 1.17	0.57
0.79 – 0.84	9.55 ± 1.25	1.12	7.76 ± 1.23	1.59
0.84 – 0.88	9.64 ± 1.29	0.82	8.27 ± 1.04	0.75
0.88 – 0.91	5.73 ± 1.08	0.88	7.51 ± 0.95	1.95
0.91 – 0.94	3.76 ± 1.00	0.38	6.59 ± 1.21	1.63
0.94 – 0.97	6.56 ± 2.69	0.03	7.93 ± 1.52	0.12
0.97 – 1.005	7.90 ± 1.19	1.35	6.74 ± 0.96	0.61

Table 1.5.1: valeur de la pente de la distribution P_t^2 mesurée en DIS et PHP

Afin d'étudier les propriétés du "leading" proton, des calculs numériques et de simulation Monte Carlo basés sur des modèles théoriques développés dans le cadre de la QCD perturbative et la théorie de Regge, ont été exécutés. Ce travail est présenté en détail au septième chapitre où l'on aperçoit que, malgré les divergences entre les prévisions théoriques inclues dans les générateurs Monte Carlo utilisés et nos mesures, les calculs numériques reproduisent avec précision les mesures que nous avons effectuées. Fig. 1.6.1 montre la comparaison de nos mesures avec les prédictions des générateurs Monte Carlo et Fig. 1.6.2 la comparaison de nos mesures pour le spectre x_L avec les résutats des calculs numériques basés sur la théorie de Regge et la fonction de fractrure QCD.

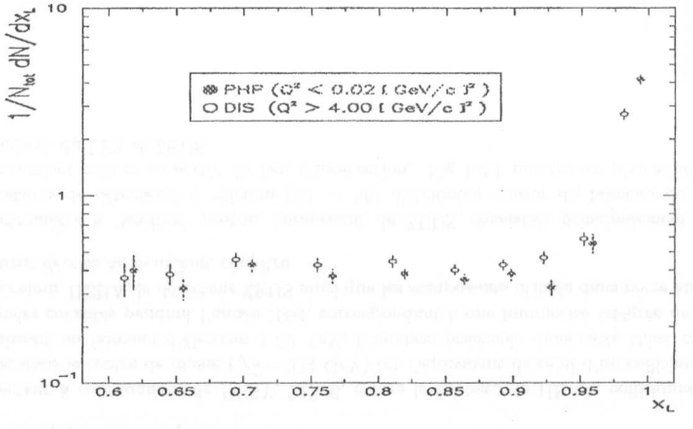

Figure 1.5.1: Comparaison de la distribution x_L measurée en PHP et DIS. Ces distributions sont normalisées pour le nombre total N_{tot} des évènements PHP ou DIS dont le LPS a été activé pour adquisition des données.

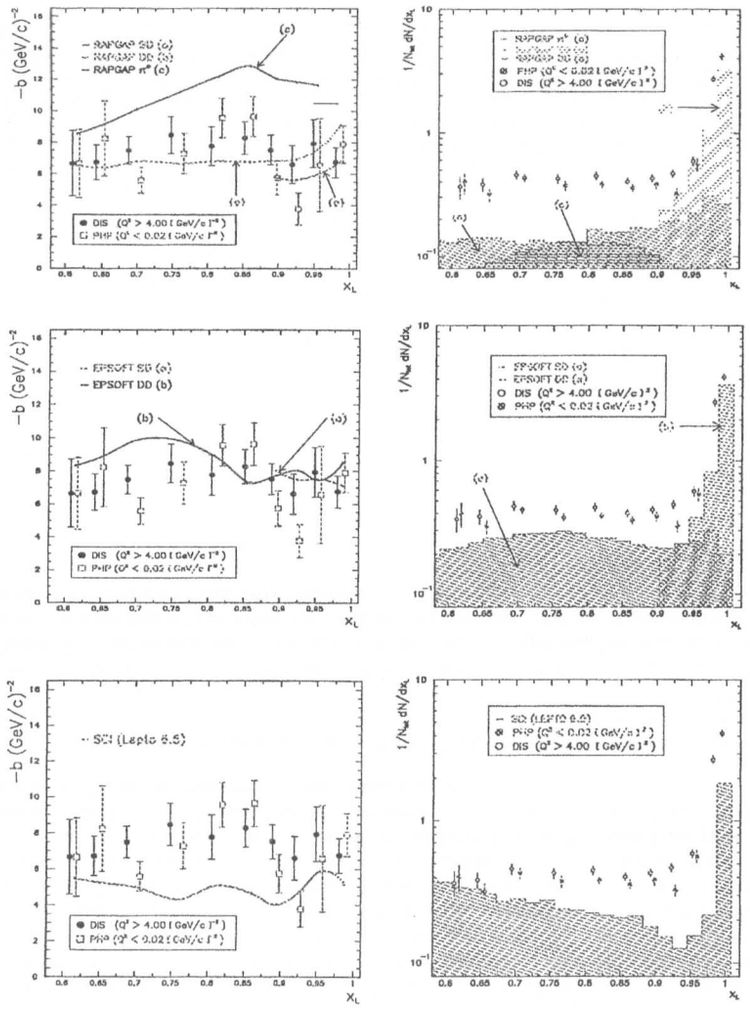

Figure 1.6.1: Comparaison de nos mesures avec les prédictions des générateurs Monte Carlo RAPGAP, EPSOFT et LEPTO.

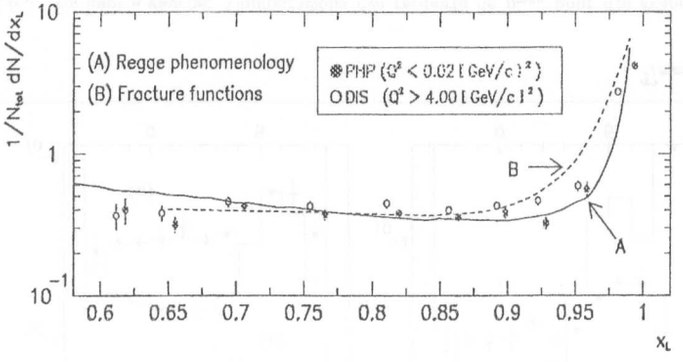

Figure 1.6.2: Comparaison de nos mesures pour le spectre x_L avec les résultats des calculs numériques basés sur la théorie de Regge (A) et la fonction de fracture QCD (B)

Les calculs numériques montrent que la production du "leading" proton peut être expliquée, dans le cadre de la théorie de Regge, par la contribution totale de divers processus périphériques, voire l'échange de plusieurs trajectoires telles que le pomeron, pion ou, en général, un reggeon. De même, l'approche par "Fonction de fracture" développée dans le cadre de la QCD perturbative reproduit aussi remarquablement nos mesures. Ce qui est nouveau dans cette approche est qu'elle mesure la distribution partonique de l'objet échangé entre la cible hadronique et l'hadron final sans faire aucune modélisation de l'objet échangé en question. La fonction de fracture fournit un outil pour analyser, dans le cadre de la QCD perturbative, des processus diffractifs. C'est une alternative à des modèles périphériques non perturbatifs.

Entre autres, à ZEUS, les propriétés du "leading" neutron ont été aussi mesurées. De même, on dispose des données rapportant les mesures du "leading" proton dans l'ancien ISR. Le rapport de ces mesures avec nos résultats qui est également exposé dans le septième chapitre présente quelques similarités dans la comparaison de la pente de P_t^2 du "leading" neutron et du "leading" proton pour des valeurs de x_L variant entre 0,75 et 0,93. De même la pente de P_t^2 du "leading" proton mesurée à ZEUS et celle mesurée à l'ISR sont comparables pour des valeurs de x_L au delà de 0,97.

En poursuivant notre analyse, de par la faible statistique dont nous disposons, une étude préliminaire des propriétés des événements associés à la production du "leading" proton a été faite en DIS et PHP. Cette étude, exposée au huitième chapitre, montre dans ses résultats que la production du "leading" proton pourrait être independante de Q^2 et W. Les propriétés des événements associés à la production du "leading" proton ont été mesurées topologiquement, telles que leur distribution en particules chargées et leur distribution en "maximum pseudo rapidity"[3] (η_{max}). Ces distributions présentent des configurations particulièrement similaires qui ne sont pas du tout expliquées par les

[3]Maximum pseudo-rapidity ($\eta_{max} = -\ln[\tan(\frac{\theta}{2})]$), θ est l'angle polaire dans la direction du proton

modèles théoriques inclus dans les générateurs Monte Carlo utilisés.

Les processus de dissociation simple ou double dans les interactions *ep* peuvent être identifies en étudient la distribution en η_{max} des hadrons produits. Les valeurs (théoriques) de la pseudorapidité vout de -3.4 au bord du tube du faisceau dans le calorimètre vers l'arrière à +3.8 au bord du tube du faisceau dans le calorimètre vers l'avant. Néammoins, la pseudorapidité mesurée peut excéder ces limites du fait que la reconstruction du centre du "cluster" hadronique s'éffectue á l'intérieur du tube du faisceau. La figure 1.6.3 montre les distributions en η_{max} pour des évènements avec un "leading" proton dans l'état final dans les données DIS et PHP et les prédictions pour diffèrents générateurs Monte Carlo. La distribution expérimentale montre que le "leading" proton est produit principalement dans un processus de dissociation simple.

En dépit des contraintes statistiques rencontrées en 1994, les résultats présentés dans ce travail de recherche montrent les capacités du LPS en tant qu'outil important pouvant améliorer notre connaissance de la production du "leading" proton et des processus diffractifs *ep* en général. Avec une amélioration statistique importante dans la détection du "leading" proton et dans la configuration de l'appareil expérimental, ces études seront de plus en plus approfondies dans le but de mieux comprendre le mécanisme par lequel ces "leading" protons sont produits. Nous espérons continuer notre travail de recherche dans cette direction.

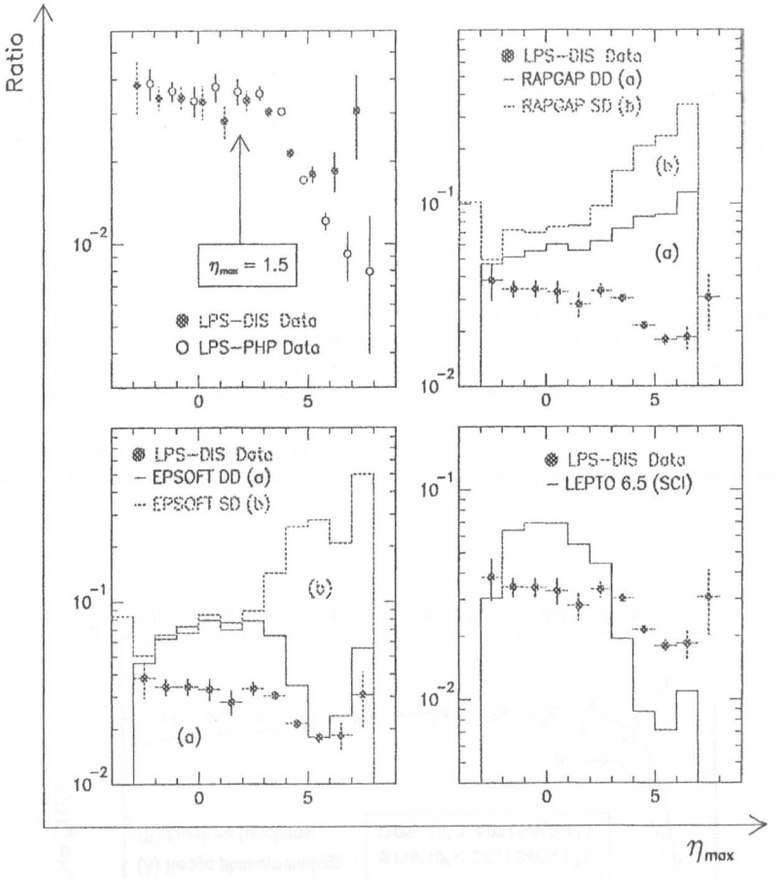

Figure 1.6.3: En haut à gauche: Comparaisons des rapports de η_{max} pour des évènements avec on "leading" proton à l'état final dans les données DIS et PHP. Il est aussi montre une coupure dans $\eta_{max} = 1.5$ utilisée pour la sélection des ces évènements à grande rapidité. En haut à droite et en bas: Comparaisons des rapports de η_{max} pour des évènements avec un "leading" proton à l'état final dans le donnée DIS avec les prédictions des générateurs Monte Carlo RAPGAP, EPSOFT et LEPTO.

2 Introduction

2.1 Overview

Since the first deep inelastic scattering experiment at the Stanford Linear Accelerator Center (SLAC) in 1967, when 20 GeV electrons were directed on a stationary target to probe the structure of a nucleon, the study of hadronic matter has been developed to reach its present status: the theory of Quantum Chromodynamics (QCD).

Influenced by the SLAC measurements [1, 2] and motivated by the assumption of Gell-Mann [3] and, independently, Zweig [4] that hadrons are combinations of more fundamental objects, the so-called quarks, the simple quark-parton model was proposed by Feynman [5] as an intuitive picture to explain the observed Bjorken Scaling [6]. In the parton model the nucleons are composed of point-like constituents, so-called partons, whose properties are identical with those of the quarks, which were originally introduced to account for hadron systems. Thus, the parton model suggested the interpretation of the quarks as constituents of hadronic matter [7]. This suggestion was later supported by the experiment [8].

Data from SLAC indicated that roughly 50% of the nucleon momentum is carried by neutral partons. Even before the discovery of scaling violation, Quantum Chromodynamics [9, 10, 11, 12] as the local gauge theory of the strong interactions predicted eight electrically neutral spin-1 gauge field bosons, the gluons. The gluons are the transmitters of the strong interaction and could explain the fraction of the nucleon momentum carried by neutral partons. With the discovery of asymptotic freedom [13], the decrease in strong coupling constant with increasing four-momentum transfer, three-jet topology at DESY, during the 1970s, Quantum Chromodynamics became a widely accepted theory of the strong interaction. QCD has been tested extensively during the last two decades.

With the advent of the HERA, the $e^{\pm}p$ collider based at DESY in Hamburg, a whole new kinematical regime has been opened up for the study of the collisions of protons with electrons or positrons. It enables us to study proton structure by means of a point-like probing boson whose invariant four-momentum transfer (virtuality), Q^2, enables the constituents of the composite proton carrying a momentum fraction, x as a small as $\approx 10^{-5}$ to be resolved. HERA extends the available range of the x and Q^2 variables by more than two orders of magnitude with respect to other, fixed target, lepton-nucleon experiments that preceded it. Fig 2.1.1 shows the kinematic limits of HERA and other experiments.

Two main experiments at HERA, ZEUS and H1, are used to study the $e^{\pm}p$ collisions. They are devoted, to the study [14] of:

- The proton structure function F_2 for charged and neutral current interactions, its evolution with x and Q^2 and the strong violations of scaling;
- Heavy quark production and its contribution to the determination of the proton structure function F_2;
- Photo-production and deep inelastic scattering simultaneously and in particular deeply inelastic reactions with a diffractive signature;

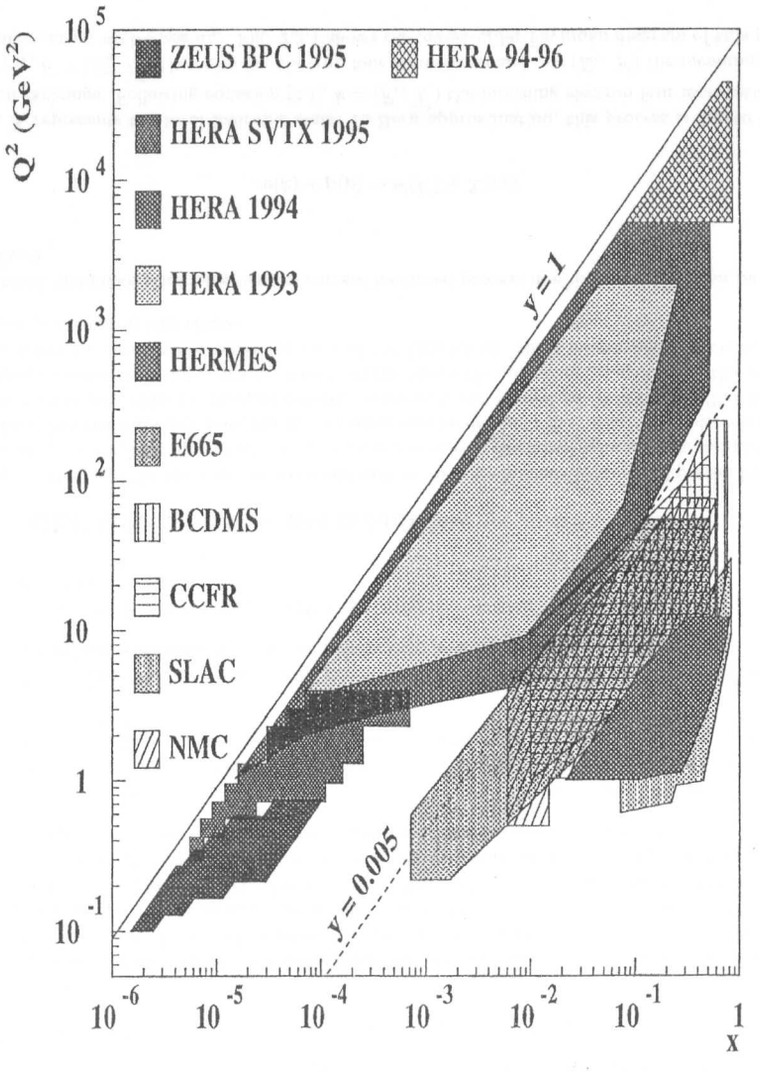

Figure 2.1.1: The $x-Q^2$ plane and the accessed kinematic regions by HERA, and other experiments

- The range of validity of perturbative QCD (pQCD) by:
  - the study of the nature of the hadronic final states and a measurement of α_s from jet rates;
  - precise measurements of the parton distributions as a function of the strong coupling constant α_s;
  - detailed study of low-x phenomena where conventional evolution equations are not required to explain the data.
- ep cross-sections at very large Q^2 as a possible place where an indication of new physics beyond the Standard Model could be found.

In particular, ZEUS is equipped with a high precision silicon tracking device, the leading proton spectrometer (LPS). It allows the detection of forward scattered protons and hence provides extra information firstly as a kinematic constraint in x and secondly in the form of its distribution in longitudinal and transverse momentum space.

For the inclusive leading proton production, the fraction of longitudinal momentum of the incoming proton x_L is connected to x through the following approximated formula:

$$x = \frac{Q^2}{Q^2 + M_X^2} \cdot (1 - x_L)$$

where M_X^2, represents the non-leading invariant mass of either neutral current ($ep \rightarrow e'p'X$) or charged current ($ep \rightarrow \nu p'X$) processes. The way the leading proton x_L relates with x gives, for example, a powerful tool to select low-x events by requiring x_L to be greater than some minimum value. Furthermore, as it will be discussed in section [2.4], for diffractive deep inelastic scattering processes, where the reaction is supposed to be mediated by the exchange of a Reggeized neutral colour object, the quantity $(1 - x_L)$ relates with a good approximation to $x_{I\!P}$, *i.e.* the fraction of the proton momentum carried by such a colour neutral object, the *pomeron*.

The motivation of this thesis is the series of measurements carried out at one of the CERN-ISR experiments, during the 1970s, where it was shown that the general properties of the produced hadrons, in pp collisions, were comparable to the ones found in e^+e^- interactions after removing the leading particle from the sample [15, 16]. This, suggested that the leading particle effect might play an important role in understanding universality features in QCD.

At HERA energies, leading particle production, might be leading protons which can be produced in a wider kinematic range in x and Q^2 than ever before achieved. The measurement of their joint momentum distributions as well as the analysis of their production mechanism are the subject of this thesis.

The remainder of this chapter defines the $e^{\pm}p$ kinematics and relevant invariants and then describes the role of the leading proton in the main classes of interactions, the nature of the $e^{\pm}p$ interactions and their classification at HERA, a review of the theoretical models used to explain the properties of the ep interactions and a description of the available models proposed to explain the production of leading baryons at HERA.

The content of subsequent chapters is as follows:

- Chapter [3]: Describes the ZEUS experiment and the HERA storage ring and points out the features which are relevant to the analysis of the leading proton.

- Chapter [4]: Regards the details of the leading proton spectrometer construction and explains how the momentum of the leading proton is reconstructed prior to the analysis.
- Chapter [5]: Relates the overall data acquisition system of ZEUS and how the LPS is integrated in it.
- Chapter [6]: Deals with the final event selection and analysis, starting with some more details of the kinematics. Then, a description of photo-production and deep inelastic scattering follows. Event samples, data binning, the analysis algorithm and its implementation are discussed in some detail. The best way of combining the prescaled data is discussed and the use of one-dimensional fits to the acceptance corrected P_t^2-distributions in various x_L bins followed by an overall fit to a smooth (x_L, P_t^2) two-dimensional distribution is implemented.
- Chapter [7]: Analyses the details of the various corrections which have been made and shows the variations in the fitted parameters including the various corrections. Furthermore, a calculation of the systematics and final fitted parameters for the production of leading protons are presented.
- Chapter [8]: Compares the results and theoretical predictions for leading proton production. In addition, a comparison with the results from other experiments is presented.
- Chapter [9]: Examines the properties of the global event topology associated with the production of leading protons.

2.2 HERA Kinematics and definitions

At fixed energies of the incoming electron and proton, for unpolarised electron and proton beams the inclusive $ep \rightarrow e'p'X$ or $ep \rightarrow \nu pX$ kinematics is completely described by a set of two independent variables. For neutral current events the variables can be derived either from the scattered electron or the current jet, while for charged current events only the current jet is available. The following discussion concentrates on neutral current events where the measured quantities of the scattered electron can be used in the reconstruction of the kinematics, these events being relevant for the analysis presented in this thesis.

In general, the kinematics for a neutral current mediated process in $e^{\pm}p$ interactions can be written as follows:

$$\mathrm{e}(k) + \mathrm{p}(p) \rightarrow \mathrm{e}'(k') + \mathrm{X}(x_h) \tag{2.1}$$

Here, X represents the total hadronic state. In Born approximation, this process is due to a single photon exchange. Following equation [2.1], $k = (E_e, \overrightarrow{k})$ the incoming electron four momentum with mass m_e, $k' = (E'_e, \overrightarrow{k'})$ the outgoing electron four momentum and $p = (E_p, \overrightarrow{p})$ the incoming proton four momentum with mass m_p. Fig. 2.2.1 shows the lowest-order Feynman diagram of this process.

The quantities that can be measured in the experiment are the energies and angles of the outgoing electron or positron, hadrons and leading baryons. The variables that best describe the HERA kinematics are:

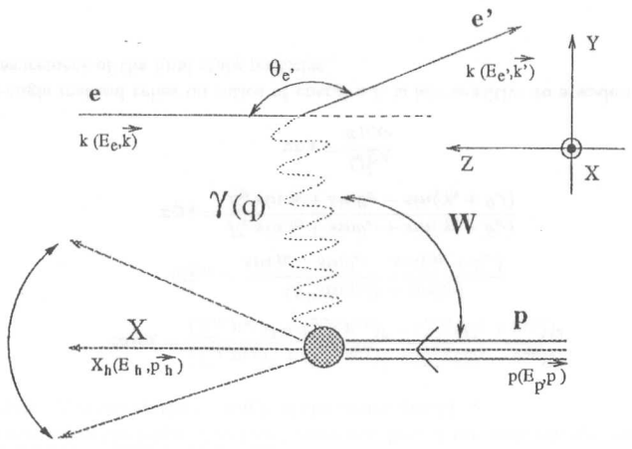

Figure 2.2.1: Lowest-order Feynman diagram for a general $e^{\pm}p$ process

- square of the available energy in the ep center of mass system

$$s = (k+p)^2 = {m_p}^2 + 2k{\cdot}p \simeq 4E_eE_p$$

- square of the four momentum transfer at the electron vertex

$$Q^2 = -q^2 = -(k-k')^2$$

- fraction of the proton $(E + p_{\parallel})$ carried out by the struck quark or Bjorken variable

$$x = Q^2/(2q{\cdot}p) = Q^2/(2m_p\nu)$$

- energy of the photon (γ) in the proton rest frame

$$\nu = (qp)/m_p$$

- fraction of the energy lost by the electron in the proton rest system or in general, the fraction of $(E - p_{\parallel})$ carried by the photon

$$y = (p{\cdot}q)/(p{\cdot}k)$$

- square of the hadronic final state invariant mass in the γp system

$$W^2 = (p+q)^2 \simeq sy(1-x)$$

- mass square of the hadronic system including the leading proton

$$M_x^2 = sy(1-x)$$

- mass square of the hadronic system excluding the leading proton

$$M_x^2 = sy(1-x-x_L)$$

- four momentum transfer, t, if a leading proton with four momentum p' is detected

$$t = p - p'$$

- fraction of the longitudinal momentum carried out by the outgoing proton

$$x_L = p_z'/p_z$$

- fraction of the *pomeron* momentum carried by the struck parton[1]

$$\beta = Q^2/[2(p-p'){\cdot}q]$$

In deep inelastic scattering processes the outgoing hadrons are related to the current jet and the target remnant jet. Taking into account the current jet and the scattered electron, we have four quantities for the reconstruction of the kinematic variables such as x, y and Q^2: the energy and the angle of the electron and the energy and angle of the current jet. Any combination of two of these four quantities can be used to reconstruct the mentioned kinematic variables with a given efficiency and accuracy [17]. The methods [18] to reconstruct them are:

- The electron method: Uses the polar angle (θ_e) and energy $(E_{e'})$ of the scattered electron. From the previous definitions the electron method yields:

$$y = 1 - \frac{E_{e'}}{2E_e}\cdot(1-cos\theta_{e'})$$

$$Q^2 = 2E_eE_{e'}\cdot(1+cos\theta_{e'})$$

$$x = \frac{E_{e'}}{2yE_p}\cdot(1+cos\theta_{e'})$$

and the inverse relations:

$$E_{e'} = (1-y)E_e + xyE_p$$

$$cos\theta_{e'} = \frac{xyE_p - (1-y)E_e}{xyE_p + (1-y)E_e}$$

$$E_{e'}^2 sin^2\theta_{e'} = 4xy(1-y)E_eE_p$$

This method is very sensitive to the initial state radiation where a photon is emitted by the incident electron taking part of its four momentum and therefore shifting the overall energy scale of the event.

- The hadronic method: From the hadron system X_h (excluding the proton remnant) with energy E_h and production angle[2] θ_h one finds:

$$y = \frac{E_h}{2E_e}\cdot(1-cos\theta_h)$$

[1] if the leading proton is produced by the exchange of a colourless object, the *pomeron*, γp interactions can be understood as a peripheral process in which the partonic constituent of the colourless object being exchanged is resolved

[2] θ_h is defined as the angle between the central axis of the hadron system, X_h, and the z axis direction

$$Q^2 = E_h^2 \cdot \frac{sin^2\theta_h}{(1-y)}$$

$$x = \frac{E_h}{2E_p} \cdot \frac{1+cos\theta_h}{(1-y)}$$

and

$$E_h = yE_e + x(1-y)E_p$$

$$cos\theta_h = \frac{(1-y)xE_p - yE_e}{(1-y)xE_p + yE_e}$$

$$E_h^2 sin^2\theta_h = 4xy(1-y)E_eE_p = Q^2(1-y)$$

.

- The Jacquet - Blondel Method [19]: The hadron variables can be determined approximately by summing the energies (E_h) and transverse (p_{Th}) and longitudinal momenta (p_{zh}) of all final states. The method rests on the assumption that the transverse momentum carried by those hadrons which escape detection through the beam hole can be neglected. The result is:

$$y_{JB} = \frac{\sum_h (E_h - p_{zh})}{2E_e}$$

$$Q^2_{JB} = \frac{(\sum_h p_{xh})^2 + (\sum_h p_{yh})^2}{1 - y_{JB}}$$

$$x_{JB} = \frac{Q^2_{JB}}{sy_{JB}}$$

- The mixed or double-angle method [17]: Uses the electron scattering angle and the angle γ_h which characterises the longitudinal and transverse flow of the hadronic system (in the naive parton model γ_h is the scattering angle of the struck quark):

$$cos\gamma_h = \frac{(\sum_h p_{xh})^2 + (\sum_h p_{yh})^2 - (\sum_h (E_h - p_{zh}))^2}{(\sum_h p_{xh})^2 + (\sum_h p_{yh})^2 - (\sum_h (E_h + p_{zh}))^2}$$

$$Q^2_{DA} = \frac{4E_e^2 sin\gamma_h(1+cos\theta_{e'})}{sin\gamma_h + sin\theta_{e'} - sin(\gamma_h + \theta_{e'})}$$

$$x_{DA} = \frac{E_e\, sin\gamma_h + sin\theta_{e'} + sin(\gamma_h + \theta_{e'})}{E_p\, sin\gamma_h + sin\theta_{e'} - sin(\gamma_h + \theta_{e'})}$$

$$y_{DA} = \frac{Q^2_{DA}}{x_{DA}s}$$

As the double-angle method relies on ratios of energies it is less sensitive to a scale uncertainty in the energy measurement of the final state particles.

2.3 The HERA $e^{\pm}p$ Events

The most general form of the cross-section for the process in equation [2.1], for which the details of the calculations can be found in [20], for an unpolarised beam is:

$$\frac{d^2\sigma}{dxdQ^2} = \frac{2\pi\alpha^2}{xQ^4}\left[Y_+F_2(x,Q^2) - y^2F_L(x,Q^2) - Y_-xF_3(x,Q^2)\right](1+\delta_r(x,Q^2)) \qquad (2.2)$$

Where:

$$F_L = F_2 - 2xF_1 \quad \text{and} \quad Y_\pm = 1 \pm (1-y)$$

and:

- α: the electromagnetic coupling constant
- F_2: the generalised structure function which includes both photon and Z^0 exchange
- F_L: the longitudinal structure function
- F_3: the parity violating term arising only from the Z^0 exchange
- δ_r: the electroweak radiative correction
- $Y_\pm$: function which contains the helicity dependence of electroweak interactions

At values of Q^2 below the mass of Z^0 the dominant contribution to the process in equation [2.1] is due to a single photon exchange and the generalised form of the cross-section in equation [2.2] becomes:

$$\frac{d^2\sigma}{dxdQ^2} = \frac{2\pi\alpha^2}{xQ^4}\left[Y_+F_2(x,Q^2) - y^2F_L(x,Q^2)\right] \qquad (2.3)$$

The nature of the structure functions, in general terms, reveal somehow our ignorance of the mechanism by which the X_h in equation [2.1] is produced. There are many theoretical approaches in which the behaviour of the structure functions can be explained, each of them in a certain kinematic (x,Q^2) range.

At HERA, these structure functions of the proton can be measured, in particular F_2 has already been measured over several orders of magnitude in x and Q^2 with a precision of about 5%. Figs. 2.3.1 and 2.3.2 show show the results of these measurements. An extensive review and discussion of the measurements of the structure functions as well as the details of their theoretical interpretations can be found in references [21] and [22].

The $e^{\pm}p$ interaction at HERA can be classified following some specific criteria. One classification may be the hardness of the reaction characterised by the virtuality of the probe, *i.e.* the invariant four momentum transfer, another could be the total energy in the γ^*p system, another, a non-kinematical classification might be the nature of the struck quark in the proton, a valence quark or a quark which is a fluctuation of a gluon or a colour neutral object.

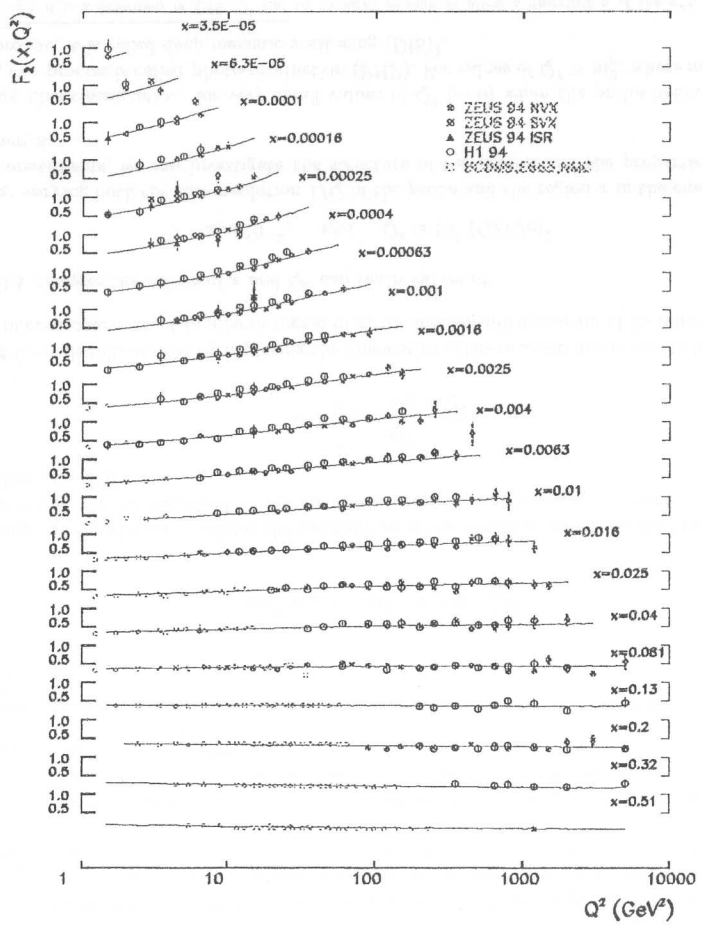

Figure 2.3.1: The proton structure function F_2 measured at HERA and fixed-target experiments as a function of Q^2. The abbreviations NVX and SVX mean *normal vertex* and *shifted vertex* position which relates to changes in the angular range of acceptance of the central detector. The label ISR refers to *initial state radiation* in which the detection and measurement of a photon produced in the initial state allows events with a lower incident electron beam energy to be measured within the same data set as the normal events. The curves shown are the ZEUS NLO DGLAP QCD fit. The description of the DGLAP evolution is given in section [2.3.1].

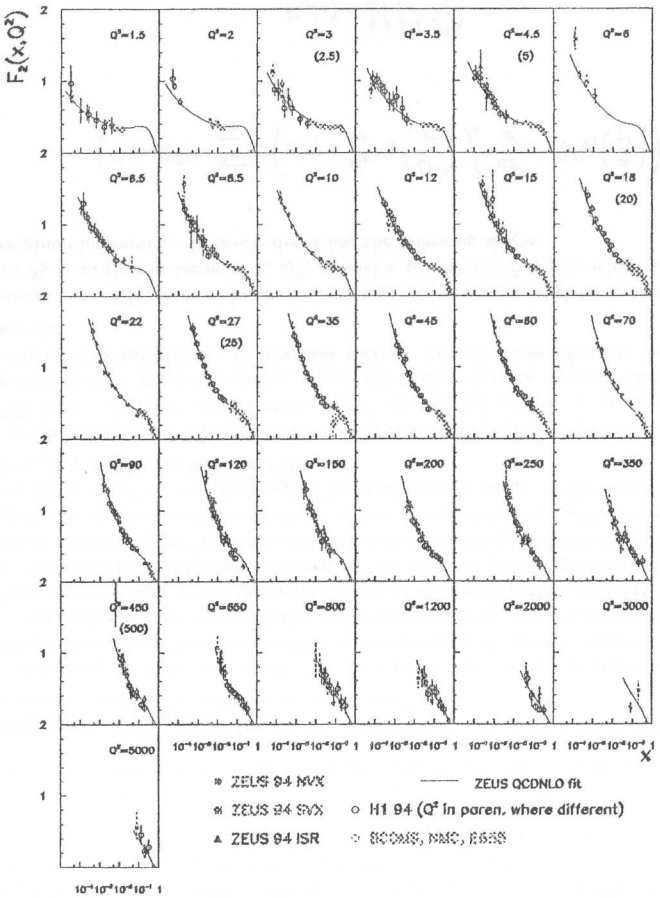

Figure 2.3.2: The proton structure function F_2 measured at HERA and fixed-target experiments as a function of x. The abbreviations NVX and SVX mean *normal vertex* and *shifted vertex* position which relates to changes in the angular range of acceptance of the central detector. The label ISR refers to *initial state radiation* in which the detection and measurement of a photon produced in the initial state allows events with a lower incident electron beam energy to be measured within the same data set as the normal events. The curves shown are the ZEUS NLO DGLAP QCD fits. The description of the DGLAP evolution is given in section [2.3.1].

Choosing the hardness of the reaction as a classification criteria lets us define two kinematic regions in which the structure of the proton can either be resolved or not. This choice, according to [23] is supported by the fact that in a general $ep \to e'p'X$ interaction, as shown in Fig. 2.2.1, the electron four-momentum $-Q^2$ which is transferred to the proton target by means of a probe, denoted γ^* has a wave length λ of order:

$$|q^2|^{-1/2} = 1/Q$$

The value of Q turns out to be the resolution by which the probe may resolve the structure of the target, the incoming proton. In the quark-parton model, a high energy proton is assumed to be made up of point-like particles called partons, freely moving inside the proton. Among them there are electrically charged particles, the quarks and anti-quarks, which are able to interact with the photon probe. Thus, the photon hits a quark carrying a fraction x of the total momentum of the incoming proton. The point-like quark (or anti-quark), is scattered but not 'destroyed' by the photon as is the case for a compound particle. Once the quark is expelled by the interaction, the proton generally explodes into numerous particles.

Following the momentum conservation law at the proton vertex, the following equation can be derived:

$$(xp)^2 \approx (xp+q)^2 \Longrightarrow x \approx \frac{-(q)^2}{2pq} \tag{2.4}$$

This result is crucial since it relates the momentum of the struck quark, x, to the kinematics of the reaction which can be measured in the apparatus. Indeed, it is possible to rewrite the right-hand side of formula [2.4] as:

$$x = \frac{Q^2}{W^2 - M_p^2 + Q^2}$$

The last formula tells us that by exploring the kinematics of the reaction one is able to investigate the proton microscopic content in a large region of x, the momentum spectrum of its inner constituents.

At HERA energies the values of x and Q^2 can reach values of:

$$x \approx 10^{-5}; \quad \text{and} \quad Q^2 \approx 10^5 \ (\text{GeV/c})^2$$

Thus, by varying both the size-resolution $1/Q$ of the probe and the region x in the energy spectrum of the constituents, we can investigate the structure of the proton and the properties of its inner constituents.

Following this classification, for very small values of Q^2 (~ 0) when the probe behaves like a real photon, the process is called photo-production (PHP). For values of $Q^2 > m_p^2$, where m_p is the mass of the proton, it is called deep inelastic scattering (DIS)[3].

[3]Although it is a definition of DIS, Q^2 has to be large enough to allow a description of the $e^{\pm}p$ interactions by perturbative QCD

2.3.1 General Deep Inelastic Scattering (DIS)

Deep inelastic scattering can be understood as a hard process where the virtual particle exchanges a high $Q^2 >> m_p^2$. Because of the large transfer of energy, the initial state proton will often break up and lose its identity. This kind of process occurs at small distances (order of $\sim 1/\sqrt{Q^2}$), can select a large fraction of the initial nucleon momentum $x \approx 1$ and so can be analysed in perturbative QCD (pQCD). Its cross-section (Equation [2.3]) decreases with increasing Q^2.

However, there are processes which occurs at large values of Q^2 and low values of x ($x \approx 10^{-4}$). According to QCD, at such values of x and Q^2, a nucleon consists predominantly of gluons and sea quarks. Their densities grow rapidly in the limit $x = 0$ leading to spatial overlap and to interactions between the partons. In this region, several novel physical phenomena are expected when the parton densities are high, as e.g. shadowing or semi-hard processes appearing with large cross sections in the high energy hadronic interactions.

Several classes of process that contribute to the DIS sample are considered as follows:

- Scattering on a parton inside the proton: Intuitively, in the framework of QCD, it can be understood as a scattering on a valence or sea quark.

  The scattering on a valence quark gives a scattered quark and a spectator diquark (Fig. 2.3.3(A)). The strong force responsible for confinement of quarks, leads to hadron production (materialisation) in re-establishing colour neutral states, pions as a first step. This kind of scattering can be best viewed in the framework of the quark parton model (QPM) introduced by R. Feynman [5] which was motivated by the *Bjorken scaling hypothesis* [6] of the proton structure function F_2 and by the assumption that DIS undergoes direct interaction with one of the point-like *partons* constituents of the proton. Scaling behaviour of F_2 works approximately in the region of Q^2 of few times m_p^2. The quark parton model is the lowest order Feynman diagram in perturbative QCD (pQCD).

  The scattering on a sea quark comes from the virtual process $g \to q\bar{q}$ inside the proton (Fig. 2.3.3(B-left)). At large enough values of Q^2, the virtual photon γ^* is probing the parton substructure deep inside the proton where the valence quarks interact with each other by exchanging coloured gluons. F_2 increases with Q^2 for low values of x and decreases at high values of x.

  A general form of F_2, to describe the above mentioned processes, is given in perturbative QCD, where F_2 is written in terms of x, Q^2, α_s and a probability function which accounts for the quark-gluon interaction. In first order it has the following shape:

$$\frac{1}{x}F_2(x,Q^2) = \sum_q e_q^2 \left(q(x) + \frac{\alpha_s}{2\pi} \log\left(\frac{Q^2}{\mu^2}\right) \int_x^1 \frac{dx'}{x'} q(x') P_{qq}\left(\frac{x}{x'}\right) \right) \tag{2.5}$$

  where

$$P_{qq}(z) = \frac{4}{3}\left(\frac{1+z^2}{1-z^2}\right)$$

  $P_{qq}(z)$ is the probability that a quark radiates a gluon leaving a quark which carries a fraction of its longitudinal momentum z. $P_{qq}(z)$ is one of the perturbative QCD splitting functions which describes the amplitude at which partons are radiated from other partons (Fig. 2.3.3(B-right)).

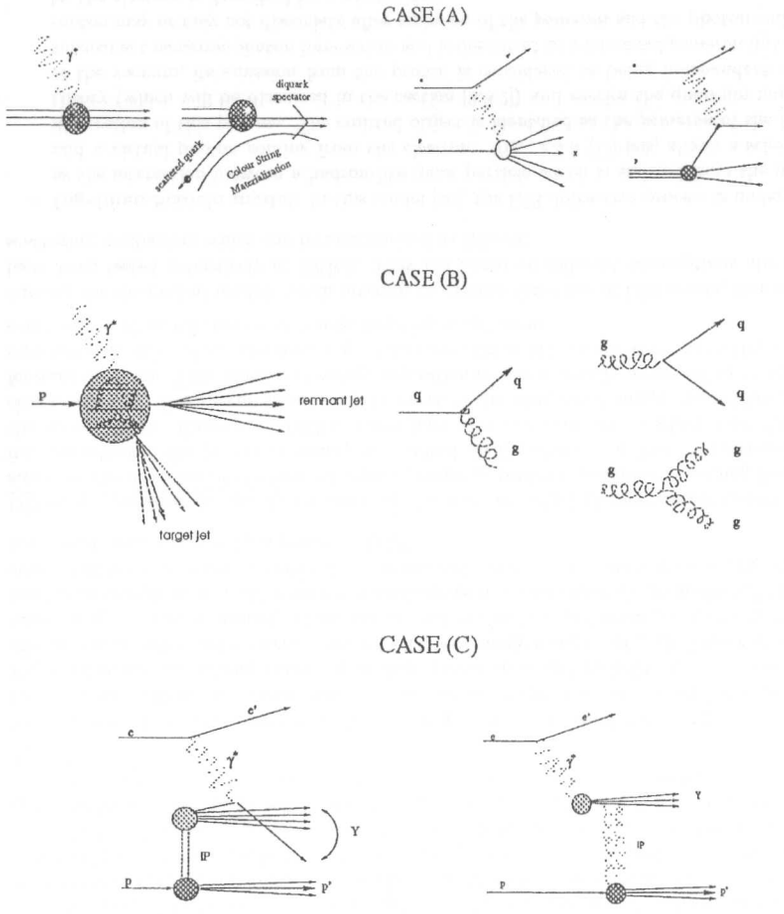

Figure 2.3.3: Three cases of DIS events at HERA. (A)-left: Intuitive picture of a standard DIS, the virtual photon knock-off a constituent valence quark and, as a result of the strong interactions, a materialisation fills the gap between the scattered quark and the diquark spectator. (A)-right: Low-order Feynman diagrams for this processes. (B)-left: Intuitive picture of the resolving power of the probe (γ^*) to resolve the internal structure of the partons. (b)-right: Feynman diagrams for the pQCD splitting functions which accounts for the probable interaction mechanisms of quarks and gluons inside the proton. (C): Examples of two models to explain the diffractive DIS. The Ingelmann-Schlein (left) and Nikolaev-Zakharov (right) model.

The presence of the $\log Q^2$ factor in equation [2.5] means that the parton model scaling prediction for the structure functions should be violated. That is, in QCD, F_2 is a function of Q^2 as well as x, but the variation in Q^2 is only logarithmic. The violation of Bjorken scaling is a signature of gluon emission.

The second term in equation [2.5] which are identified as the quark density functions, $q(x, Q^2)$, with:

$$\Delta q(x, Q^2) \equiv \frac{\alpha_s}{2\pi} \log\left(\frac{Q^2}{\mu^2}\right) \int_x^1 \frac{dx'}{x'} q(x') P_{qq}\left(\frac{x}{x'}\right) \tag{2.6}$$

depends on Q^2. This is interpreted as arising from a photon with larger Q^2 probing a wider range of transverse momentum within the proton. The Q^2 evolution of the quark densities is determined by QCD through equation [2.6]. By considering the change in the quark density, $\Delta q(x, Q^2)$, when one probes a further interval of $\Delta \log Q^2$, equation [2.6] can be rewritten as an integro-differential equation for $q(x, Q^2)$:

$$\frac{dq(x, Q^2)}{d\log Q^2} = \frac{\alpha_s}{2\pi} \int_x^1 \frac{dx'}{x'} q(x', Q^2) P_{qq}\left(\frac{x}{x'}\right) \tag{2.7}$$

This is an "Altarelli Parisi evolution equation" and mathematically expresses the fact that a quark with momentum fraction x could have come from a parent quark with larger momentum fraction x' which has radiated a gluon. The probability that this happens is proportional to $\alpha_s P_{qq}(x/x')$.

To include contributions where a gluon in the initial proton produces a quark-antiquark pair to which the virtual photon couples, that is the higher order process $\gamma^* g \rightarrow q\overline{q}$, equation [2.7] is rewritten as:

$$\frac{dq_i(x, Q^2)}{d\log Q^2} = \frac{\alpha_s}{2\pi} \int_x^1 \frac{dx'}{x'} \left(q_i(x', Q^2) P_{qq}\left(\frac{x}{x'}\right) + g(x', Q^2) P_{qg}\left(\frac{x}{x'}\right) \right) \tag{2.8}$$

The second term in equation [2.8] considers the possibility that a quark with momentum fraction x is the result of a $q\overline{q}$ pair creation by a parent gluon with momentum fraction x' ($> x$) and probability $\alpha_s P_{qg}(x/x')$. The equation for the evolution of the gluon density in the proton, analogous to equation [2.8] is:

$$\frac{dg(x, Q^2)}{d\log Q^2} = \frac{\alpha_s}{2\pi} \int_x^1 \frac{dx'}{x'} \left(\sum_i q_i(x', Q^2) P_{gq}\left(\frac{x}{x'}\right) + g(x', Q^2) P_{gg}\left(\frac{x}{x'}\right) \right) \tag{2.9}$$

where the sum $i = 1, ...2n_f$ runs over quarks and antiquarks of all flavours.

Perturbative QCD does not predict the absolute value of the parton distribution inside the nucleon, but rather determines how they vary from a given input. For instance, from a given initial distribution at some scale Q_0^2, the Dokshitzer-Gribov-Lipatov-Altarelli-Parisi (DGLAP) [24] evolution equation enables us to determine the distribution at higher Q^2. The DGLAP evolution resums the leading $\alpha_s \ln(Q^2/Q_0^2)$ terms where, in a physical gauge, the $\alpha_s^n \ln^n(Q/Q_0)$

contribution is associated with a space-like chain of n-gluon emissions in which the successive gluon transverse momenta are strongly ordered along the chain, that is $q^2_{T1} << ... << q^2_{Tn} << Q^2$.

At sufficiently high center of mass energy $\sqrt{s}$, a second large variable, $1/x \sim s/Q^2$, is found and the leading $\alpha_s \log(1/x)$ contributions must be resummed. The resummation is accomplished by the Balitsky-Fadin-Kuraev-Lipatov (BFKL) equation [25]. In this case there is no ordering in $\ln(q^2_{Ti})$ along the chain, but rather, as one evolves to smaller x, one has a diffusion or random walk in $\ln(q^2_{Ti})$. The lack of strong ordering means that one has to work in terms of the gluon distributions $f(x, k^2_T)$ unintegrated over the gluon transverse momentum k_T. Proceeding to small values of x, via the BFKL equation, the gluon density f is predicted to increase as x^λ with $\lambda \sim 0.5$ (on account of the increased q_{Ti} phase space) and to posses a Gaussian-type distribution in $\ln(k^2_T)$ which broadens as $\sqrt{\ln(1/x)}$. This singular type of growth in x, accompanied by the diffusion in $ln(k^2_T)$, is the characteristic of the BFKL gluon density $f(x, k^2_T)$.

The increase of the gluon density with decreasing x cannot proceed indefinitely. Eventually, the so-called critical line where gluon recombination effects become appreciable is reached. Fig 2.3.4 shows the validity range where these evolution equations hold. At the onset, these effects can be estimated by perturbative QCD, but finally a region of high density of weakly interacting partons is reached, where the normal methods of perturbation theory cannot be used even though α_s is small -a region of much speculation and interest. At higher Q^2 one can evolve further in x before the critical line is reached, since the resolution goes as $1/Q$ and the transverse area occupied by a parton $\sim 1/Q^2$.

- Diffractive processes in DIS: Experimentally, the standard $e^\pm p$ DIS events show energy deposition in the direction of the forward region (outgoing proton), presumably coming from the fragmentation of the proton remnant, from initial QCD radiation or from fragmentation of the struck quark. However at HERA, there have been observed events which have different characteristics. The special feature of the event is the absence of energy deposition in the forward direction. This absence of energy deposition or *gap* is usually measured as an angular separation in units of pseudorapidity η. Diffractive DIS at HERA corresponds to this kind of event and is often referred to as "Large Rapidity Gap" event.

  Among the theoretical models which attempt to explain this class of DIS events, two models have been tested extensively at HERA. They are based on different assumptions about the scattering mechanism which can be summarised as follows:

  - **Ingelman-Schlein model:** In this model [26], the DIS diffractive process is understood as the interaction between a hadron-like quasi particle which is emitted from the proton and a virtual photon coming from the electron. Fig. 2.3.3 (C)-left, shows a schematic illustration of this process. The emitted object is identified as the *pomeron* of the Regge theory (which will be discussed in the section [2.3.2]) and carries the quantum numbers of the vacuum, its emission from the proton is considered as being independent of the subsequent *pomeron*-photon interaction and is described as a universal *pomeron* flux. The proton may or may not dissociate after emission of the *pomeron* and the photon emission by the electron is described by a photon flux.

    With increasing Q^2 of the photon, the internal structure of the *pomeron* can be probed in the same way as for the partons inside the proton. The *pomeron* structure function is introduced by analogy to the proton structure function. The hard scattering sub-process can then be interpreted as the interaction between the exchanged photon and a parton, carrying a fraction x_p of the *pomeron* momentum. The remaining *pomeron* momentum

fraction $1 - x_p$ is carried by the *pomeron* remnant Y. For the parton distribution inside the *pomeron* different assumptions can be made. One can postulate a hard distribution (valence-like), where only few partons carry the *pomeron* momentum or soft one (sea-like), where many partons share the momentum of the *pomeron*.

The first evidence for partonic structure of the *pomeron* was detected in $p\bar{p}$ collisions at the CERN SPS collider by the UA8 experiment [27]. The model has been tested with different assumptions on the momentum distributions of the partons inside the *pomeron*, suggesting a hard parton distribution. At HERA, evidence for gluonic content of the *pomeron* has been found indicating that between 30% and 80% of the *pomeron* momentum carried by the partons is due to a gluonic content.

- **Nikolaev-Zakharov model:** In this model [28] the incoming virtual photon fluctuates into $q\bar{q}$ or $q\bar{q}g$ Fock states that interact through their colour dipole moment with an object which is emitted from the proton. This object is called a *pomeron* and is understood not as a particle but rather as a coupling mechanism. To lowest order it can be viewed as a colour singlet of two noninteracting and seemingly uncorrelated gluons emitted with different flux factors from the proton. This model is often referred to as photon diffractive dissociation on the proton (Fig 2.3.3 (C)-right).

  Factorisation and meaning of *pomeron* structure function are not applicable in this model. However, it has been shown [29] that in the framework of perturbative QCD BFKL equation, the hadron-like behaviour of this *pomeron* can be understood as an asymptotic feature allowing the derivation of an equivalent to a *pomeron* structure function:

$$\beta P_{NZ}(\beta, Q^2) = C \cdot (A \cdot \beta(1-\beta)^2 + B \cdot (1-\beta)^3)$$

  where $\beta = x/x_P$. Here, in contrast to the Ingelman-Schlein model, x_P is the fraction of the proton longitudinal momentum carried by the *pomeron* and x is the Bjorken scaling variable. The first term of this two component structure function is referred to as "hard" component and it can be interpreted as the interaction with the $q\bar{q}$-state of the photon. The second term reflects the "soft" contribution of the interaction with the $q\bar{q}g$-state of the photon. The factors A and B give the relative size of their contribution and are predicted by the model to be 65% and 35% respectively, C representing an overall normalisation factor.

  An important aspect of this model is the prediction that photon dissociative diffraction contributes $\sim 15\%$ to the DIS cross section.

2.3.2 General Photo-production (PHP)

Intuitively, photo-production, in $e^\pm p$ interactions, can be understood as processes which occur at large distances comparable with the radius of the target hadron($\sim R_{hadron}$). At high energies, previous fixed-target experiments showed that the photon does not necessarily interact as a gauge boson. It rather exhibits a hadronic type of scattering which can be explained by the fact that it can fluctuate into a hadron [30] before it scatters off the proton.

Photo-production is usually described as a γp scattering which is characterised for its large cross section in the region of low $Q^2 \sim 0$ and intermediate x. It reveals properties similar to hadron-hadron scattering.

Different theories attempting to describe γp interactions have been proposed. Among them, a brief summary of those which have been very successful in describing the γp interactions are presented.

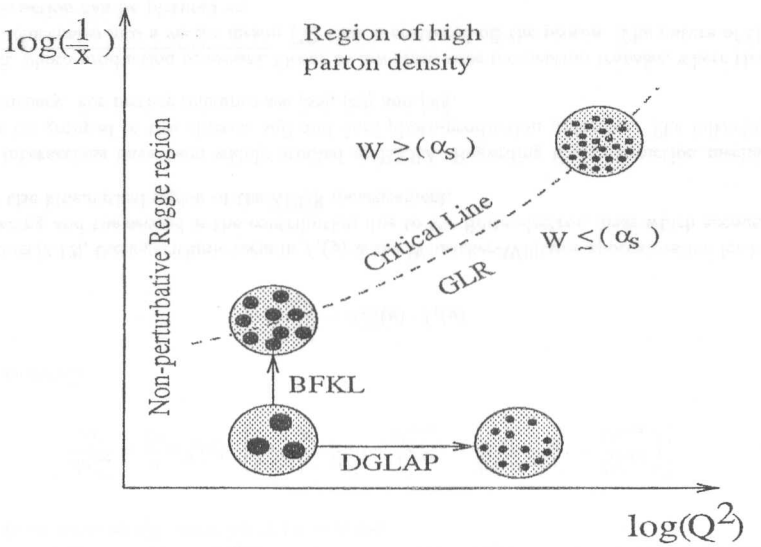

Figure 2.3.4: The gluon content of the proton as "seen" in various deep inelastic (x, Q^2) regimes. The critical line, where gluon recombination becomes significant, occurs when $W \approx O(\alpha_s)$. W is the ratio of the quadratic recombination term to the term linear in the gluon density which occur on the right hand side of the evolution equation. The label GLR stands for Gribov-Levi-Ryskin evolution equation, which takes into account non linear effects such as shadowing and can be solved as a perturbation series in the region where $W < \alpha_s$.

- Vector Dominance Model (VDM) [31]: Describes the fluctuation of real photons into a superposition of vector mesons V with quantum numbers equal to the photon. The photon may, according to Heisenberg's uncertainty principle, be in such a state for a short time, defined by:

$$t_f = \frac{2k}{m_V^2}$$

  where k is the photon energy in the proton rest frame and m_V the mass of the vector meson. Although this time period is short, it is long enough for a photon with HERA energies to travel a distance which is many hundred times longer than the proton radius. As a result it has a probability to fluctuate into a vector meson and interact with the proton via the strong force.

- Regge theory: In view of the vector dominance model, Regge theory can be used to describe the γp interactions as an exchange of a trajectory, *Reggeon* or *Pomeron*. It is based on the analysis of the properties of the S scattering matrix and on the study of the location of its singularities in the complex angular momentum plane [32] $(\alpha(t), t)$. This applies to a two body interaction in the t-channel ($\alpha(t)$, being the angular momentum of the exchanged trajectory).

  With the addition of the optical theorem, for a Regge trajectory exchange, the total cross-section of a two-body scattering process in the high energy limit $(s \to \infty)$ with t fixed, can be approximated as:

$$\sigma_{tot} \sim \left(\frac{s}{s_o}\right)^{\alpha(0)-1} \tag{2.10}$$

where s and t are the Mandelstam variables characterising such a process and $s_o \sim 1\text{GeV}$ a scale parameter.

Regge theory has been very successful in describing hadron-hadron interactions. However, since all known trajectories have an intercept $\alpha(0) \leq 0.5$, the cross section shown in equation [2.10] should decrease asymptotically with increasing energies. This behaviour can be avoided by introducing a new trajectory with $\alpha(0) = 1$ with the quantum numbers of the vacuum [33]. This trajectory is called *pomeron*, in honour to I.V. Pomeranchuck who demonstrated a theorem [34] which states that in the the high energy limit the difference between the particle and anti-particle cross-section should vanish.

The behaviour of the total hadronic cross-section was further studied by M. Froissart who showed that in the limit $s \to \infty$, it has an upper bound [35] defined by:

$$\sigma_{tot} \leq \frac{\pi}{m_\pi^2} \ln^2\left(\frac{s}{s_o}\right)$$

where m_π is the mass of the pion. Furthermore, on the basis of the Regge approach, Donnachie and Landshoff [36] predicted that the behaviour of the total cross-section for hadron-hadron and photo-production interactions, in the high energy limit, can be pictured as the sum of two powers. One power is associated with the exchange of ρ, ω, f_2, and $a2$, Regge trajectories with a common intercept $\alpha_R(0) \sim 0.5$ which describes the initial rise of the cross-section at low energies, and the other power is associated with the *pomeron* exchange dominating the behaviour of the cross-section at higher energies, so that:

$$\sigma_{tot} = X s^\epsilon + Y s^\eta$$

where the quantities X and Y depend on the reaction, whereas ϵ and η are related to the *pomeron* and *reggeon* intercepts. For instance:

$$\epsilon = \alpha_{I\!P}(0) - 1 = 0.0808$$
$$\eta = \alpha_R(0) = -0.4525$$

To evaluate the total γp cross-section, equation [2.2] is often rewritten in terms of the fraction of $(E - p_{||})$ of the incoming electron carried by the photon (y) rather than in terms of the fraction $(E + p_{||})$ carried by the struck quark (x). Thus:

$$\frac{d^2\sigma}{dydQ^2} = \frac{4\pi\alpha}{Q^2}\left[\left(\frac{1+(1-y)^2}{y} - \frac{2(1-y)}{y}\cdot\frac{Q^2_{min}}{Q^2}\right)\cdot xF_1(x,Q^2) + \frac{(1-y)}{y}\cdot F_L(x,Q^2)\right]$$

$F_1(y, Q^2)$, and $F_L(y, Q^2)$ can now be replaced by the photon-proton cross-section $\sigma_T(W_{\gamma p}, Q^2)$ and $\sigma_L(W_{\gamma p}, Q^2)$ for transversely and longitudinally polarised photons,

$$xF_1(x,Q^2) = \frac{1}{4\pi^2\alpha}\frac{Q^2}{2}\sigma_T^{\gamma p}(W_{\gamma p}, Q^2), \quad \text{and} \quad F_L(x,Q^2) = \frac{1}{4\pi^2\alpha}\frac{Q^2}{2}\sigma_L^{\gamma p}(W_{\gamma p}, Q^2)$$

This yields

$$\frac{d^2\sigma}{dydQ^2} = \frac{1}{2\pi}\left[\left(\frac{1+(1-y)^2}{y} - \frac{2(1-y)}{y}\frac{Q^2_{min}}{Q^2}\right)\sigma_T^{\gamma p}(W_{\gamma p}, Q^2) + \frac{(1-y)}{y}\sigma_L^{\gamma p}(W_{\gamma p}, Q^2)\right] \quad (2.11)$$

Equation [2.11] relates the electro-production and photo-production cross-sections. For γp interactions with almost real photons, VDM predicts:

$$\sigma_T^{\gamma p}(W_{\gamma p}, Q^2) = \sum_{V=\rho,\omega,\phi} \frac{c^2}{f_V^2}\left(\frac{m_V^2}{m^2+Q^2}\right)^2 \sigma_T^{Vp}(W_{\gamma p})$$

$$\sigma_L^{\gamma p}(W_{\gamma p}, Q^2) = \sum_{V=\rho,\omega,\phi} \frac{c^2}{f_V^2}\left(\frac{m_V^2}{m^2+Q^2}\right)^2 \sigma_T^{Vp}(W_{\gamma p}) \cdot \frac{\xi_V Q^2}{m_V^2}$$

Here, f_V is a probability function for the $\gamma \to V$ transition, c is the speed of light, $\sigma_T^{\gamma p}(W_{\gamma p}, Q^2)$ is the total cross-section for scattering of a transversely polarised vector meson $V = \rho, \omega, \phi$ off a proton at center of mass energy W and $\xi_V = \sigma_L^{Vp}(W_{\gamma p})/\sigma_T^{Vp}(W_{\gamma p})$. The value of ξ_V is expected to be in the range $0 \leq \xi_V \leq 1$, as longitudinally and transversely polarised hadrons may not have the same cross-section [37].

For very small values of $Q^2 << m_V^2 \sim 1$ (GeV/c)^2 the longitudinal component of the cross-section can be neglected and integrating over Q^2 from Q^2_{min} to Q^2_{max}, where Q^2_{max} is set by the ZEUS geometrical acceptance for low angular scatter of electrons ($Q^2_{max} = 0.002$ (GeV/c)^2), and ignoring any Q^2 dependence of $\sigma_T^{\gamma p}$, equation [2.11] becomes:

$$\frac{d\sigma_{tot}^{ep}}{dy} = \frac{\alpha}{2\pi}\sigma_{tot}^{\gamma p}(y) \cdot \left[\frac{1+(1-y)^2}{y}\ln(\frac{Q^2_{max}}{Q^2_{min}}) - \frac{2(1-y)}{y}\left(1 - \frac{Q^2_{min}}{Q^2_{max}}\right)\right] \quad (2.12)$$

or more generally:

$$\frac{d\sigma_{tot}^{ep}}{dy} = \sigma_{tot}^{\gamma p}(y) \cdot f_\gamma(y)$$

In equation [2.12], the logarithmic term in $f_\gamma(y)$ is the Weizäcker-Williams approximation for low-Q^2 ep scattering and the second is the contribution due to the finite electron mass which accounts for $\sim 7\%$ in the kinematical region of the ZEUS measurement.

The γp interactions have been widely studied at HERA. Regarding their interaction mechanism, they can be grouped in two classes: *soft* and *hard* photo-production processes. The following is a short summary. For further reference see [38], [39] and [40].

- Soft photo-production processes: Occur at low transverse momentum transfer, where the photon fluctuates into a vector meson (V) that is scattered off the proton. The nature of the Vp interaction can be pictured as:
  - Quasi-elastic diffraction scattering with cross-section σ_{elas}. This process has a vector meson and the proton in the final state (Fig. 2.3.5-A).

  - Inelastic diffractive scattering, which allows either the proton or the vector meson to dissociate into final states of higher mass with the same quantum numbers as the incident particles. In the reaction $A + B \to X$, σ_{sd}^{AX} and σ_{sd}^{BX} describes the cross-section for single dissociation of one of the scattering particles whereas σ_{dd} stands for the case when both particles dissociate into diffractive final state (Fig. 2.3.5-B).
  - Soft-non-diffractive interactions, which are described as the scattering of a vector meson and a proton with exchange of quantum numbers (Regge trajectory). This process is characterised by the presence of a multi-particle final state. Its cross section σ_{minb} is small (Fig. 2.3.5-C).

The soft photo-production cross section can be written as follows:

$$\sigma_{soft}(s) = \sigma_{elas}(s) + \sigma_{sd}^{AX}(s) + \sigma_{sd}^{BX}(s) + \sigma_{dd}(s) + \sigma_{minb}(s)$$

- Hard photo-production processes: In which high transverse momentum partons are present in the final state, the γp scattering may be described via perturbative QED and QCD through the following definitions:
  - Direct γp interactions, where the photon interacts directly with a charged parton from the proton. In this case all the photon momentum x_γ is transferred in the interaction (Fig. 2.3.6-A).
  - Resolved γp interactions, where the interaction can be described as a two-step process in which the photon first resolves into partons and then one of the parton participates in the hard interaction. Thus, the photon and the proton are parametrised *via* parton density functions, describing the probability that the interacting partons of the photon (or proton) has a longitudinal momentum fraction x_γ (or x_p) (Fig. 2.3.6-B).

The meanings of *direct* and *resolved* γp interactions are well defined and they are separated by appropriate cuts in the reconstruction of x_γ. So that for *direct* process:

$$x_\gamma = 1$$

whereas for *resolved* process:

$$x_\gamma < 1$$

The hard photo-production cross-section can be written, in the framework of leading order calculations as:

$$\sigma_{hard}(s) = \sigma_{dir}(s) + \sigma_{res}(s)$$

2.4 Leading Baryons at HERA

At HERA, in most $e^\pm p$ events the debris of the proton is emitted at very small forward angles and escapes undetected down the beam pipe. It is, however, experimentally possible to gain access to the very forward region for a class of events which contains a leading baryon in the final state.

Leading baryons, and especially leading protons, are detected by placing low-angle detectors very near to the beam pipe so that in conjunction with the bending magnets of the accelerator, they provide a high precision spectrometer for fast forward going protons.[4] The production of leading protons yields a fraction of fully contained neutral current $e^\pm p$ events.

[4] Detailed description of the experimental setup to detect leading protons is given in chapter [4].

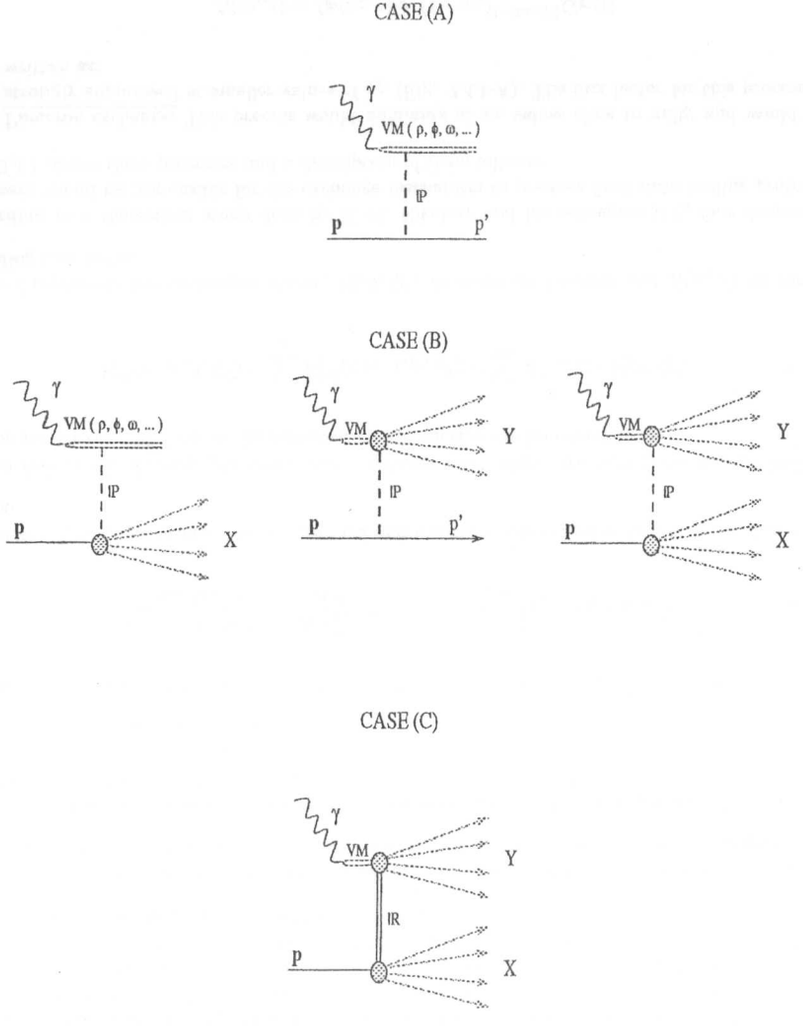

Figure 2.3.5: Soft photo-production subprocesses: (A) elastic diffractive, (B) diffractive proton, photon and double dissociation (C) non diffractive

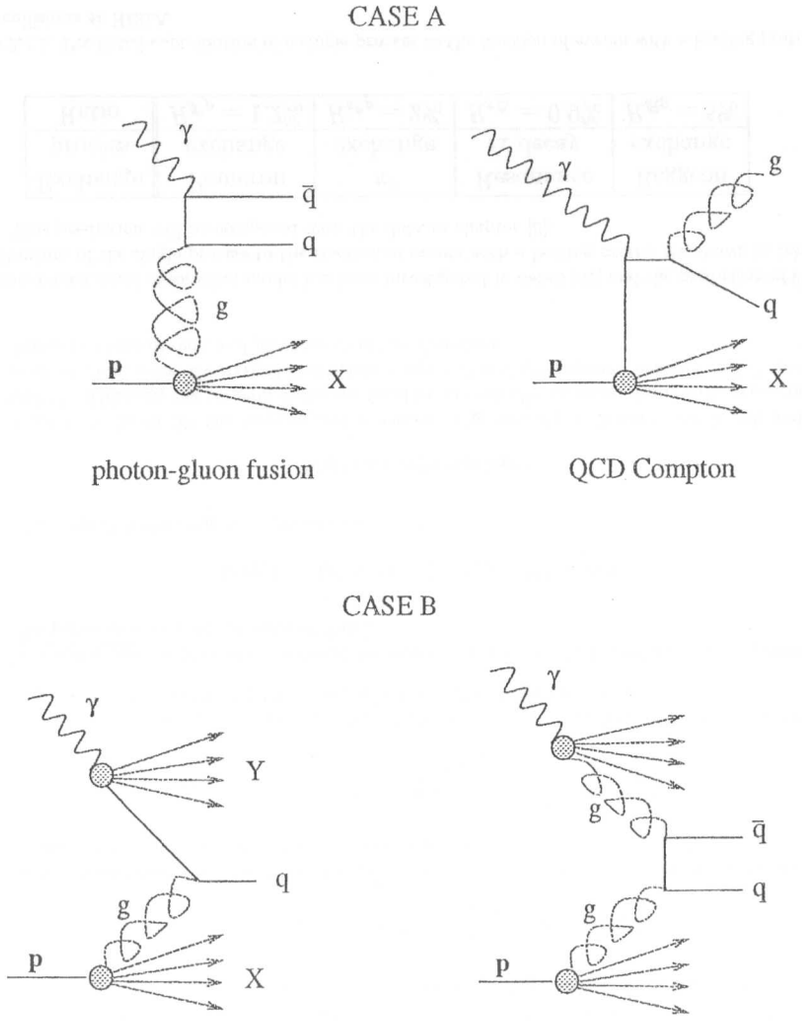

Figure 2.3.6: Hard photo-production subprocesses: (A) direct (γg fusion and QCD compton) (B) resolved (examples)

A complete QCD description of the $e^{\pm}p$ interaction should be able to correctly describe the observed x_L and t distribution of the leading proton. However, although the present theoretical status allows us explain the generalities of the $e^{\pm}p$ reactions, there are processes which are not well explained in the framework of QCD. Especially those processes which involve the production of a leading particle. Hence, a detailed study of leading particle production, in particular of the leading proton, will provide the necessary measurable quantities to test the available models and provide a more complete understanding of its production mechanism.

Among the processes expected to generate leading protons are soft and hard photo-production, diffractive deep inelastic scattering, and also neutral and charged current interactions in general.

In the following, two theoretical models, proposed to explain the leading proton production at HERA will be discussed in some detail

2.4.1 Regge phenomenology

Equation [2.3], can be rewritten, for the semi-inclusive processes $ep \rightarrow e'p'X$, as follows:

$$\frac{d^4\sigma(ep \rightarrow e'p'X)}{dxdQ^2dx_Ldt} = \frac{2\pi\alpha_{em}^2}{xQ^2}\left[2(1-y) + \frac{y^2}{1+R}\right]F_2^{(4)}(x_L, t, \beta, Q^2) \tag{2.13}$$

where $R = \frac{\sigma_L}{\sigma_T}$, is the ratio of the longitudinal and transverse cross-section for photon-proton scattering.

In the framework of Regge phenomenology, exchange mechanisms are responsible for the leading proton production. $F_2^{(4)}$ under the factorisation assumption can be rewritten as:

$$F_2^{(4)}(x_L, t, \beta, Q^2) = \sum_i F_2^{(4)}(i; x_L, t, \beta, Q^2) = \sum_i f_i(x_L, t) \cdot F_2^i(\beta, Q^2) \tag{2.14}$$

where i represents the exchanged object, $F_2^i(\beta, Q^2)$ its structure function and $f_i(x_L, t)$ its corresponding flux factor.

According to a theoretical study done by N. N. Nikolaev and his colleagues [41], four dominant processes would be responsible for the exchange mechanism to produce final state leading protons. Fig. 2.4.1 shows these processes and a description of them follows:

- Pomeron exchange: This process would dominate at x_L values close to unity and would be strongly suppressed at smaller values of x_L (Fig. 2.4.1-A). The flux factor for this process is written as:

  $$f_i(x_L, t) = f_{I\!P}(x_L, t) \propto (1 - x_L)^{1-2\alpha_{I\!P}(t)} G_{I\!P}(t)$$

  With: $G_{I\!P}(t) = G_o exp(B_{I\!P} t)$, being the *pomeron* form factor. G_o and $B_{I\!P}$ are calculated from Regge analysis of hadronic diffractive scattering and found to be 21 mb and 3.8 GeV^{-2} respectively

- π-exchange and Δ resonance: Processes that generate either a spectator proton (Fig. 2.4.1-B) or a baryon resonance that then decays into a proton (Fig. 2.4.1-C).

  In the first case, the spectator proton is generated by the fragmentation of the πp Fock state of the physical proton (one-pion exchange mechanism). The flux factor is written as:

  $$f_i(x_L, t) = f_{\pi^o p}(x_L, t) \propto (1 - x_L)\frac{-t}{(t - m_\pi^2)^2}|F_{\pi N}(x_L, t)|^2$$

  In the second case, the predominant contribution comes from the $\Delta \rightarrow p\pi$ reaction mediated by pion exchange. The flux factor for this process is:

  $$f_i(x_L, t) = f_\Delta(x_L, t) \propto (1 - x_L)\frac{((m_\Delta + m_N)^2 - t)^2((m_\Delta - m_N)^2 - t)}{m_N^2 m_\Delta^2 (t - m_\pi)^2}|F_{\pi\Delta}(x_L, t)|^2$$

  In either case, $F_2^i(\beta, Q^2) = F_2^\pi(\beta, Q^2)$ represents the structure function of the pion. $F_{\pi N}$ and $F_{\pi\Delta}$ are the form factors for the pion-nucleon and pion-resonance vertex.

- Reggeon exchange: Processes mediated by reggeon exchange might produce leading protons. The parametrisation of the reggeon flux is:

  $$f_i(x_L, t) = f_{I\!R}(x_L, t) \propto (1 - x_L)^{1-2\alpha_{I\!R}(t)} G_{I\!R}(t)$$

  where $\alpha_{I\!R}(t)$ is the reggeon trajectory and

  $$G_{I\!R}(t) = G_{I\!R}(0)\exp(B_{I\!R} t)$$

  is the form factor for the reggeon-proton vertex. $G_{I\!R}$ and $B_{I\!R}$ is found to be 76 mb and 4 GeV^{-2}. Although the reggeon structure function is basically unknown from an experimental point of view, some theoretical arguments suggest β and Q^2 dependences at small β values similar to those of pion and *pomeron* structure functions.

The above mentioned theoretical model has been investigated in detail [41] and the prediction of the contributions of the single process to the fraction of events with a leading proton are shown in table 2.4.1. This prediction will be compared with the data in chapter [8].

Exchange process	Pomeron exchange	π^o exchange	Resonance Δ decay	Reggeon exchange
Ratio	$R_{I\!Pp} = 1.2\%$	$R_{\pi^o p} = 2\%$	$R_{\pi\Delta} = 0.9\%$	$R_{I\!Rp} = 5\%$

Table 2.4.1: Predicted contribution of a single process to the fraction of events with a leading proton in ep collisions at HERA

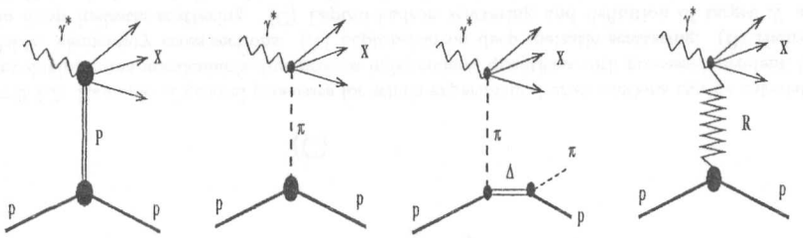

Figure 2.4.1: Processes contributing to the production of leading protons according to Regge theory: (A) pomeron exchange; (B)one-pion exchange; (C) delta resonance via one pion exchange; (D) reggeon exchange

2.4.2 The QCD Fracture functions

Fracture functions [42] have been introduced to extend the usual QCD improved parton description of semi-inclusive deep inelastic process to the low transverse momentum region of phase space, where the target fragmentation contribution becomes important.

As explained by L. Trentadue and G. Veneziano [42], [43]: experimental cross-sections can be computed, in the framework of the QCD improved parton model, by convoluting some uncalculable, but process independent, quantities with process-dependent, but calculable, elementary cross-sections. This is the case of the structure functions, which are measured in deep inelastic lepton-hadron scattering in some kinematical regime and then used to compute either the same process or a completely new hard reaction at a different scale.

For any given process, initiated by the hadrons A and B: $A + B \to A' + B' + ...$, it is possible to write it in terms of a point like, partonic cross-section $d\sigma$ convoluted with suitable defined structure and fragmentation functions, F_A^i and $D_j^{A'}$ [43]. The cross-section written in the factorized form is:

$$d\sigma(Q^2) = \sum_{k,...} \int dx_i dx_j ..dz_k .. F_A^i(x_i, Q^2) F_A^j(x_j, Q^2) ... d\sigma_{ij}^{k,\cdots}(Q^2) D_k^{A'}(z_k, Q^2) ... \tag{2.15}$$

where $d\sigma_{ij}^{k,\cdots}(Q^2)$ is the point like partonic cross-section. The universal structure and fragmentation functions $F_A^i(x, Q^2)$ and $D_i^{A'}(z, Q^2)$ obey the evolution equations:

$$F_A^i(x, Q^2) = \sum_b \int_x^1 \frac{dz}{z} E_i^b(\frac{x}{z}, Q^2, Q_o^2) \cdot F_A^b(z, Q_o^2)$$

$$D_i^A(x, Q^2) = \sum_b \int_x^1 \frac{dz}{z} E_i^b(\frac{x}{z}, Q^2, Q_o^2) \cdot D_b^A(z, Q_o^2)$$

Under this formulation, the cross-section of a deep inelastic lepton hadron scattering, $\sigma(l + N \to l' + H + X)$ (Fig 2.4.2-A), in which no particular hadron is singled out in the hadronic final state $H + X$, takes the form:

$$\sigma_{l+N \to l'+H+X} = \sum_i \int_0^1 \frac{dx}{x} F_N^i(x, Q^2) \sigma_H^i(x, Q^2) \tag{2.16}$$

where, Q^2 is the virtuality of the photon and $F_N^i(x, Q^2)$ is the structure function of the target N. Here, H can represent any kind of hard process. The factorized form of equation [2.16] corresponds to the fact that, as a result of the hardness of the collision, the final state is composed of two well separated cluster of particles, one (denoted by X) originating from the target fragmentation and from the evolution of the active parton and the other (denoted by H) coming from subsequent hard interaction of the active parton with the lepton.

In the case of hadron-hadron collisions, the cross sections for $A + B \to H + X_A + X_B$ (Fig. 2.4.2-B) can be analogously factorized as:

$$\sigma_{A+B \to H+X_A+X_B} = \sum_{ij} \int \frac{dx_i}{x_i} \frac{dx_j}{x_j} \cdot F_A^i(x_i, Q^2) F_B^j(x_j, Q^2) \sigma_{hard}^{i+j \to H}(x_i, x_j; Q^2) \tag{2.17}$$

Equation [2.17] does not contain, under this factorization hypothesis, new uncalculable quantities besides the ones measured in deep inelastic scattering.

If a single hadron is detected in the final state then the simplest case corresponds to the cross section:

$$\frac{d\sigma_{e^+e^- \to h+X}}{dz} = \sum \sigma_{e^+e^- \to q_i \bar{q}_i} D_i^h(z, Q^2) \tag{2.18}$$

which can be used to determine from the data the perturbatively uncalculable fragmentation function $D_i^h(z, Q^2)$. Thus, in this case, even processes with no initial hadron provide important non-perturbative information.

According to the previous discussion, the general process of a general deep inelastic lepton nucleon scattering, $l + A \to l' + h + H + X$ (Fig. 2.4.2-C), will receive contributions from two well separated kinematical regions for the produced hadron:

$$\sigma_{l+A \to l'+h+H+X} = \sigma_{current} + \sigma_{target} = \sigma_{l+A \to l'+(h+H')+X} + \sigma_{l+A \to l'+H+(h+X')} \tag{2.19}$$

For the first term, apart from the factor arising from the target structure function, no knowledge other that the one on fragmentation functions D is needed [44]. The second term require a new non-perturbative (but measurable) quantity, a fragmentation-structure or "fracture" function:

$$\sigma_{target} = \int_0^{1-z} \frac{dx}{x} M_{A,h}^i(z, x; Q^2) \sigma_{hard}^i(x, Q^2) \tag{2.20}$$

where $M_{A,h}^i(z, x, Q^2)$ represents the probability of finding the parton i in the hadron A with momentum fraction x while observing the hadron h in the inclusive final state with momentum fraction z. This form implies a new factorization which will permit to describe the full target fragmentation in terms of the single function M without separating the contributions of the active parton and that of the spectators. Furthermore, the factorized form in equation [2.19] implies that, once M

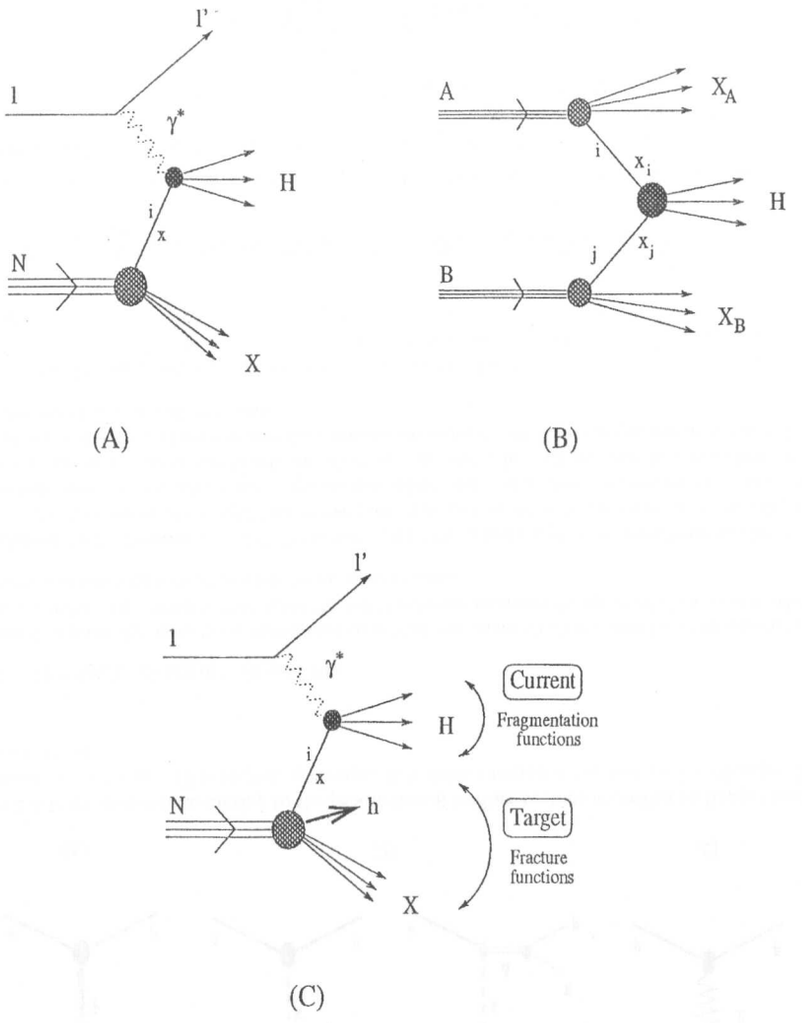

Figure 2.4.2: Example of general processes for which experimental cross sections can be calculated by convoluting some uncalculable, but process independent, quantities with process-dependent, but calculable, elementary cross-sections: (A) Lepton-hadron deep inelastic scattering. (B) Hadron-hadron deep inelastic scattering. (C) Lepton-hadron scattering and definition of target X and current H hemispheres. Indicated is also (if produced) the leading baryon, h.

is measured in deep inelastic scattering no extra input is needed in order to compute analogous quantities in hadron-hadron collisions.

The fracture function, M, measures the parton distribution of the object exchanged between the target and the final hadron, without making any model about what that object actually is. In the case of a leading baryon production in which the momentum transfer, t, is measured, $M^{i}_{A,h}(z,x,Q^2)$ is rewritten as $M^{i}_{A,h}(z,x,t,Q^2)$, a t-dependent (extended) fracture function.

This formalism has been used and applied to describe the leading baryon production at ZEUS by R. Sassot and D. de Florian [45, 46]. They concluded that this approach allows a unique perturbative QCD description of diffractive and leading baryon phenomena without the usual assumptions about approximate Regge factorization. The predicted results for leading proton production are presented in chapter [8].

3 HERA and ZEUS

3.1 The HERA $e^{\pm}p$ Collider

The *Hadron Elektron Ring Anlage*, HERA, located at the DESY (Deutsches Elektronen-Synchrotron) laboratory in Hamburg is the first electron-proton collider in the world [47]. It was designed to study electron-proton interactions in a kinematic regime with center-of-mass energies one order of magnitude larger than the values obtained in previous experiments. The beams of electrons and protons were designed to achieve maximum energies of 30 GeV and 820 GeV respectively. This results in a center-of mass energy of $\sqrt{s} = 314$ GeV which is equivalent to a fixed target experiment using ~ 52 TeV electrons.

The HERA tunnel has a circumference of 6.3 km and is situated $10 - 25$ m underground, the plane of the accelerator being tilted relative to the horizontal. Electrons and protons are guided in two separate storage rings which cross each other in the two interaction points and are used for the experiments ZEUS (South Hall) and H1 (North Hall). Two other experiments HERMES (East Hall) and HERA B (West Hall) are also installed and placed in the electron and proton beam respectively. HERMES is a polarised gas-jet internal target experiment devoted to measure the *spin distributions of quarks in the proton and neutron*, while HERA B focuses its research on *CP violation in the B system* using an internal (Cu-wire) target in the proton ring. A plan of the HERA *ep*-collider with its pre-accelerator system and the injection scheme at DESY is shown in Fig. 3.1.1 and the main parameters are listed in Table 3.1.1.

The initial 1994 period was with electrons but the beam current was limited because positively charged dust particles from the electron beam getter pumps were attracted to the electron beam causing excessively short beam lifetime. As a result the beam was switched to positrons which repel the dust and thus most of the existing data was on $e^{+}p$ interactions[1]. Fig. 3.1.2, shows the luminosity delivered by HERA.

One of the features which distinguishes HERA from other conventional colliders, is the asymmetry in beam energy. While the high momentum of the proton beam requires superconducting magnets, the electrons are controlled with conventional magnets. The HERA proton ring consists of 422 main dipoles delivering a bending field of up to 4.65 T and 244 main quadrupoles. Standard cells of 47 m length combining 4 dipoles, 4 quadrupoles, 4 sextupoles and correction magnets are installed in the arcs of the proton ring and are cooled down to 4.2 K.

The conventional electron ring consists of 456 main dipoles of up to 0.164 T and 605 main quadrupoles grouped in 12 m long magnet modules which contain one dipole, one quadrupole, one or two sextupoles and several correction dipoles. The bending magnets are C-magnets with the open side of the magnet directed away from the proton beam.

The energy lost in case of synchrotron radiation is compensed by 500 MHz copper cavities installed in the straight sections of HERA. In addition 16 superconducting 4-cell cavities with a field gradient of 5 MV/m are used to accelerate the electrons from 14 GeV (injection energy) to the maximum energy of 27.5 GeV. Direct synchrotron radiation is a background source for the LPS [48] and thus,

[1]For convenience the word electron will be used to refer either to electrons (e^{-}) or positrons (e^{+})

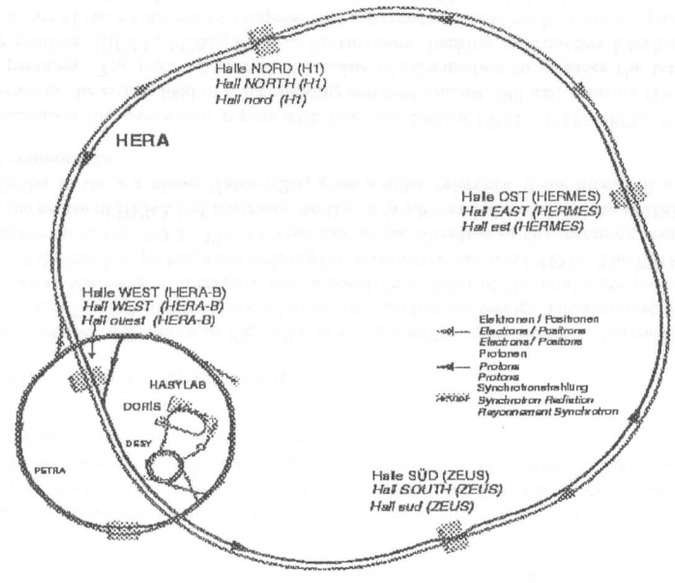

Figure 3.1.1: Plan view of the HERA accelerator

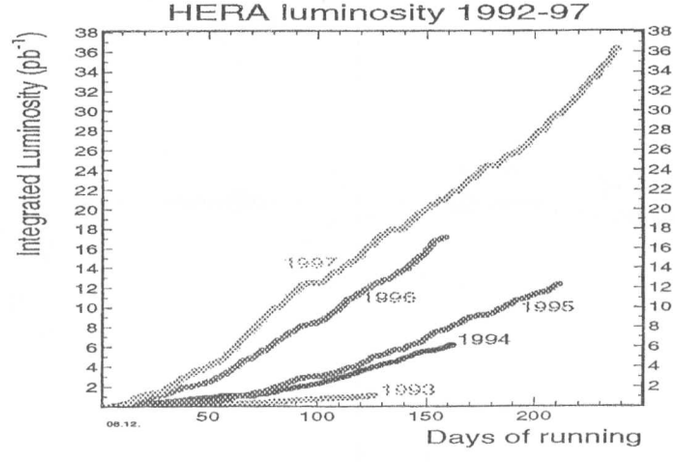

Figure 3.1.2: Integrated luminosity delivered by HERA

Hera parameters	Nominal values		1994	
	Electron	Proton	Positron	Proton
Beam energy (GeV)	30	820	27.5	820
Centre of mass energy (GeV)	314		300	
Injection energy (GeV)	14	40	*same*	
Circumference (m)	6336			
Magnetic field (T)	0.165	4.65	*same*	
Injection time (min)	15	20	45	60
Energy loss per turn (MeV)	127	$1.4{\cdot}10^{-10}$	*same*	
Luminosity ($cm^{-2}s^{-1}$)	$1.7\,10^{31}$		$2.3\,10^{30}$	
Specific luminosity ($cm^{-2}s^{-1}mA^{-2}$)	$3.9\,10^{29}$		$3.4\,10^{29}$	
Integrated luminosity (pb)	100		6.0	
Bunch crossing time (ns)	96		96	
Colliding bunches	210		$153+15$	$153+17$
Bunch crossing time ns	96		96	
Average beam current (mA)	58	163	28	38
Horizontal beta function β^*	2	10	2	7
Horizontal spread σ_x (mm)	0.30	0.27	0.27	0.18
Vertical beta function β^*	0.9	1	0.9	0.7
Vertical spread σ_y (mm)	0.06	0.09	0.06	0.06
Longitudinal spread σ_z (cm)	0.80	11	0.8	11
Total RF power (MW)	1		13.2	
RF frequency (MHz)	52.033/208.13	499.667	*same*	*same*

Table 3.1.1: HERA design parameters and settings during the 1994 data taking period

special studies and precautions are needed.

The HERA injection system is based on a chain of pre-accelerators including the ring accelerators DESY and PETRA. Electrons are pre-accelerated in the linear accelerators LINAC I (220 MeV) or LINAC II (450 MeV) followed by an acceleration up to 9.0 GeV in the DESY II synchrotron. Then the electrons are transferred to PETRA where the energy is increased to 14 GeV after which the electrons are injected into the HERA electron ring. The proton injection starts with negative hydrogen ions (H^-) from the 50 MeV proton LINAC. After the two electrons have been stripped off, the protons are accelerated via DESY III and PETRA to 7.5 GeV and 40 GeV, respectively, which is the injection energy for the HERA proton ring.

The electrons and protons are stored in separate bunches with a distance of 28.8 m between two successive bunches. This distance corresponds to a bunch crossing time of 96 ns. In order to achieve an adequate luminosity each ring can be filled with up to 210 bunches of particles in the total 820 bunches. A group of buckets is always kept to allow the beams to be steered onto a beam dump in a controlled way, a fast kicker magnet being switched on as the group of buckets. The empty bunches used for electrons and protons do not completely overlap, and so some of them are used for measuring background of the beam-gas type. They also proved to be invaluable for synchronising the spectrometer signals with the rest of the ZEUS components as the time of flight of protons down the spectrometer and the cable delay of the signals corresponds to eight beam crossing intervals.

The final radiofrequency is 208.13 MHz, a harmonic of the bunch crossing frequency chosen to achieve

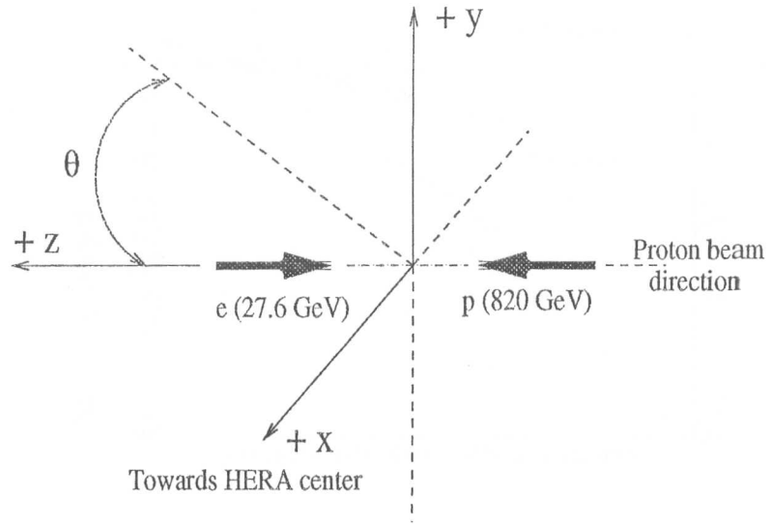

Figure 3.2.1: The ZEUS coordinate system

a longitudinal bunch compression of the proton bunch to have as short as possible an interaction length. The effect of this is seen as a background source for the LPS, as sometimes an adjacent unwanted radiofrequency bunch contains satellite protons which give unwanted events with incorrect leading proton momentum measurement unless special precautions are taken.

3.2 The ZEUS Experiment

The ZEUS detector [49] shown in Fig. 3.2.2 is a large multipurpose detector designed to study the wide spectrum of HERA physics observed in electron-proton scattering. The asymmetry of the beam energies before the collision translates into a boost ($\gamma = 2.82$) of the final state particles into the direction of the incident proton, thus defining the asymmetric layout of ZEUS. The ZEUS coordinate system is shown in Fig. 3.2.1. The $+z$-axes goes in the direction of the incoming proton; $+x$-axes towards the centre of HERA but horizontal so that it is 5.8 mrad above the plane of HERA; $+y$-axes perpendicular to the x-z plane. Table 3.2.1, gives a quick reference of the mnemonics used for the detector components.

ZEUS surrounds the interaction region with tracking devices (VXD, CTD, RTD, FDET, TRD) that operate in the strong field of a surrounding solenoid magnet [50] and measure the momenta of charged particles. The next detector shell consists of calorimeters to measure the total energy of outgoing particles (RCAL, FCAL, BCAL). Furthermore, backing calorimeters interleave detectors between layers of the return yoke to improve the calorimeter resolution by measuring the leakage of hadronic showers (BAC). At the perimeter of the detector additional chambers detect muons (FMU, BMU, RMU) that penetrate the calorimeters and the yoke. To give a clear muon signal they are in coincidence with similar chambers just inside the yoke. At low scattered angles with respect to the

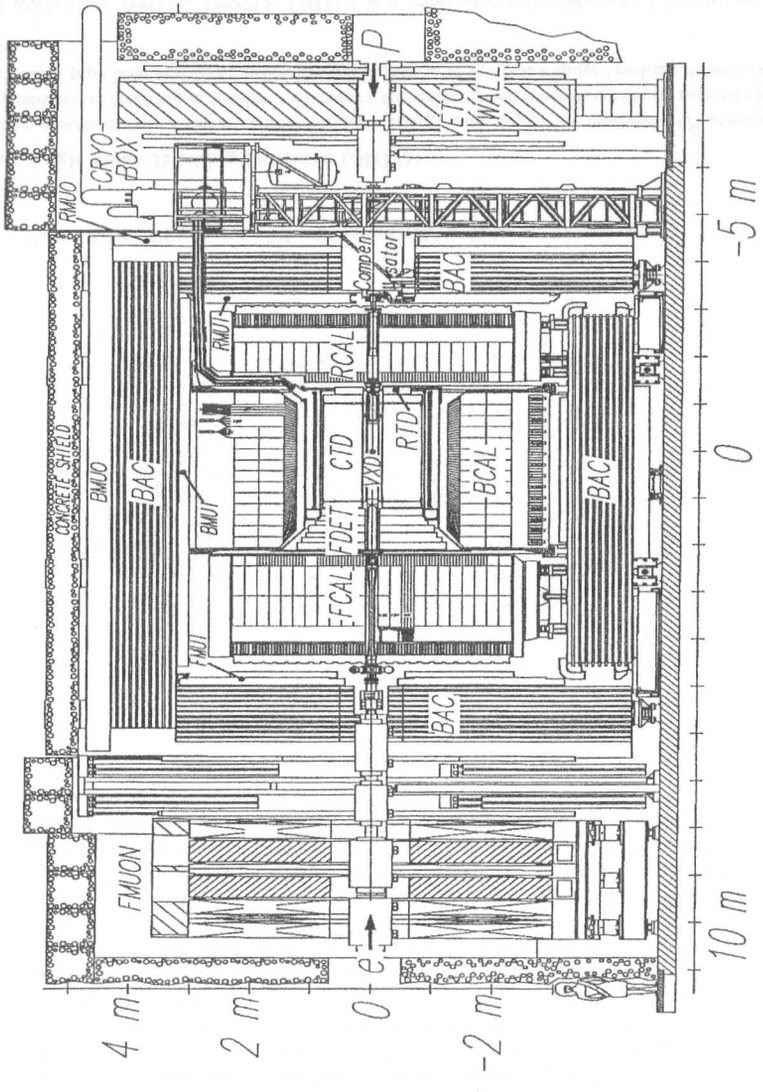

Figure 3.2.2: Artist's view of the ZEUS detector

Component	Mnemonics
Vertex detector	VXD
Central tracking detector	CTD
Forward tracking detector	FDET
Rear tracking detector	RTD
Transition radiation detector	TRD
Small rear tracking detector	SRTD
Forward muon detector	FMUON ,FMUI
Barrel muon detector	BMUO, BMUI
Rear muon detector	RMUO, RMUI
Rear Calorimeter	RCAL
Forward calorimeter	FCAL
Barrel calorimeter	BCAL
Backing calorimeter	BAC
Luminosity monitor	LUMI-E, LUMI-G
Beam pipe calorimeter	BPC
Leading Proton Spectrometer	LPS
Forward neutron spectrometer	FNC
C5 counter & Veto wall	-

Table 3.2.1: Mnemonics used to label the ZEUS components

electron and the proton beam, scattered electrons, protons and neutrons are registered by low angle tagging devices (LUMI-E, BPC, LPS, FNC). Finally, the HERA beam properties such as luminosity and background rate are monitored (LUMI-G, C5 counter and Veto wall).

3.2.1 Detector components

In this section, the components used for the analysis of leading proton production are described. These components are the inner tracking chambers (VXD, CTD and SRTD), the high-resolution calorimeter (FCAL, BCAL and RCAL), the luminosity monitor (LUMI-E and LUMI-G) and the components for background suppression (C5 counter and Veto wall).

The Vertex Detector (VXD)

The main purpose of the vertex detector is the detection of short-lived particles which give rise to secondary vertices, and the improvement of the vertex determination after combining its information with the central tracking detector.

It is a high precision cylindrical drift chamber that surrounds the beam pipe which consists of 3000 drift wires, 1560 field wires and 1440 sense wires parallel to the beam axis. It is divided into 120 cells which surround the beam pipe axis, each cell contains 12 sense wires with 1590 mm length parallel to the beam axis. The chamber is filled with dimethylether (DME) with a trace of oxygen to attain a slow drift velocity (5μm/ns) for the electrons which allows a spatial resolution of 35μm for the detection of charged particles. The vertex detector has an inner radius of 8.8 cm and an outer radius of 16.2 cm and covers the angular region between 8.6^o and 165^o with respect to the beam axis.

The Central Tracking Detector (CTD)

The central tracking detector is used to reconstruct tracks of charged particles at polar angles from 15° to 164°. It is a cylindrical drift chamber with nine sets of wires called super-layers, each with eight planes of sense wires constructed in a cylindrical shape. The detector is 2.41 m long and has an inner/outer radius of 16.2/85.0 cm. Fig. 3.2.3 shows one octant of the wire layout. The odd numbered superlayers have wires parallel to the beam axis while the even ones are tilted (in azimuth) by small stereo angles of approximately ±5° to allow a three dimensional reconstruction of tracks. The design resolution in the $r-\phi$ plane is about 100-200μ depending on the polar angle θ and is 1.0-1.4 mm in the z direction. The momentum resolution at 90 degrees is σ_p/p =0.0021p[GeV] $\bigoplus$ 0.0029. This is relevant for the overall trigger, reconstruction accuracy and for providing reconstructed ρ particles which were used for the LPS calibration. The minimum penetration for adequate track definition is usually considered to be three superlayers. This is particularly important when trying to reconstruct the maximum number of elastic ρ events for calibrating the LPS.

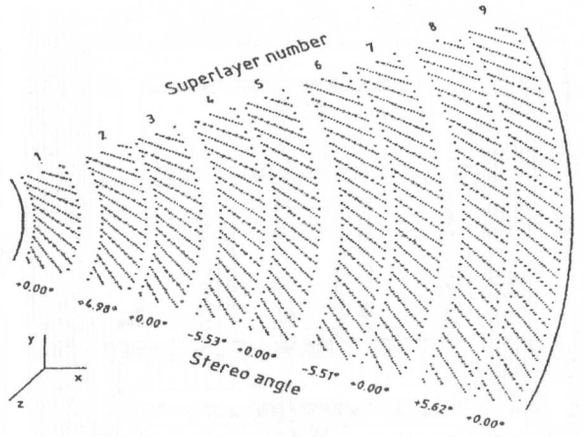

Figure 3.2.3: Wire layout of the Central Tracking Detector for one octant

The Small Angle Rear Tracking Detector (SRTD)

For a precise measurement of the scattered electron energy and angle, for moderate Q^2 events in low-x DIS, additional tracking is needed to improve the calorimeter reconstruction in regions close to the rear beam pipe hole and to enhance the performance of the other inner tracking detectors in this region.

The Small angle Rear Tracking Detector (SRTD) is a scintillator strip detector of dimensions 68 cm by 68 cm located at the face of the RCAL (z =-148 cm) around the beam pipe hole [51]. In this region inactive material (cables, flanges, etc.) causes particles to shower and lose energy before reaching the calorimeter. The additional information provided by the SRTD can be used to correct for these losses. FIG. 3.2.4 shows a schematic of the detector layout. Charged particles are detected by two planes of orthogonally arranged (x,y) strips with a 1 cm pitch which provide position and pulse height information via photo-multiplier readout. Each plane is divided into four quadrants as

shown in the figure. SRTD hit information is used in conjunction with that from the CTD for track reconstruction. The SRTD is also used to reject background by providing a fast timing measurement to the trigger, complementing the rejection provided by the C5 and vetowall counters.

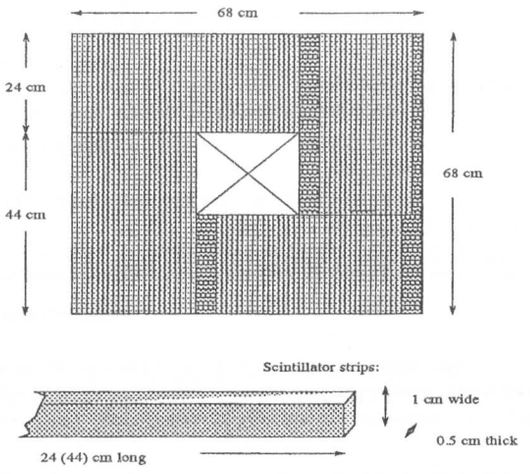

Figure 3.2.4: A schematic of the SRTD showing the orientation of the scintillator strips in the two orthogonal planes. The dimensions of the detector and a typical strip are also shown. The beam-pipe is accommodated in the central hole.

The ZEUS Calorimeter

In practice, the most important types of calorimeters are the *homogeneous* and the *sampling* calorimeters. Homogeneous calorimeters are made of a material that simultaneously absorbs the particle energy and transfers a small fraction of the energy into a measurable signal. Sampling calorimeters are made of alternating passive and active layers where the active layers produce a measurable signal (scintillating light or ionization charge) while the shower is mainly developed in the heavy (high Z) material of the passive layer.

The high resolution ZEUS calorimeter [52], [53] is a compensating sampling calorimeter with equal response to electrons and hadrons (e/h = 1) using absorber plates of depleted uranium (DU) and plastic scintillator layers for the active plates. The depleted uranium plates have the composition of 98.1 % U^{231}, 1.7 % Nb and less than 0.2 % U^{235}. The optical readout is performed via plastic wavelength shifters, lightguides and photomultipliers. In order to obtain equal calorimeter response to electrons (photons) and hadrons, 3.3 mm thick uranium plates corresponding to one radiation length alternate with 2.6 mm thick scintillator plates.

The main features of the calorimeter are:

- hermeticity over the entire solid angle (99.7 % of the laboratory solid angle is covered),
- nominal energy resolution for hadrons and jets of $\sigma(E)/E = 35\%/\sqrt{E} \bigoplus 2\%$,

- energy resolution for electrons of $\sigma(E)/E = 18\%/\sqrt{E} \oplus 2\%$,
- calibration of absolute energy scale to 1%,
- precise angular resolution for particles ($\leq 10mrad$),
- longitudinal segmentation for hadron-electron separation,
- short signal processing time at the nano-second level.

The ZEUS calorimeter completely surrounds the solenoid and the inner tracking detectors as shown in Fig. 3.2.5. It is divided into three parts: the forward calorimeter (FCAL), the barrel calorimeter (BCAL) and the rear calorimeter (RCAL). Each part of the calorimeter cover polar angles from θ= 2.2° to θ= 36.7°, θ= 36.7° to θ= 129.1° and θ= 128.1° to θ= 176.5°, respectively.

The three calorimeter components are structured similarly and are subdivided longitudinally into an electromagnetic calorimeter (FEMC, BEMC, REMC) with a depth of $\sim 25\ X_o$ equivalent to one interaction length λ, which is sufficient to fully contain the electromagnetic showers, and a hadronic calorimeter (HAC). In FCAL and BCAL the HAC sections are divided into two subsections HAC1 and HAC2, while the RCAL has only one HAC section.

The whole calorimeter has a modular structure. The FCAL and RCAL calorimeters consist, each one, of 24 modules, which follow the same construction principles, as shown in Fig. 3.2.6 where an isometric view of FCAL module is presented. The FCAL and RCAL modules have the same width of 20 cm and have a height varying from 2.2 m to 4.6 m so that roughly a cylindrical structure with a radius of $\approx$ 2.3 m can be built. The depth varies from 7.1 λ in the central region to 5.6 λ for the outer horizontal regions. The centre module of the FCAL and the RCAL calorimeter are split into a separate upper and lower module. The horizontal segmentation is determined by the width of the modules.

The transverse segmentation depends on the height of the scintillators and the wavelength shifters which collect the scintillator light. Each longitudinal section (EMC, HAC1, HAC2) is read out on both sides by independent wavelength shifters. For FCAL the segmentation of the EMC sections is 5 x 20 cm, and for RCAL 10 x 20 cm. These sections are called EMC towers. The hadronic towers of FCAL and RCAL have a segmentation of 20 x 20 cm. Fig. 3.2.5 shows a front view of FCAL, as seen from the interaction point, assembled from the 24 modules and the same front view including the transverse segmentation of the FCAL. In addition Fig. 3.2.5 presents a cross section of the calorimeter along the beam pipe and the three calorimeter components FCAL, BCAL and RCAL with their longitudinal segmentation.

The optical readout combined with photomultipliers enables the performance of a fast readout processing which allows the determination of the arrival times of incoming particles at the nano-second level. This feature is used to discriminate background events when an incoming particle in a bunch showers into the calorimeter modules on the incident side of the interaction region, such as in a beam-gas interaction.

The calibration of the calorimeter is performed using several redundant tools, which are described in reference [53]. The main calibration source is the use of the natural uranium radio-activity, the so-called uranium noise (UNO), which produces a low background current in the photomultipliers. The integrated signal of the UNO provides a stable diagnostic tool for monitoring and calibration of the high resolution calorimeter.

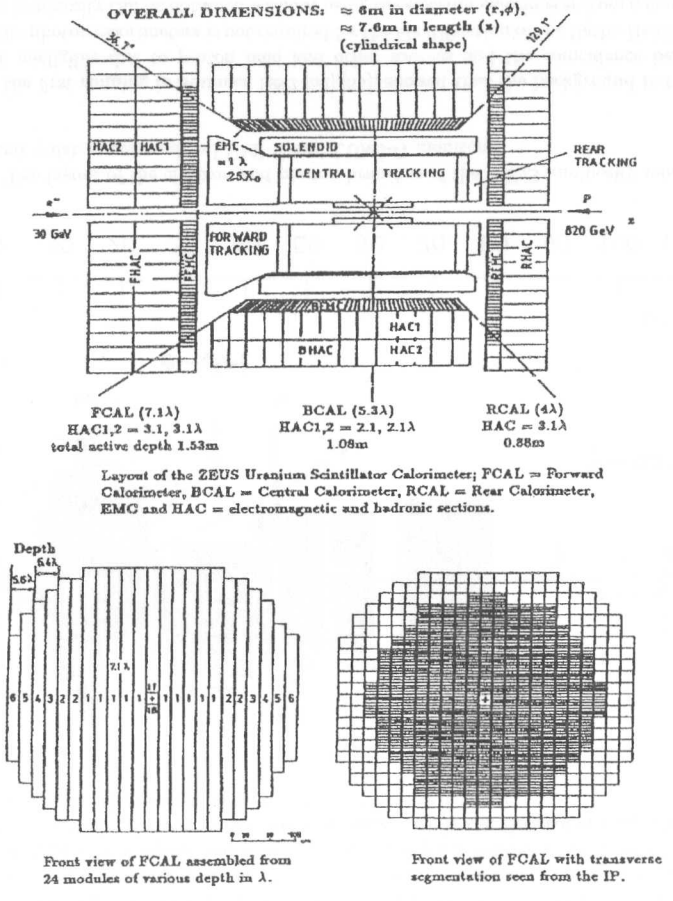

Figure 3.2.5: Layout of the high resolution calorimeter and two front views of the FCAL. Top: vertical section; bottom left: end view showing the module (mechanical) arrangement; bottom right: showing the tower arrangement (optical readout segmentation).

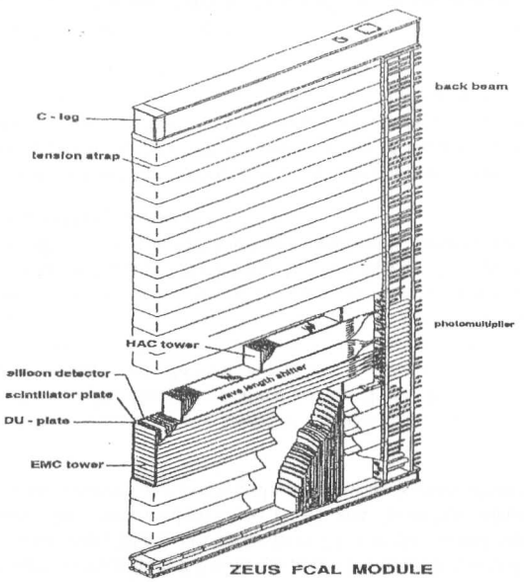

Figure 3.2.6: Internal structure of an FCAL module

To identify electrons inside jets and to improve the position resolution of showers an additional device called HES (hadron electron separator) is built into the calorimeter. It consists of a plane of silicon diode arrays, each diode having an active surface of 3cm by 3cm. The plane is inserted at 3.3 X_o in the RCAL. The insertion of HES planes in FCAL and BCAL are forseen at 6.3 X_o and 3.3 X_o, respectively. At this depth the narrow electromagnetic showers reach their maximum and therefore give rise to large signals in the HES diodes. Hadronic showers, however, are much wider and generally reach their maximum at greater depths. The signal in the HES resembles more a signal from minimum ionising particles.

The C5 Counter and the Vetowall

The C5 is made of two lead-scintillator sandwich counters and is situated at a position z=-3.15m which is just behind the RCAL. This counter is used to measure the timing and longitudinal spread of the proton and electron bunches and to register halo particles outside the beam pipe.

The Vetowall detector consists of an iron wall located about z = -7.5 m from the interaction point near the tunnel exit and two scintillator layers, before and after the wall. The Vetowall serves firstly as an absorber to protect the detector against upstream interactions produced by beam halo and off momentum protons striking the proton beam elements. Secondly it serves as a detector for charge particles which pass through the iron wall and hit the scintillator counters. If these particles arrive in coincidence with the proton beam bunch the position of the passing particles is estimated and this information can be used to reject beam-gas induced events.

The Luminosity monitor (LUMI-E, LUMI-G)

The measurement of the luminosity at ZEUS is based on the Bethe-Heitler Bremsstrahlung process $ep \rightarrow e'p\gamma$. This process has a clean experimental signature, which is the coincidence of a final state electron and a photon at small angles with respect to the electron direction and with an energy sum $E_{e'} + E_\gamma = E_e$. The final state electron and photon produced at very small angles are measured in electromagnetic calorimeters of the luminosity monitor positioned at z = -33 m (LUMI-E) and z = -100 m (LUMI-G) of the central detector. A layout of the luminosity monitor is given in Fig. 3.2.7. Final state electrons with energies lower than the beam energy are deflected by dipole (BH) magnets, pass through an exit window and hit the electron tagger, while the Bremsstrahlung photons leave the beam pipe at z = -92 m immediately before the LUMI-G detector.

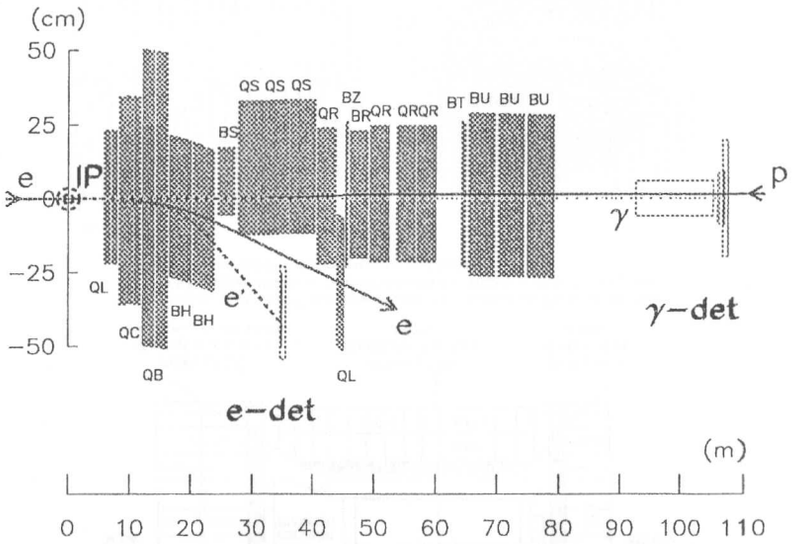

Figure 3.2.7: The layout of the electron and photon branches of the ZEUS luminosity monitor. The labels e-det and γ-det correspond to LUMI-E and LUMI-G monitors.

Studies from the first running in Summer 1992 [54],[55], showed that the background in the photon calorimeter is negligible due to proton halo and other sources and the coincidence between the electron and the photon calorimeters is not required for the identification of the Bethe-Heitler process. Therefore, the luminosity can be obtained without using the electron calorimeter from a measurement of $R_{ep}(E_\gamma{}^{th})$, the rate of ep-Bremsstrahlung photons above an energy threshold $E_\gamma{}^{th}$ = 5 GeV, and $\sigma_{ep}{}^{acc}(E_\gamma{}^{th})$, the corresponding Bremsstrahlung cross section calculated from the Bethe-Heitler formula [56] and corrected for detector acceptance and resolution. Hence, the luminosity is calculated using the following formula:

$$L = \frac{R_{ep}(E_\gamma{}^{th})}{\sigma_{ep}{}^{acc}(E_\gamma{}^{th})} \qquad (3.1)$$

The luminosity monitor also allows the tagging of photoproduction events by a signal from the electron tagger combined with the absence of an energetic photon measured with the photon tagger. For photoproduction, the electron tagger covers the Q^2 range from $4{\cdot}10^{-8}$ (GeV/c)^2 to $2{\cdot}10^{-2}$ (GeV/c)^2. In this thesis, events will be referred to as *photoproduction* events if the energy of the scattered electron is in the range 5 GeV $< E_{e'} <$ 25 GeV and the energy of the photon tagger is below 0.5 GeV.

4 The Leading Proton Spectrometer (LPS)

4.1 Introduction

The LPS is a single-arm spectrometer formed by placing detector stations at suitable positions along the first 90 m of the outgoing proton beam. Since the stations had to fit into the beam-line wherever possible and because the acceptance was restricted by the 10σ profile of the beam and by the vacuum chamber limits, the spectrometer was designed with six stations so as to piece together a reasonable acceptance. Thus, the number of stations and their positions were chosen to cover as much as possible of the scattered proton phase space within the limits of practicability and finance.

The spectrometer has an overall r.m.s. momentum resolution of 0.4% at 820 GeV and can achieve 0.16% in selected regions of phase space. Since the stations had to fit into the beam-line wherever possible, the geometric acceptance is very dependent on the values of the longitudinal and transverse momentum. To give a general idea in words, one can average over azimuth and over transverse momentum assuming a typical $t-$distribution and quote a mean acceptance of ~30% at intermediate momenta and ~3% at 820 GeV.

The coordinate system used by the LPS follows the ZEUS convention that $+z$, the proton beam line is drawn to the left, y is normal to the plane of HERA and x points to the centre of HERA. Fig. 4.1.1 shows how the coordinate systems of HERA, ZEUS and the LPS relate to each other.

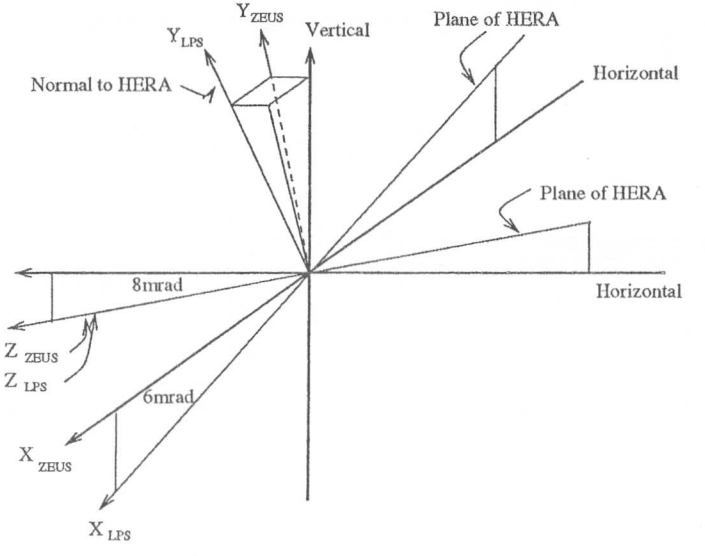

Figure 4.1.1: Relationship between the HERA, ZEUS and the LPS coordinate systems

4.2 Beam optics and spectrometer layout

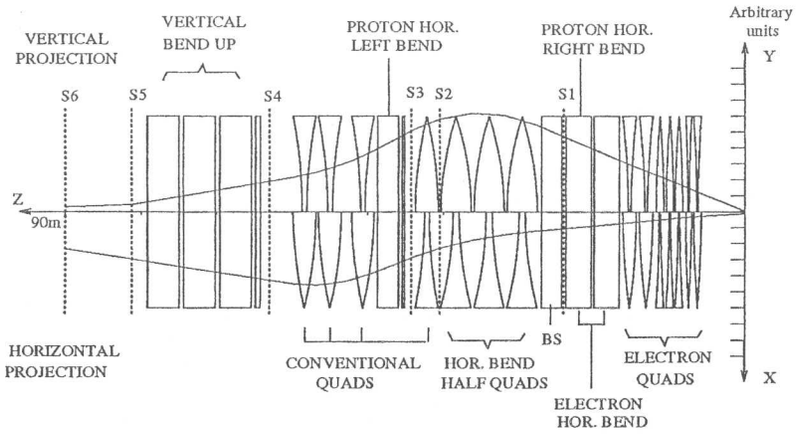

Figure 4.2.1: Optics of the leading proton spectrometer and the proton beam line. S1, S2 and S3 are horizontally moving mono stations while S4 and S6 are vertically moving double stations.

Figs. 4.2.1 and 4.2.2 show the optics and beam-line drawings. The beam-line starts with a set of weak quadrupole magnets which focus the electron beam. Their effect on the proton beam is reduced by a factor $\frac{E_e}{E_p} \sim 0.03$ but should nevertheless be taken into account. Then follow two electron horizontal bending magnets BH which sweep the electron beam away from the proton beam. When the protons arrive at the station $S1$, the net effect of these weak magnets is a deflection of $\sim 1mm$.

Immediately after $S1$, a current septum magnet BS deflects the proton beam to the right and this deflection is then increased by three magnetic-septum half quadrupoles QS after which is placed $S2$. Station $S3$ is then placed after the next, conventional, quadrupole $QR42$. At this point along the beam, 820 GeV protons have been deflected horizontally by a distance of 15.8 mm. This indicates the dispersion in this first, horizontally-bending section of the spectrometer and should be compared with the r.m.s. position resolution in the detectors of about $25\mu m$ to appreciate the possible momentum resolution.

Following $S3$ there is a horizontal left-bending magnet $BT47$ which returns the proton beam parallel to its initial direction at the interaction point. Another three conventional quadrupoles complete the focusing system of the straight section.

The final section of the spectrometer consists of the three stations $S4$ to $S6$ with 5.8 mradian-total vertical bending magnets, BU, between them. Nominally, the first three stations are designed to handle low momenta while the last three stations are designed to handle high momenta but in fact the first three stations do contribute significantly to the high momentum acceptance.

Beam position monitors (not shown) are located near $S3$ and $S4$, in addition to the vertical orbit-correcting magnets BZ and BY. Fig. 4.2.1 also shows the 10σ profiles of the beam relative to the nominal beam line in the horizontal and vertical planes. Numerical values of the 10σ horizontal and

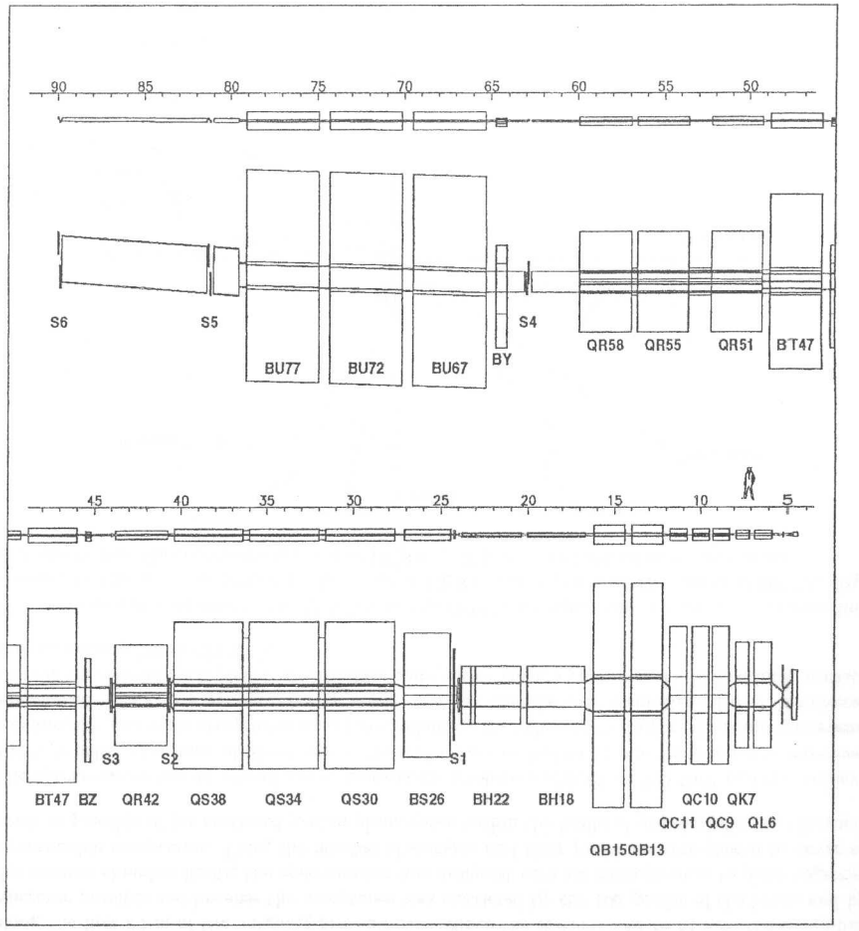

Figure 4.2.2: View of the LPS Geometry as drawn by GEANT. The lower half of it is drawn from just after the interaction point at $z = 0\ m$ to $z = 50\ m$ and the upper half is drawn from $z = 45\ m$ to $z = 90\ m$. Both plan view and elevation are shown. The plan view is drawn to scale, but in the elevation, the vertical dimension is expanded to show more detail. The magnet labels are identification types and numbers. The detector stations are labelled S1 to S6. The horizontal scale is in metres from the interaction point.

vertical beam sizes are given in Table 4.2.1.

Station	S1	S2	S3	S4	S5	S6
$10\sigma_x$ (mm)	7.0	14.0	18.5	27.5	19.4	15.0
$10\sigma_y$ (mm)	19.6	24.5	20.9	7.6	3.5	5.0

Table 4.2.1: 10σ beam sizes at the stations

Detector shapes are matched to these profiles which limit the closeness of the detectors to the beam line. Hence the acceptance at 820 GeV is given by those protons which can squeeze between the 10σ profiles and the walls of the vacuum chamber. At lower energies, however, protons which are produced at low p_T and are inside the angular spread of the beam can be detected because the bending magnets sweep them away from the beam.

4.3 Detectors

Silicon detectors[1] were chosen for the following reasons:

- As mentioned above, the spectrometer uses the HERA straight section beam optics near to the interaction point at ZEUS. In order to increase acceptance, close adaptation to the optical properties of the beam was necessary and as a result the detectors needed to be shaped. Fig. 4.3.1 shows how critical the acceptance can be. It shows the acceptance contours in the transverse momentum plane and the dependence on azimuth which results from the varying beam optics and vacuum aperture limitations. Fig. 4.3.1 a) and b) shows the plot under most favourable and least favourable beam conditions at $x_L = 0.8$. In poor beam conditions, the detectors had to be placed further from the beam, so resulting in reduced acceptance.
- The detectors and associated front-end electronics had to be placed close to the beam, and thus had to be radiation hard. Radiation doses accumulate during beam filling, beam tests, stable beam operation and uncontrolled beam loss. The radiation is composed of neutrons from p-beam losses, synchrotron radiation in the HERA tunnel, back-scattered synchrotron radiation, and from charged particles produced by p-beam gas interactions and by halo from off-momenta scattered protons in the beam elements. It is estimated that the total dose of ionising radiation will be less than 10 KGy per year during stable running and machine development. This dose was reduced by an order of magnitude by designing the detector system to be near the beam only during very clean beam conditions and parking it more than 30 cm away from the beam during unfavourable conditions.
- Kinematic variables x_L and p_t, of the leading proton need to be reconstructed as accurately as possible. They depend on the reconstruction of the position and the detectors need to have a very good resolution measurement for charged particles.

The choice made was to use single sided n-doped high resistivity silicon material with p-type microstrip implantations which have orientations of 0^o and $\pm 45^o$ relative to the pot axis, that is perpendicular to the beam. A set of six detector planes per pot are used, two 0^o, two $+45^o$ and two -45^o. These particular strip orientations and the number of planes per pot were chosen for the following reasons:

[1]The detectors use by the LPS were manufactured by Micron Semiconductor, Camberra and Eurosys, formerly Intertechnique

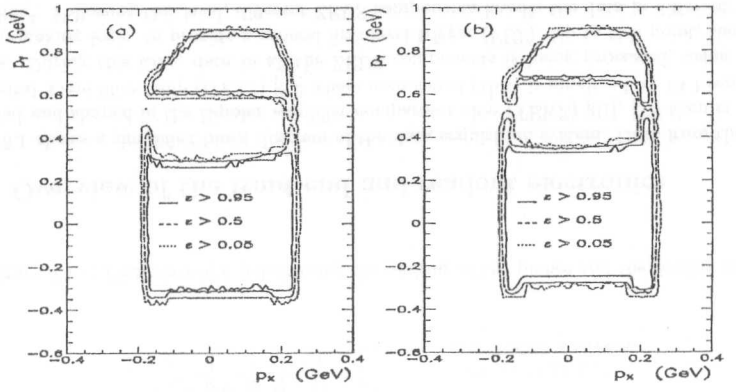

Figure 4.3.1: Geometrical acceptance in the transverse momentum plane: (a) Best case and (b) less favourable case at $x_L = 0.8$

- to resolve ambiguities in the reconstruction of charged particles. These ambiguities may come from detector and electronic noise, photon hits and extra hits from multiple tracks in a given event.
- to have a very strong suppression of photon background per pot
- to have redundancy (*i.e.* to measure the xy coordinate of the track more than once in a single pot) so as to improve accuracy and to insure against data loss due to failure of planes when there are long time periods between access and service periods.

Double-sided detectors were considered but not used because of the high synchrotron radiation environment. If double sided detectors were used, a synchrotron radiation photon which leaves a signal in only one plane would be readout in two coordinates.

There are also smaller trigger planes which can select protons with greater than 0.95 of the beam energy. Detailed information about the LPS detectors can be found in [57], [58] and [59]. Table 4.3.1 shows some relevant parameters of these detectors.

Each detector is mounted on a multi-layer hybrid Printed Circuit Board (PCB) which is also used to hold the front end electronics and the cooling system. Fig. 4.3.2 shows a basic front-end element for a single plane.

4.4 Mechanical System

To be able to withdraw the detectors to about 500 mm, away from the beam so as to reduce the effects of radiation damage to the detectors and electronics during the beam filling and manipulations together with the need to have the front-end electronics very near to the detectors, a modification

Properties	Detector type		
Strip orientation	$\pm$ 45°	0°	trigger
Pitch (μ)	$115/\sqrt{2}$	115	750
Strip width (μ)	20	20	20
Depletion voltage (V)	40 - 60		80
Bias voltage (V)	~ 60	~ 60	~ 60
Capacitance[2] (pF/cm)	$\sim 1.$		4 ± 1
Leakage current (nA)	$\sim 3.$		≤ 3

Table 4.3.1: Characteristics of the Si detectors used by the LPS

of the Roman Pot technique developed at CERN was used. This technique keeps the detectors at atmospheric pressure and maintains the vacuum properties inside the proton beam pipe.

At its end nearest to the beam, the pot is shaped around the detector cutout so that both can fit snugly against the beam profile. Thin windows, 0.4 mm thick are let into the upstream and downstream sides of the pots to reduce multiple scattering. The pots themselves can be positioned nearer or further from the beam and also have limited lateral movement to search for the closest position to the beam. The vacuum is sealed by welded-plate bellows which permit the pot movements and finally support mechanics are precision machined to move and position both the pots and detectors.

Fig. 4.4.1 shows the end view of a pot, seen from the end which is close to the beam. The closely packed structure indicates how little space have been available between magnet elements in the worst

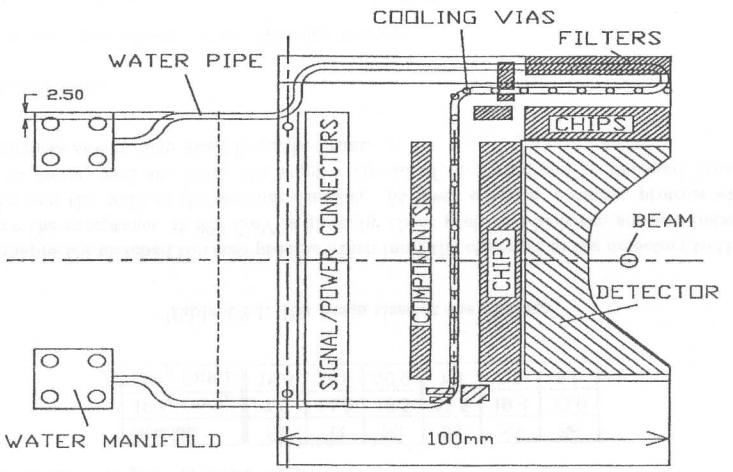

Figure 4.3.2: Plan view of a detector plane and support board with indications of the chip and component layout and the cooling systems

case. Fig. 4.4.2 shows a picture of a vertically mounted system with detector and shielded cable bundle supported on a vertical arm which ends in a carriage moving along the vertical guide on the right. The detector packet is just clear of the mouth of the pot, some 500 mm above the beam. Fig. 4.4.3 is a labelled line-drawing of a horizontally mounted pot system, which has a somewhat different design. Again the hybrid, support hand and arm mounted on the small carriage to the right are drawn retracted from the beam on the horizontal guide. A limited vertical adjustment is provided by a wedge and guide system. In the S4 station where the in/out movement is vertical, the transverse movement is obtained by displacing the whole mechanical structure plus vacuum system.To balance the atmospheric force on the pot and bellows, there is a constant tension spring system [60], with two springs, a force summing system in the triangular frame and a system of levers to apply the force to the pot entrance flange.

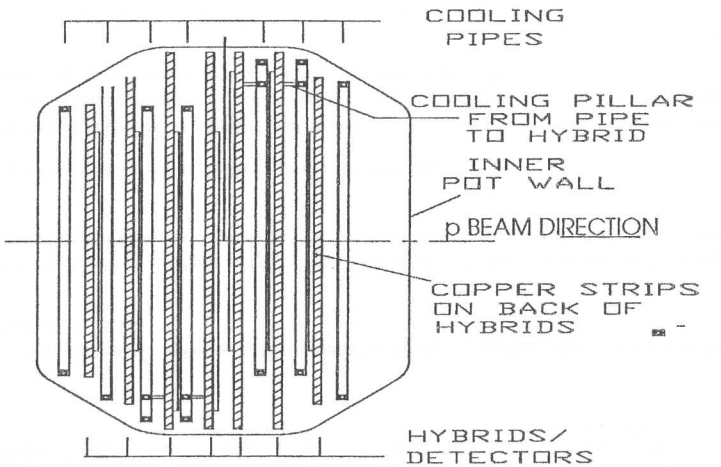

Figure 4.4.1: Plan view of a pot showing the packing of the planes and the cooling system

4.5 Overview of the front-end and readout electronics

Fig. 4.5.1 shows a simplified block diagram of the data acquisition system. Data from the strips is amplified and shaped in the Bipolar amplifier-comparator chip (TEKZ) [61], [62] then is passed to the Digital Time Slice Chip (DTSC) [63] where each signal (1bit) is pipelined for 64 beam crossing periods. During this time, data in all the ZEUS components is being processed, using pipelined decision-making logic, to provide a general first level trigger (FLT). Up to this point, there is zero dead-time[3]. Following this level, different ZEUS components handle the data in different ways and some dead-time can occur. In the LPS a double series of buffers has been implemented to allow serial readout through 100m of cable and still have negligible dead-time. A detailed description of the different level triggers at ZEUS will be given in chapter [5].

[3]A definition and further discussion of dead-time is provided in section [5.1]

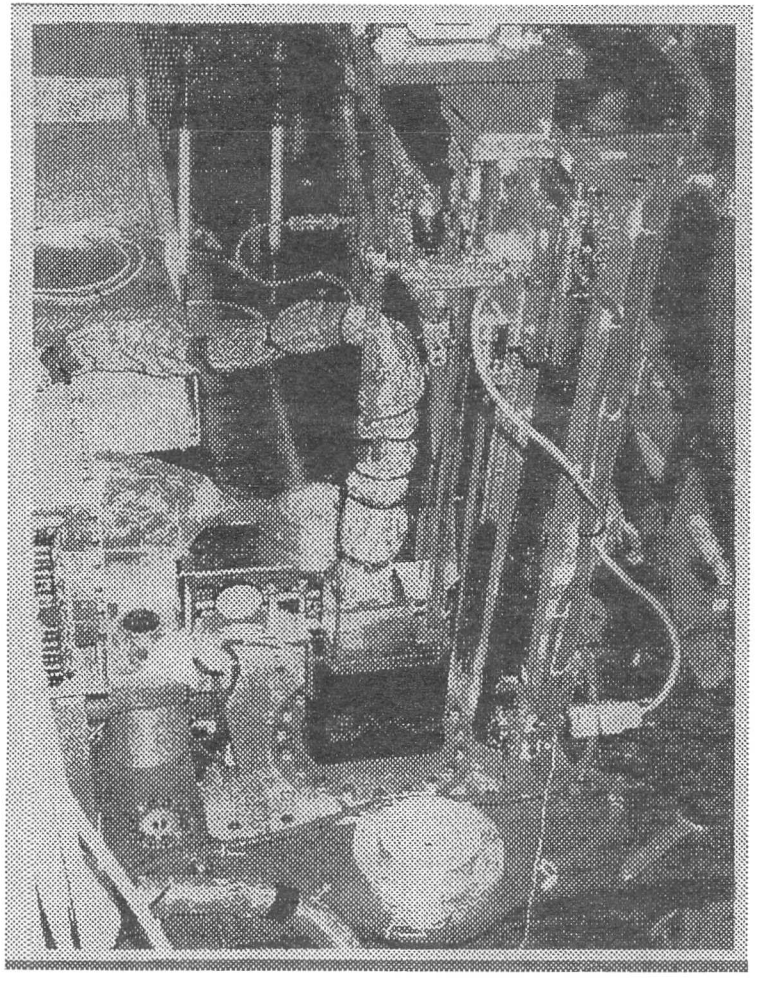

Figure 4.4.2: Photograph of a vertically moving pot showing the support and guide system, detector packet and pot opening. The detector packet is shown withdrawn from the pot into a safe position ready for beam filling. The beam pipe passes out of the picture "at the top of the picture".

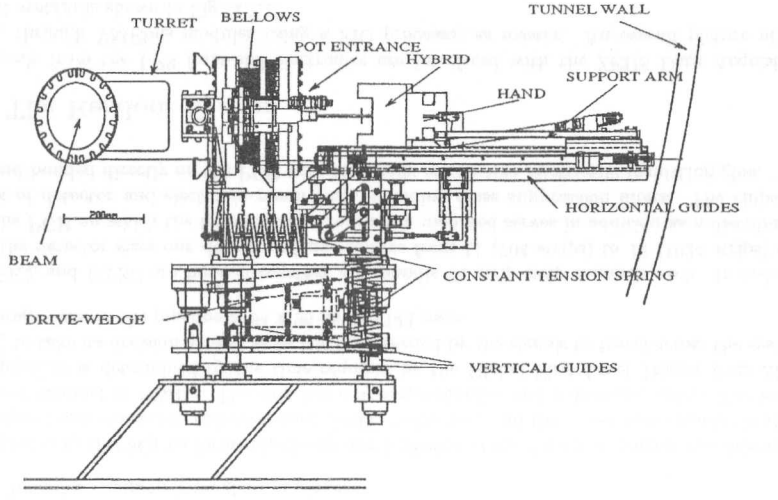

Figure 4.4.3: Line drawing of the mechanical construction of a horizontally-moving pot

The first sequence of buffers is a 32-level buffer on the DTSC which buffers the serial readout operation which is enabled for each event soon after the FLT signal. Data is received by a readout controller module (ROC) which decodes the serial signals and stores them in the second port of the double buffer, implemented in memory in the ROC, at which point some of the data can be used for second level trigger decisions.

A second level trigger (SLT), based on software decisions from all ZEUS components is sent to the LPS local read-out processor (FIC) which organises picking up the correct event from the SRC buffer, formatting it and transmitting the data to a dual port memory from which it is picked up as needed by an event builder process and may be used in third level trigger (TLT) decisions.

4.6 The front-end electronics

As explained earlier, the detector planes are mounted and bonded to multi-layer hybrid PCBs which support the front-end electronics. Each channel consists of an analog amplifier and comparator chip[4] (TEKZ) and of a digital chip pipeline and event buffering[5] (DTSC). Fig. 4.6.1 shows a block diagram of the LPS front-end.

The design requirements include high rate capability (the time between two bunch crossings in HERA is 96 $nsec$), high channel density, low noise, low power consumption and high radiation resistance, all calling for specialised VLSI technology. The LPS readout has zero dead-time loss.

The analog chip (TEKZ) consists essentially of an amplifier followed by a 1-bit analog to digital converter comparator. Each chip has 64 input channels, each one being 72 μm wide and separated

[4]Designed at the University of Santa-Cruz California (USCC) and fabricated by Tektronix
[5]Also designed at USCC and realized by UTMC, California

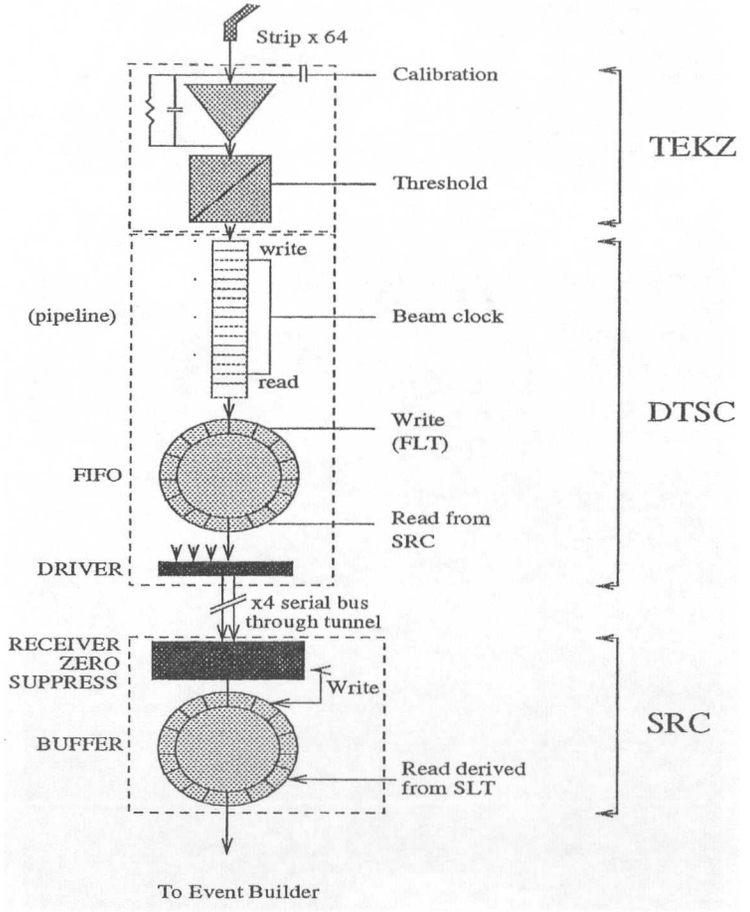

Figure 4.5.1: Schematics of the LPS acquisition system

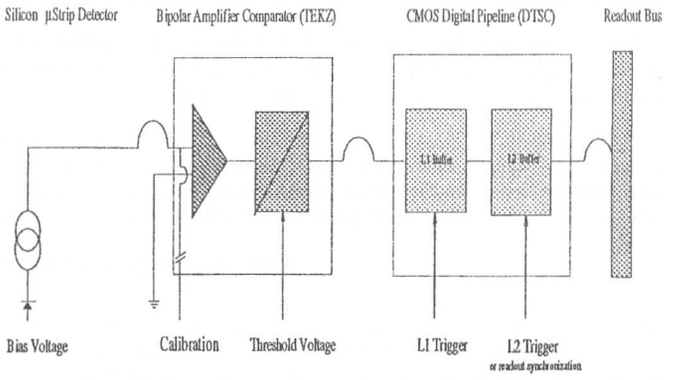

Figure 4.6.1: Block diagram of the LPS front-end

by a grounded line connected to the substrate at regular intervals to minimise cross talk. A test input is provided for each channel, and for test pulses amplifiers are grouped into 4 sets of 16, each channel being coupled to the input through a 40 ff capacitor. The amplifier shaping time is $\tau = 25$ ns and the overall gain is about 150 mV/fC. The signal-to-noise ratio for a minimum ionising pulse is about 20:1 with a 10 pf input capacitance and the dissipated power is less than 2.5 mW/channel. The outputs are pulses of about 40 ns width and 800 mV amplitude, they are written into the DTSC pipeline at the machine clock frequency (MCLK = 96 ns). The comparator threshold level is set externally and is common throughout a plane.

The digital chip (DTSC) performs pipelining and buffering of the data flow output line drivers. It was designed and realised in radiation hard CMOS technology and the power consumption is about 2 mW per channel at 10MHz. The chip has a 64-stage pipeline and a 32-stage buffer. The length of the pipeline is determined by the time required by the Global First Level Trigger from ZEUS (GFLT) to take its decision as well as by the time needed by the signals to travel across the system. The storage time in the pipeline is 64 x 96 ns = 6.144 μsec.

The TEKZ and DTSC are bonded together and handle 64 strip strip channels each. In order to match the detector sizes one detector plane requires from 11 (704 strips) to 16 (1024 strips) chip sets. The PCB on which the front-end electronics are mounted serves in addition as a distribution network of detector and electronic power lines including noise suppression filters. The chips are glued and bonded directly on the PCB with thermally conductive electrically insulating glue.

4.7 The Readout System

The signals from the LPS front-end electronics are interfaced with the ZEUS Data Acquisition System, through VMEbus modules using a FIC processor as master. An overall picture of the Readout system is shown in Fig. 4.7.1.

The Readout Controller

The signals responsible for managing the front-end buffers are driven by the LPS Read-Out Controller

(ROC) [64]. This VMEbus module is linked to the GFLT of ZEUS. The ROC output is then fanned out to the different stations through the Fast-Fan-Out VMEbus modules. The ROC thus interfaces between the GFLT, the VMEbus readout process and the front-end. It contains a section of memory organised like a copy of the front-end digital chips so as to associate flags and trigger information with each beam crossing just as if it were part of the detector data.

The main functions of the ROC are to:

- transmit the beam crossing synchronisation signal, MCLK, from GFLT to front-end
- interrupt the FIC readout processor when the GFLT data are ready in the front-end buffer
- record in the "copy" front-end buffers the GFLT information. This buffer map has one entry for each level-one accept crossing
  - L1 trigger number (0...255)
  - bunch crossing number (0...219)
  - L1 ambiguity (0...3)
  - empty-p empty-e flags (2 bits)
  - read-out type (5 bits)
  - activity state of the SRCs at the moment when the bunch for this event passed the detector
- In the case of an alternative operating mode, the L2-driven mode, where data remain in the front-end buffer until the second level trigger decision, manage the pointers of the 32 stage Level 2 buffer located in the DTSC in response to the Level 2 accept signal (this mode has not been used).

The ROC may operate in a "stand-alone" mode, independently from the GFLT. This feature is important for debugging purposes and for LPS detector studies.

The Fast Fan-Outs

The control signals produced by the ROC are fanned out to the different stations where they must arrive with a phase error less than $\pm$10ns. For practical reasons cable delays to the front-end are not accurately adjusted to meet this requirement. This is done by programmable delay modules: the Fast Fan Outs (FFOs) [65]. In addition the FFOs serve to fan out the control signals. This allows an adjustment of the delays by steps of one clock cycle over a range of eight beam crossings as well as the fine steps of $\pm$10 ns. Delay programming is done from the VMEbus as part of the slow control which is programmed in a MVME 147 processor running under OS9.

One FFO manages the six planes in one pot but 2 independent channels are provided in order to control separately each of the two sets of 3 planes (U,V,Y) to allow delay curves and efficiency measurements. The whole spectrometer thus needs nine FFOs[6].

The Serial Readout Controllers

The data transfer between the front-end and the VMEbus environment is managed by the Serial Readout Controllers (SRCs) [66]. They are triggered by the ROC when the next event can be

[6] As explained in section [4.2], the LPS is composed of six stations. The first three stations ($S1 \rightarrow S2$) are mono-pots and the and the second three ($S4 \rightarrow S6$) double pots. The whole spectrometer is then composed of nine pots, each one housing a package of six silicon detector planes.

transfered and then operate autonomously until that event transfer is completed. One SRC serves one pot and is interfaced with the VMEbus and the VME Sub-system Bus (VSB).

In order to reduce cabling, the data transfer is multiplexed in such a way that for each pot, 4 signals (4 strips) are received in the SRC memory at a time. The SRC is equipped with a zero-suppressor, in such a way that only 4-strip groups containing at least one hit in the group are recorded in the memory. One 16-bit data word then encodes the 4-strip pattern and the address of this pattern within a pot.

Total transfer time is less than 300 μsec for the complete spectrometer. As the ZEUS design GFLT accept rate is nominally 1 KHz, up to 700 μsec are then available for LPS Level 2 calculations, but this extra available time fluctuates depending on the state of the on-chip buffer.

The main parts of the SRC are:

- Programmable Logic Devices (PLD): the sequence in which the DTSCs are read out is fully software programmable. It can accept or exclude any DTSC from the list. It is even possible to include the same DTSC several times per readout. These features are useful in the case of a faulty DTSC. In addition the programming permits one to label a subset of DTSCs which define a restricted detector region contributing to the LPS Level 2 trigger.
- Two dual port RAMs where the zero-suppressed data are stored. Each RAM is dedicated to 3 detector planes (section A and section B) and acts as a buffer while waiting for the SLT decision. They are accessible from VSB in order to avoid VMEbus overload.
- A control register encoding the state of the zero-suppression. Timeout may occur in case of chip malfunction. In this case the serial transfer is stopped. Overrun occurs if one of the RAM becomes full during a transfer. The transfer is then stopped for this section. The error flags are monitored by the LPS slow control.
- Auxiliary location (64 words per section) where a copy of the data contributing to a Level 2 decision is stored.

The SRCs have facilities to generate pseudo-random data. This is useful for software debugging, as the front-end electronics is not involved in such a process and the hit pattern is known. At the end of the serial transfer, a VMEbus interrupt is generated by the SRC. The SRCs can be chained together in a manner such that only one of them interrupts the readout processor when all SRCs have terminated the transfer.

The addressing of the front-end and the zero-suppression are pipelined in the sense that the following chip is addressed while data from previous strips are being zero-suppressed. Due to the long cables (1 μsec round trip time) this is essential to obtain maximum readout speed.

4.8 Cooling system of the front-end electronics

The fact that the detector is mounted in the same support as its front-end electronics with up to seven such systems in a small pot with no convection cooling, required the construction of a special printed circuit board (PCB) to keep the junction temperatures produced by the front-end chips as low as possible and to reduce the electronic noise. As explained in section [4.6], every front end cell produces a dissipation power of about 0.47 Watts per centimetre square along the edge of the

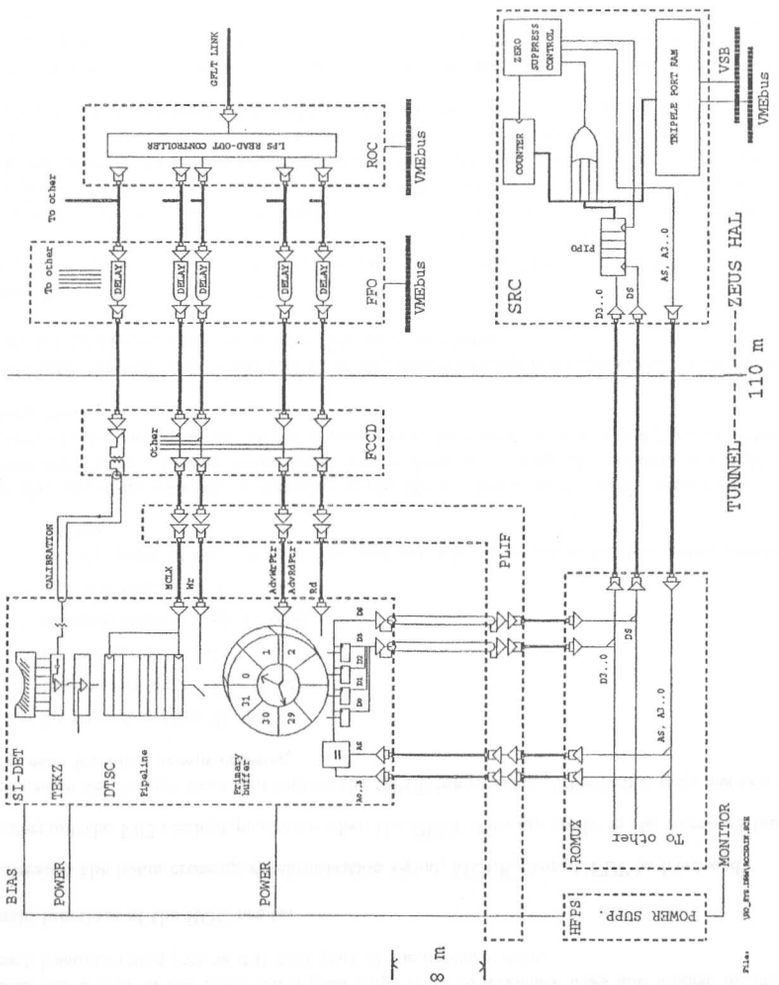

Figure 4.7.1: The LPS Readout system

board. Dark current in the detector depends strongly on the operating temperature, changing by a factor of about nine for a 25°C change in temperature[7]. As a result, the operating temperature has a very strong influence on the useful life of the detector. This is due to the fact that we expect the limit of the detector's working life to be set by noise levels which are decreased by lowering the temperature. In addition, noise levels will increase with radiation damage because of the extra energy levels created in the detector. Therefore to compensate for decreases in signal collection time the operating voltage has to be increased.

To achieve this cooling, a special multi-layer hybrid PCB was designed [67], [68] and constructed. It consists of interleaved layers of epoxy-fibre, copper and invar. Thermal dissipation is maximised by using thermal vias connected to an external cooling water pipe. In order to enhance the heat transfer flux, thin copper plates are located at the back of the PCB. Fig. 4.8.1 shows a two-dimensional model used in the design of the cooling system which corresponds to a side view of the PCB together with the isothermal lines computed using the program *poisson* [69]. Fig. 4.8.2 shows a detail of the layer structure which is built with a symmetric layer structure to avoid distortion with change in temperature. The ratios of copper and invar are chosen to match the board's coefficient of thermal expansion to that of the silicon wafer. The resultant structure has anisotropic thermal conductivity that is high along the plane but low transverse to the plane, which is why the thermal vias exist. These vias extend through the board, making contact with the metal planes and are internally plated so that the metal support pillars can more easily conduct the heat to the cooling tubes.

For a row of chips producing 0.47 Watts per square centimetre of board, this cooling system allows to keep the board temperature below the chips down to within $10°C$ of the temperature of the cooling water.

On a prototype board, measurements were made to check the calculated temperature differences. A rectangular copper tube threaded by heating resistors was cemented to the board to simulate the chips. Water was fed through the cooling tubes by gravity and its temperature was measured. Platinum resistance thermometers were glued to the board adjacent to the heat source and temperature differences were measured until stable conditions were established. The measured temperature difference between water and heat source was 8.0°C compared with the calculated value of 10.08°C.

The validity of our calculations is also supported by direct measurements using heat probes installed in the PCB. The average temperature of the board near the chips is ~35°C which, compared with the water temperature at ~23°C, gives a temperature difference of ~12°C.

4.9 The Slow control

Since the apparatus and about 80% of the electronics are placed in the HERA tunnel, a remote monitoring [70] (Slow Control) system has been developed and implemented.

Remote monitoring is implemented in:

- the LPS *equipment* computer, which consists of a Motorola 68030 processor (MVME 147) managed under OS9 operating system, installed in a VMEbus crate.
- the LPS *component* computer which in turn is a micro Vax (LPSVXD) running VMS operating system.

[7] This value can be derived from the formula which permits evaluate the thermal current in a diode due to thermal excitation

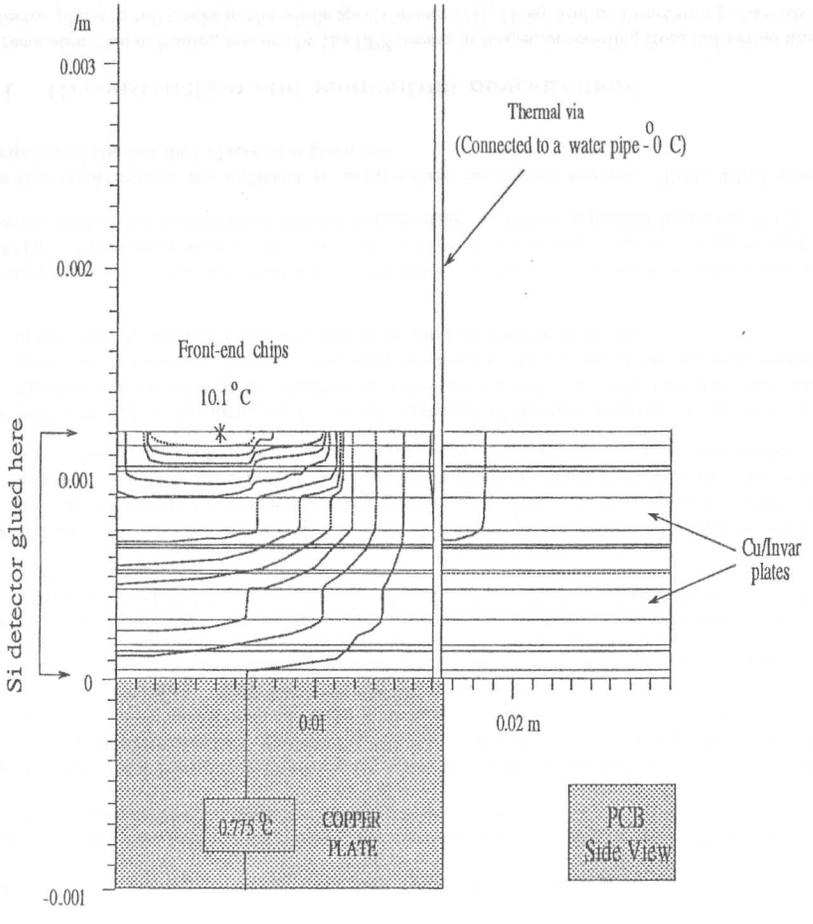

Figure 4.8.1: Isothermal lines computed for a full size prototype of the multi-layer hybrid PCB and the temperatures calculated at the places where the front-end chips and copper plates are located

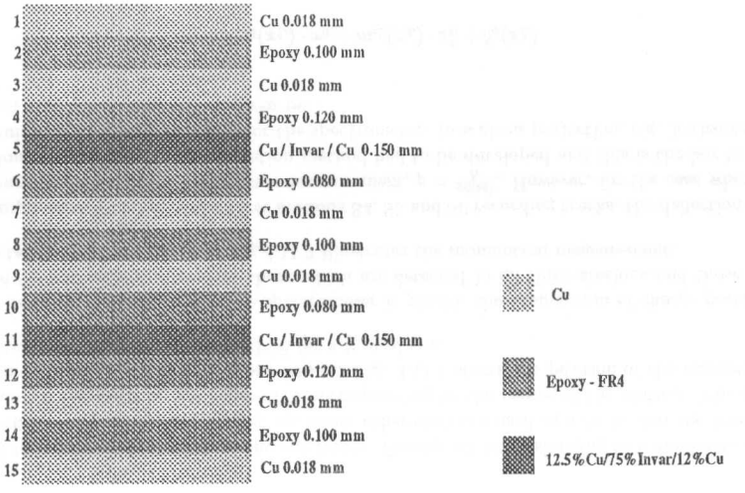

Figure 4.8.2: Layer structure inside the multi-layer hybrid PCB

Both *equipment* and *component* computers are connected through Ethernet. Among the features of the remote monitoring are:

- Detector positioning: A very important and delicate task to place the detectors as close as possible to the 10σ p-beam profile.The nominal p-beam zero position changes from run to run and needs to be considered as well as the fact that the 10σ p-beam profile grows in time due to the beam emittance.
- Front end electronic monitoring: Dedicated to monitor the input and threshold voltages of the TEKZ and DTSCs as well as to monitor the temperature. Due to the high channel density to be monitored and the fact that no real time measurement is necessary, a multiplexing technique to read the signals has been implemented.
- Bias supplies: To supply the necessary voltage to deplete the Si detectors. Bias voltage values are programmable, controlled by Digital Analog Converters (DACs) in a VMEbus and monitored by Analog Digital Converters (ADCs). Bias values ranges from 30 to 170 Volts depending of the silicon detector manufacture.
- Timing: To synchronise the ZEUS-LPS data acquisition system interface, adjust the timing of the fast signals on the pipeline inputs and to establish the beam crossing synchronisation.
- Radiation monitoring: Life time of the detectors and front-end electronics is narrowly bound to the accumulated dose. This is monitored by using small Si-pin diodes located at eight different places along the spectrometer.
- Slow control alarms: If any of the above monitoring systems detects a failure, it sends an alarm signal to the ZEUS Slow Control Manager. An alarm signal may be a *warning* or a *fault* message depending of the nature of the alarm. Slow control alarms are also software-coded and may give information regarding the precise location of the faulty element.

All these features are performed by dedicated tasks running on the MVME147 processor. Programmable commands are sent from LPSVXD and data are returned across Ethernet by the means of OS9 and VMS socket interface. Commands and data can also be directly handled with some dedicated user interface programs on OS9.

4.10 LPS configuration during 1994 data taking

During the 1994 data taking period only three stations ($S4 \rightarrow S6$) were installed. Their choice and place for installation resulted from the following considerations:

- A CERN-LAA Research & Development agreement, which was meant to develop new leading proton detectors, capable of operating in a high radiation dose by having retractable detectors and purely mechanical, radiation hard force compensation and position monitoring. For financial reasons the two stations $S5$ and $S6$, former SPS roman pots, were recuperated and modified to match the HERA optics while $S4$ was entirely designed and built from scratch.
- Space and beam-optics restrictions as well as acceptance and resolution studies in the straight section of the HERA tunnel indicated placing the $S5$ and $S6$ stations at distances of $z = 83\ m$ and $z = 90\ m$.
- Between $S4$ and $S5$ there is a dipole bending magnet (BU), which, used together with $S4$, $S5$ and $S6$ provides a momentum measurement of a charge particle passing through them independently of the first part of the beam optics where the track went through. Two stations were considered, but for this a direct measurement of the interaction vertex was needed.
- Positions had to be convenient for optical alignment of the spectrometer. Accelerator survey methods use the tops of the magnets for reference and only vertically mounted pots can be measured in this way. Even so, the survey accuracy could not match the intrinsic resolution of the system, and other methods had to be used for greater precision.

The above mentioned choices turned out to be essential for alignment, because reconstructed tracks of 820 GeV diffracted protons in $S4 - BU - S5 - S6$ were used to align this set of stations and the preceding part of the spectrometer relative to each other, as will be explained in section [4.12]

Thus this configuration was sufficient to acquire data for physics analysis. Table 4.10.1 gives a description of the installed planes in a given pot.

4.11 Reconstruction and momentum measurement

The reconstruction of leading protons by the LPS occurs in stages, proceeding from individual hits in a detector plane to full tracks in the whole spectrometer [71]. Noisy and malfunctioning channels are masked out and clusters of adjacent hit strips are searched for in each detector plane. Most clusters are one strip wide only, but in general $\sim 25\%$ of the clusters have more than one strip. Track segments are then found independently in each detector assembly. As a first step, matching clusters in the two planes with the same strip orientation are combined. Candidate local track segments are then found by combining pairs of clusters belonging to different projections. When a pair of such clusters intersects within the region covered by the sensitive area of the detectors, a corresponding cluster in the remaining projection is searched for. In order to reduce the number of candidates, local track segments that transverse the overlap region of the detectors in the upper and the lower

Pot	Type	Installed planes	Read planes	Readout Channels	Comments
$S4_{UP}$	x	-	-	-	
	u	2	2	2048	
	v	2	1	1024	
$S4_{DOWN}$	x	-	-	-	Plane 4, 1 DTSC dead
	u	2	2	2048	
	v	2	2	1984	
$S5_{UP}$	x	-	-	-	Plane 2, 1DTSC dead
	u	2	2	1856	
	v	2	1	1920	
$S5_{DOWN}$	x	2	2	1152	1 dead plane (30/09/94)
	u	2	1	960	
	v	2	2/1	1920/960	
$S6_{UP}$	x	-	-	-	half of a plane is dead
	u	2	2	1472	
	v	2	2	1920	
$S6_{DOWN}$	x	2	1/2	448/896	Plane 1 recovered (30/08/94)
	u	2	2	1856	Plane 2, 1 DTSC dead
	v	2	2	1920	
Total	min	28	24	21568	
	max	28	26	22976	

Table 4.10.1: Spectrometer configuration in the 1994 data taking. The labels UP and DOWN refers to the up and down parts of the double LPS stations.

halves of the station are treated as one candidate. Finally, all hits belonging to a candidate (up to ten for tracks crossing the two halves, up to six otherwise) are used in a fit to find the transverse coordinates of the track at the value of Z corresponding to the centre of the station. The spatial resolution of these coordinates is about 30 μm. Fig. 4.11.1 shows the position of the reconstructed coordinates in the stations S4, S5 and S6 for a typical run.

Due to the beam optics in which the spectrometer is placed, the momentum of charge particles is measured for two classes of events: those which are detected in all three stations and those which are detected in only two stations. Fig.4.11.2 illustrates the momentum measurement.

In the simple case, 4.11.2 a, of the three stations S4, S5 and S6 recording tracks, the deflection in the dipole magnet gives a direct momentum measurement, $p = \frac{const}{h}$. However, for the case when only two stations S_i and S_j are hit, a 2-station method had to be developed and this is the key to being able to build up a viable acceptance for the spectrometer. In a given projection, e.g. horizontal, the position of a proton at station i is given by:

$$x_i = m_{i0}(x_L) \cdot x_0 + m_{i1}(x_L) \cdot x_0' + b_o(x_L) \tag{4.1}$$

where the m_i and b_i are known functions of x_L depending on the magnet strengths and geometries and x_0 and x_0' are the trajectory position and direction at the nominal vertex at $z = 0$. To illustrate this method, we can assume the approximate transverse position of the interaction point, $x_o = 0$.

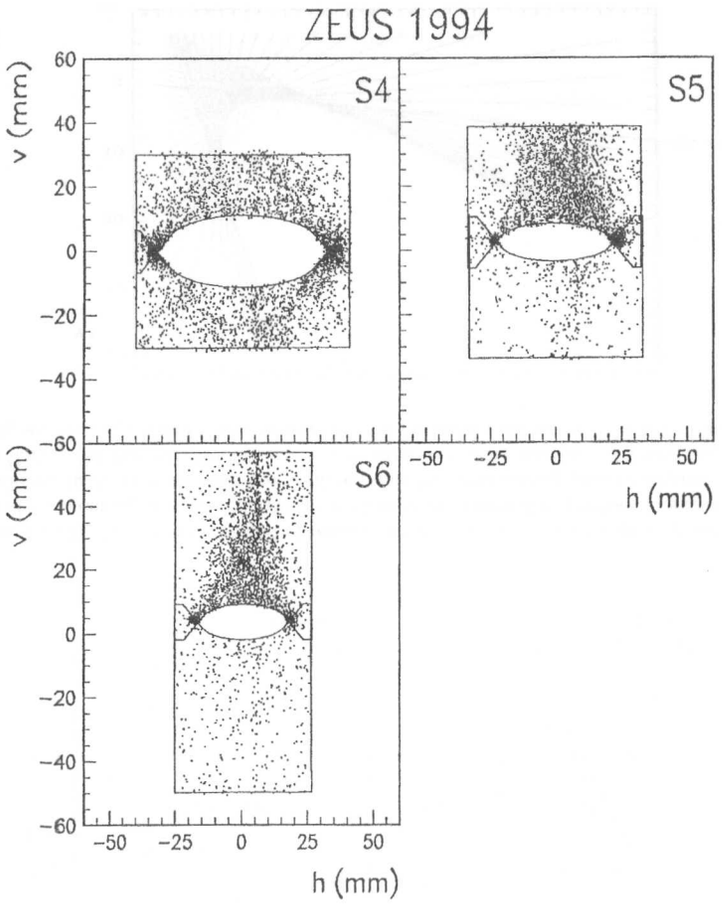

Figure 4.11.1: Positions of the reconstructed track impact points in S4, S5 and S6. For each plot the origin of the reference frame coincides with the position of the nominal proton beam at the value of Z corresponding to the centre of the station. The continuous lines approximately indicate the sensitive region of the detector planes.

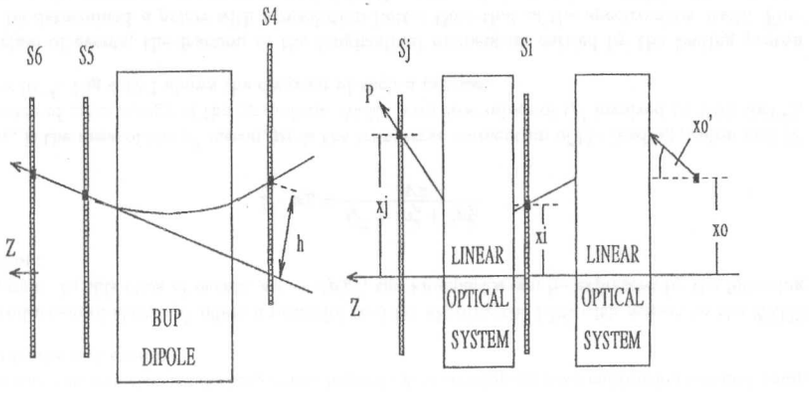

Figure 4.11.2: The two methods used for measuring momentum: a) using three stations; b) using two stations

In practice, the small errors introduced by this assumption are corrected. Then, by measuring the track positions in stations i and j, setting $x_0 = 0$ and eliminating x_0' one obtains the equation

$$\frac{x_i - b_{i0}(x_L)}{m_{i1}(x_L)} = \frac{x_j - b_{j0}(x_L)}{m_{j1}(x_L)} \tag{4.2}$$

Since the m and b coefficients are known functions of x_L the solution for x_L can be conveniently found using a look-up table method. Similarly, in the y-plane an independent estimate of x_L can be found and the two can be combined. Once x_L is determined, the equations are re-arranged to solve for x_0' and y_0' to give the transverse momentum.

In the chosen spectrometer design, the contributions to the momentum resolution from the size of the interaction region, from the detector resolution and from multiple scattering in the detectors and pot windows are all comparable.

When stations $S4$, $S5$ and $S6$ are all hit, an unambiguous momentum measurement is made in the vertical plane while in the horizontal plane straight-line tracks must be found. However, for certain pairs of stations in the two-station method there can be double solutions which are resolved by comparing the solutions in the two projections. Fig.4.11.3 shows typical problem cases. In the left-hand figure, one set of lines (near vertical) are lines of constant x_L in one region of x_L and the other set belong to a different region of x_L. The point shown has two solutions, found by interpolating in directions (1) and (2) as indicated, and both of them are accurate as indicated by the widely spaced lines.

The situation shown in the right hand figure also occurs in certain regions. The lines of constant x_L form an envelope which separates a permitted region from a forbidden region. Tracks near the boundary, (3), have larger errors and some special care is taken when, for example, multiple scattering throws a track into the forbidden region. Fig.4.11.4 shows in greater detail the lines of constant X_L and the scatter of hits before any event selection, calibration or alignment has been

carried out. After the alignment, the envelope of the lines becomes the outer boundary of the denser band of points.

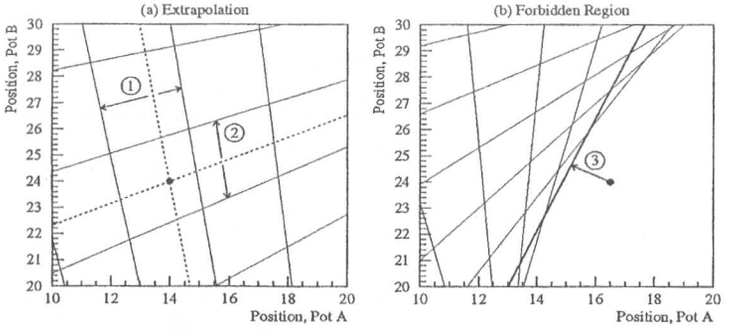

Figure 4.11.3: The two-pot method of reconstruction. The LPS reconstruction generates a grid of lines of constant x_L in a lookup table. (a) Most tracks (large dot) produce hits that fall between these lines. In this case, x_L solutions are determined by extrapolating between adjacent neighbouring lines (1)(2). (b) For hits that fall in the forbidden region, the nearest line (dark line) is chosen as the x_L solution (3). The x_L lines drawn here are for illustration and are not actual solutions.

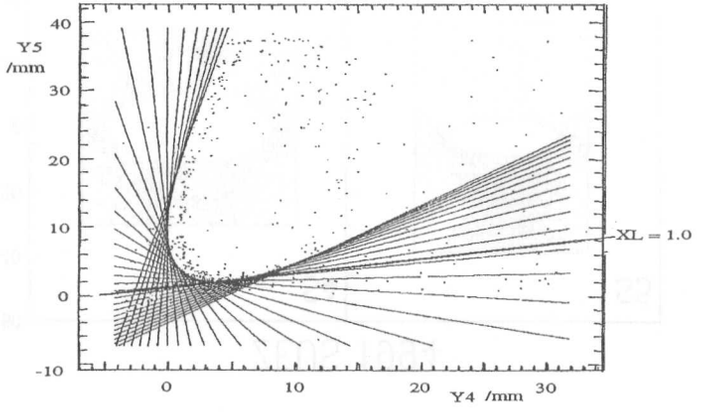

Figure 4.11.4: Correlation plot of vertical positions in S4 and S5 with lines of constant x_L calculated before alignment was made

4.12 Calibration and alignment

The first attempt to align the LPS stations was done using a careful geometrical survey of the detector installation. It was supplemented by a dedicated alignment technique composed of a collimated HeNe laser source - zone plate - CCD optical system used to check the stability of a survey over a period of a year. The laser technique was shown to give a relative alignment of external reference points on the S4, S5 and S6 stations with a precision of 10 μm [72]. It was used to define a straight line which, together with the measurements of the positions of the detectors relative to the optical system, completed the information needed to define a straight line in terms of detector strip addresses.

The laser alignment to check the stability of the survey worked as follows:

- The surveyers measure the coordinates of the elements (fiducials) of the laser system at each station. The laser alignment method compares the results of the survey at S6 with the extrapolation of the S4-S5 survey measurements to S6 using the laser beam. This then gives an internal consistency check of the surveyers measurements. The differences observed are shown in table 4.12.1.

Year	x_6 extrapolated	y_6 extrapolated
1993	-0.039 mm	0.084 mm
1995	-0.270 mm	-0.0251 mm

Table 4.12.1: Differences found,using the laser alignment, of the surveyers measurements at station S6.

  Therefore, we assume the survey measurements with a standard deviation of 0.14 mm.

- The transfer from these fiducials down to the detector supports was made by a survey in the laboratory, with about 0.05 mm precision.

Since these errors, 0.14 mm on the S4-S5 extrapolation to S6 are about a factor of 2.5 greater than the intrinsic detector resolution, it was important to develop an auto-calibration method using physical tracks and events.

Photoproduction of elastic ρ^0 offers a powerful tool for aligning the LPS with respect to the ZEUS main system. In this class of events, $ep \to e'p'\rho^0$, the kinematics can be expressed by the following formulation:

$$1 - x_L = \frac{Q^2 + m_\rho^2 + 2p_T^2}{W^2}$$

where m_ρ is the mass of the ρ^0 meson, p_T is the transverse momentum of the leading proton and W is the centre of mass energy of the γp system. At the very low values of Q^2 involved (≤ 0.02 GeV^2), $1 - x_L \sim 10^{-4}$. Fig 4.12.1 shows the diagram of such a process.

In this class of events, the fraction of the longitudinal momentum carried by the leading proton x_L, can be determined *a priori* with a resolution better than that of the spectrometer itself. Furthermore, as the transverse momentum carried by the scattered electron is negligible relative to the reconstruction errors, the transverse momentum carried by the leading proton should, on average, be equal and opposite to the transverse momentum of the ρ^0 meson for an on-axis beam particle.

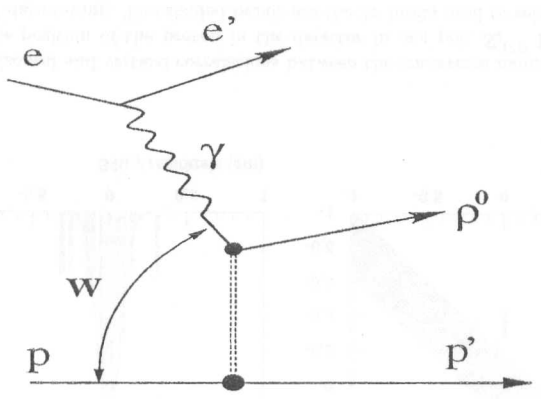

Figure 4.12.1: Feynman diagram for the photoproduction of ρ mesons

In terms of the LPS, for fixed values of x_L these events will form a correlation line between the transverse hit positions at any of two stations along the spectrometer. Fig. 4.12.2 shows this correlation in hit positions between pairs of pots in both the horizontal and vertical views. The strong concentration of points around the emphasised line in each correlation plot is the diffractive signal. After some cuts are made on the events this provides a very clean line at $x_L = 1.0$.

The transverse momentum calibration is made relative to the central tracking detector of ZEUS using the diffractively produced ρ^0 mesons. Their transverse momentum is plotted as a function of the position of the proton track in the LPS detectors. This calibrates both the transverse scale and also the offset, as shown in Fig. 4.12.3.

The use of these events permits the longitudinal momentum (p_L) calibration of the LPS with a resolution of up to $\Delta p_L/p_L = \pm 8 \times 10^{-4}$ and transverse momentum (p_T) resolution well within the spread of the incident beam emittance [73].

The calibration studies were first carried out with data from one of the last runs in the year 1993 when the LPS was in a test period and then implemented as a part of the alignment procedure for the 1994 data taking. A detailed analysis of the alignment of the LPS, as reported in reference [74] is performed in the following steps:

1. Use the survey to give the pot and detector positions at known motor settings and allow approximate reconstruction.

2. Take all tracks, from a single long run, which cross three stations. Rough reconstruction gives the direction of the track at a station with sufficient accuracy to align the planes in one pot relative to two reference planes $(u + v)$ in that pot. A fitting procedure is used to find the orientations and displacements of all strips relative to the strips in the two reference planes.

   At this point, the position of any track as it crosses the centre of the pot can be reconstructed in the coordinate system defined by the two reference planes.

3. Use tracks which cross the regions where the upper and lower pots at a given station overlap and fit the position and orientation of the lower pot relative to the upper pot.

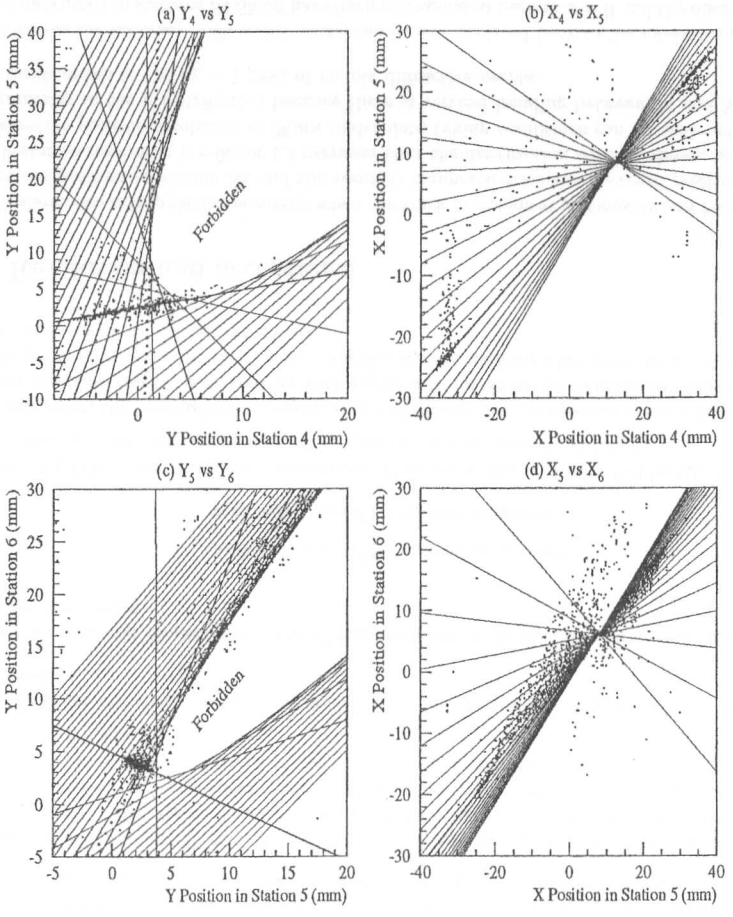

[hp!]

Figure 4.12.2: Horizontal, X, and vertical, Y, correlations between track positions in two pairs of stations. Lines are for the correlations between the x or y coordinates seen in two pots for tracks from the nominal vertex. Each line is a fixed value of x_L, from 0.5 to 2.0 in a) and b) and from 0.6 to 1.5 in c) and d). The darker line is for $x_L = 1$ and the lines rotate clockwise as x_L increases. The small dots are events and the large dots are the points on the fixed x_L lines where p_x or p_y is zero. Diffractive physics shows up as the large fraction of events clustered near $x_L = 1$.

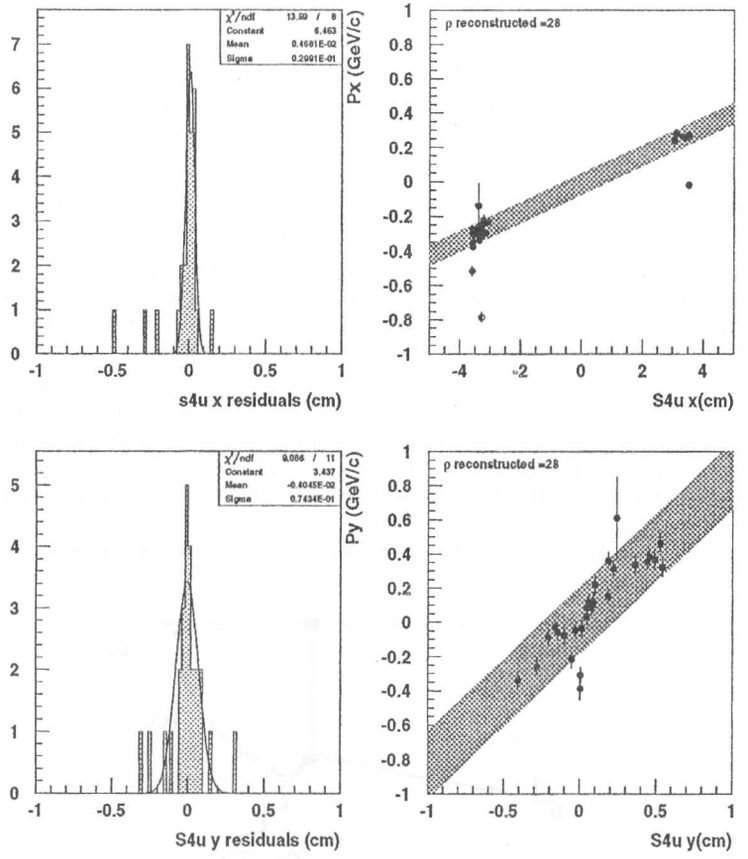

Figure 4.12.3: Horizontal and vertical correlations between the transverse momentum of the reconstructed ρ^0 and the position of the proton in the detector in one pot, $S_4{}^{UP}$ for a particular run (9783) during 1994 data taking. The shaded bands are the 2σ limits used to select data for fitting.

4. Take diffractive events (ρ^0) with coincidence in stations $S4^{UP}$, $S5^{UP}$ and $S6^{UP}$. Since the vertical bending angle in the dipole between S4 and S5 is accurately known and the bending angle in the horizontal plane is zero, a fitting procedure is used to determine the orientations (rotations about the beam direction) of two stations relative to the third. Then, by rotating tracks reconstructed in S5 and S6, extrapolating them to S4 and comparing with the observed position S4, S4 is aligned to S5 and S6.

   Then any track crossing S4, S5 and S6 can be reconstructed to give the track momentum and, as it enters S4, its position and direction relative to the S4, S5 and S6 system.

5. Now all the reconstructed tracks in (S4, S5, S6) are taken and extrapolated back down the beam line to $z = 0$. The position and orientation of the overall S4-S5-S6 system is varied so as to obtain the smallest r.m.s spread of the vertex position in the horizontal and vertical directions, checking that there is no systematic variation in the reconstructed transverse position with the reconstructed momentum.

   At this point, the momentum, vertex position and vertex direction of any track can be reconstructed.

6. Use the transverse momentum of the ρ^0 reconstructed in the ZEUS central tracking detector to form the vector:

$$p_x(\text{beam}) = p_x(\rho^0) + p_x(\text{leading proton})$$
$$p_y(\text{beam}) = p_y(\rho^0) + p_y(\text{leading proton})$$

   Hence, find the mean transverse momentum of the beam (its tilt multiplied by 820 GeV) and its spread in transverse momentum. This quantity is determined run-by-run.

   At this point, the longitudinal momentum and the transverse momentum relative to the mean beam direction can be measured for each event with an S4-S5-S6 coincidence. Furthermore, to improve acceptance the mean vertex position can be used together with the hit positions in any two stations to reconstruct a track.

4.13 Resolution and acceptance

Fig.4.13.1 shows the extrapolation accuracy when the track positions at stations S5 and S6 are used to predict the position at station S4 and the result is compared with the observed position at S4. The single station resolution is a factor 1.7 narrower than the distribution which is shown, indicating that an effective position resolution of $35\mu m$ under data taking conditions can be achieved. There is an asymmetry in the y distribution because there is vertical bending between S4 and S5 and a lower momentum tail to the $x_L = 1$ peak of mainly diffractive events.

Fig.4.13.2 shows the accuracy with which tracks can be extrapolated back to the interaction vertex. Tracks reconstructed in stations S4·S5·S6 have been extrapolated back to $z = 0$ and the distributions of the resultant transverse positions measured. The r.m.s of the distributions measures $630\mu m$ horizontally and $100\mu m$ vertically.

Fig.4.13.3 conveys the result of reconstructing the ρ events after applying the calibration results. It indicates an overall transverse momentum resolution of 38 MeV horizontally and 94 MeV vertically. These widths are mainly due to the transverse momentum spread inherent in the beam. The s.d. of the reconstructed x_L distribution was 0.3%. It is not Gaussian because the combined effect of

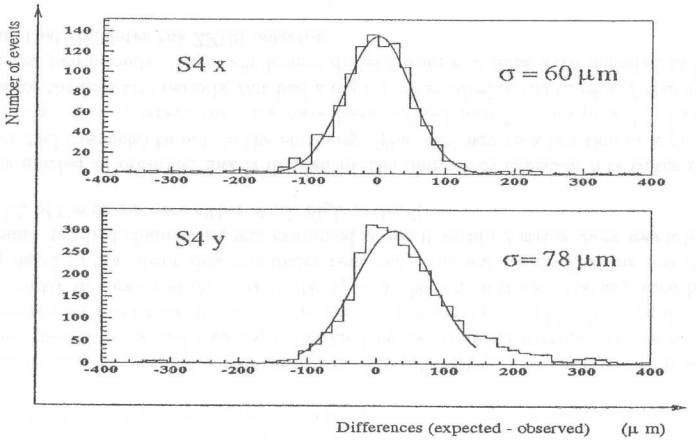

Figure 4.13.1: Differences between the coordinate at S4 and that expected from extrapolation from S5 and S6 are shown for all events in the 1994 run

bending and focusing produces a dispersion which varies across the detectors. The data near $x_L = 1$ is concentrated in two regions one on either side of the detector cutout, so the observed distribution is the sum of two distributions with different widths.

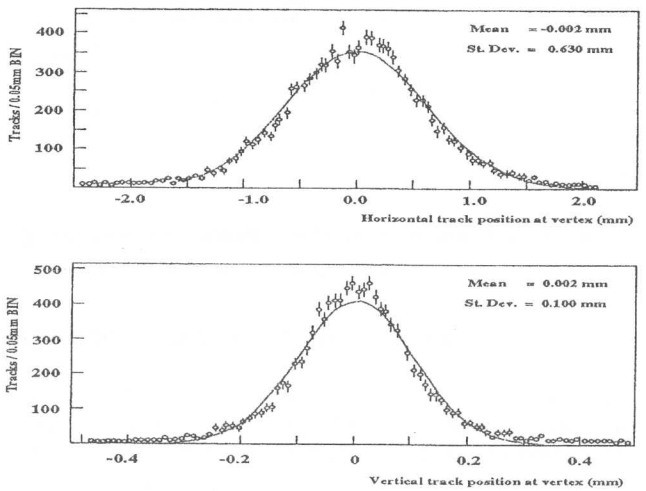

Figure 4.13.2: LPS reconstructed vertex distribution

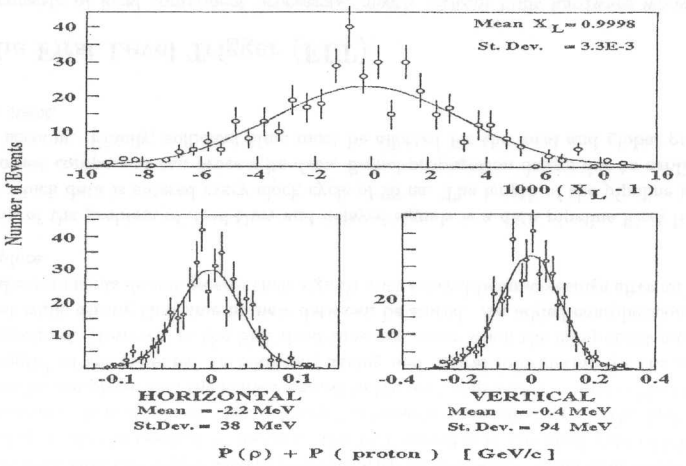

Figure 4.13.3: Reconstructed momenta in ρ events, after the spectrometer had been calibrated

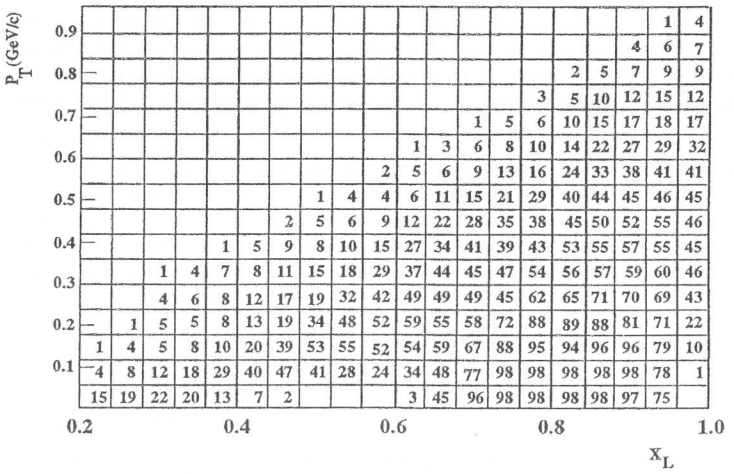

Figure 4.13.4: Nominal geometrical acceptance (%) in the (x_l, P_t) plane for the full six station spectrometer

Fig.4.13.4 shows the nominal acceptance map for the full spectrometer. In practice, during the analysis, accelerator conditions require that the detectors are further from the beam than the nominal position so that a given analysis necessitates a series of modified acceptance maps.

4.14 Performance of the Silicon detectors

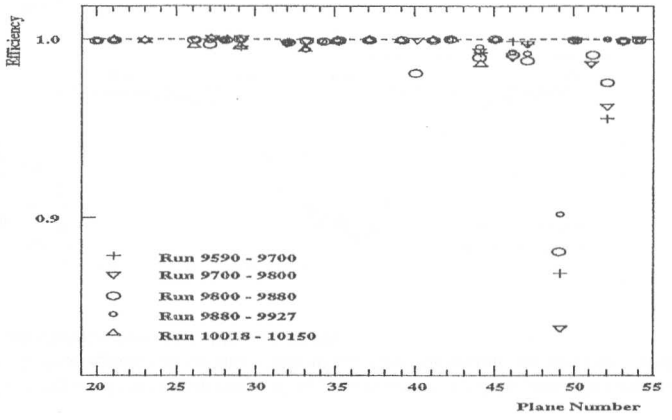

Figure 4.14.1: Efficiency as a function of plane number. For many planes data from all the runs coincide and have 100% efficiency. The lower efficiency planes correspond to S6 where the bias voltage was particularly low with respect to the others. These efficiencies derived from real data were included in MOZART, the program that simulates the ZEUS detector.

Silicon detector efficiency was calculated using a tracking algorithm. One plane at a time was selected to determine the efficiency and was not considered by the tracking routine. Tracks were then fit, and a χ^2 was required to be acceptable with at least 16 detectors planes hit. This requirement limits the tracks mostly to three station tracks with $x_L \approx 1$. For these tracks, the expected hit location was extrapolated to the silicon detector under test, and a hit was required within few strips. If no hits was found, the bad channel list was examined to see if within 2 strips there was a bad channel (typically 1% of the strips were either stuck high or dead).

Finally, the number of observed hits is divided by the number of expected hits (after suppressing hits through bad channels) to obtain the efficiency. The efficiency as a function of a plane number is shown in Fig. 4.14.1, where the runs have been divided into five run periods. Plane 40 was operational for the first two periods, but had a digital failure during the third and was switched off during the last two periods. These efficiencies derived from real data were included in MOZART, the program that simulates the ZEUS detector.

5 The ZEUS Data Acquisition System and Event Selection

5.1 Overview

The components of the ZEUS detector correspond to a total of about 250,000 electronic channels. For each interaction, they generate an event data record of about 100 kB in size. The HERA beams cross at a rate of 10.4 MHz or once every 96 ns. At the design luminosity about 1% of these crossings (several hundred kHz) will produce a signal in ZEUS. If every event were read out, this would require an archiving bandwidth of 10 GB/s. This rate can neither be stored on tape nor analysed afterwards, by means of present storage technology.

The high background rate arises from proton beam interactions with the residual gas in the beam pipe and with the wall of the beam pipe in the 70m straight section of HERA in the path of the incoming proton beam prior the interaction at ZEUS. In contrast, photo-production produces O(100) Hz and deep inelastic scattering 0(5) Hz. To achieve this, the ZEUS Data Acquisition System (DAQ) [75] employs three levels of triggering, as illustrated in Fig. 5.1.1. The design of each level is determined by the decision time available. The first Level Trigger (FLT) must handle an input rate of several hundred kHz and must reduce this to about 600 Hz. The Second Level Trigger (SLT) must reduce the output from the FLT to about 100 Hz within a few ms. The Third Level trigger (TLT) must reduce the 100 Hz rate from the SLT to about 5 Hz.

It is indispensable that the trigger system performs without dead-time. Dead-time refers to a period of time during which the readout is inactive. The FLT operates at the clock rate of HERA and is without dead-time. It is pipelined, that is, every fundamental individual step in the decision making process must be completed and the answer passed to the next step within a time of Nx(96ns), where N is the length[1] of the pipeline. In addition, analog and digital information for the second level trigger is pipelined. However, at the SLT dead-time can occur when the component analog signals are digitised while during this time no new data can be stored. An added complication is the fact that several components do not receive their signals until several beam-crossings after an interaction has taken place.

The solution of the problem of dead-time and delayed signals is a data pipeline First In First Out (FIFO), in which data is entered every clock cycle of 96 ns. The length of the pipeline is chosen so that the slowest component can process its data. Signal propagation delays due to cabling are also taken into account. Finally, sufficient time must be allotted for the local and global processors to analyse an event.

5.2 The First Level Trigger (FLT)

The FLT consists of local component processors, mostly custom built hardware whose decisions are sent to a Global FIRST Level Trigger (GFLT). The FLT is used to reject online, part of the

[1]The length of the pipeline at the FLT is 5 μs (Fig. 5.1.1).

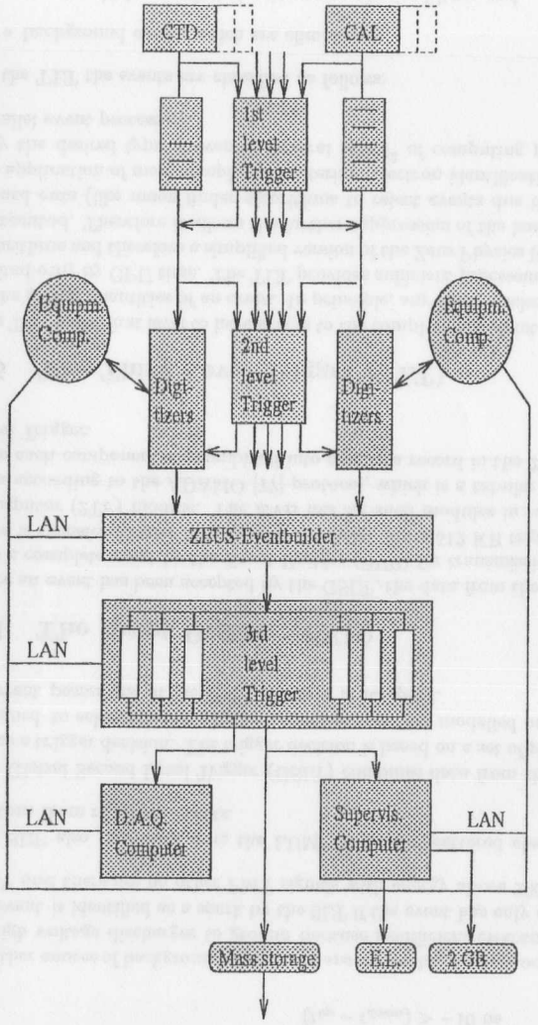

Figure 5.1.1: A schematic of the ZEUS trigger system

background from beam-gas, halo and cosmic ray events, reducing the event counting rates down to 1 KHz.

Due to the very short time period between two successive *ep* collisions at HERA, the GFLT allows 26 clock cycles for the local FLT components to evaluate their data and send a result to the GFLT. Within another 20 clock cycles the GFLT must provide an event decision based on these data. Allowing for delays in signal propagation, this requires that the component data pipelines must be 58 clock cycles or 5μs or greater in length (the LPS uses 6.14 μs). If the event input rate to the GFLT is higher than its internal CPU rate, the events are lost and the time in which the GFLT is inactive is also called dead-time.

In the 1994 data taking configuration the event input rate at the Second Level Trigger was between 120 - 180 Hz with a dead-time of up to 1%. The components participating in the FLT decision were the uranium calorimeter, central tracking detector, the muon chambers, the luminosity monitors and the background counters (C5 and the Veto Wall). The LPS trigger system for high x_L events, based on small trigger detectors in the pots and a hardware matrix coincidence between hit strips in various pots was still under construction at this time.

5.3 The Second Level Trigger (SLT)

The SLT has available to it a decision time of a few ms, and therefore it can be implemented on programmable processors. Transputer[2] networks are used by some components, others use digital signal processor chips, and components with little to add at the SLT stage may just say 'yes'. Iterative algorithms can be executed on these processors. For example, the CAL-SLT utilises an algorithm to search for clusters, which are adjacent energy deposits in the calorimeter. These clusters can be used to identify the primary scattered electron in an *ep* collision. The CAL-SLT also calculates global energy sums, using the data from calorimeter cells.

Background rejection at the SLT [76] is performed using timing information from the calorimeter. Particles originating from an *ep* collision at the nominal interaction point and travelling near the speed of light are defined to arrive at time t=0 at the faces of the calorimeter. In contrast, events originating in the proton path before its arrival to the detector produce earlier signals in RCAL, at $t \sim$ -10 ns.

An event at the SLT is rejected if the RCAL time is:

$$|t_{RCAL}| > 8 \text{ ns}$$

or the FCAL-RCAL time difference is:

$$|t_{FCAL} - t_{RCAL}| > 8 \text{ ns}$$

or the FCAL time is:

$$|t_{FCAL}| > 8 \text{ ns}$$

Cosmic-ray induced events are rejected based on the difference between the upper and lower BCAL calorimeter time. These events enter at the top of the ZEUS detector due to their cosmic origin, and are vetoed if the measured time:

[2]Processor, memory and communications hardware on a single chip

$$(t_{up} - t_{down}) > -10 \text{ ns}$$

Another source of background signals are *spark* events. A spark occurs when a calorimeter phototube at high voltage discharges to ground because insufficient clearance was left in the PMT assembly. An event is identified as a spark by the SLT if the event has only one PMT signal with energy above 2GeV and there are no other PMT signals with energy above 200 MeV.

The SLT also uses data from the LUMI to detect scattered electrons from photo-production and photons from radiative events.

The Global Second Level Trigger (GSLT) combines data from the component SLT processors, and forms a trigger decision. The trigger decision is based on a set of *physics filters*. These are algorithms designed to select specific physics processes, and are modelled on the Third level Trigger filters. If an event passes one of the GSLT filters it is accepted.

5.4 The Event Builder (EVB)

Once an event has been accepted by the GSLT, the data from the various components are assembled into a complete event by the Event Builder (EVB) for transmission to the third level trigger (TLT). Data is transferred over EVB transputer links into a 512 KB triple-ported memory (TPM) in a two transputer (2TP) module. The EVB has six such modules in total. Each component formats the data according to the ADAMO [77] protocol, which is a tabular data format. The ADAMO tables from each component are combined into one data record in the 2TP module for access by the Third Level Trigger.

5.5 The Third Level Trigger (TLT)

The TLT is the first level to have access to the complete raw event data, which allows the exploitation of the global quantities of an event. In principle, any off-line selection can be performed at the TLT, limited only by CPU time. The TLT provides sufficient processing power to execute iterative off-line algorithms and therefore a simplified version of the Zeus Physics Reconstruction (ZEPHYR) program is executed. Therefore it allows the further suppression of the background contamination using more refined cuts (like muon finder algorithms to reject events due to cosmic or beam gas muons) and the application of more complicated filtering (electron identification and jet reconstruction) to select only the desired type of events. Several MIPS[3] of computing power are used in each each of the parallel event processors.

At the TLT the events are classified as follows:

- background events which are eliminated,
- events which are selected using some physics filters, and
- events which cannot be classified under the previous two categories.

Only the events belonging to the second category and a limited fraction of the third category are transferred and archived in tapes.

[3]Million Instructions Per Second

5.6 Event Selection

The analysis presented here uses two different classes of *ep* events, each one defined in a very different kinematic region. These event classes are:

- Photo-production (PHP): *ep* scattering at very small values of the electron four momentum transfer ($Q^2 \leq 0.02$ (GeV/c)^2). The scattered electron escapes down the beam pipe undetected by the Uranium calorimeter. However, in most of the cases it is detected by a special calorimeter (LUMI-E) placed at z=-33 m from the interaction point of ZEUS. Since the scattered electron is detected by the LUMI-E, this class of events is also called *tagged photo-production events* which were collected using the Photo-production trigger
- Neutral current Deep Inelastic Scattering (DIS): *ep* scattering at large values of the electron four-momentum transfer ($Q^2 > 2.0$ (GeV/c)^2). A typical signature of this event is an isolated electromagnetic cluster in the calorimeter belonging to the scattered electron and a jet of hadrons which are the remnants of the materialisation process when a quark from the proton has received the four-momentum transfer.

5.6.1 Photo-production Trigger

Photo-production events were collected using the tagged photo-production trigger which requires the coincidence of signals in the main calorimeter and the LUMI electron tagger. Due to the large luminosities delivered by HERA, the rate of these photo-production events was too high and thus needed to be prescaled at different stages of the trigger logic as shown in Fig. 5.6.1.

All the tagged photo-production data come from one FLT slot (slot nr 36) requiring the coincidence of the LUMI-E subtrigger with the REMC or REMCth subtriggers. The LUMI-E subtrigger was activated in cases in which the energy deposited in the LUMI electron calorimeter exceeded 5 GeV. The REMC subtrigger required that the energy deposited in any of the towers of the RCAL EMC section, excluding the towers immediately adjacent to the beam pipe, to be more than 464 MeV. In the REMCth subtrigger the energy from all the RCAL EMC towers (including the beam pipe region) of at least 464 MeV was summed and compared to the threshold of 1250 MeV. Additionally, to reduce the contamination from p-gas background already at the first triggering level, the events with a background hit in the C5 counter were rejected. In order to decrease the rate of tagged photo-production subtrigger, only every second event was accepted by the FLT (prescale 2).

At the SLT the tagged photo-production event stream was further cleaned from the background (as described in section [5.3]) and some parts of the event sample were further prescaled. The events from the tagged photo-production FLT slot were processed by physics filters and assigned to one of the streams shown in Fig. 5.6.1, listed as follows:

- Stream 1:
  A particular set of events are selected and classified as background from Bremsstrahlung and electron pilot bunch events. This selection requires one of the following conditions to be satisfied:
  - 10 GeV $< E_{e'} <$ 19 GeV, which corresponds to events in the highly populated central band in Fig. 5.6.2.
  - $E_{e'} + E_{\gamma} >$ 23 GeV, which are identified as Bremsstrahlung.
  - event belonging to an e-pilot bunch

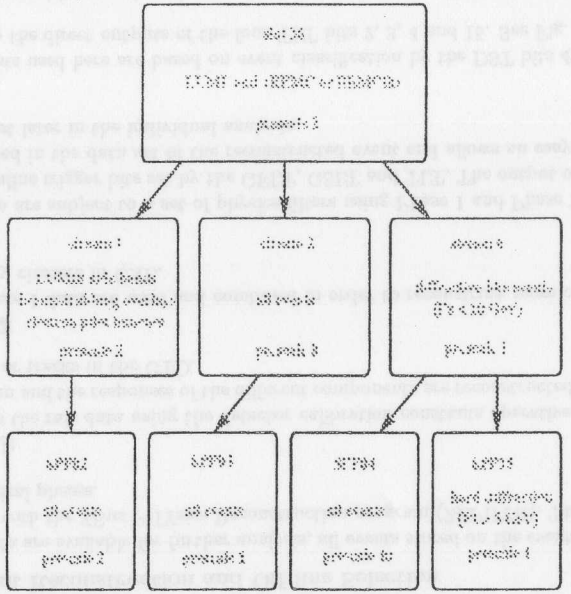

Figure 5.6.1: Schematic diagram of the tagged photo-production trigger implemented in 1994

$E_{e'}$ and E_γ correspond to the energy measurements carried out with the LUMI-E and LUMI-G calorimeters for the scattered electron and the Bremsstrahlung γ. These events were assigned with a prescale factor 2.

- Stream 2:
  All tagged photo-production triggers were accepted following prescaling by a factor 8.
- Stream 6:
  Selects diffractive candidates characterised by a small energy deposit in the FCAL, and requiring the total longitudinal momentum of the event observed in the ZEUS calorimeter to be:

$$p_z^{total} < 10 \text{ GeV}$$

  The events were passed with no prescale.

At the TLT, the various physics filters applied to the tagged photo-production events are assigned the four trigger bits shown in the diagram in Fig. 5.6.1. The first three TLT bits, SPP02, SPP03 and SPP04 do not apply further selection to data, but the SPP15 bit selects diffractive candidates requiring a calorimeter transverse energy greater than 5 *Gev*.

The different prescale factors applied at each stage were adjusted to optimise the usage of the event-tape storage.

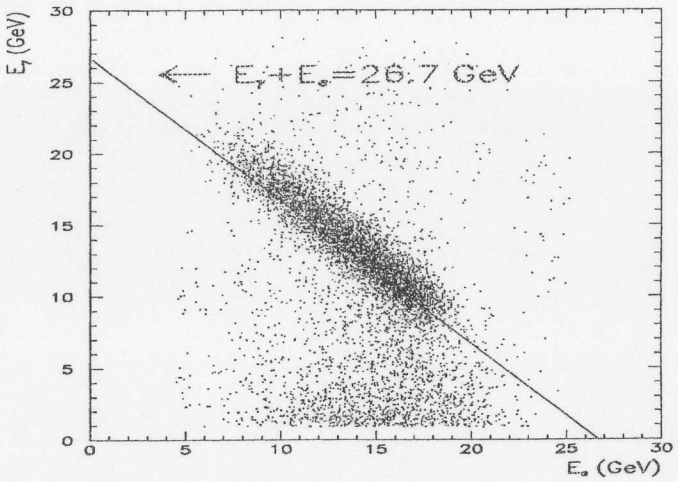

Figure 5.6.2: Correlation plot of the electron ($E_{e'}$) and photon (E_γ) energies as measured in the LUMI-E and LUMI-G calorimeters of the luminosity monitor

5.6.2 Deep Inelastic Scattering trigger

Neutral current DIS events are selected by a logic OR of a subset of FLT filter bits which correspond to an energy threshold in CAL sections and isolated energy deposits in combination with vetoes from C5, the Veto Wall and SRTD. The physics filter associated with this selection is called **DISFF**. It imposes a minimum activity in the calorimeter associated with a DIS events.

In addition another physics filter **DIS1** is used which requires a threshold:

$$(E - p_z)^{total} + 2{\cdot}E_\gamma > 24 \text{ GeV}$$

for events which pass **DISFF** or which have a deposited transverse energy in CAL, $E_t > 25$ GeV. This cut indicates a reconstructed scattered electron in the calorimeter with a possible initial state photon with energy E_γ detected in the photon calorimeter of the luminosity monitor.

At the TLT level the preselection of the neutral current DIS data sample is organised in 5 trigger slots as follows:

- DIS01: Selects data according to:
  - GSLT filter **DISFF** selection
  - $(E - p_z)^{total} + 2{\cdot}E_\gamma > 24$ GeV
  - electron found with any of the standard electron finder algorithms with energies:

$$E_{e'} > 4 \text{ GeV}$$

- DIS02: Selects data according to:
  - absence of a cosmic muon in the event
  - reduction of the contributions from photo-production events, where the scattered electron leaves CAL undetected by applying the following cuts:

$$(E - p_z)^{total} > 25 \text{ GeV}$$

$$E_t^{total} > 40 \text{ GeV}$$

- DIS05: Same as DIS01 but without the electron requirement
- DIS06: Same as DIS01 but without the $(E - p_z)^{total}$ requirement
- DIS07: GSLT filter **DISSF** selection with:

$$(E - p_z)^{total} > 20 \text{ GeV}$$

The standard algorithms used at ZEUS to identify electrons are called ELEC5, LOCAL, EXOTIC and SINISTRA whereas the algorithm ISITAMU is used to identify muons. All those algorithms are available in PHANTOM, a ZEUS software library for physics analysis.

5.6.3 Event Reconstruction and Off-line Selection

Before the data are available for further analysis, all events stored on the event-tape storage are "reconstructed" with the ZEus PHYsics Reconstruction program (ZEPHYR). This program is divided into three logical phases.

- Phase 1:
  Corrects the raw data using the detector calibration constants operative at the time the data was taken and the responses of the different components are reconstructed, e.g. energy deposits in CAL or tracks in the CTD.
- Phase 2:
  The Phase 1 data are used and combined in order to reconstruct more complex objects, such as energy clusters in CAL.
- DST:
  The data are subject to a set of physics filters using Phase 1 and Phase 2 information as well as the online trigger bits set by the GFLT, GSLT and TLT. The output of these physics filters is included in the data set of the reconstructed event and allows an easy access to the events of interest later in the individual analysis.

The PHP events used here are based on event classification by the DST bits 49, 50, 51 and 62 and corresponds to the direct outputs of the four TLT bits 2, 3, 4 and 15. See Fig. 5.6.1.

The DIS events used here are based on event classification by the DST bit 21 which select the events according to the and of the following conditions:

- DIS01 **.OR.** DIS02 **.OR.** DIS05 **.OR.** DIS06 **.OR.** DIS07

- $(E - p_z)^{total} + 2 \cdot E_\gamma > 35$ GeV
- Spark event rejection in CAL
- Beam halo muon event rejection
- $E_{e'} > 5$ GeV
- $y_{JB} > 0.02$ [4]

The spark rejection algorithm recalculates the energy sums in the FLT trigger regions excluding cells with high energy imbalance. If the recalculated energy falls below a certain threshold the event is rejected. Beam halo muon rejection searches for anomalous structures such as many consecutive BCAL towers with energy depositions but no tracks in the CTD.

The cut in the reconstructed electron energy[5] ensures high efficiency and purity for the electron finding algorithms. A correctly reconstructed scattered electron is very effective in removing photo-production events. The cut in y_{JB} removes events with low Bjorken-y that would move to low Bjorken-x if the double angle method were used and therefore improves the resolution in the measurement of Bjorken-x.

[4] JB refers to the Jacquet - Blondel Method described in section [2.2]
[5] The methods used for identifying electrons were described in section [2.2]

6 The Leading Protons at HERA

6.1 Overview

As explained in section [2.3], *ep* collisions can be classified regarding the hardness of their interactions, which are related to the electron four momentum transfer (Q^2). Usually, at HERA, following these classification criteria, the events are grouped as photo-production (PHP), if $Q^2 \leq 0.02$ (GeV/c)^2 and deep inelastic scattering (DIS) if $Q^2 \geq 2$ (GeV/c)^2. In those events only a small fraction contains a leading proton.

In addition to the prescriptions applied to select the PHP and DIS data, some other refinements have been carried out prior to the search for leading protons in our sample. In the following sections, a detailed explanation of the selection of the final sample in PHP and DIS data is presented. In particular, special attention is paid to the PHP sample which was prescaled with four different prescale factors. Finally a measurement of the transverse and longitudinal momentum distributions of the leading protons in both PHP and DIS data is also reported.

6.2 Data sample

The data used in this analysis was collected following, at online level, the steps presented in section [5.6]. In addition, at off-line level, a further selection criterion was applied to ensure the quality of the data as follows:

- **PHP data**
  - Validation of the photo-production trigger selection as explained in section [5.6.1].
  - No electron found in the central calorimeter. The search was performed using a Neural Network electron finder algorithm, *sinistra* [78].
  - Scattered electron identification with LUMI-E detector as described in section [3.2.1], for energies:

    $$12 \text{ GeV} \leq E_{e'} \leq 18 \text{ GeV}$$

    this corresponds to the W range of:

    $$176 \text{ GeV} \leq W \leq 225 \text{ GeV}$$

    and four momentum transfer of:

    $$Q^2 \leq 0.02 \text{ (GeV/c)}^2$$

- **DIS data**
  - Validation of the DIS trigger as examined in section [5.6.2].
  - At least one electron found in the central calorimeter using the *sinistra* electron finder. If more than one electron is found, the one with higher probability to be an electron is kept.

  - Reconstructed kinematic variables using the double-angle method[1] with the following restrictions:

    $$35 \text{ GeV} < (E - P_z)_{total} < 60 \text{ GeV}$$

    $$E'_e \geq 8 \text{ GeV}$$

    $$y < 0.95$$

    $$45 \text{ GeV} < W < 225 \text{ GeV}$$

  - Additional restrictions were required in the reconstruction of y and Q^2 if they were reconstructed using the Jacquet-Blondel and direct electron identification method[2], respectively. These restrictions are relevant to the energy resolution measurement in the central calorimeter and were set as follows:

    $$y > 0.04$$

    $$Q^2 > 4 \text{ (GeV/c)}^2$$

In both PHP and DIS selections, a beam gas type of background rejection was applied by requiring that:

- events should not belong to an empty *ep* bunch
- strict calorimeter event timing relative to the arrival time of the bunches at the interaction point is as follows:

  $$|T_{FCAL}| < 6 \text{ ns}, \quad |T_{RCAL}| < 6 \text{ ns}$$

  $$|T_{FCAL} - T_{RCAL}| < 6 \text{ ns}$$

The remaining samples of PHP and DIS data were 120621 and 138350 events respectively. Tables 6.2.1 and 6.2.2 show, step by step, how the statistics of the final sample was reached.

Table 6.2.1: Event statistics in the final selection of PHP data during the 1994 data taking period

Selection	Events
PHP Trigger validation	331866
ep bunch	330278
Calorimeter event timing	303177
No e^- found in the central calorimeter	259664
LUMI-E electron found	205128
12 GeV $< E'_e <$ 18 GeV	120621
leading proton (after all cuts)	3122 ($\sim$ 2.6%)
leading proton ($0.6 < x_L < 1.02$)	2956 ($\sim$ 2.5%)

Only a subsample of the ZEUS events has a final state leading proton which can be detected using the LPS. Events are lost because of the limited geometric acceptance of the LPS and because in each fill of the machine the LPS positioning and setting up procedure can start only after stable beam has been established and data taking has started in the main ZEUS detector. Consequently

[1] Description of the double-angle method is provided in section [2.2].
[2] Description of the Jacquet-Blondel and electron method is provided in section [2.2].

Table 6.2.2: Event statistics in the final selection of DIS data during the 1994 data taking period

Selection	Events
DIS trigger validation	401815
ep bunch	400305
Calorimeter event timing	392642
e^- found in the central calorimeter	277338
35 GeV $< (E - P_Z)_{total} <$ 60 GeV	261245
$E'_e > 8$ GeV	251724
$0.04 < y < 0.95$	168418
$Q^2 > 4$ (GeV/c)^2	151633
45 GeV $< W <$ 225 GeV	138350
leading proton (after all cuts)	3739 ($\sim$ 2.7%)
leading proton ($0.6 < x_L < 1.02$)	3507 ($\sim$ 2.5%)

the integrated luminosity with the LPS operational was [79], $\mathcal{L}_{lps} = 1.3pb^{-1}$ out of a total $\mathcal{L}_{zeus} = 3.7pb^{-1}$ accumulated by ZEUS from $\mathcal{L}_t = 6.2pb^{-1}$ delivered by HERA.

To select a clean sample of those protons, the following restrictions were applied to the reconstructed leading protons:

- At least one track had to be reconstructed online in the LPS
- The distance of minimum approach of the track to the beam pipe had to be greater than 0.5 mm. This cut is required to reject events in which the reconstructed track comes from particles produced when the proton scrapes the beam pipe.
- The reconstructed track quality cut had to be:

$$\chi^2/\text{NDOF} \leq 6$$

- A fractional longitudinal momentum (x_L) of the leading proton in the range $0.60 < x_L < 1.02$ was required.

The surviving event sample is not completely free of background. This can be:

- p-beam halo in coincidence with an ep event triggered by the main detector. This kind of background is present in both, DIS and PHP, samples
- Bremsstrahlung reactions from $ep \rightarrow e'\gamma p'$ or, more generally, $eN \rightarrow e'\gamma N'$, an interaction of an incoming e with the residual gas in the beam pipe. This type of background is mainly present in PHP data.

These backgrounds can be divided in two types: *tagged* background, if it is clearly identifiable and isolated in phase space; *untagged* background if it is not distinguishable from the physics events. The contamination of the sample from *untagged* background can be estimated only during the analysis of the data. The *tagged* background sample is used to estimate the rate of background contamination expected in the event sample. Then the *untagged* background sample is statistically subtracted,

applying, on an event by event basis, a negative weight to the *tagged* background events [80], [81], [82] and [83]. The weight is defined by:

$$W_{bkg} = -\frac{\#\text{of untagged background events}}{\#\text{of tagged background events}}$$

The negative weight method of background correction is applied to the data for:

- p-beam halo coincidences:
  This background, which is common to both DIS and PHP sample, is identified by requiring the approximative conservation of $E + P_z$ in an event. E and P_z are the total energy and total longitudinal momentum of the event. The exact conservation of $E + P_z$ holds if the event is fully contained in the detector calorimeter.

  Thus for a fully contained event:

$$E + P_z = 2 \cdot E_p + \epsilon_p < 1655 \text{ GeV} \tag{6.1}$$

  where $\epsilon_p \sim 15$ GeV takes into account the resolution of the measurement. In the presence of a leading proton detected by the LPS, equation [6.1] can be rewritten as follows:

$$(E + P_z)_{total} + 2 \times 820 \times x_L < 1655 \text{ GeV}$$

  p-beam halo coincidences populates a kinematic region around x_L =1 and are statistically subtracted if:

$$(E + P_z)_{total} + 2 \times 820 \times x_L \geq 1655 \text{ GeV} \tag{6.2}$$

  The negative weight to be applied to data was estimated to be [71]: $W_{halo} = -0.37$, and was statistically subtracted on an event by event basis from both PHP and DIS sample.

  Fig. 6.2.1 shows the total $E + P_z$ as measured in the calorimeter versus the longitudinal momentum of the leading proton as measured in the LPS. The kinematic limit corresponds to equation [6.2]. Indicated are also the events populating the vertical band, mainly as p-beam halo background. The space between the two vertical lines containing these events corresponds to two standard deviation of the resolution in the measurement of the longitudinal momentum of the leading protons by the LPS.

- Bremsstrahlung events:
  It is one of the most important sources of contamination of the PHP sample. This kind of background can be produced through the reactions $ep \rightarrow e\gamma p$ or $eN \rightarrow e\gamma N$, N being the nucleus of the residual gas which is left in the beam pipe.

  Most of the detected Bremsstrahlung events originate near the interaction point and have a photon and electron detected by the LUMI-G and LUMI-E calorimeters respectively. These kind of events are referred to as *tagged* Bremsstrahlung and the sum of their energies deposited in the two LUMI calorimeters is around the electron beam energy:

$$E_{e'} + E\gamma \sim 27.5 \text{ GeV}$$

If the Bremsstrahlung reaction is not produced in the interaction point but in coincidence with a ZEUS physics trigger, the photon is not detected by the LUMI-G calorimeter. These events are indistinguishable from accepted physics triggers and are called *untagged* Bremsstrahlung events.

The negative weight applied to the tagged Bremsstrahlung events is:

$$W_{brem} = -\frac{\#\text{ untagged Bremsstrahlung events}}{\#\text{ tagged Bremsstrahlung events}} = \frac{P_{\text{untagged}}}{P_{\text{tagged}}}$$

where P_{tagged} is the probability for a Bremsstrahlung photon to be detected by the LUMI-G calorimeter and $P_{\text{untagged}} = 1 - P_{\text{tagged}}$.

Untagged Bremsstrahlung background events have been calculated and statistically subtracted from the PHP sample on a run-to-run basis from tagged Bremsstrahlung spectra collected by the LUMI acquisition system [80].

Fig. 6.2.2 is a correlation plot of $E_{e'}$ versus E_γ and the distribution of the weights W_{brem} as a function of the run number for the 1994 data taken period. The spread of the weights indicate the rate at which *untagged* Bremsstrahlung events at produced for a given HERA run condition

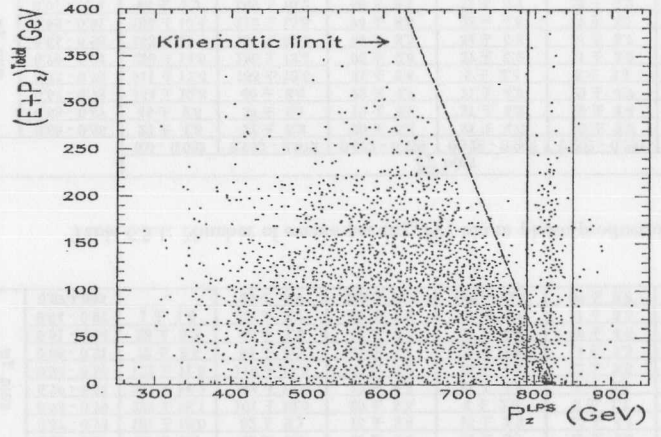

Figure 6.2.1: Correlation between the total $E+P_z$ as measured in the calorimeter and the longitudinal momentum of the leading proton as measured in the LPS. The events populating the vertical band are identified, mainly as p-beam halo background and are statistically subtracted. This kind of background is present in both DIS and PHP data. Data in this plot correspond to the PHP sample.

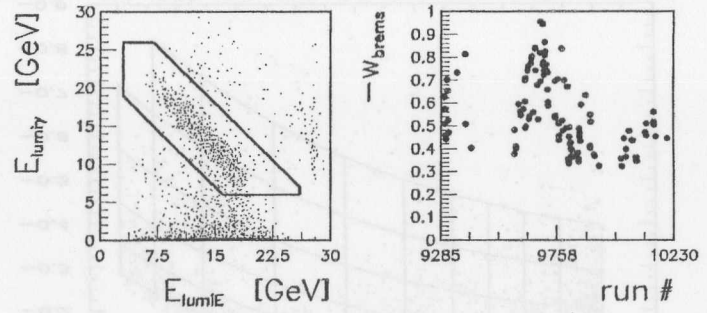

Figure 6.2.2: Left: Correlation plot of the electron versus the photon energy as measured by the LUMI-E and LUMI-G respectively. Data inside the polygon are identified as *tagged* Bremsstrahlung background. Right: Distribution of the weights as a function of the run number. The scatter of the weights relates to the production of Bremsstrahlung events due to different p-beam conditions. The weights are used to statistically subtract the *untagged* Bremsstrahlung events. Data in this plot correspond to PHP triggered events.

6.3 Binning the LPS data

Binning was selected taking into account the available statistics and the overall geometrical acceptance of the spectrometer. For this reason a variable binning in (x_L, P_t^2) was implemented.

We have chosen to use P_t^2 instead of t in order to have a more natural way to account for a general process in which the leading proton is produced. However, the choice is subjective because it is not clear which variable to use. It would be t if the leading proton were produced in a direct process which could be described by simple diagrams or perturbation theory, but this would not be so obvious if it were produced in a random walk from real or virtual cascade process in which the target proton is broken by the probe. The variables t and P_t^2 are connected through:

$$t = M_p^2 \cdot \frac{(1-x_L)^2}{x_L} - \frac{P_t^2}{x_L}$$

One of the advantages of choosing P_t^2 is that $P_t^2 = 0$ is a kinematic limit and for a maximum value of x_L ($x_L = 1$), $t \sim P_t^2$. However, an analysis method is introduced which is capable of producing results which do not depend on the details of the binning.

The final leading proton kinematic range was constrained to:

$$0.0\ (\text{GeV/c})^2 \leq P_t^2 \leq 0.4\ (\text{GeV/c})^2$$
$$0.6 \leq x_L \leq 1.005$$

Figs. 6.3.1 and 6.3.2 show the selected data for both PHP and DIS in the (x_L, t) plane as well as the binning choice with which our measurements were analysed. This demonstrates the differences which would occur if bins of t were used. In order to have reasonable statistics per bin, wide bins

in x_L must be used so that if t-bins were used inconvenient partly-occupied bins would result in the lowest t-bins. The number of events per each (x_L, P_t^2) bin are shown in Tables 6.3.1 and 6.3.2 respectively.

		P_t^2 bins					
		0.0 - 0.032	0.032 - 0.072	0.072 - 0.129	0.129 - 0.202	0.202 - 0.291	0.291 - 0.397
x_L bins	0.60 - 0.63	12 ± 3.5	18 ± 4.2	23 ± 4.8	14 ± 3.7	7 ± 2.6	-
	0.63 - 0.67	35 ± 5.9	42 ± 6.5	11 ± 3.3	14 ± 3.7	13 ± 3.6	5 ± 2.2
	0.67 - 0.73	101 ± 10.0	82 ± 9.1	15 ± 3.9	15 ± 3.9	22 ± 4.7	18 ± 4.2
	0.73 - 0.79	227 ± 15.1	101 ± 10.0	30 ± 5.5	4 ± 2.0	3 ± 1.7	15 ± 3.9
	0.79 - 0.84	202 ± 14.2	144 ± 12.0	72 ± 8.5	21 ± 4.6	6 ± 2.4	2 ± 1.4
	0.84 - 0.88	122 ± 11.0	119 ± 11.0	46 ± 6.9	18 ± 4.2	12 ± 3.5	8 ± 2.8
	0.88 - 0.91	72 ± 8.5	84 ± 9.2	44 ± 6.6	23 ± 4.8	11 ± 3.3	11 ± 3.3
	0.91 - 0.94	28 ± 5.3	68 ± 8.2	48 ± 6.9	23 ± 4.8	16 ± 4.0	6 ± 2.4
	0.94 - 0.97	1 ± 1.0	33 ± 5.7	49 ± 7.0	22 ± 4.7	11 ± 3.3	6 ± 2.4
	0.97,1.005	-	35 ± 5.9	379 ± 19.5	188 ± 13.7	97 ± 9.8	28 ± 5.3

Table 6.3.1: Number of events per (x_L, P_t^2) bin in photo-production

		P_t^2 bins					
		0.0 - 0.032	0.032 - 0.072	0.072 - 0.129	0.129 - 0.202	0.202 - 0.291	0.291 - 0.397
x_L bins	0.60 - 0.63	23 ± 4.8	27 ± 5.2	30 ± 5.4	21 ± 4.6	10 ± 3.2	-
	0.63 - 0.67	46 ± 6.8	37 ± 6.1	19 ± 4.5	27 ± 5.2	19 ± 4.4	6 ± 2.4
	0.67 - 0.73	164 ± 12.8	80 ± 8.9	22 ± 4.7	21 ± 4.6	22 ± 4.7	13 ± 3.6
	0.73 - 0.79	311 ± 17.6	158 ± 12.6	31 ± 5.6	6 ± 2.4	6 ± 2.4	10 ± 3.2
	0.79 - 0.84	223 ± 14.9	180 ± 13.4	93 ± 9.6	27 ± 5.2	11 ± 3.3	6 ± 2.4
	0.84 - 0.88	163 ± 12.8	151 ± 12.3	69 ± 8.3	34 ± 5.8	14 ± 3.7	8 ± 2.8
	0.88 - 0.91	109 ± 10.4	110 ± 10.5	74 ± 8.6	23 ± 4.8	17 ± 4.1	9 ± 3.0
	0.91 - 0.94	68 ± 8.2	105 ± 10.2	66 ± 8.1	32 ± 5.7	18 ± 4.2	11 ± 3.3
	0.94 - 0.97	6 ± 2.4	41 ± 6.4	83 ± 9.1	42 ± 6.5	18 ± 4.2	7 ± 2.6
	0.97 - 1.005	-	33 ± 5.7	245 ± 15.7	121 ± 11.0	72 ± 8.5	24 ± 4.9

Table 6.3.2: Number of events per (x_L, P_t^2) bin in deep inelastic scattering

6.4 Acceptance and resolution of the LPS

To calculate the (x_L, P_t^2) acceptance and resolutions, a Monte Carlo sample of 220,000 protons was generated and processed through the ZEUS detector simulation program. These protons were generated with a flat x_L spectrum and with a transverse momentum P_t according to:

$$\frac{dN}{dP_t^2} \propto e^{-6P_t^2}$$

The Monte Carlo events were generated for a particular run of the LPS in which the position of the detectors was as close as possible to the 10σ p-beam profile as the simulation of different positions for the LPS detectors under the ZEUS Monte Carlo environment program MOZART [84] is a difficult task. Fig. 6.4.1 shows the geometrical acceptance for this particular run, in percent, per every (x_L, P_t^2) cell used in this analysis. The effects of detector positioning in the acceptance calculations will be discussed in chapter [7].

On average, the resolution in P_t^2 is found to be $\sim 0.033(\mathrm{GeV/c})^2$ while the resolution in x_L amounts to $\sim 0.2\%$ of the total proton beam momentum. Fig. 6.4.2 shows the resolution of P_t^2 in bins of x_L whereas Fig. 6.4.3 indicates the resolution of x_L in bins of P_t^2.

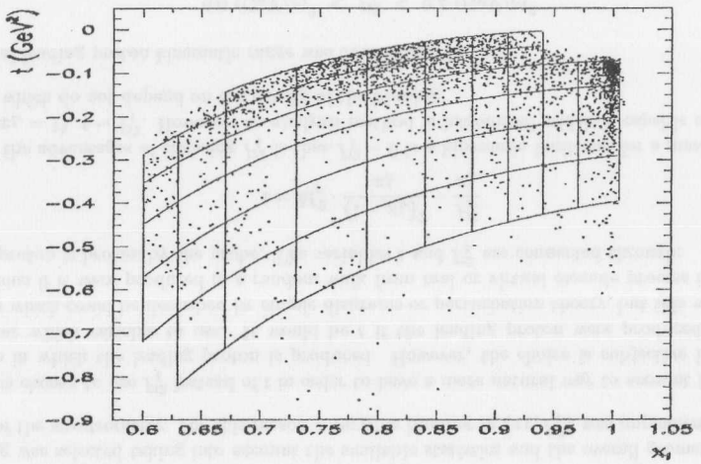

Figure 6.3.1: The (x_L, t) plane and P_t^2 contours showing the ZEUS-LPS PHP data and the binning choice with which the present analysis was performed

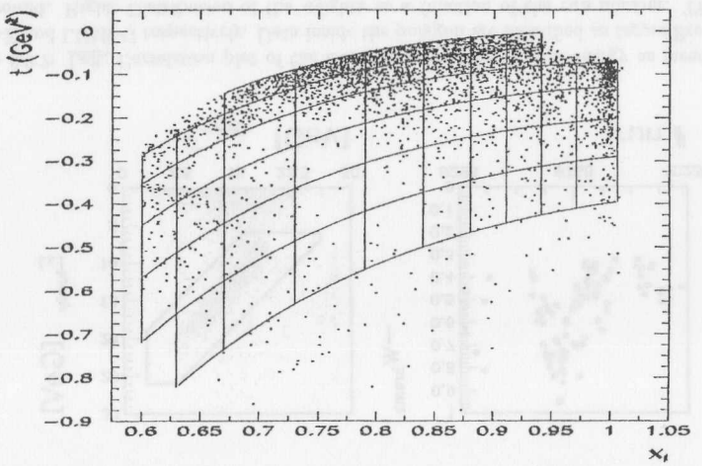

Figure 6.3.2: The (x_L, t) plane and P_t^2 contours showing the ZEUS-LPS DIS data and the binning choice with which the present analysis was performed

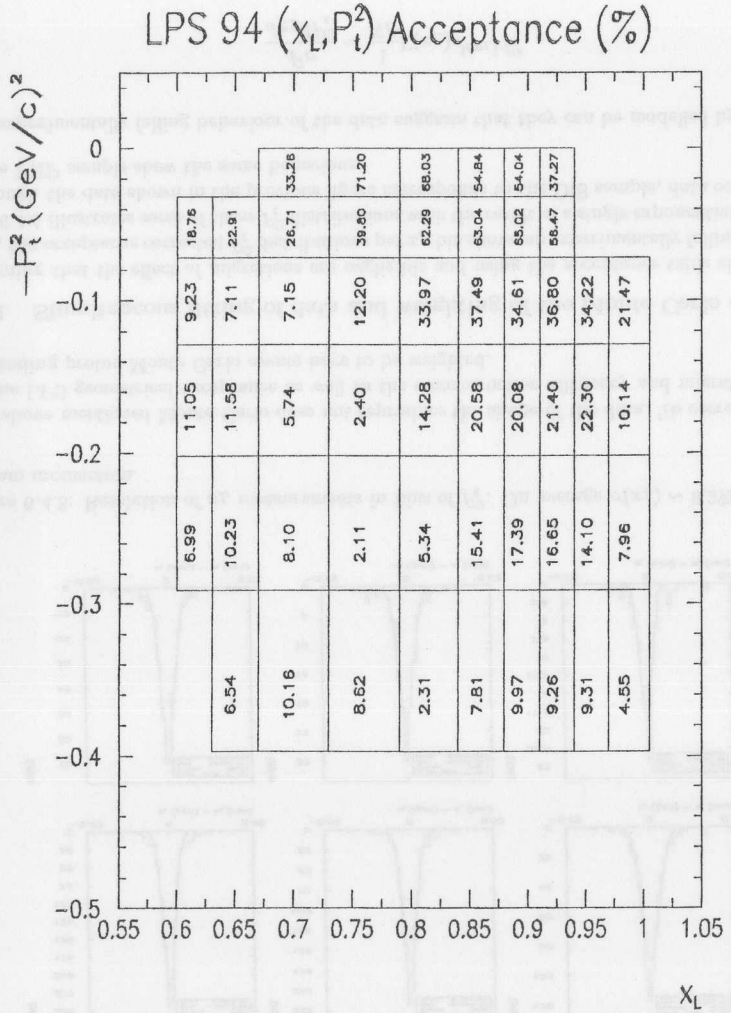

Figure 6.4.1: LPS geometrical acceptance in the (x_L, P_t^2) plane for a particular run of the LPS in which the position of the detectors was as close as possible to the 10σ p-beam profile. The binning used in the present analysis is also indicated.

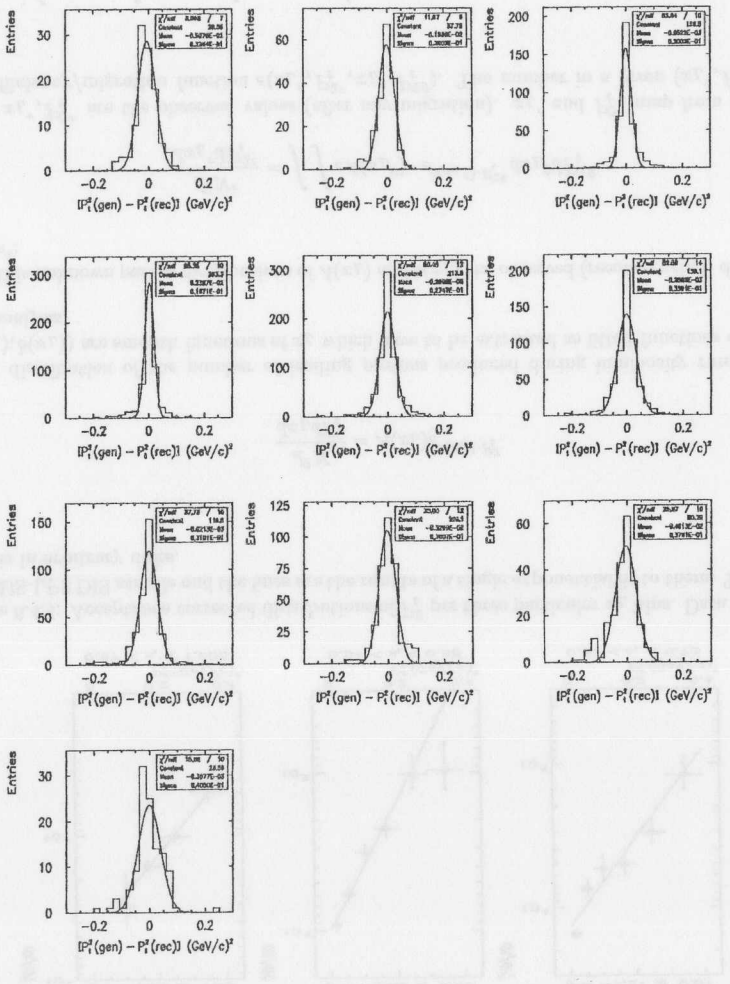

Figure 6.4.2: Resolution of P_t^2 measurements in bins of x_L. On average $\sigma(P_t^2) \sim 3.3{\cdot}10^{-2}$ (GeV/c)^2.

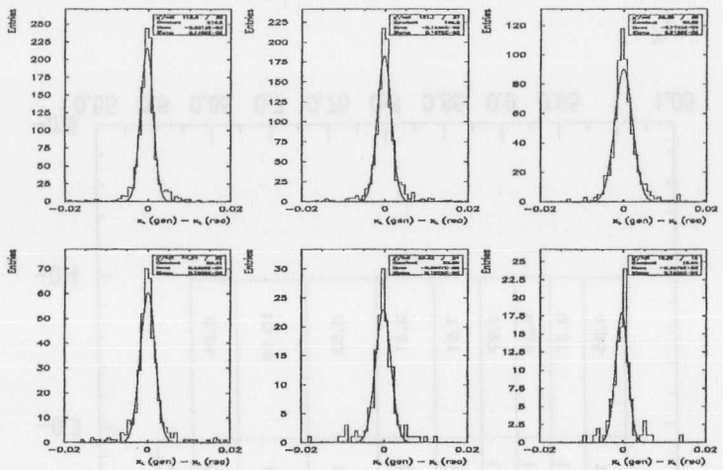

Figure 6.4.3: Resolution of x_L measurements in bins of P_t^2. On average $\sigma(x_L) \sim 0.2\%$ of the total p-beam momentum.

The above mentioned Monte Carlo does not reproduce the shape of the data. To correctly account for the LPS geometrical acceptance as well as the reconstruction efficiency and migration[3] effects, the leading proton Monte Carlo events have to be weighted.

6.4.1 Simultaneous fitting of data and weighting of the Monte Carlo events

Assuming that the effect of migrations are negligible and using the acceptance table shown in Fig. 6.4.1, the acceptance corrected P_t^2 distributions per x_L bin shows an experimentally falling behaviour. Fig. 6.4.4 illustrates some of these P_t^2 distributions with the result of a single exponential fit to them. Although the data shown in the previous figure corresponds to the DIS sample, data corresponding to the PHP sample show the same behaviour.

The experimentally falling behaviour of the data suggests that they can be modelled by:

$$\frac{d^2\sigma}{dx_L dP_t^2} = \frac{1}{E\mathcal{L}}\Gamma(x_L)e^{b(x_L)\cdot P_t^2} \tag{6.3}$$

where $\Gamma(x_L)$ is the value of $\frac{d^2\sigma}{dx_L dP_t^2}$ at $P_t^2 = 0$, $b(x_L)$ the slope of the P_t^2 distribution, E the mean combined trigger, data acquisition and geometric efficiency and $\mathcal{L}$ is the nominal integrated luminosity. Thus,

[3]Migration occurs when events belonging to a particular (x_L, P_t^2) cell are reconstructed in neighbouring ones.

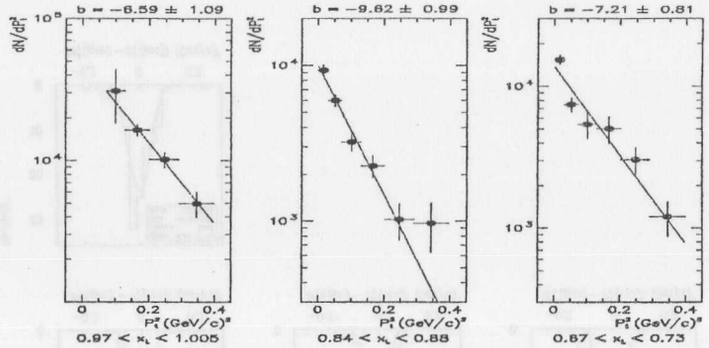

Figure 6.4.4: Acceptance corrected distributions of P_t^2 per three particular x_L bins. Data correspond to ZEUS-LPS DIS sample and the lines are the results of a single exponential fit to them. The vertical scale is in arbitrary units.

$$\frac{d^2N}{dx_L dP_t^2} = A(x_L)e^{b(x_L)\cdot P_t^2} \tag{6.4}$$

is the distribution of the number of leading protons produced during luminosity running and - $(A(x_L), b(x_L))$ are smooth functions of x_L which have to be extracted as fitted functions of x_L using a χ^2 analysis.

With this unknown parent distributions of $A(x_L)$ and $b(x_L)$ the observed (reconstructed) distribution will be[4]:

$$\frac{d^2N^r}{dx_L{}^r dP_t^{2r}} = \int\int \varepsilon A(x_L{}^g)\cdot e^{b(x_L{}^g)\cdot P_t^{2g}} dx_L{}^g dP_t^{2g} \tag{6.5}$$

where $x_L{}^r, P_t^{2r}$ are the observed values (after any migration). $x_L{}^r$ and P_t^{2r} map from $(x_L{}^g, P_t^{2g})$ with efficiency/migration function $\varepsilon(x_L{}^r, P_t^{2r}, x_L{}^g, P_t^{2g})$. The number in a given $(x_L{}^r, P_t^{2r})$ bin is then:

$$N_{ij} = \int_{bin\ i} dx_L{}^r \int_{bin\ j} dP_t^{2r} \int_{all\ x_L{}^g} dx_L{}^g \int_{all\ P_t^{2g}} dP_t^{2g} \varepsilon(x_L{}^r, P_t^{2r}, x_L{}^g, P_t^{2g}) A(x_L{}^g)\cdot e^{b(x_L{}^g)\cdot P_t^{2g}} \tag{6.6}$$

(i,j) is a particular bin in the $(x_L{}^r, P_t^{2r})$ plane and the integration together with the evaluation of the function ε is done by importance sampling as follows.

[4]To denote the Monte Carlo reconstructed and generated variables, upper indices are used: g = generated Monte Carlo and r = reconstructed Monte Carlo

Defining:

$$\xi = \frac{x_L^g - x_L^{g\,min}}{x_L^{g\,max} - x_L^{g\,min}}$$

where:

$$0 \le \xi \le 1, \quad x_L^{g\,min} = 0.6, \quad x_L^{g\,max} = 1 \quad \text{and} \quad dx_L{}^g = 0.4\, d\xi$$

and defining:

$$\zeta = e^{-6 \cdot P_t^{2g}}, \quad \text{where } 0. \le \zeta \le 1.$$

A flat generation of ξ gives, $\frac{dP}{d\xi} = \frac{1}{0.4}$. Also, a flat ζ generation means $\frac{dP}{d\zeta} = 1$. Then:

$$\frac{dP}{dP_t^2} = \frac{d\zeta}{dP_t^2} \cdot \frac{dP}{d\zeta} = (-6) \cdot e^{-6 \cdot P_t^{2g}} \cdot \frac{dP}{d\zeta} \tag{6.7}$$

and

$$dP_t^2 = \frac{d\zeta}{-6 \cdot e^{-6 \cdot P_t^{2g}}}$$

hence:

$$N_{ij} = \int_{bin\ i} dx_L{}^r \int_{bin\ j} dP_t^{2r} \int_0^1 d\xi \int_0^1 d\zeta \cdot \varepsilon \cdot A(\xi) \cdot e^{b(\xi) \cdot P_t^{2g}} \cdot \left(\frac{0.4}{6 \cdot e^{-6 \cdot P_t^{2g}}}\right) \tag{6.8}$$

To cast this as Monte Carlo generator, one allows

$$\int\int d\xi d\zeta \longrightarrow \sum_{MC\ throws} \frac{(x_L{}^g, P_t^{2g})_{bin\ size}}{N_{gen}}$$

where the total sampled unit square in ξ and ζ is divided into N_{gen} random sized pieces. Moreover, for a given throw, $\varepsilon = 0$ if the track is lost else ε is a δ function casting the track into a particular $(x_L{}^r, P_t^{2r})$ bin. Hence:

$$N_{ij} = \sum_{i,j} \frac{1}{N_{gen}} \cdot A(x_L{}^g) \cdot e^{b(x_L{}^g) \cdot P_t^{2g}} \cdot \left(\frac{0.4}{6 \cdot e^{-6 \cdot P_t^{2g}}}\right) \tag{6.9}$$

where $\sum_{i,j}$ is taken over all MC generated events going in that particular reconstructed (i,j) bin. Then, each MC event must be given a weight:

$$W = \frac{1}{15 \cdot N_{gen}} \cdot A(x_L) \cdot e^{b(x_L) \cdot P_t^2} \cdot e^{6 \cdot P_t^2} \tag{6.10}$$

This formulation of the problem is independent of the way the binning is made (provided that there are not too few bins). Unknown parameters are contained in the functions $A(x_L)$ and $b(x_L)$ and are not associated with any particular set of bins. The binning becomes a convenient way of defining a χ^2, and could be quite different (for example the low-P_t events could be split into more x_L bins than are the higher P_t events). However, to allow a comparison with conventional t-distribution analysis, fixed x_L bins have been used. Finally, the algorithm used in the implementation of the method is sketched in Fig. 6.4.5.

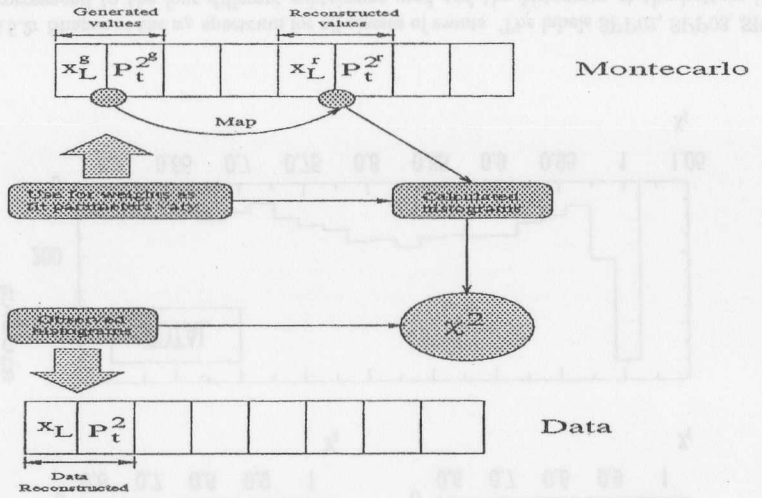

Figure 6.4.5: Algorithm used in the implementation of the method of weighting the Monte Carlo events

6.4.2 Implementation of the method

The implementation takes two steps:

1. <u>One dimensional fit:</u> The fit of the P_t^2 distribution is done in individual x_L bins. This is based on the assumption that the shape of the distribution in one x_L bin needs to have nothing in common with the shape in the adjacent x_L bin. The variable fitting parameters $A(x_L)$ and $b(x_L)$ in the equation [6.10] will become constants and therefore two independent parameters $A = A(x_L)$ and $b = b(x_L)$ are introduced for each x_L bin. The resultant A and b are obtained by a simple iterative χ^2 minimisation processes between the observed data and the reconstructed Monte Carlo sample after it has been corrected by a factor (weight) given in equation [6.10].

   The χ^2 minimisation function is written as follows:

$$\chi^2 = \sum_i^{P_t^2\ bin} \frac{(N_{data}(i) - N_{mc}(i))^2}{\sigma_{data}^2(i) + \sigma_{mc}^2(i)}$$

   where:

$$N_{mc}(i) = \sum_j^N W_j \cdot j; \qquad \sigma_{mc}^2(i) = \sum_j^N (W_j \cdot j)$$

   N, being the number of events in a particular P_t^2 bin.

2. <u>Two dimensional fit:</u> This is a simultaneous fit of x_L and P_t^2. It assumes that the parameters $A(x_L)$ and $b(x_L)$ are continuous smooth functions of x_L. This assumption has proven to be correct, as will be shown in the following sections.

The smooth functions are chosen to be cubic splines defined in such a way that they pass through all the A and b parameters found in the one dimensional fit procedure. The resultant is a two dimensional surface in (x_L, P_t^2) that will represent the best estimate of a fit to our data. In addition, we will not only have fits along P_t^2 but also along x_L.

At the end of the minimisation procedure, the P_t^2 distributions corrected by the acceptance are fitted with a single exponential. The b values obtained in this way are compared with the ones found in the one dimensional fitting procedure in order to estimate the systematic errors due to the correlation of errors in the (x_L, P_t^2) plane.

The fits have been performed using the Minuit [85] program for function minimisation and error analysis.

6.5 Fitting the ZEUS-LPS PHP data

As described in section [5.6.1], due to the high rates, the photo-production data were prescaled and stored in four different classes. Each of them was affected with different prescale factors that were computed on a run-to-run basis to account for the trigger efficiency. Fig. 6.5.1 shows the distribution of the prescale factors. The scatter and miscalculation in prescale factors was due to a bias in the algorithm used in the trigger system, which in some cases had the effect that the prescale applied during data taking reached the nominal value only asymptotically during each run. Figs. 6.5.2 and 6.5.3 indicates how those classes of events contribute to our final sample. The labels SPP02, SPP03, SPP04 and SPP15, correspond to the four different subsamples sketched in Fig. 5.6.1.

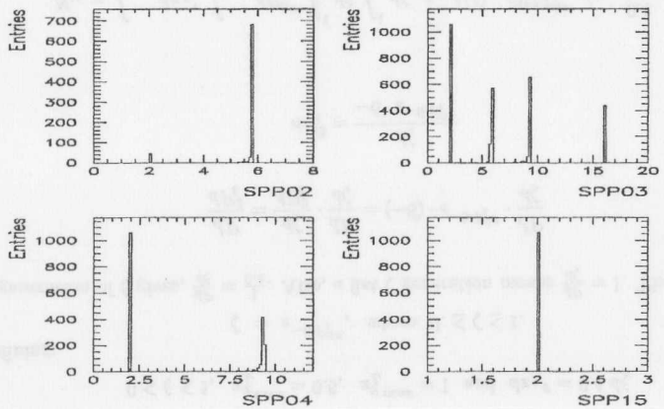

Figure 6.5.1: Distribution of the prescale factors. The scatter and miscalculation in prescale factors shown was due to a bias in the algorithm used in the trigger system. In some cases this had the effect that the prescale applied during data taking reached the nominal value only asymptotically during each run.

The shapes of these x_L spectra indicate the presence of different subprocesses, all together con-

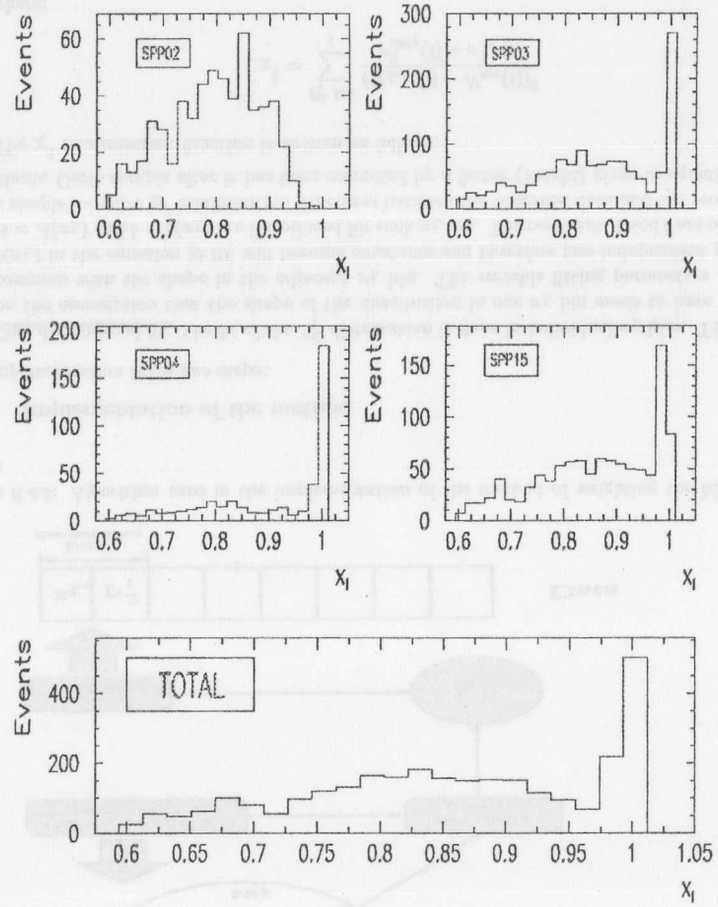

Figure 6.5.2: Shapes of the x_L spectrum for all classes of events. The labels SPP02, SPP03, SPP04, SPP15 correspond to the four different subtriggers used and the histogram at the bottom is the total: SPP02 = background, SPP03 = all PHP candidates, SPP04 = diffractive like, SPP15 = hard diffractive.

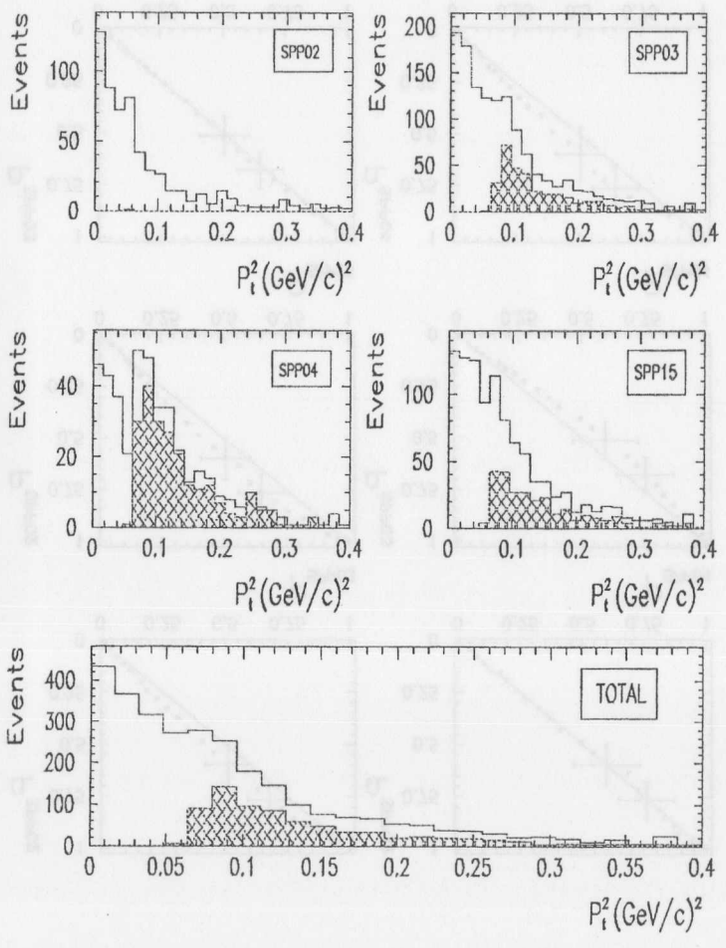

Figure 6.5.3: Shapes of the bare P_t^2 spectrum for all classes of events. The labels SPP02, SPP03, SPP04, SPP15 correspond to the four different subtriggers used and histogram at the bottom is the total. The hatched histograms correspond to the diffractive peak contribution ($x_L > 0.97$).

tributing with certain statistics to our sample. In order to build up an inclusive spectrum one can find out whether or not the use of prescale factors associated to each class of data is essential in the analysis. This is done by comparing the shapes of the various x_L and P_t^2 spectrum via the normalised cumulative distributions.

Several sets of these prescale data could be combined and analysed in two ways:

1. add the data sets together and then predict in terms of the fit parameters of these distributions and the prescale factors how many events should be in each bin.
2. give each event a weight equal to its inverse prescale factor and fit the inclusive weighted spectrum.

In the second method, if data sets have very different weights as in the present case where prescale factors of 10 are involved, inclusion of these high prescale events leads to a loss in statistical information as they dominate the statistical fluctuations. However, if the component spectra have significantly different shapes, then there is no alternative to the weighted method. As a result, the objective is to determine if there are significant shape differences in the spectra. If there are not any difference we will combine the spectra without weights so that we can have the best statistical information.

Let us define the normalised cumulative distributions as follows:

$$P_i = \frac{\int_{0.6}^{x_L} (\frac{dN}{dx_L})_i \cdot dx_L}{\int_{0.6}^{1} (\frac{dN}{dx_L})_i \cdot dx_L} \tag{6.11}$$

where $i = 1, 4$ are indices to label the four PHP subtriggers (SPP02, SPP03, SPP04, and SPP15). The plot of P_i versus P_j will show us either the differences or agreement of the x_L and P_t^2 spectrum associated to each PHP subtrigger. If the shapes are in agreement, the plot of P_i versus P_j will lie along a 45° line.

The comparison is done in two regions of of the x_L spectrum:

1. High-x_L spectrum, defined in the interval: $0.97 < x_L < 1.005$
2. Low-x_L spectrum, defined in the interval: $0.60 < x_L < 0.97$

Fig. 6.5.4 and 6.5.5 show the comparisons of x_L and P_t^2 distributions for the low x_L spectra together with the error bars where a maximum deviation is found in any of two comparisons. The shape differences of the x_L and P_t^2 distributions do not differ more than one standard deviation of its statistical error from the 45° line. This suggests that the use of prescale factors will not be essential for the analysis of this region of the x_L spectrum. Therefore we can rely on our data as it is and implement our simultaneous fitting procedure without prescaling.

Implementing the same procedure of comparing histogram shapes is a more difficult task for values of $x_L > 0.97$ because the contribution from the subtrigger bit SPP02 is negligible. However, we can proceed with the comparisons avoiding the histogram related to the background subtrigger bit SPP02.

Fig. 6.5.6 (A) and (B) show the comparisons of the x_L and P_t^2 distributions respectively for the high x_L region. The error bars have been drawn where a maximum deviation is found in any of

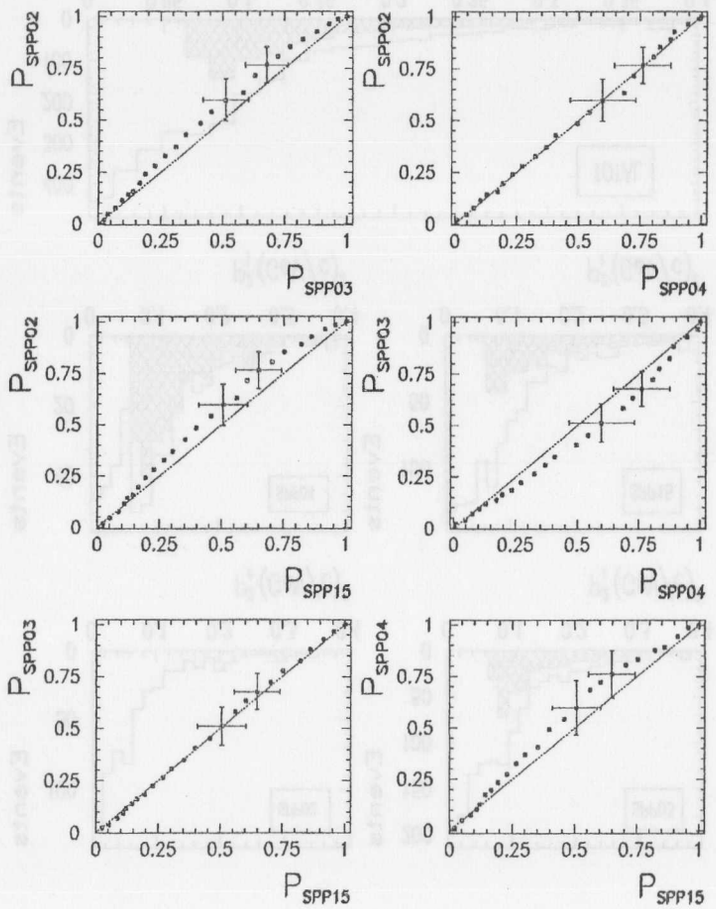

Figure 6.5.4: Comparison of the normalised cumulative distributions of the low x_L spectrum corresponding to the four PHP sub-triggers. The error bars, where a maximum deviation is found in any of two comparisons, are also shown.

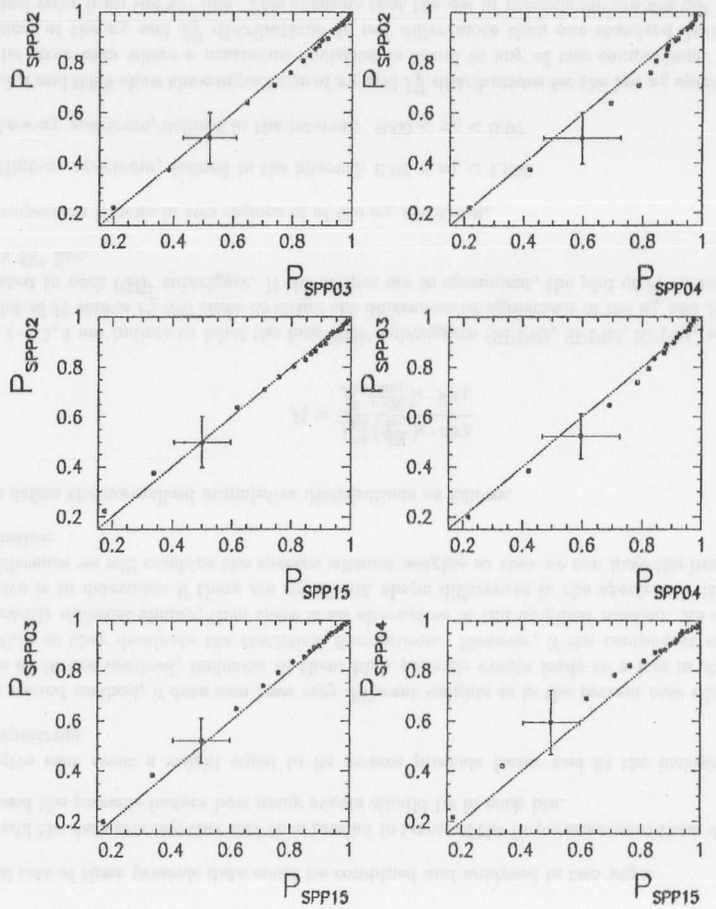

Figure 6.5.5: Comparison of the normalised cumulative distributions for P_t^2 distributions of the low x_L spectrum corresponding to the four PHP subtriggers. The error bars, where a maximum deviation is found in any of two comparisons, are also shown.

two comparisons. The shape differences of P_t^2 distributions do not differ more than a fraction of one standard deviation of its statistical error from the 45° line but in the x_L distributions the differences are very strong going up to four standard deviations from its statistical error. However, it will be shown in section [6.5.1] that this effect produces small variations while implementing our simultaneous fitting procedure with and without prescaling. As a result, the use of the prescale factors is not essential for our analysis. However, it will be included in the estimation of systematic effects.

6.5.1 One dimensional fit to data

As explained in section [6.4.2], the one-dimensional analysis is the first step towards a two dimensional fit procedure. Fig. 6.5.7 shows the results in two cases, one with no corrections for prescale factors and one with the prescale factors taken into account and the curved lines corresponds to a cubic spline fit to data. Fig. 6.5.8 shows the comparisons for both results. The values of A for prescaled data have been scaled-down by a factor of 0.13 for convenience of comparisons.

We choose the cubic splines in order to have the minimum number of parameters to produce a smooth fit to A (or b). If one parameter per bin is used, the cubic splines will tend to behave as polynomia and hence will force a structure in the distributions of A (or b) while implementing the two dimensional fit procedure. Since we are assuming that A (or b) will vary smoothly along x_L, the number of parameters to define the cubic splines has to be chosen in such a way that it reproduce the smoothest variation in A (or b).

This number of parameters is found by trial and error. It should be taken into account that at this stage the analysis is subjective because one can obtain similar shapes with slightly different sets of points. The aim is to achieve the smallest number of points to represent the shape and the values of A (or b) at a chosen point in the spline. The smallest number of parameters will be selected as input parameters in the two dimensional fit procedure. Furthermore, as it will be shown in chapter [7], this cubic splines will be used to visualise the variations in A (or b) for the different corrections that need to be applied to data to extract its final values.

From Fig. 6.5.8 it is clear that the measurement of b is more sensitive to the inclusion of the prescale factors. Moreover, it can be seen that the changes in the profiles of A are very small. On average this change is about a fraction of a standard deviation. Tables 6.5.1 and 6.5.2 illustrate the data plotted in the above mentioned pictures.

Sensitivity to prescale factors for b is small and its changes are within one standard deviation from its statistical error. Particular attention is paid to the $x_L > 0.97$ region where the shapes of the x_L distributions from the different subtriggers do not match. In this region the value of b changes within a fraction of a standard deviation from its statistical error. Due to this fact our analysis will take the data that are not prescaled.

6.5.2 Two dimensional fit to data

With the assumption that the parameters A and b calculated previously in section [6.5.1], are $(A(x_L), b(x_L))$, smooth functions of x_L, we implement the two dimensional fit procedure as explained in section [6.4.2]:

1. The parameters which define the cubic spline fits to the A and b distributions shown in Fig. 6.5.7 are now used as input parameters in the two dimensional minimisation function, thus

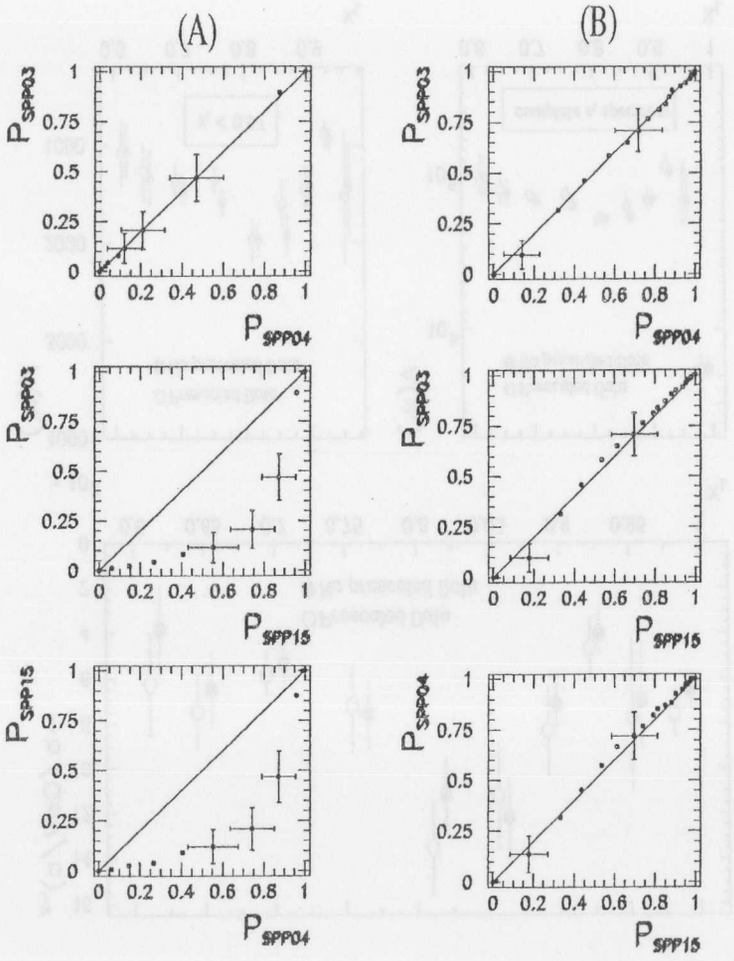

Figure 6.5.6: Comparison of the normalised cumulative distributions for (A) x_L and (B) P_t^2 distributions at the diffractive peak ($x_L > 0.97$). The error bars, where a maximum deviation is found in any of two comparisons, are also shown.

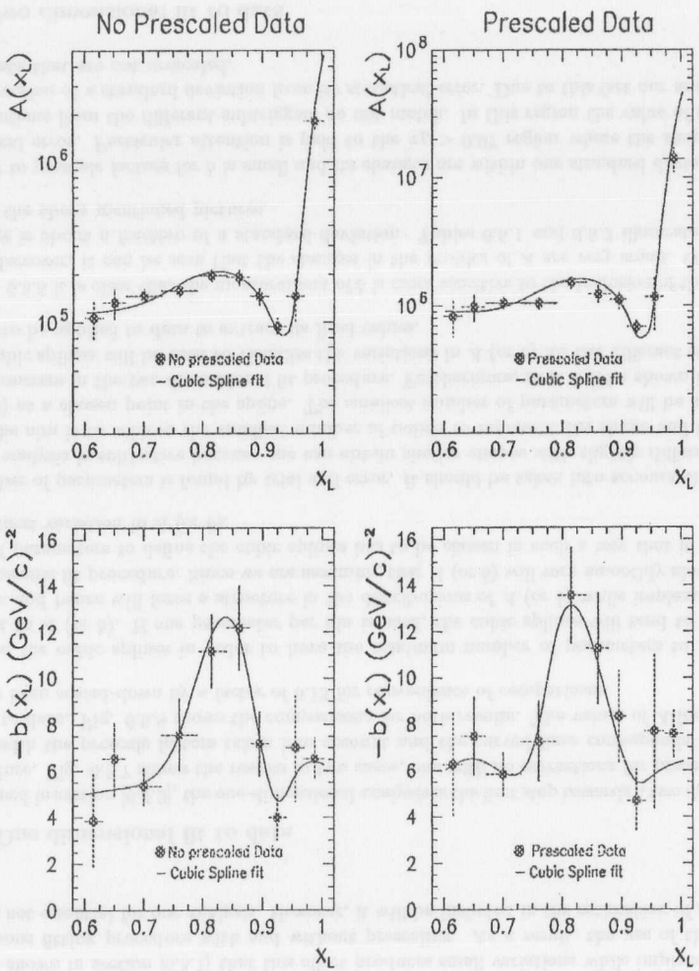

Figure 6.5.7: One dimensional fit results for unprescaled and prescaled photo-production data. The curved lines corresponds to a cubic spline fit to them. The horizontal bars represent the size of the bins and the vertical bars indicate the statistical errors.

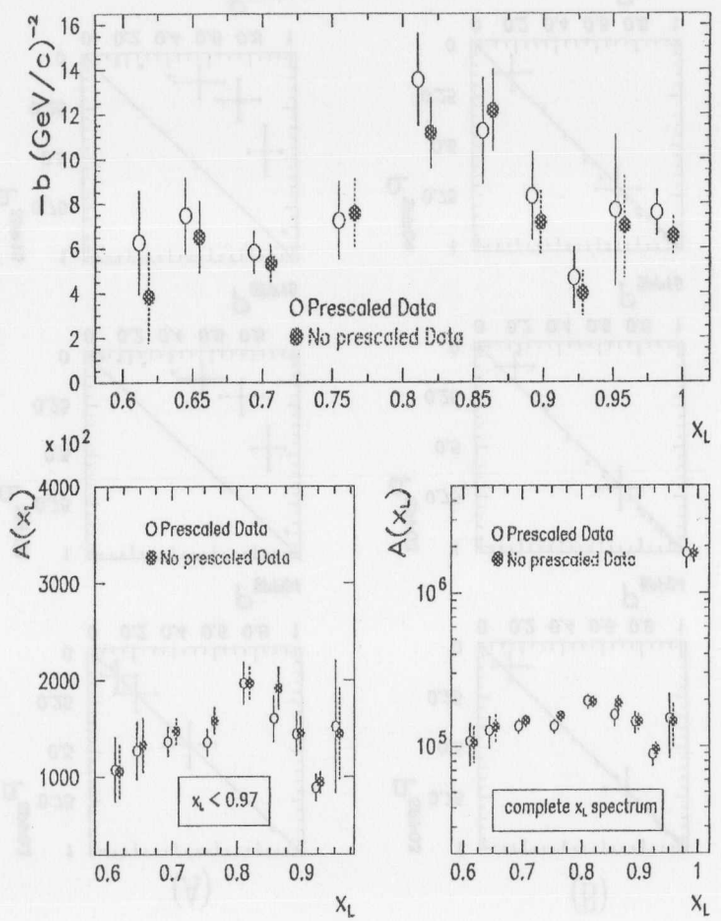

Figure 6.5.8: Comparison of A and b for both unprescaled and prescaled photo-production data. In order to compare the histogram shapes, the values of A have been scaled-down by a factor of 0.13. The points are displaced for clarity in the comparison and the vertical bars represent the statistical errors.

x_L bin	No Prescaled ZEUS-LPS PHP data		
	-b	A	χ^2
0.60 – 0.63	3.831 ± 2.051	1.06E+5 ± 2.84E+4	5.39
0.63 – 0.67	6.524 ± 1.597	1.33E+5 ± 2.83E+4	1.49
0.67 – 0.73	5.284 ± 0.823	1.45E+5 ± 1.36E+4	5.12
0.73 – 0.79	7.554 ± 1.548	1.58E+5 ± 1.37E+4	7.90
0.79 – 0.84	11.165 ± 1.598	1.96E+5 ± 1.77E+4	2.31
0.84 – 0.88	12.177 ± 1.822	1.92E+5 ± 2.19E+4	8.55
0.88 – 0.91	7.157 ± 1.390	1.45E+5 ± 1.75E+4	4.15
0.91 – 0.94	3.982 ± 0.969	9.43E+4 ± 1.12E+4	5.24
0.94 – 0.97	6.998 ± 2.332	1.45E+5 ± 4.67E+4	0.85
0.97 – 1.005	6.529 ± 0.893	1.81E+6 ± 2.37E+5	4.66

Table 6.5.1: A and b values obtained without prescale factors

x_L bin	Prescaled ZEUS-LPS PHP data		
	-b	A	χ^2
0.60 – 0.63	6.853 ± 2.309	8.29E+5 ± 2.56E+5	6.79
0.63 – 0.67	7.466 ± 1.690	9.80E+5 ± 2.31E+5	2.42
0.67 – 0.73	5.836 ± 0.959	1.05E+6 ± 1.16E+5	1.13
0.73 – 0.79	7.244 ± 1.738	1.04E+6 ± 1.07E+5	6.00
0.79 – 0.84	13.552 ± 2.076	1.52E+6 ± 1.68E+5	3.11
0.84 – 0.88	11.264 ± 2.393	1.23E+6 ± 1.86E+5	7.32
0.88 – 0.91	8.325 ± 1.977	1.11E+6 ± 1.76E+5	3.65
0.91 – 0.94	4.674 ± 1.361	6.81E+5 ± 1.06E+5	3.09
0.94 – 0.97	7.691 ± 3.372	1.17E+6 ± 5.27E+5	1.08
0.97 – 1.005	7.575 ± 1.018	1.40E+7 ± 2.02E+6	4.01

Table 6.5.2: A and b values obtained with prescale factors

defining a starting two dimensional surface from which by iterative χ^2 minimisation, the minimisation function will calculate the corrections to be applied to the Monte Carlo events defined in section [6.4] and according to the formula [6.10].

2. When the iterative χ^2 minimisation procedure converges, the starting input parameters, described in item [1], become now the parameters that define the two dimensional fitted function that best represent the data in the (x_L, P_t^2) plane. In addition, a covariance matrix is obtained for these parameters which are used to calculate the errors associated to every parameter.

   These parameters, together with their errors computed from the covariance matrix are used to describe the best distributions of A and b along x_L.

3. At the end of the minimisation procedure, the corrected acceptances are calculated in every (x_L, P_t^2) cell and then applied to the data. The acceptance corrected P_t^2 distributions which now contains the correction factors derived from the two dimensional fit results are fitted with a single exponential. The resultant slopes of the exponentials derived in this way are compared with the ones found in the original one dimensional fit. Their differences together with their errors will show the effect of the error correlation if a one dimensional fit analysis is preferred in the extraction of the slope parameter b.

At this point a test of the usefulness of the method is done by comparing data and Monte Carlo histograms in x_L and P_t^2 slices.

Fig. 6.5.9 shows the result of the two dimensional continuous fit together with the one dimensional fits to A and b. The band around the continuous line represents the error calculated from the covariance matrix at the end of the minimisation procedure.

The data corrected by the acceptance is fitted with a single exponential. Fig. 6.5.10 shows the comparison of the slope parameters of these exponentials with the ones found in the one dimensional analysis. The differences of these b values (Δb), can be fitted with a constant line (Δb=0.128±0.523). This difference represents a fraction of a standard deviation from the statistical error in the measurement of b.

In order to ensure that the method used is correct (cf. item [3]), we compare the data and weighted Monte Carlo events in x_L and P_t^2 slices. Figs. 6.5.11 and 6.5.12 show these comparisons. At a first glance we see an overall agreement, but in fact there are bins in x_L and P_t^2 where the agreement is broken. These disagreements can be due to a miscalculation of the (x_L, P_t^2) acceptance. This will be discussed in section [7.1].

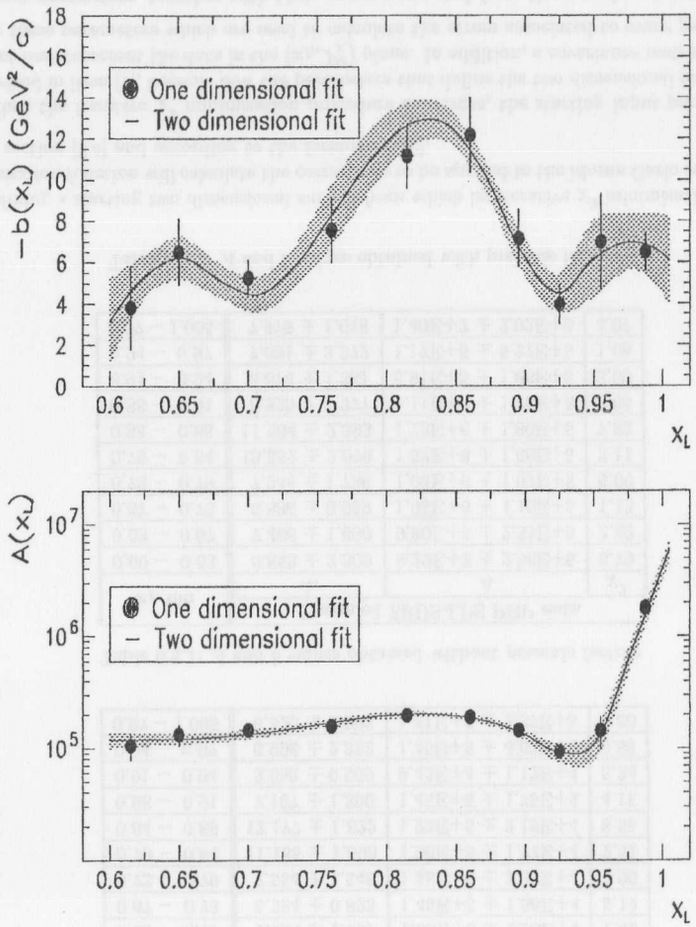

Figure 6.5.9: Result of the two dimensional continuous fit (solid line) for A and b. The band around the continuous line represents the error computed from the covariance matrix at the end of the minimisation procedure and the full circles are the one dimensional fits to A and b.

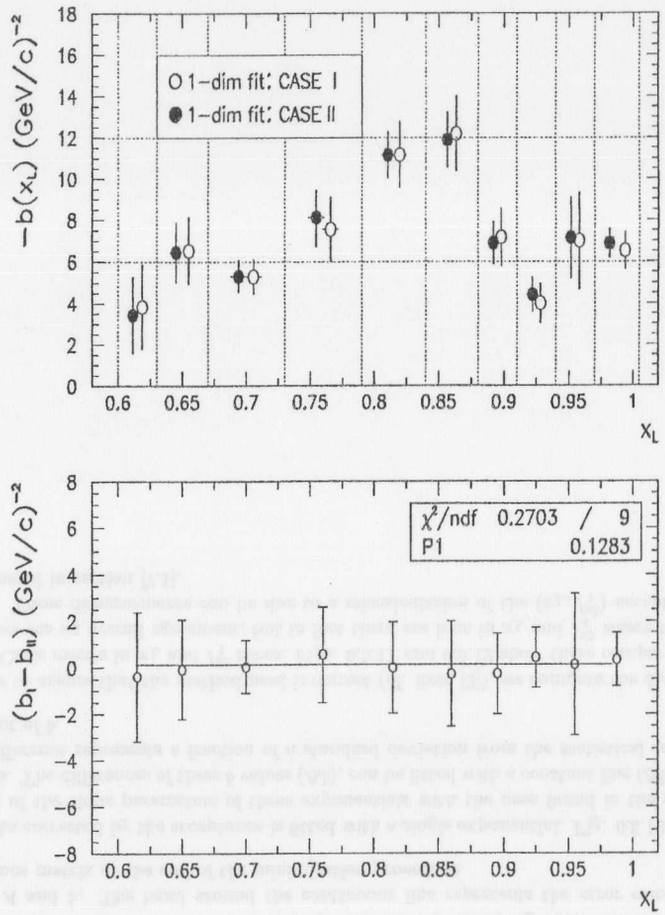

Figure 6.5.10: Comparison of the slope parameter b for the two cases: One dimensional fit as in section [6.5.1] (CASE I) and one dimensional fit to the acceptance corrected data with correction factors derived from the two dimensional fit results (CASE II). The histogram at the top shows a comparison of the fits and the histogram at the bottom the differences from both measurements together with a constant line ($\Delta b = b_I - b_{II} = 0.128 \pm 0.523$) fit to them.

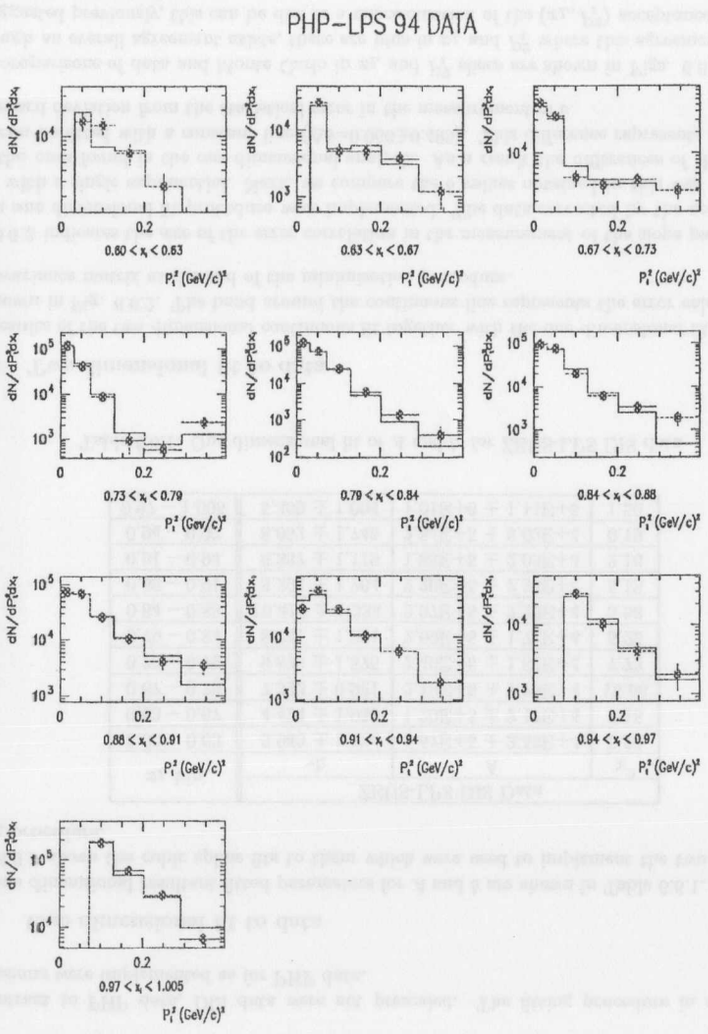

Figure 6.5.11: Comparison of data and Monte Carlo in bins of x_L. The solid histograms correspond to Monte Carlo whereas the full dots correspond to ZEUS-LPS PHP 94 data.

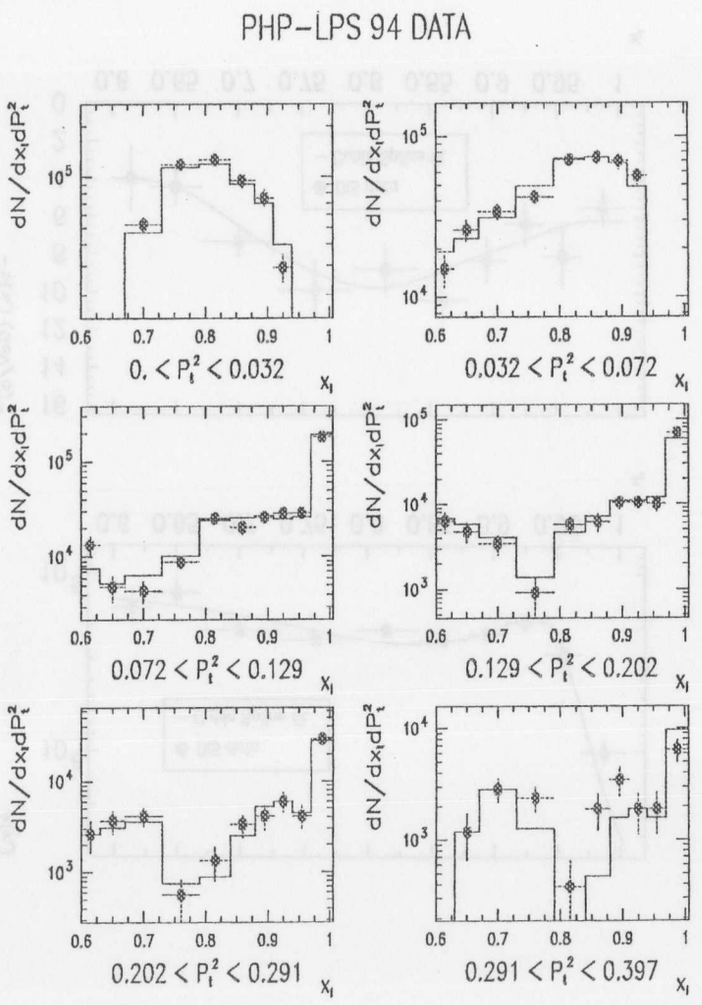

Figure 6.5.12: Comparison of data and Monte Carlo in bins of P_t^2. The solid histograms correspond to Monte Carlo whereas the full dots correspond to ZEUS-LPS PHP 94 data.

6.6 Fitting the ZEUS-LPS DIS data

In contrast to PHP data, DIS data were not prescaled. The fitting procedure in one and two dimensions were implemented as for PHP data.

6.6.1 One dimensional fit to data

The one dimensional resultant fitted parameters for A and b are shown in Table 6.6.1. In addition, Fig. 6.6.1 shows the cubic spline fits to them which were used to implement the two dimensional fitting procedure.

x_L bin	ZEUS-LPS DIS Data		
	-b	A	χ^2
0.60 – 0.63	3.943 ± 1.734	1.57E+5 ± 3.53E+4	5.24
0.63 – 0.67	4.424 ± 1.039	1.29E+5 ± 2.17E+4	3.15
0.67 – 0.73	7.322 ± 0.921	2.10E+5 ± 1.78E+4	15.66
0.73 – 0.79	9.876 ± 1.575	2.40E+5 ± 1.82E+4	7.72
0.79 – 0.84	8.741 ± 1.301	2.09E+5 ± 1.71E+4	5.25
0.84 – 0.88	10.418 ± 1.334	2.37E+5 ± 2.22E+4	5.58
0.88 – 0.91	8.292 ± 1.264	2.20E+5 ± 2.26E+4	5.13
0.91 – 0.94	6.337 ± 1.119	1.88E+5 ± 2.03E+4	2.16
0.94 – 0.97	8.052 ± 1.745	2.84E+5 ± 6.62E+4	0.19
0.97 – 1.005	5.469 ± 1.004	1.01E+6 ± 1.11E+5	1.50

Table 6.6.1: One dimensional fit of A and b, for ZEUS-LPS DIS data

6.6.2 Two dimensional fit to data

The results of the two dimensional continuous fit together with the one dimensional fits to A and b are shown in Fig. 6.6.2. The band around the continuous line represents the error calculated from the covariance matrix at the end of the minimisation procedure.

Fig. 6.6.3 indicates the size of the error correlation in the measurement of the slope parameter b, if only a one dimensional fit procedure were implemented. The data corrected by the acceptance are fitted with a single exponential. Next, we compare the b values obtained in this way (full circles) with the ones found in the one dimensional analysis. As a result the differences of these b values (Δb) can be fitted with a constant line (Δb=0.066±0.499). This difference represents a fraction of a standard deviation from the statistical error in the measurement of b.

The comparisons of data and Monte Carlo in x_L and P_t^2 slices are shown in Figs. 6.6.4 and 6.6.5. Although an overall agreement exists, there are bins in x_L and P_t^2 where this agreement is broken. As suggested previously, this can be due to a miscalculation of the (x_L, P_t^2) acceptance and will be discussed in section [7.1].

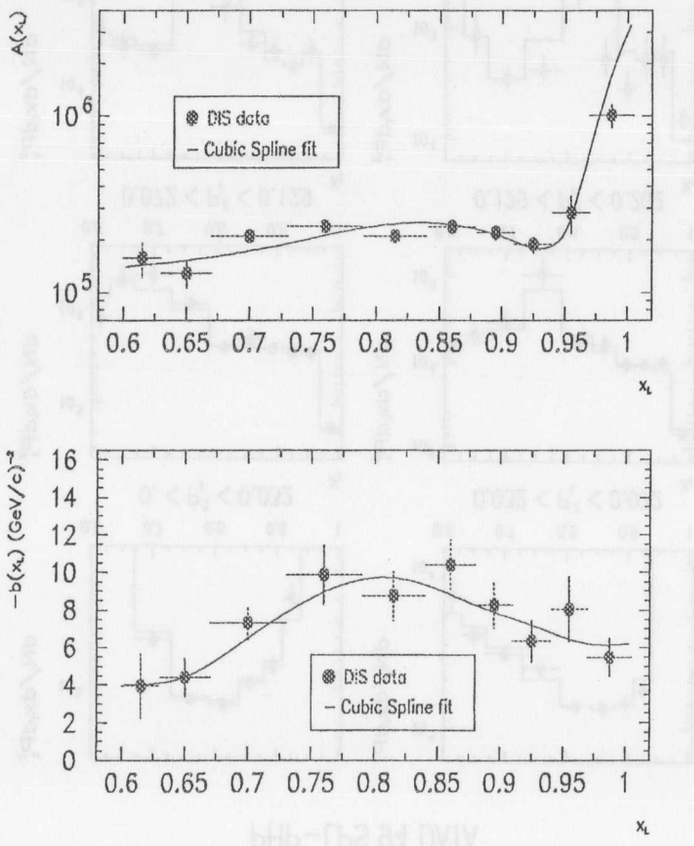

Figure 6.6.1: One dimensional fit results for A and b in ZEUS-LPS DIS data. The curved lines corresponds to a cubic spline fit to them. The horizontal bars represent the size of the bins and the vertical bars indicate the statistical errors.

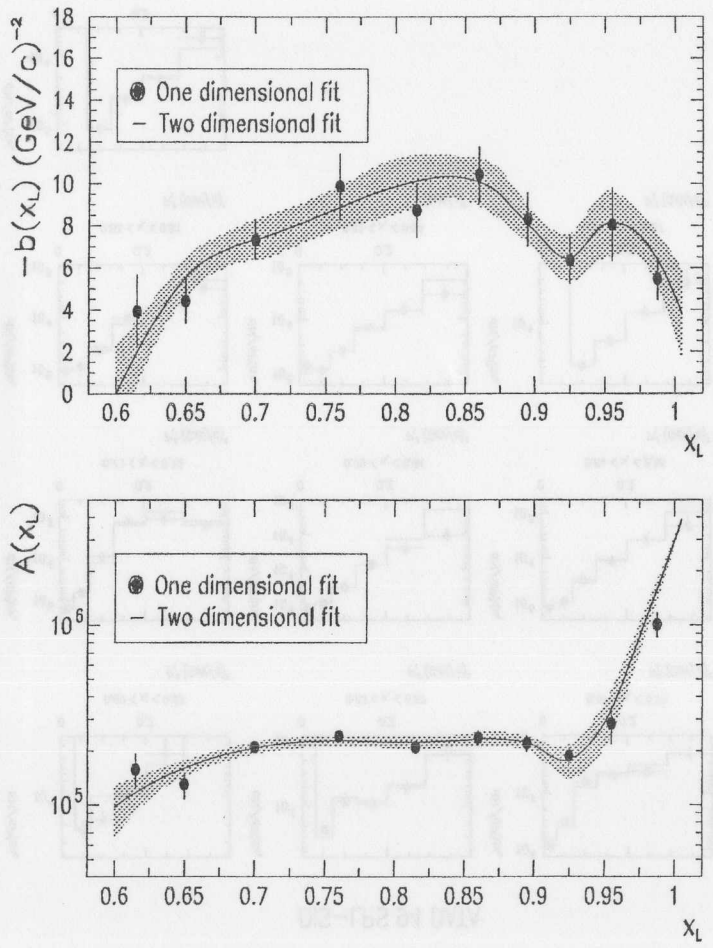

Figure 6.6.2: Result of the two dimensional continuous fit (solid line) for A and b in ZEUS-LPS DIS data. The band around the continuous line represents the error computed from the covariance matrix at the end of the minimisation procedure and the full circles are the one dimensional fits to A and b.

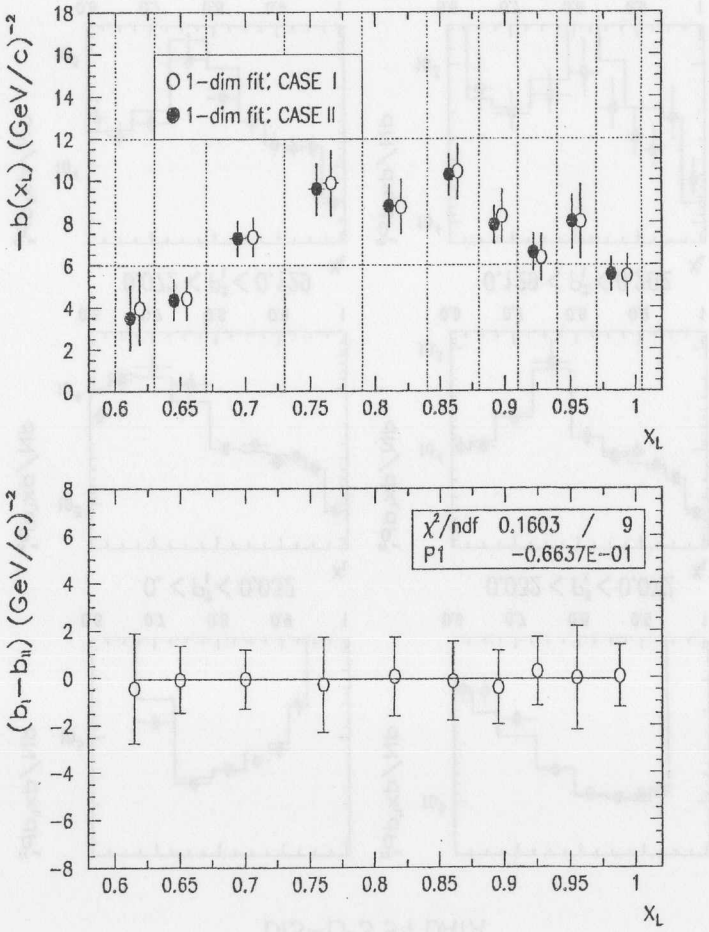

Figure 6.6.3: Comparison of the slope parameter b for the two cases: One dimensional fit as in section [6.5.1] (CASE I) and one dimensional fit to the acceptance corrected data with correction factors derived from the two dimensional fit results (CASE II). The histogram at the top shows a comparison of the fits and the histogram at the bottom indicates the differences from both measurements together with a constant line ($\Delta b = b_I - b_{II} = 0.066 \pm 0.499$) fit to them.

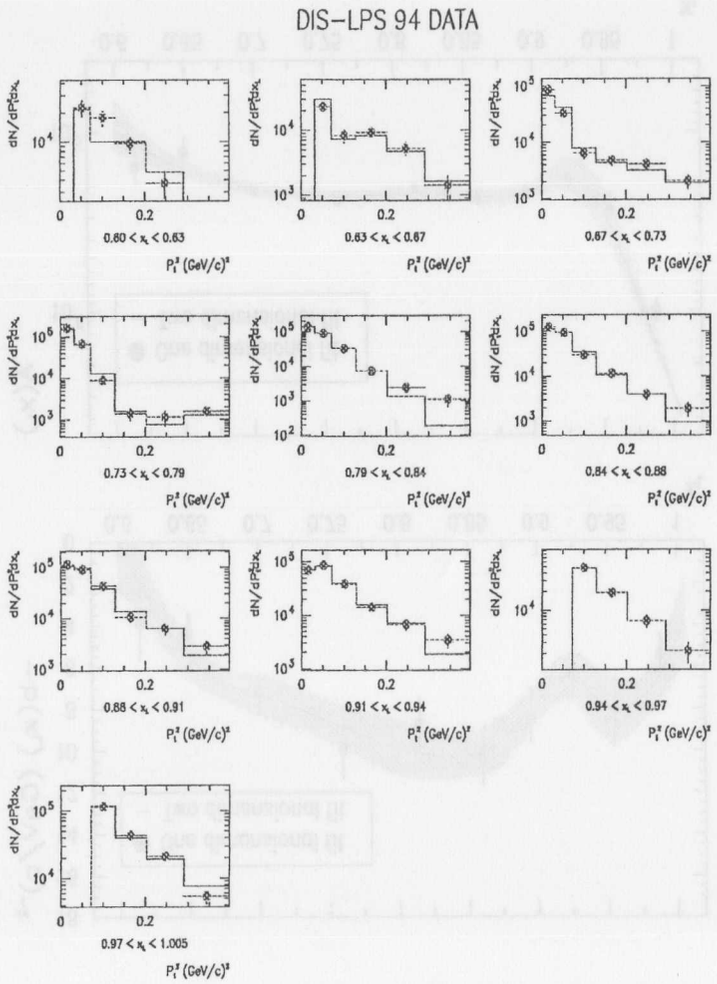

Figure 6.6.4: Comparison of data and Monte Carlo in bins of x_L. The solid histograms correspond to Monte Carlo whereas the full dots correspond to ZEUS-LPS DIS 94 data.

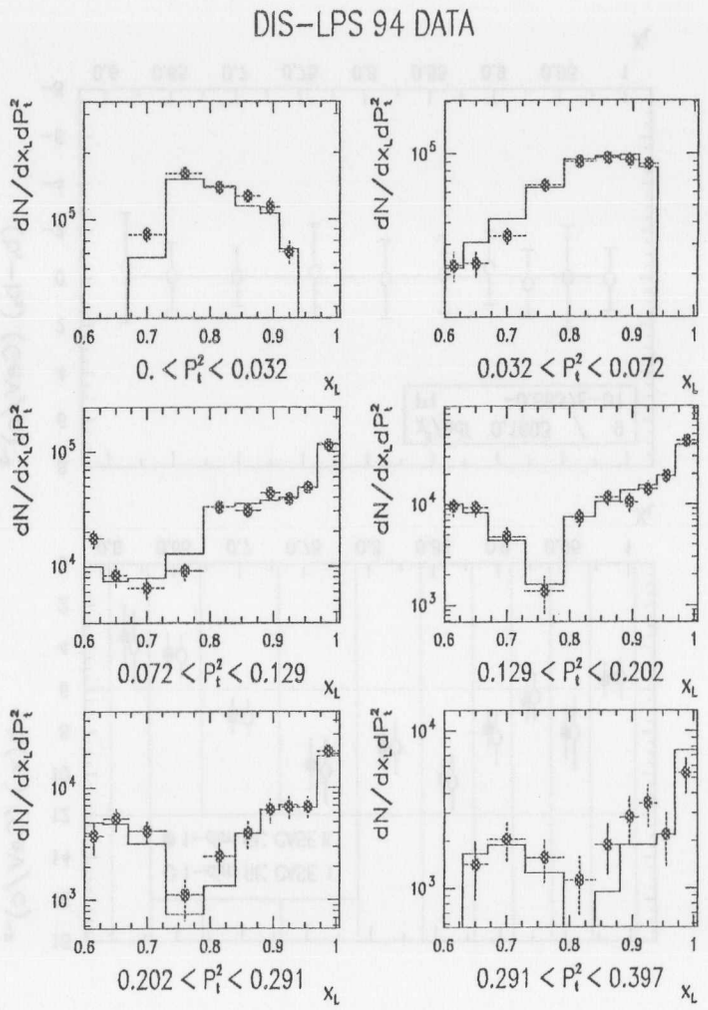

Figure 6.6.5: Comparison of data and Monte Carlo in bins of P_t^2. The solid histograms correspond to Monte Carlo whereas the full dots correspond to ZEUS-LPS DIS 94 data.

6.7 Summary of the measurements

In this chapter, a preliminary analysis of the leading proton data belonging to PHP and DIS samples has been carried out.

Although PHP data was prescaled with four different prescale factors, it has been demonstrated that its inclusion was not essential in our analysis. The inclusion of prescale factors produced small variations (order of a fraction of the statistical error) in the measurement of the slope of the P_t^2 distributions.

In addition, a method is discussed which consists of a two dimensional fitting procedure of the leading proton (x_L, P_t^2) distributions to weight the leading proton Monte Carlo events. To correctly account for efficiency and migration effect, which occurs when events belonging to a particular (x_L, P_t^2) cell are reconstructed in neighbouring ones, the (x_L, P_t^2) distribution were parametrised according to the formula [6.3]. This parametrisation is supported by the fact that the P_t^2 distribution of the leading proton follows an experimentally falling behaviour in both PHP and DIS samples.

The slopes of the acceptance corrected P_t^2 distribution of the leading protons in both PHP and DIS samples has been measured. These slopes are summarised in table 6.7.1.

x_L bin	ZEUS-LPS PHP Data		ZEUS-LPS DIS Data	
	-b	χ^2	-b	χ^2
0.60 – 0.63	3.43 ± 2.81	2.55	3.50 ± 1.54	2.37
0.63 – 0.67	6.30 ± 0.44	4.75	4.34 ± 0.96	0.90
0.67 – 0.73	5.30 ± 1.44	1.39	7.27 ± 0.84	3.48
0.73 – 0.79	7.48 ± 1.90	1.94	9.59 ± 1.24	1.85
0.79 – 0.84	11.85 ± 0.31	0.31	8.79 ± 1.03	1.39
0.84 – 0.88	12.03 ± 2.50	2.50	10.27 ± 0.99	1.54
0.88 – 0.91	6.79 ± 1.11	1.11	7.88 ± 0.88	1.28
0.91 – 0.94	4.04 ± 1.04	1.08	6.60 ± 0.90	0.70
0.94 – 0.97	5.74 ± 0.37	0.63	8.04 ± 1.30	0.04
0.97 – 1.005	7.58 ± 1.54	2.79	5.54 ± 0.82	1.21

Table 6.7.1: Slopes of the acceptance corrected P_t^2 distributions as measured in PHP and DIS samples

The measurements of the slope parameters, b, shown in table 6.7.1 indicate a structure at intermediate values of x_L. However, although the data used to perform this measurement is free from background contamination as described in section [6.2], there is still need for some corrections. The nature of the corrections as well as their implementation in this analysis will be discussed in chapter [7].

7 Corrections to the LPS data

7.1 Overview

The reconstruction of the LPS data is by itself sensitive to many parameters. The most relevant are the detector positioning during data taking, the reconstruction efficiency and accuracy and the interaction vertex reconstruction. As will be seen, each of these parameters contributes with a given error in the determination of the longitudinal and transverse momenta of the leading protons and, as a result to account for these errors, our measurements have to be corrected.

The nature of the parameters for which our measurements have to be corrected are the following:

- Detector positioning: The positions of the detectors are not the same from one data taking period to another, because the HERA p-beam conditions are not always constant. The p-beam optics may have very small changes due to the luminosity tuning, thus modifying either the p-beam profile or its orbit. Any changes in the p-beam optics translate in different positions for the LPS detectors. Fig. 7.1.1 shows the beam position distribution for all the available runs in our analysis.

  As explained in section [6.4], the Monte Carlo sample used in this analysis has simulated a particular run condition in which the detector positions were as close as possible to the 10 σ p-beam profile.

  To account for the various positions of the LPS detectors in the Monte Carlo sample, a Fortran routine has been written [86] and implemented in our analysis. Monte Carlo events are weighted on an event-by-event basis and then used to correct the (x_L, P_t^2) acceptance.

  The weight is calculated for each generated event in which there is an LPS track. A ray-tracing Monte Carlo is executed which test whether that track would have been observed under run conditions different from those simulated in Mozart. Since movements of the p-beam influence the decisions on how to place the detectors for data taking, the vertex position and p-beam tilt at the interaction point are also taken into account for every run. Fig. 7.1.2 shows, as an example, the average weight factors applied to Monte Carlo events to account for run-to-run changes in the detector and beam positions.

- Reconstruction accuracy: The reconstruction accuracy is another parameter related to the reconstruction process which can affect the measurements. A leading proton is reconstructed with a certain accuracy, defined mainly by the path it follows through the spectrometer and the number of active detector planes it hits. This information can be accessed off-line via $P(\chi^2, \text{NDoF})$, the probability of a leading proton to be reconstructed with a given χ^2 and number of degree of freedoms for a reconstructed track. It is found that a cut in $P(\chi^2, \text{NDoF}) > 0.05$ will select the most accurate reconstructed leading protons. Fig. 7.1.3 shows a three dimensional view of (NDoF,χ^2/NDoF,$P(\chi^2, \text{NDoF})$) where a long tail at values of $P(\chi^2, \text{NDoF}) < 0.05$ reveals inaccuracies in the reconstruction of the leading protons.

  The remaining leading protons, after requiring this selection were 2381 and 2830 for PHP and DIS sample respectively.

- Vertex reconstruction: The LPS reconstruction assumes that every leading proton is produced from a fixed interaction vertex during the whole year: this value is taken as an average value

given by the central tracking detector. However, there are events in which the vertex is not reconstructed, badly reconstructed or produced in a interaction region where a satellite proton bunch populates. As a result, a vertex requirement in our sample would ensure that we are not dealing with unwanted events. This can be achieved by applying a longitudinal vertex cut of $|V_z| < 3\sigma$, σ ($\sim$ 10.7 cm), being the half width size of the vertex distribution along z coordinate. Fig. 7.1.4 shows the longitudinal vertex distribution together with the 3σ selection for each (PHP and DIS) set of data.

The remaining leading protons, after requiring this selection were 2062 and 2598 for PHP and DIS respectively.

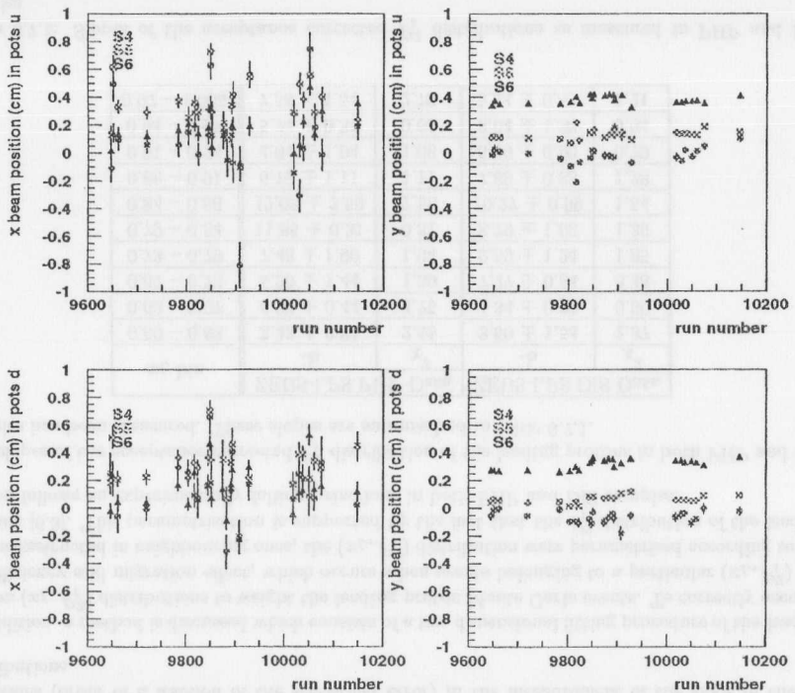

Figure 7.1.1: Beam position versus run number for all pots. The labels u and d in axe titles refer to *up* and *down* sections of the LPS stations (pots).

The above mentioned corrections are implemented consecutively in a cumulative way. These corrections modify the acceptance map showed in section [6.4].

Since we are going to analyse the variation of our measurements while applying these corrections, we will include back a measurement relating to the corrections for p-beam halo coincidences. Table 7.1.1 shows the order in which this corrections are applied while table 7.1.2 shows the number of events left for analysis after applying the selections for reconstruction accuracy and vertex reconstruction.

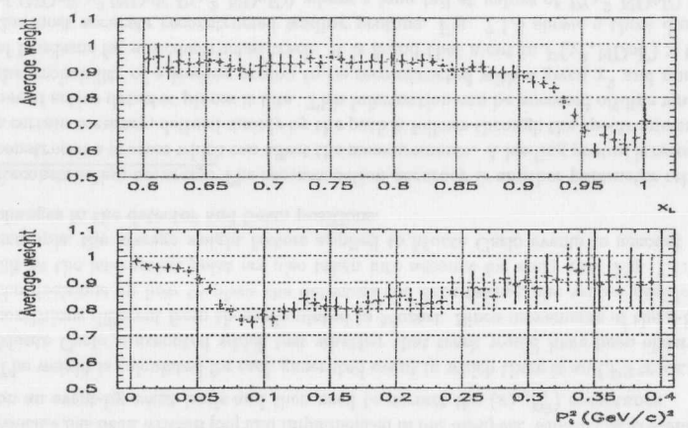

Figure 7.1.2: Average value of weight applied to Monte Carlo events to account for run-to-run changes in detector and beam positions

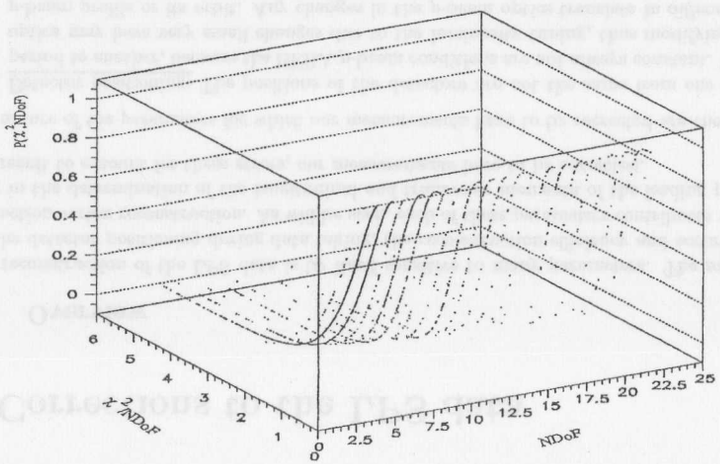

Figure 7.1.3: Three-dimensional view of (NDoF,χ^2/NDoF,$P(\chi^2,\text{NDoF})$). A long tail at values of $P(\chi^2,\text{NDoF}) < 0.05$ indicates the presence of badly reconstructed leading protons.

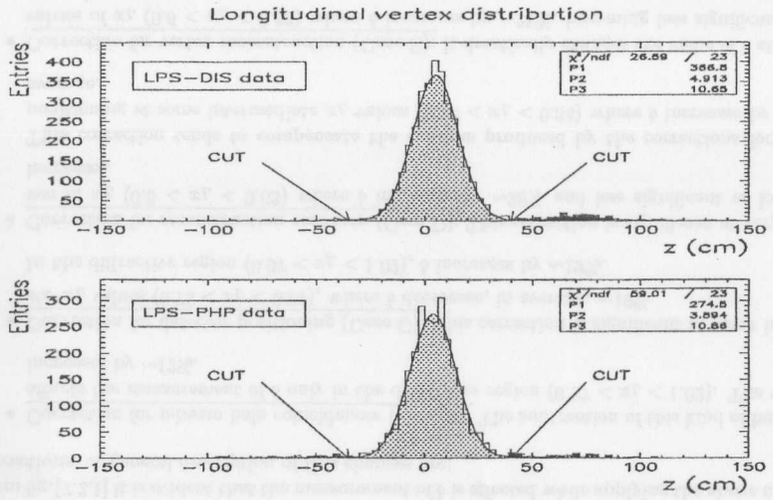

Figure 7.1.4: Longitudinal vertex distributions for DIS (top) and PHP (bottom) data containing a leading proton information. It is also shown the 3σ cut applied to both samples.

Fig 7.1.5 illustrate the changes due to detector positioning, reconstruction accuracy and vertex reconstruction in terms of the cumulative ratios.

Correction Type	Description
CASE A	Bare data (no corrections at all)
-CASE B-	Background beam-halo subtracted
CASE C	Run-to-Run variations
CASE D	P(χ^2,NDoF) > 0.05
CASE E	$\|V_z\| \leq 3\sigma$ ($\sigma \sim 10.5$ cm)

Table 7.1.1: Implementation type applied to the LPS data. These corrections are applied in a cumulative way (ie. A, $A+B$, $A+B+C$, etc.). Data belonging to CASE B, were the one used to perform the one and two dimensional fits in chapter [6].

Data	Nominal	P(χ^2,NDoF) > 0.05	$\|V_z\| \leq 3\sigma$
PHP	2766 (100%)	2381 (-13.9%)	2062 (-25.5%)
DIS	3273 (100%)	2830 (-13.5%)	2598 (-26.6%)

Table 7.1.2: Number of events left for analysis after applying the selections for reconstruction accuracy and vertex reconstruction. The label *Nominal* refers to data used for analysis in chapter [6]. The vertex reconstruction cut was applied after the reconstruction accuracy cut.

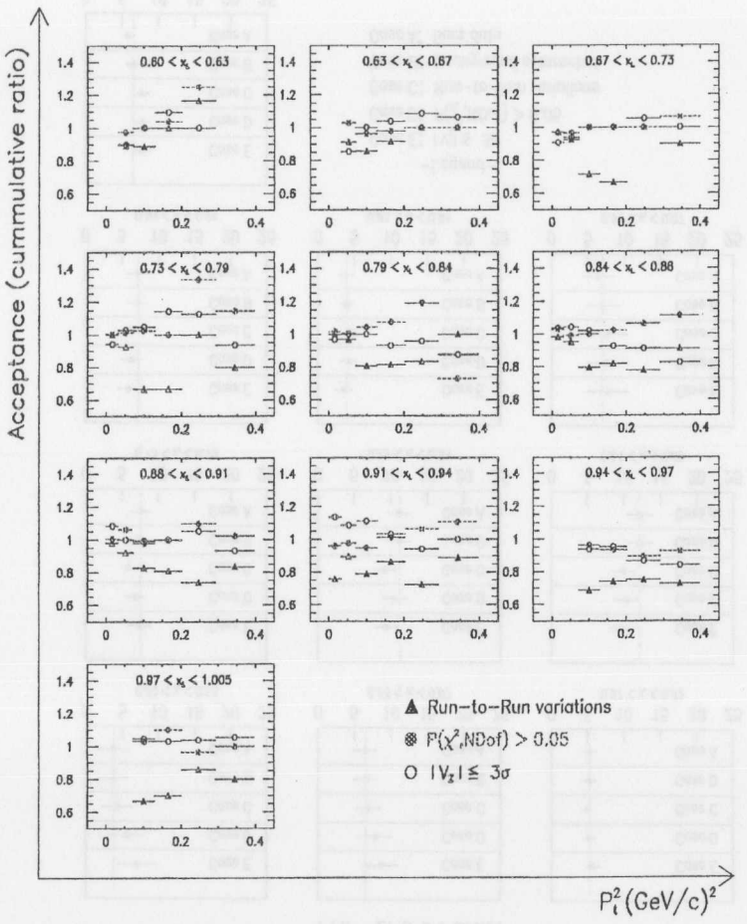

Figure 7.1.5: Ratio of changes in the acceptance calculation due to corrections for detector positioning, reconstruction accuracy and vertex reconstruction as a function of P_t^2. The changes are plotted in terms of the ratio of the corrected acceptance to the uncorrected one. The corrections are implemented consecutively in a cumulative way.

7.2 Corrections to the ZEUS-LPS PHP data

The analysis presented in chapter [6] has been repeated by varying the above mentioned conditions to find out to what extent the results change from the one computed previously.

7.2.1 One dimensional fit to data

Fig. 7.2.1 show the results obtained in the one dimensional implementation of the method and Fig. 7.2.2 indicates the same but in terms of the cubic spline fits to data. Data from fig. 7.2.1 is included in table. 7.2.1

x_L bin	Case A		Case B		Case C		Case D		Case E	
	-b	χ^2	-b	χ^2	-b	χ^2	-b	χ^2	-b	χ^2
0.60 - 0.63	3.83±2.05	5.39	3.83±2.05	5.39	4.36±2.05	5.79	5.60±2.34	4.14	7.01±2.61	2.54
0.63 - 0.67	6.52±1.60	1.49	6.52±1.60	1.49	6.96±1.57	1.24	7.85±2.26	2.79	8.63±2.51	2.91
0.67 - 0.73	5.33±0.83	5.30	5.28±0.82	5.12	4.86±0.70	0.65	5.16±0.81	1.22	5.69±0.88	1.11
0.73 - 0.79	7.55±1.55	7.90	7.55±1.55	7.90	5.76±0.97	3.46	6.89±1.19	2.13	7.28±1.42	4.11
0.79 - 0.84	11.16±1.60	2.31	11.16±1.60	2.31	9.16±1.48	2.30	10.47±1.65	3.40	9.45±1.64	4.33
0.84 - 0.88	12.18±1.82	8.55	12.18±1.82	8.55	9.93±1.53	5.09	10.37±1.61	4.57	9.64±1.58	2.16
0.88 - 0.91	7.16±1.39	4.15	7.16±1.39	4.15	6.04±1.24	3.18	6.22±1.33	2.91	5.83±1.40	2.44
0.91 - 0.94	3.84±0.95	5.27	3.98±0.97	5.24	4.43±1.05	2.45	4.26±1.11	3.96	3.60±1.10	3.97
0.94 - 0.97	6.49±2.19	0.88	6.99±2.33	0.85	7.83±2.50	0.96	7.69±2.65	0.63	7.73±2.72	0.78
0.97 - 1.005	5.81±0.78	2.72	6.53±0.89	4.66	7.78±0.96	4.74	7.83±1.01	4.29	7.71±1.16	3.27

Table 7.2.1: Results of a one dimensional fit to the acceptance corrected P_t^2 distributions. The labels Case A, B, C, D and E refer to the different corrections mentioned in section [7.1].

From fig.[7.2.1] it is evident that the measurement of b is affected while applying the above mentioned corrections. A general description of this changes are:

- Correction for p-beam halo coincidences (Case B): The subtraction of this kind of background affects the measurement of b only in the diffractive region ($0.97 < x_L < 1.02$). The value of b increases by ∼12%.

- Correction for detector positioning (Case C): This correction is significant at some intermediate x_L values ($0.73 < x_L < 0.91$), where b decreases, in average, ∼19%.

  In the diffractive region ($0.97 < x_L < 1.02$), b increases by ∼19%.

- Correction for reconstruction accuracy (Case D): This correction is significant at very low values of x_L ($0.6 < x_L < 0.63$) where b increases by ∼28% and less significant as long as x_L increases.

  This correction tends to compensate the changes produced by the corrections for detector positioning at some intermediate x_L values ($0.73 < x_L < 0.84$) where b increases by ∼17% in average.

- Correction for vertex reconstruction (Case E): It drastically changes the value of b at very low values of x_L ($0.6 < x_L < 0.63$) where b increases by ∼25%, becoming less significant as long as x_L increases.

  At some intermediate values of x_L ($0.79 < x_L < 0.94$), the value of b decreases, in average, by ∼10% and become negligible afterwards.

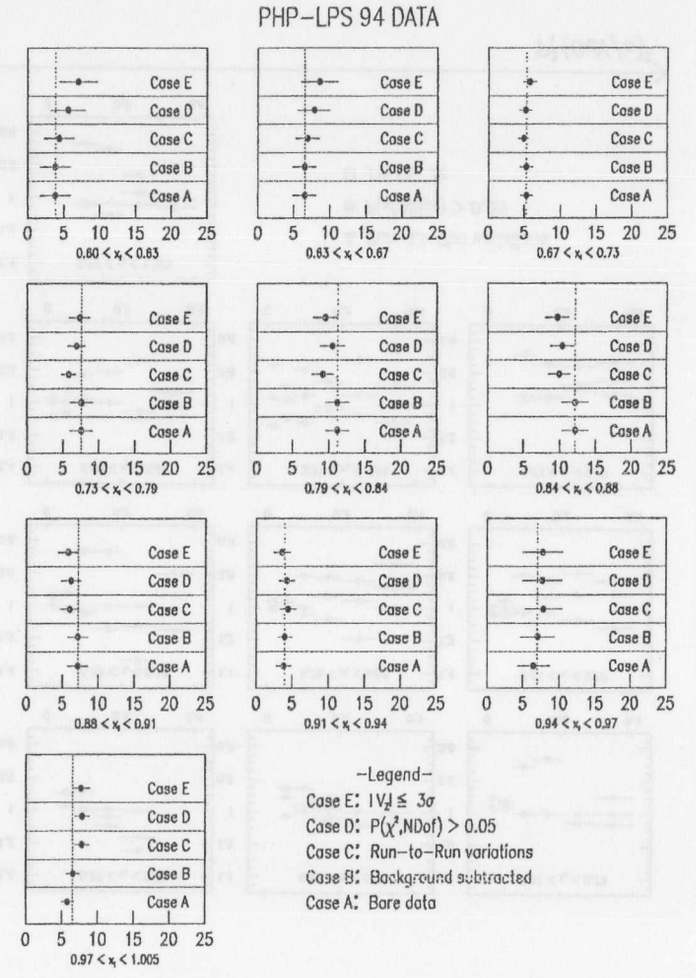

Figure 7.2.1: One dimensional fit results showing the changes in the measurements of b for ZEUS-LPS PHP data due to different conditions. The vertical dotted line give a reference so that the size of the variation with respect to a value of b found in chapter [6] can be appreciated.

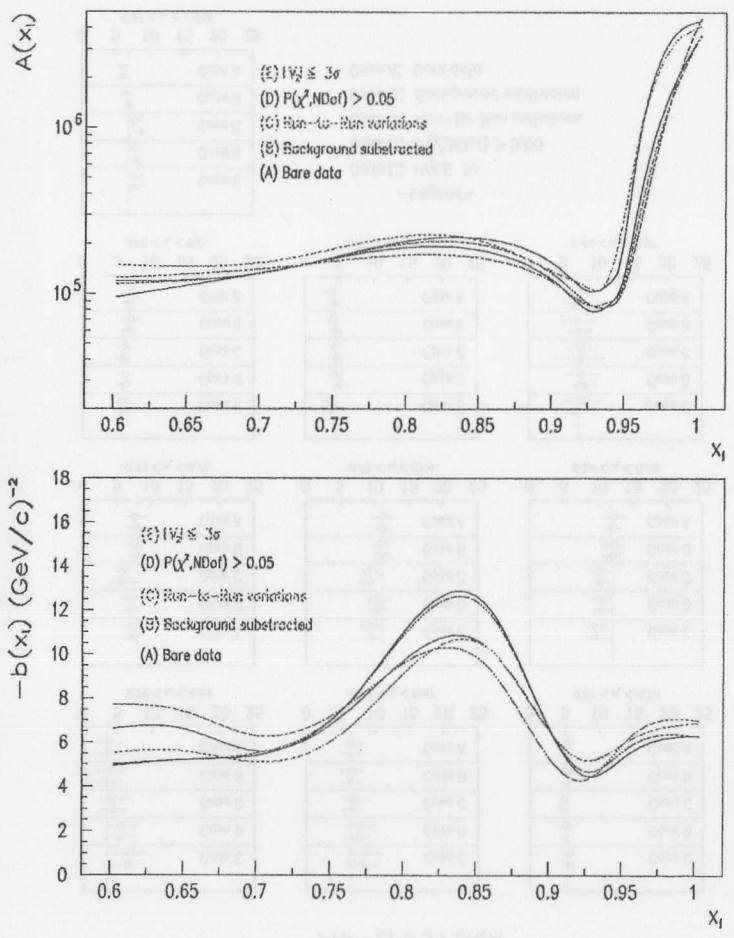

Figure 7.2.2: One dimensional fit results showing the variations in measurements of A and b for ZEUS-LPS PHP data due to different conditions in terms of the cubic spline fits to data

7.2.2 Two dimensional fit to data

Fig. 7.2.3 shows the comparison of the slope parameters computed using both, one and two dimensional analysis, per every correction. Table. 7.2.2 show the data corresponding to Fig. 7.2.3.

x_L bin	Case A		Case B		Case C		Case D		Case E	
	-b	χ^2	-b	χ^2	-b	χ^2	-b	χ^2	-b	χ^2
0.60 - 0.63	3.47±1.83	2.81	3.43±1.86	2.55	4.43±1.87	2.73	5.21±2.14	2.19	6.64±2.18	1.58
0.63 - 0.67	6.33±1.43	0.44	6.30±1.42	4.75	6.64±1.42	0.38	7.37±1.87	0.69	8.23±2.38	1.13
0.67 - 0.73	5.24±0.78	1.44	5.30±0.78	1.39	4.77±0.65	0.20	5.15±0.76	0.44	5.57±0.82	0.48
0.73 - 0.79	8.07±1.35	1.90	7.48±1.27	1.94	5.67±0.91	0.49	7.00±1.02	0.23	7.27±1.28	0.91
0.79 - 0.84	11.16±1.13	0.31	11.85±1.18	0.31	8.63±1.23	0.75	10.45±1.28	1.02	9.55±1.25	1.12
0.84 - 0.88	11.90±1.35	2.50	12.03±1.35	2.50	10.19±1.26	1.82	10.32±1.29	1.53	9.64±1.29	0.82
0.88 - 0.91	6.89±1.02	1.11	6.79±1.03	1.11	5.91±0.98	1.04	5.95±1.03	0.92	5.73±1.08	0.88
0.91 - 0.94	4.20±0.84	1.04	4.04±0.83	1.08	4.51±0.92	0.20	4.88±1.01	0.37	3.76±1.00	0.38
0.94 - 0.97	6.84±1.79	0.37	5.74±2.20	0.63	7.37±3.57	0.35	8.11±1.79	0.05	6.56±2.96	0.03
0.97 - 1.005	6.00±0.67	1.54	7.58±0.86	2.79	8.77±0.99	1.81	7.85±0.85	1.46	7.90±1.19	1.35

Table 7.2.2: Results of a one dimensional fit to the acceptance corrected P_t^2 distribution with correction factors derived from the two dimensional fitting procedure. The labels Case A, B C, D and E, refer to the the different corrections mentioned in section [7.1].

The result of the two dimensional fit, for the total corrections (CASE E), is shown in Fig. 7.2.4 as a continuous curve plus an error band. The error band is calculated from the covariance matrix at the end of the two dimensional minimisation procedure while the full circles correspond to the result of the one dimensional analysis.

For the total corrections, the results of a single exponential fit to the acceptance corrected P_t^2 distributions, which now take migration fully into account, are compared with the ones found in the one dimensional analysis. Fig. 7.2.5 shows this comparison in terms of the slope parameters b. The differences (Δb) of the slope parameters, would give a measurement of the error correlation effect if only a one dimensional analysis were implemented. These differences can be fitted with a constant line (Δb = -0.33±0.597). Δb represents a fraction of a standard deviation from the statistical error in the measurement of b.

Fig. 7.2.6 and 7.2.7 shows, for the total corrections, the comparison, of data and Monte Carlo in both P_t^2 and x_L slices. Although the agreement in this comparison is clearer than the one shown in section [6.5.2], there are still a few kinematic regions in which Monte Carlo does not reproduce very well the data. Because of the limited statistics, the few points in disagreement with the data could not be further studied.

In section [6.4] we assumed that our data was modelled by equation [6.3], which in terms of event distributions was written as follows:

$$\frac{d^2N}{dx_L dP_t^2} = A(x_L)e^{b(x_L)\cdot P_t^2}$$

Here, $A(x_l)$ and $b(x_L)$ in our fits represent the best parameters that approximate the real distribution for the production of leading protons. From the previous equation it is clear that $\frac{dN}{dx_L}$ can be calculated by integrating over P_t^2 and hence:

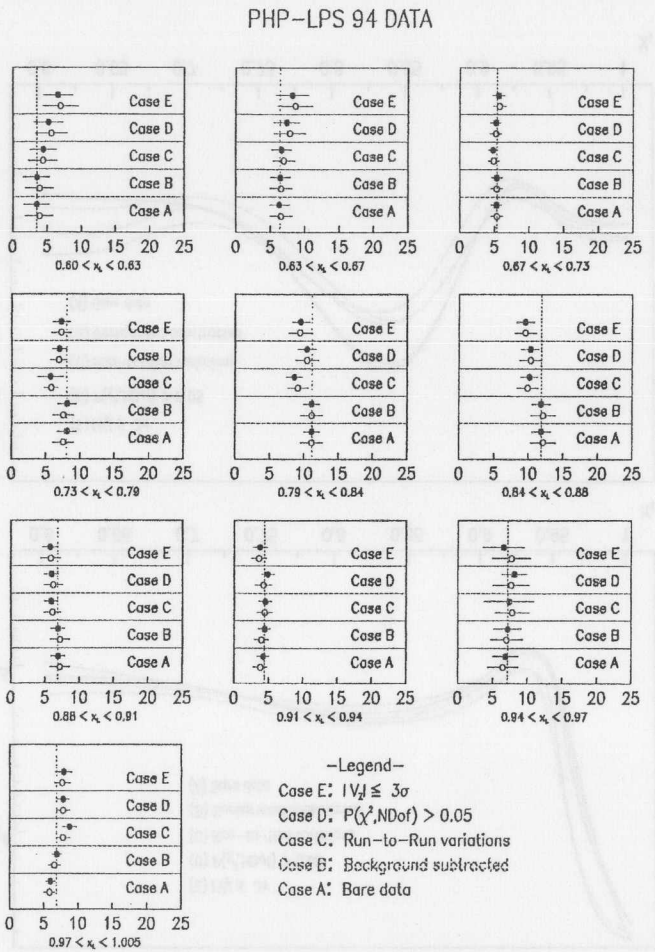

Figure 7.2.3: Comparison of changes in b as measured from: One dimensional fit (open circles) and one dimensional fit to the acceptance corrected data with correction factors derived from the two dimensional fit results (full circles). The vertical dotted line gives a reference so that the size of the variation with respect to a value of b calculated in chapter [6] can be appreciated (which is a one dimensional fit of b after the beam halo coincidences have been subtracted).

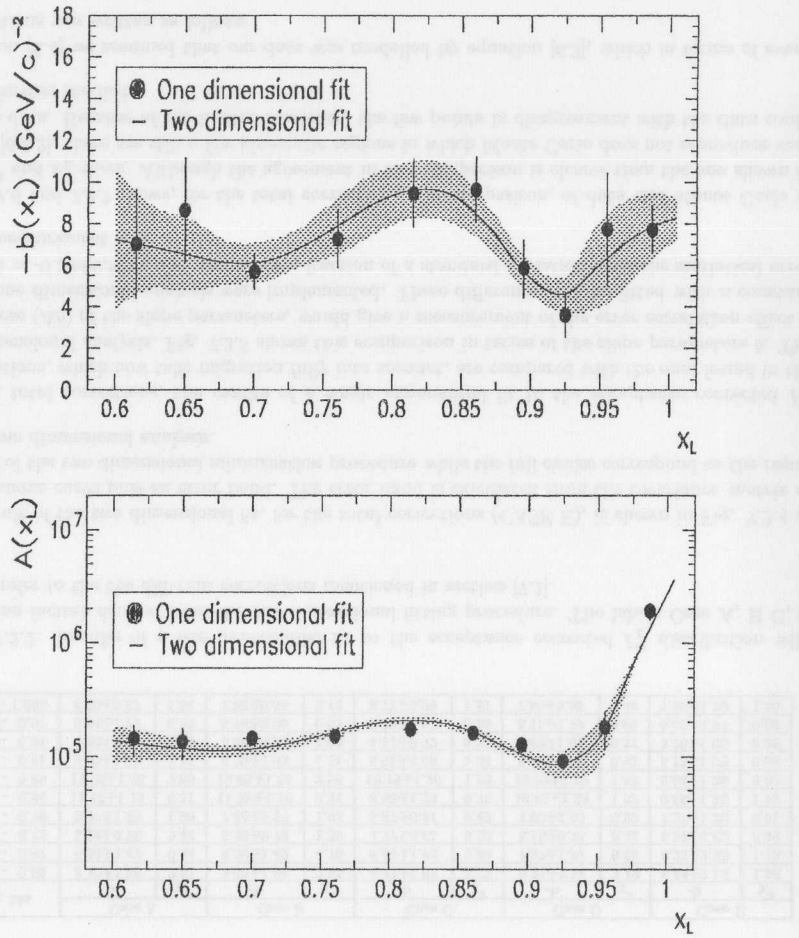

Figure 7.2.4: Result of the two dimensional continuous fit (solid line) for A and b in ZEUS–LPS PHP data after all the correction to the LPS data have been taken into account (CASE E). The band around the continuous line are the errors computed from the covariance matrix at the end of the minimisation procedure. The full circles represent the one dimensional fits to A and b.

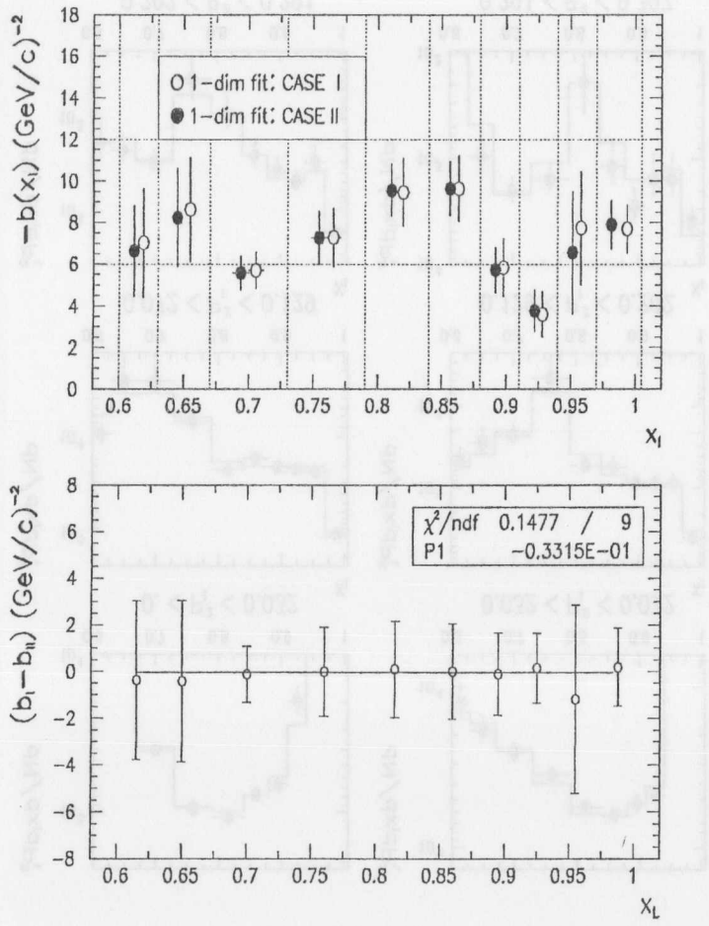

Figure 7.2.5: Comparison of the ZEUS-LPS PHP slope parameters for the two cases: one dimensional fit as in section [6.5.1] (CASE I) and one dimensional fit to the acceptance corrected P_t^2 distribution with correction factors derived from the two dimensional fit results (CASE II). The histogram at the top shows a comparison of the fits whereas the histogram at the bottom indicates the differences from both measurements together with a constant line ($\Delta b = b_I - b_{II} = -0.033 \pm 0.597$) fit to them.

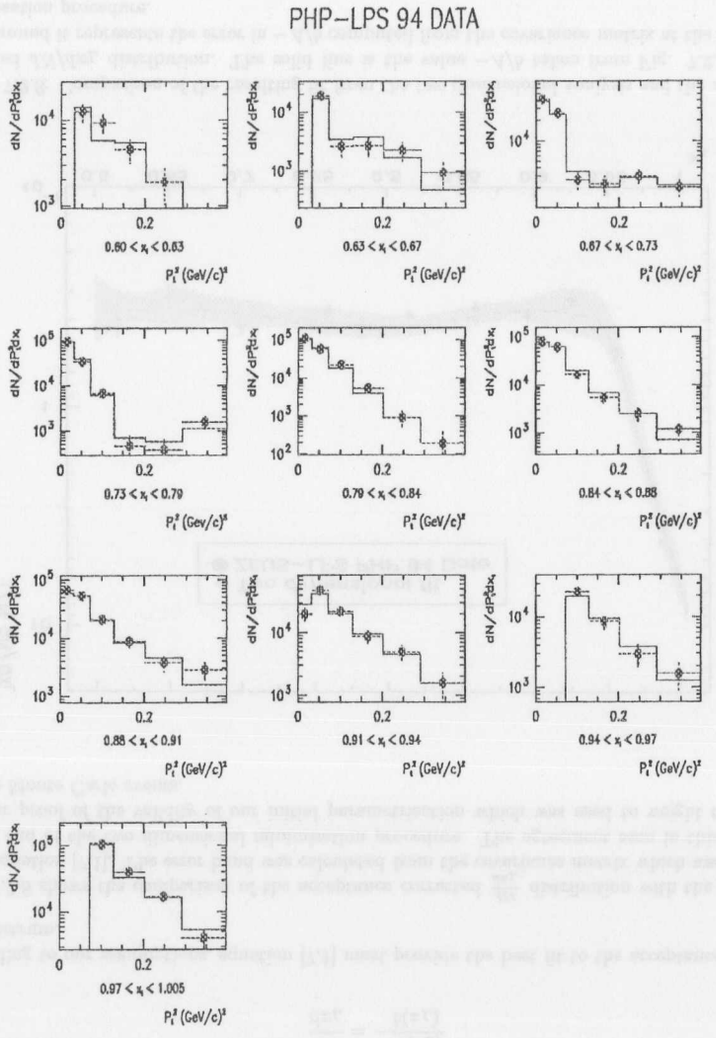

Figure 7.2.6: Comparison of data and Monte Carlo in bins of x_L after all the corrections have been taken into account (CASE E). The solid histogram corresponds to Monte Carlo and the full circles correspond to ZEUS-LPS PHP 94 data.

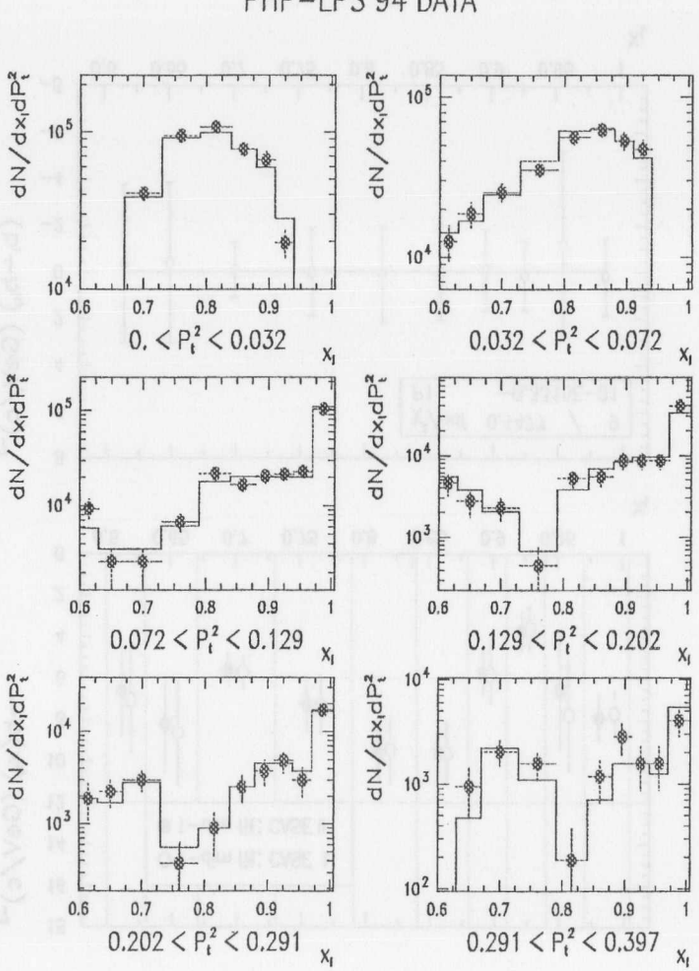

Figure 7.2.7: Comparison of data and Monte Carlo in bins of P_t^2 after all the corrections have been taken into account (CASE E). The solid histogram corresponds to Monte Carlo and the full circles correspond to ZEUS-LPS PHP 94 data.

$$\frac{dN}{dx_L} = -\frac{A(x_L)}{b(x_L)} \tag{7.1}$$

According to our assumptions, equation [7.1] must provide the best fit to the acceptance corrected x_L spectrum.

Fig. 7.2.8 shows the comparison of the acceptance corrected $\frac{dN}{dx_L}$ distribution with the fit derived from equation [7.1]. The error band was calculated from the covariance matrix which was produced at the end of the two dimensional minimisation procedure. The agreement seen in this picture is another proof of the validity of our initial parametrisation which was used to weight the leading proton Monte Carlo events.

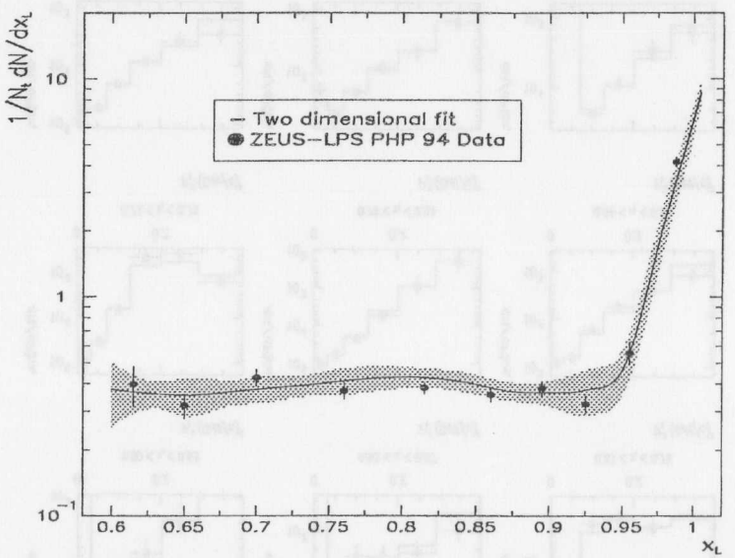

Figure 7.2.8: Comparison of the resulting fit from the two dimensional analysis and the acceptance corrected dN/dx_L distribution. The solid line is the value $-A/b$ taken from Fig. 7.2.4 and the band around it represents the error in $-A/b$ computed from the covariance matrix at the end of the minimisation procedure.

The two dimensional surface that gives the best fit to the $\frac{d^2N}{dx_L dP_t^2}$ distribution is shown in Fig. 7.2.9. The two dimensional surface is computed using the A and b curves shown in Fig. 7.2.4 and was drawn for the low x_L region only.

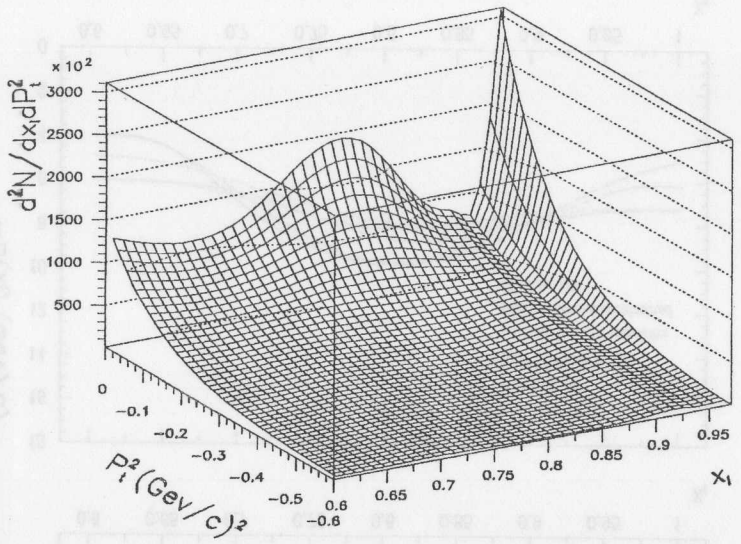

Figure 7.2.9: Two dimensional surface representing the best fit to $dN/dx_L dP_t^2$ for the ZEUS-LPS PHP 94 data. The parameters that defines this surface are the continuous fits from Fig. 7.2.4 and it has been drawn for the low x_L spectrum ($x_L < 0.97$) only.

7.3 Correction to the ZEUS-LPS DIS data

The corrections to the ZEUS-LPS DIS data follow the same procedure as for the ZEUS-LPS PHP data.

7.3.1 One dimensional fit to data

Fig. 7.3.1 shows the results obtained in the one dimensional implementation of the method and Fig. 7.3.2 shows the same but in terms of the cubic spline fits to data. Data from Fig. 7.3.1 is written in table 7.3.1.

As for the case of photo-production data, the slope parameters of the fitted P_t^2 distributions are affected if the corrections mentioned in section [7.1] are applied. The way the slope parameters changes follows approximately the same pattern. These changes can best be described as follows:

- Correction for p-beam halo coincidences: The subtraction of this kind of background affects the measurement of b only in the diffractive region ($0.97 < x_L < 1.02$). The value of b increases the value by ~12%.

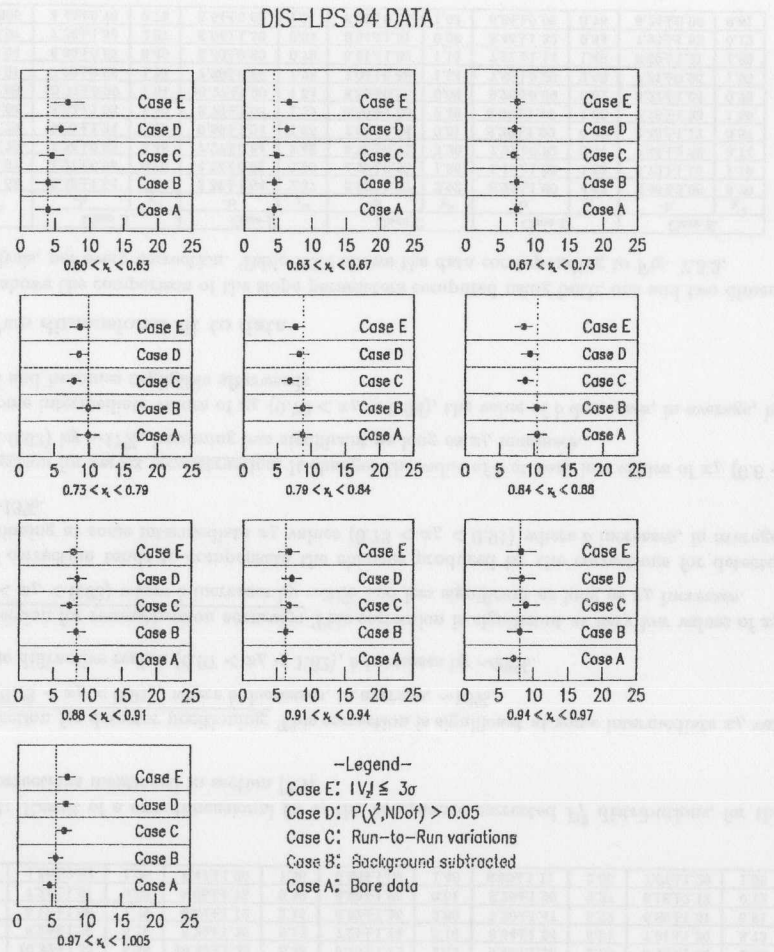

Figure 7.3.1: One dimensional fit results showing the changes in the measurements of b for ZEUS-LPS DIS data due to different conditions. The vertical dotted line give a reference so that the size of the variation with respect to a value of b found in chapter [6] can be appreciated.

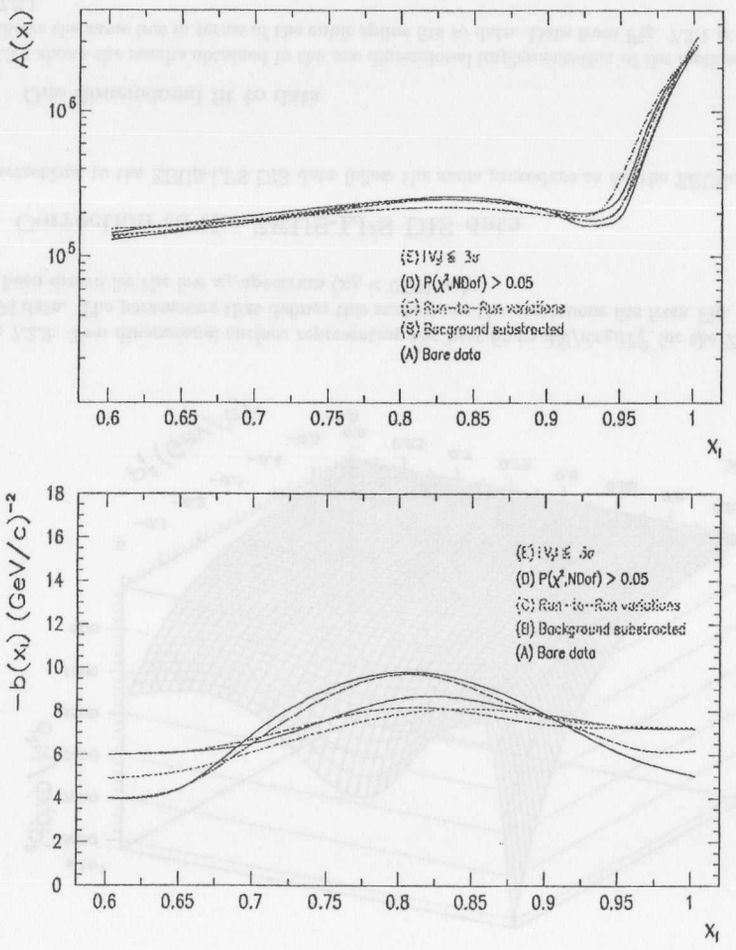

Figure 7.3.2: One dimensional fit results showing the variations in measurements of A and b for ZEUS-LPS DIS data due to different conditions in terms of the cubic spline fits to data

x_L bin	Case A		Case B		Case C		Case D		Case E	
	-b	χ^2	-b	χ^2	-b	χ^2	-b	χ^2	-b	χ^2
0.60 - 0.63	3.94±1.73	5.24	3.94±1.73	5.24	4.49±1.73	5.72	5.79±2.19	8.10	6.79±2. 39	6.34
0.63 - 0.67	4.42±1.04	3.15	4.42±1.04	3.15	4.78±1.03	3.99	6.23±1.19	4.45	6.61±1. 24	3.57
0.67 - 0.73	7.32±0.92	15.66	7.32±0.92	15.66	6.88±0.80	14.71	7.03±0.90	16.40	7.48±0. 97	14.27
0.73 - 0.79	9.88±1.57	7.72	9.88±1.57	7.72	7.81±0.99	1.92	8.50±1.28	2.94	8.65±1. 43	3.80
0.79 - 0.84	8.74±1.30	5.25	8.74±1.30	5.25	6.82±1.20	4.35	8.16±1.45	6.74	7.61±1. 43	5.36
0.84 - 0.88	10.42±1.33	5.58	10.42±1.33	5.58	8.75±1.12	2.32	9.40±1.23	2.28	8.46±1. 20	2.08
0.88 - 0.91	8.29±1.26	5.14	8.29±1.26	5.13	7.21±1.14	5.16	8.34±1.34	5.91	7.81±1. 30	5.73
0.91 - 0.94	6.12±1.08	1.79	6.34±1.12	2.16	6.82±1.26	2.88	7.20±1.47	5.22	6.85±1. 51	5.91
0.94 - 0.97	7.21±1.61	0.03	8.05±1.75	0.19	8.89±1.86	0.01	8.26±1.90	0.27	8.18±2. 13	0.12
0.97 -1.005	4.58±0.82	1.20	5.47±1.00	1.50	6.68±1.06	1.48	6.89±1.11	2.00	7.07±1. 20	1.08

Table 7.3.1: Result of a one dimensional fit to the acceptance corrected P_t^2 distributions, for the different corrections mentioned in section [7.1]

- Correction for detector positioning: This correction is significant at some intermediate x_L values ($0.73 < x_L < 0.91$), where b decreases, in average, ~18%.

  In the diffractive region ($0.97 < x_L < 1.02$), b increases by ~22%.

- Correction for reconstruction accuracy: This correction is significant at very low values of x_L ($0.6 < x_L < 0.63$) where b increases by ~30% and less significant as long as x_L increases.

  This correction tends to compensate the changes produced by the corrections for detector positioning at some intermediate x_L values ($0.73 < x_L < 0.91$) where b increases, in average, by ~13%.

- Correction for vertex reconstruction: It changes the value of b at very low values of x_L ($0.6 < x_L < 0.63$) by ~17%, becoming less significant as long as x_L increases.

  At some intermediate values of x_L ($0.79 < x_L < 0.94$), the value of b decreases, in average, by ~7% and becomes negligible afterwards

7.3.2 Two dimensional fit to data

Fig. 7.3.3 shows the comparison of the slope parameters computed using both, one and two dimensional analysis, per every correction. Table 7.3.2 shows the data corresponding to Fig. 7.3.3.

x_L bin	Case A		Case B		Case C		Case D		Case E	
	-b	χ^2	-b	χ^2	-b	χ^2	-b	χ^2	-b	χ^2
0.60 - 0.63	3.48±1.54	2.37	3.50±1.54	2.37	3.98±1.57	2.92	6.22±1.90	4.33	6.66±2.08	3.70
0.63 - 0.67	4.27±0.96	0.90	4.34±0.96	0.90	4.90±0.95	1.36	6.16±1.06	1.68	6.72±1.10	1.19
0.67 - 0.73	7.34±0.85	3.48	7.27±0.84	3.48	6.76±0.73	3.20	7.21±0.82	3.41	7.48±0.88	3.14
0.73 - 0.79	9.65±1.24	1.85	9.59±1.24	1.85	7.62±0.84	0.81	8.38±1.02	0.49	8.46±1.17	0.57
0.79 - 0.84	8.83±1.03	1.39	8.79±1.03	1.39	6.59±1.00	9.49	8.00±1.18	1.63	7.76±1.23	1.59
0.84 - 0.88	10.27±0.99	1.54	10.27±0.99	1.54	8.86±0.95	0.89	9.26±0.99	0.62	8.27±1.04	0.75
0.88 - 0.91	7.90±0.88	1.33	7.88±0.88	1.28	7.04±0.86	1.54	7.80±0.96	2.08	7.51±0.95	1.95
0.91 - 0.94	6.50±0.86	0.49	6.60±0.90	0.70	6.61±1.02	1.13	7.21±1.14	1.46	6.59±1.21	1.63
0.94 - 0.97	7.38±1.33	2.87	8.04±1.30	0.04	8.94±1.31	0.08	8.46±1.32	0.34	7.93±1.52	0.12
0.97 - 1.005	4.43±0.70	0.73	5.54±0.82	1.21	6.99±0.99	1.03	6.84±0.95	0.76	6.74±0.96	0.61

Table 7.3.2: Results of a one dimensional fit to the acceptance corrected P_t^2 distributions with correction factors derived from the dimensional fit results. The labels Case A, B, C, D and E refer to the corrections mentioned in section [7.1].

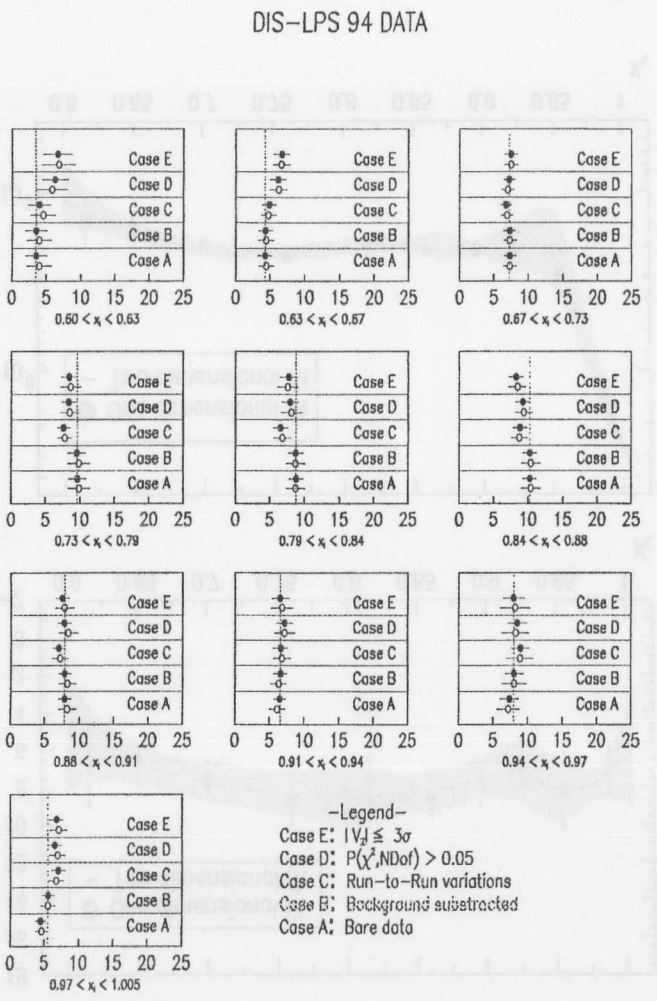

Figure 7.3.3: Comparison of changes in b as measured from: one dimensional fit (open circles) and one dimensional fit to the acceptance corrected data with correction factors derived from the two dimensional fit results (full circles). The vertical dotted lines gives a reference so that the size of the variation with respect to a value of b calculated in chapter [6] can be appreciated (which is a one dimensional fit of b after a beam halo coincidences have been subtracted).

The result of the two dimensional fit, for the total corrections (CASE E), is shown in Fig.7.3.4 as a continuous curve plus an error band. This error band is calculated from the covariance matrix at the end of the two dimensional minimisation procedure and the full circles correspond to the result of the one dimensional analysis.

For the total corrections, the results of a single exponential fit to the acceptance corrected P_t^2 distributions, derived from the two dimensional analysis, are compared with the ones found in the one dimensional analysis. Fig. 7.3.5 shows the comparison in terms of the slope parameters b. The differences (Δb) of the slope parameters, would give a measurement of the error correlation effect if only a one dimensional analysis were implemented. These differences can be fitted with a constant line ($\Delta b = -0.123 \pm 0.597$). Δb represents a fraction of a standard deviation from the statistical error in the measurement of b.

For the total corrections the comparison of data and Monte Carlo in both P_t^2 and x_L slices is shown in Fig. 7.3.6. Although an overall agreement is found in these comparisons, there are still a few kinematic regions in which Monte Carlo does not reproduce very well the data. As for the case of PHP data, because of the limited statistics, the few points in disagreement with the data could not be further studied.

As explained in the preceding section, the A and b values in our fits represent the best parameters that approximate the real distribution for the production of leading protons. Equation [7.1] provides the best fit to the acceptance corrected x_L spectrum.

Fig. 7.3.8 shows the comparison of the accepted corrected $\frac{dN}{dx_L}$ distributions with the fit derived from equation [7.1]. The error band was calculated from the covariance matrix which was produced at the end of the two dimensional minimisation procedure. The agreement seen in this picture is another proof of the validity of our initial parametrisation which was used to weight the leading proton Monte Carlo events.

Fig. 7.3.4 illustrates the two dimensional surface that gives the best fit to the $\frac{d^2N}{dx_L dP_t^2}$ distribution. The two dimensional surface is computed using the A and b curves shown in Fig. 7.3.4. It was drawn for the low x_L region only.

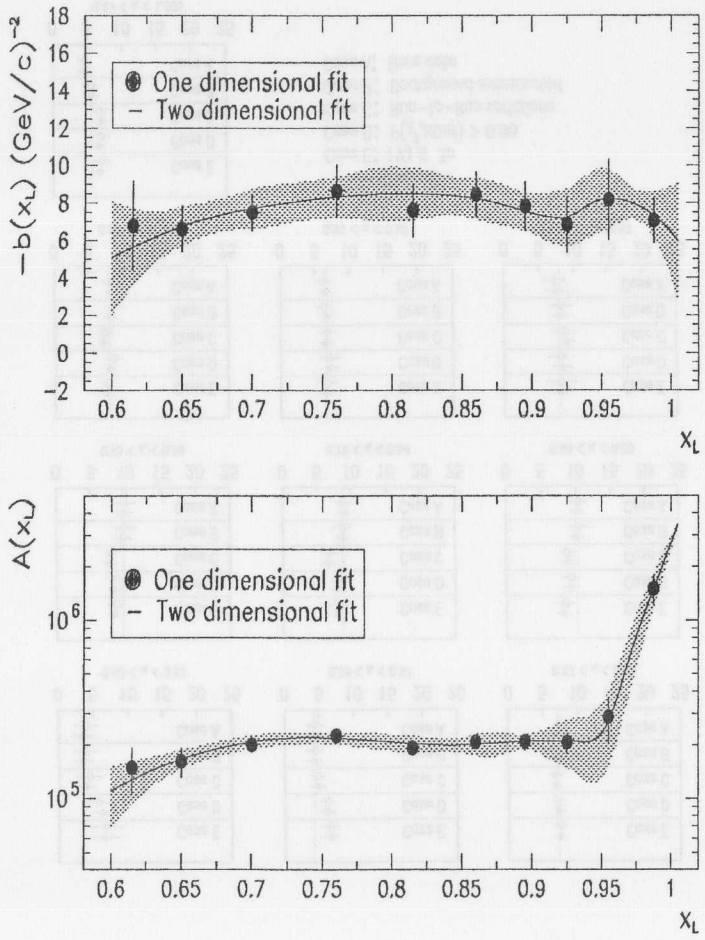

Figure 7.3.4: Result of the two dimensional continuous fit (solid line) for A and b in LPS-DIS data after all the correction to the LPS data have been taken into account (CASE E). The band around the continuous line represents the errors computed from the covariance matrix at the end of the minimisation procedure. The full circles represent the one dimensional fits to A and b.

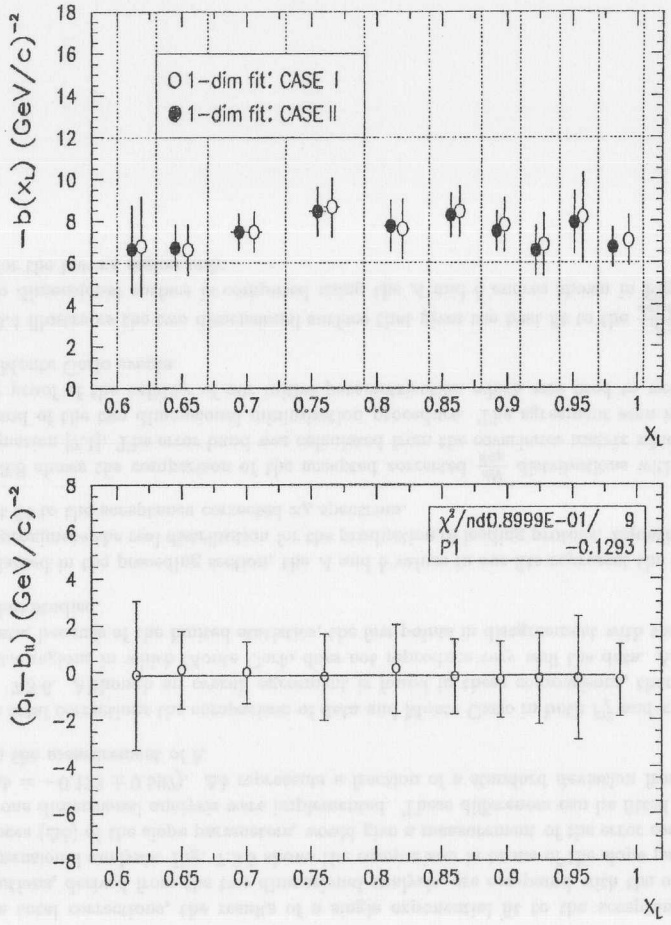

Figure 7.3.5: Comparison of the ZEUS-LPS DIS slope parameters for the two cases: one dimensional fit as in section [6.5.1] (CASE I) and one dimensional fit to the acceptance corrected P_t^2 distribution with correction factors derived from the two dimensional fit results (CASE II). The histogram at the top shows a comparison of the fits whereas the histogram at the bottom indicates the differences from both measurements together with a constant line ($\Delta b = b_I - b_{II} = -0.123 \pm 0.597$) fit to them.

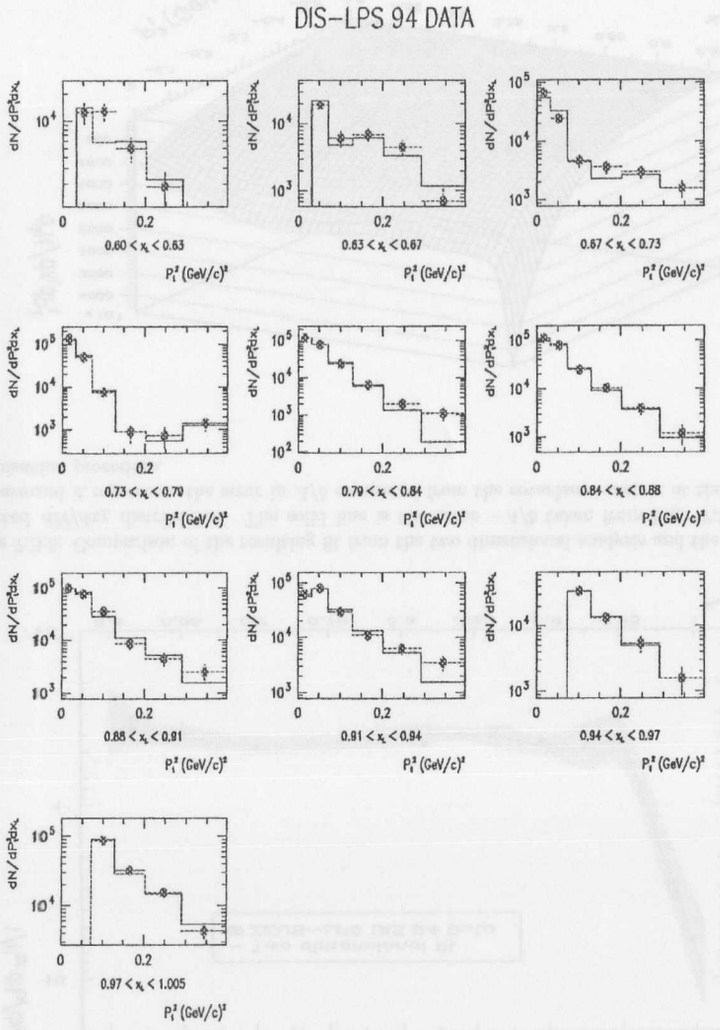

Figure 7.3.6: Comparison of data and Monte Carlo in bins of x_L after all the corrections have been taken into account (CASE E). The solid histogram corresponds to Monte Carlo and the full circles corresponds to ZEUS-LPS DIS data.

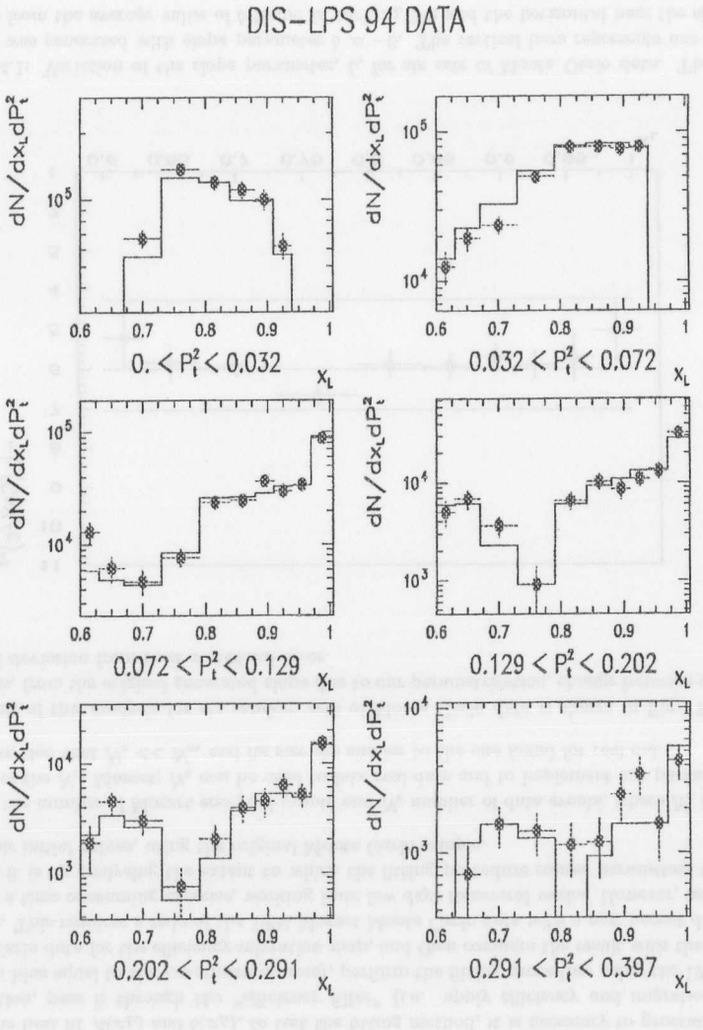

Figure 7.3.7: Comparison of data and Monte Carlo in bins of P_t^2 after all the corrections have been taken into account (CASE E). The solid histogram corresponds to Monte Carlo and the full circles correspond to ZEUS-LPS DIS 94 data.

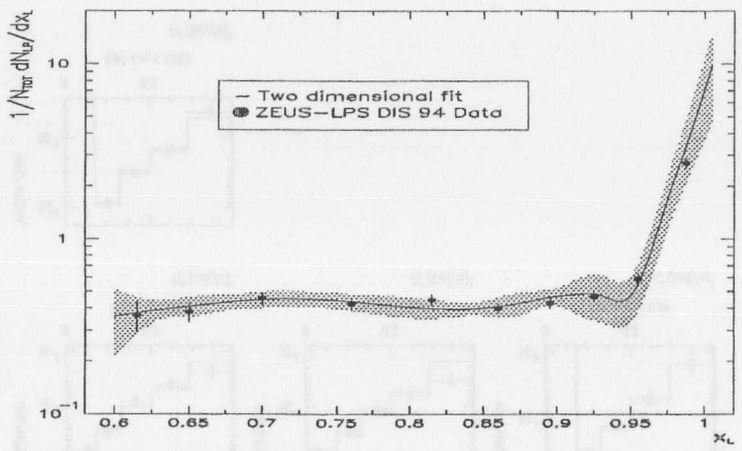

Figure 7.3.8: Comparison of the resulting fit from the two dimensional analysis and the acceptance corrected dN/dx_L distribution. The solid line is the value $-A/b$ taken from Fig. 7.3.4 and the band around it represents the error in A/b computed from the covariance matrix at the end of the minimisation procedure.

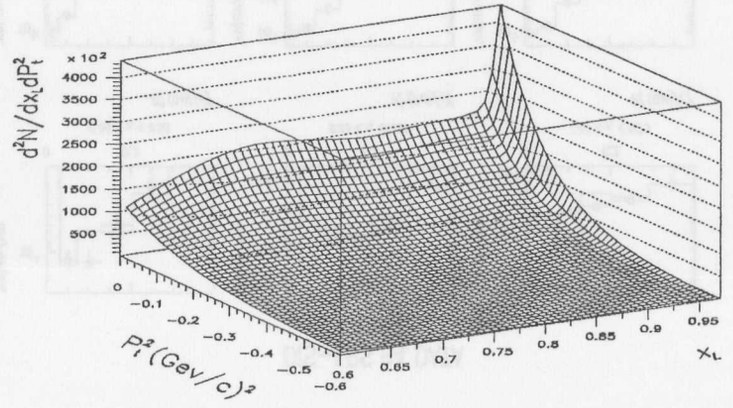

Figure 7.3.9: Two dimensional surface representing the best fit to $dN/dx_L dP_t^2$ for the ZEUS-LPS DIS 94 data. The parameters that define this surface are the continuous fits from Fig. 7.3.4, drawn for the low x_L spectrum ($x_L < 0.97$) only.

7.4 Testing of the fitting procedure

Given the best fit $A(x_L)$ and $b(x_L)$, to test the fitting method, it is necessary to generate a known distribution, pass it through the "efficiency filter" (i.e. apply efficiency and migrations, collect events in bins equal to the experimental ones), perform the fitting procedure using the 1994 Mozart Monte Carlo data for the efficiency-migration map, and then compare the result with the generated function. This requires a redo of the 1994 Mozart Monte Carlo data with a new parent distribution which is a time consuming exercise, working from few days to several weeks. However, another way of doing it is by analysing the extent to which the fitting procedure causes parameters to migrate from their initial values, using the original Monte Carlo sample.

If N_m is the number of Mozart accepted events and N_e number of data events, where N_e is taken at random of the N_m Mozart; N_e can be used to fake real data and to implement our parametrisation on it, provided that $N_e << N_m$ and its size are similar to the one found for real data.

The result of this analysis for six random sets of Monte Carlo data is shown in Fig. 7.4.1. The variations, from the original generated slope due to our parametrisation, change between one to two standard deviation from their statistical error.

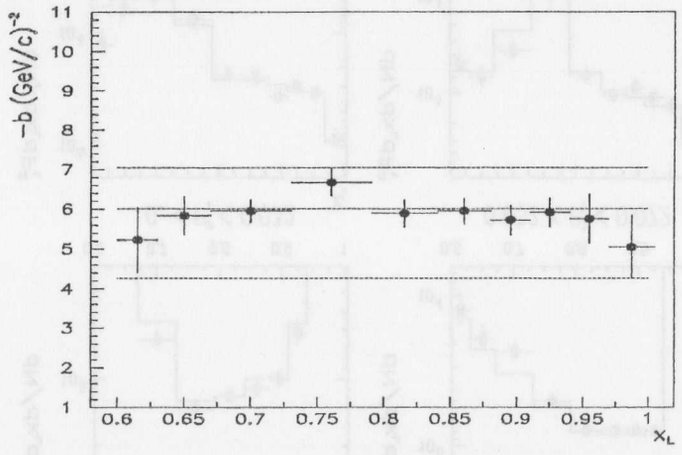

Figure 7.4.1: Variation of the slope parameter, b, for six sets of Monte Carlo data. The P_t^2 distribution was generated with slope parameter $b = -6$. The vertical bars represents one standard deviation from the average value of b found in each x_L bin and the horizontal bars the size of the x_L bins.

7.5 Summary of the measurements

In this chapter, a detailed study of changes in the calculation of the (x_L, P_t^2) acceptance due to corrections for detector positioning, reconstruction accuracy and vertex reconstruction has been performed. These corrections have been implemented in a cumulative way and, as a result, the two dimensional continuous fitting procedure improves in accuracy. The leading proton Monte Carlo events, corrected by the weights derived from the fits, better reproduce the data with few exceptions where the limited available statistics in the sample did not allow us to pursue further studies.

To test the feasibility of the method, samples of Monte Carlo events randomly selected have been used to analyse the extent to which the fitting procedure cause parameters to migrate from their initial values. The variations in the measurement of the b parameters, due to the parametrisation introduced to model the production of leading protons, in average, are consistent within one standard deviation of the statistical error of their own measurement, but could change up to two standard deviations.

Finally, for the total corrections, the acceptance corrected (x_L, P_t^2) distribution of the leading proton have been analysed. The P_t^2 distributions follows an experimentally falling behaviour and can be fitted with a single exponential. Table 7.5.1 shows the final values of b for DIS and PHP data.

x_L bin	ZEUS-LPS PHP Data		ZEUS-LPS DIS Data	
	-b	χ^2	-b	χ^2
0.60 – 0.63	6.64 ± 2.18	1.58	6.66 ± 2.08	3.70
0.63 – 0.67	8.23 ± 2.38	1.13	6.72 ± 1.10	1.19
0.67 – 0.73	5.57 ± 0.82	0.48	7.48 ± 0.88	3.14
0.73 – 0.79	7.27 ± 1.28	0.91	8.46 ± 1.17	0.57
0.79 – 0.84	9.55 ± 1.25	1.12	7.76 ± 1.23	1.59
0.84 – 0.88	9.64 ± 1.29	0.82	8.27 ± 1.04	0.75
0.88 – 0.91	5.73 ± 1.08	0.88	7.51 ± 0.95	1.95
0.91 – 0.94	3.76 ± 1.00	0.38	6.59 ± 1.21	1.63
0.94 – 0.97	6.56 ± 2.69	0.03	7.93 ± 1.52	0.12
0.97 – 1.005	7.90 ± 1.19	1.35	6.74 ± 0.96	0.61

Table 7.5.1: Slopes of the acceptance corrected P_t^2 distributions as measured in PHP and DIS samples

Integrating over P_t^2 the resultant surface which is produced by the two dimensional fitting procedure, the acceptance corrected x_L distributions for DIS and PHP data are also fitted. The comparison of these fits with the data, showed that the acceptance corrected x_L distribution in both DIS and PHP samples are approximately flat in the region $(0.6 < x_L < 0.9)$. Furthermore, there is a peak at values of $x_L > 0.95$ in both distributions indicating the presence of elastic diffractive processes in both DIS and PHP samples. The fraction of events with a leading protons as a function of x_L is calculated integrating the x_L distributions. In the region $0.6 < x_L < 0.9$ this integral gives $\approx$ 13.04 % and $\approx$ 11.77 % for DIS and PHP sample respectively. At values of $x_L > 0.9$ the value of the integral is $\approx$ 12.67 % and $\approx$ 17.19 % for DIS and PHP sample respectively.

The discussion of the process supposed to account for the production of leading proton as well as their comparisons with the data will be presented in chapter [8].

8 Discussion of results and theoretical predictions

8.1 Comparison of ZEUS-LPS DIS and PHP data

The comparison of the acceptance corrected x_L spectra for the PHP and DIS sample are shown in Fig. 8.1.1. Both distributions are approximately flat and show an overall agreement in shape in the low x_L region $(0.6 < x_L < 0.9)$. These distributions, as long as x_L approximates to unity increases in magnitude reaching a maximum in the diffractive region $(x_L = 1)$.

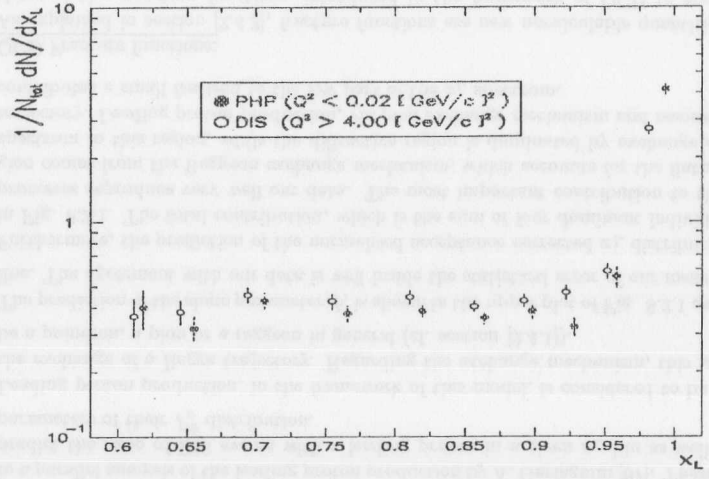

Figure 8.1.1: Comparison of the acceptance corrected x_L distribution as measured in PHP and DIS data. The distributions are normalised by the total number, N_{tot} of triggered events in the PHP or DIS sample where the LPS was active for data taken.

Fig. 8.1.2 shows the comparison of the slope parameters b, as extracted from PHP and DIS data. The general trend of both sets of data is a broad maximum in b as a function of x_L, centred near x_L =0.8. Furthermore, there is evidence of a minimum near x_L =0.9 in the photo-production data. Differences in shape can better be appreciated in the lower graph where the difference in slope is plotted as a function of x_L. The hypothesis that there is no difference, on average has a χ^2 =11.72 for 10 degrees of freedom corresponding to a confidence level of $\sim$ 80%. If a constant systematic slope difference is fitted, the result is $\Delta_b = b_{DIS} - bPHP = 0.608 \pm 0.545$, corresponding to a probability of $\sim$ 0.6 that shape differences are statistical in origin.

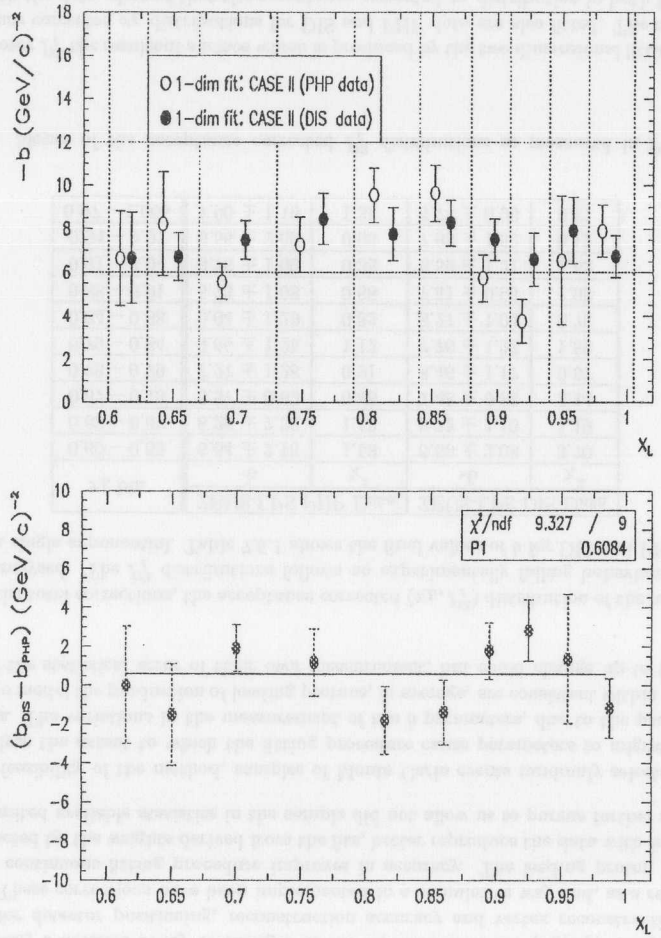

Figure 8.1.2: Comparison of the b slopes as measured in PHP and DIS data (upper plot). The differences from both measurements (lower plot) can be fitted with a constant line, resulting in: $\Delta b = b_{DIS} - b_{PHP} = 0.608 \pm 0.545$

8.2 Numerical calculations

Similarities in shape, for the acceptance corrected x_L spectrum and for the slope parameters, suggest that the processes by which leading protons are produced in both samples, might be similar. In order to study the properties of the leading proton production, numerical calculations of the theoretical models discussed in section [2.4], have been implemented and a comparison of their predictions with our data is described in the following paragraphs:

- Regge phenomenology:
  The numerical calculations for this model were provided by A. Szczurek [41] and implemented in a parallel analysis of the leading proton production by A. Garfagnini [87]. These calculations predict the ratio of DIS events with a leading proton in a given x_L bin as well as the slope parameters of their P_t^2 distribution.

  Leading proton production, in the framework of this model, is considered to be mediated by the exchange of a Regge trajectory. Regarding the exchange mechanism, this trajectory can be a pomeron, a pion or a reggeon in general (cf. section [2.4.1]).

  The prediction of the slope parameter, b, is shown in the upper plot of Fig. 8.2.1 as a continuous line. The agreement with our data is well inside the statistical error of our measurement.

  Furthermore, the prediction of the normalised acceptance corrected x_L distributions is shown in Fig. 8.2.1. The total contribution, which is the sum of four dominant individual exchange processes reproduce very well our data. The most important contribution to the low-x_L region comes from the Reggeon exchange mechanism, which accounts for the flatness of the x_L spectrum in this region, while the diffractive region is dominated by exchange of a pomeron trajectory. Leading proton production, via pion exchange mechanism and resonance Δ-decay, contributes a small fraction to the low part of the x_L spectrum.

- QCD Fracture functions:
  As explained in section [2.4.2], fracture functions are new uncalculable quantities, similar to those of the structure functions, introduced in the framework of QCD to account for the properties of the remnants fragments of the target.

  The fracture function $M^i_{A,h}(z,x,t,Q^2))$ is parametrised at a given scale Q^2_o with a functional with enough flexibility so as to reproduce de data. In addition, the shape of the t distribution is used to correct the form of $M^i_{A,h}(z,x,t,Q^2))$ and a small kinematic region in x_L is fitted. H1 data is used for this fit, which is constraint to $0.73 < x_L < 0.84$ and $x_L > 0.97$. Finally, the Altarelli-Parisi evolution equations are used to evolve in x and Q^2 *à la* F_2 and predict the shape of the fit in the whole x_L kinematic region $0.6 < x_L < 1.05$.

  In this novel approach, the numerical calculations for the normalised acceptance corrected x_L spectrum were provided by D. de Florian [88]. Fig. 8.2.2 shows the comparison of this prediction with our data where a remarkable agreement is found in the low part of the x_L spectrum ($x_L < 0.9$).

  What is important to know from the fracture function is that, it measures the parton distribution of the object exchanged between the target and the final hadron, without making any model about what that object actually is. Hence it provides an alternative tool, in the framework of QCD, to those based on Regge factorisation.

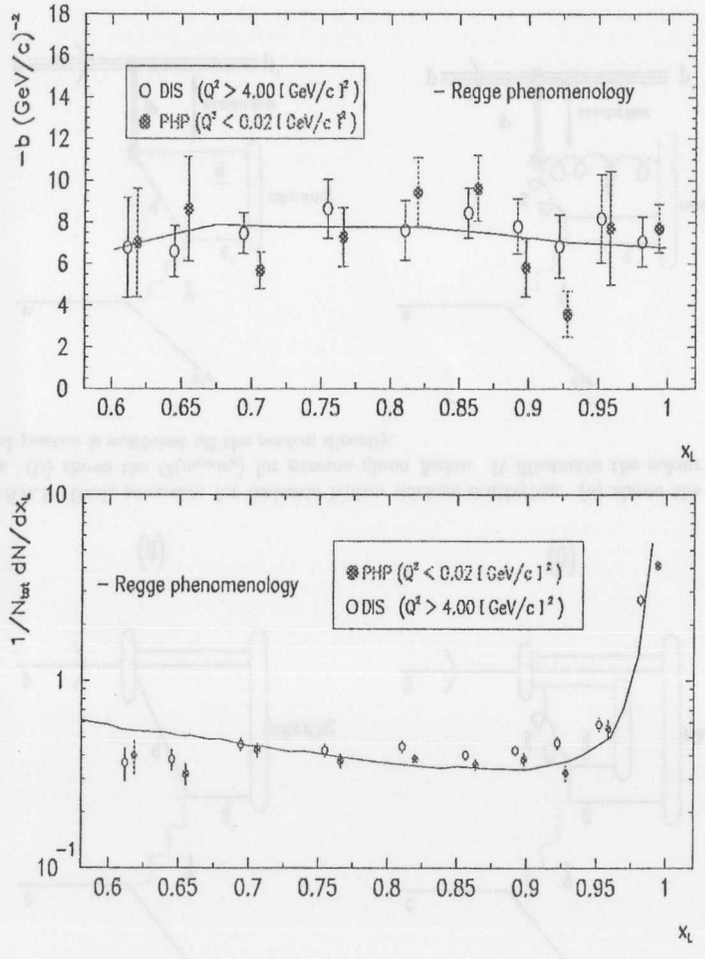

Figure 8.2.1: Comparison of the b slopes and the normalised acceptance corrected x_L spectrum with the prediction of a model developed in a Regge phenomenology framework [41]. Although this model was developed to explain the behaviour of the diffractive DIS data, PHP data is also plotted here for comparison.

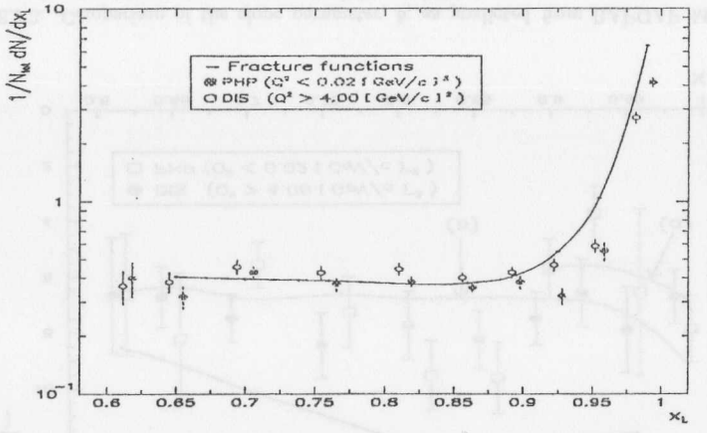

Figure 8.2.2: Comparison of the normalised acceptance corrected x_L distribution with the prediction of a numerical calculation based on the QCD-fracture function. This model was developed to study the behaviour of the diffractive DIS data but PHP data is also plotted here for comparison.

8.3 Theoretical Predictions

In order to further study the mechanism by which the leading protons are produced at HERA, three different classes of Monte Carlo event generators that simulate ep collisions with a final state leading proton have to be taken into account. An analysis of these Monte Carlo generators and a comparison of their predictions with our measurements are shown:

1. RAPGAP [89]: The version used of this generator simulates traditional deep inelastic processes and ep collisions where the electron is scattered on a pomeron coupled to a proton following the Ingelman and Schlein model [26]. In addition, it generates π-exchange events, in which the virtual photon scatters off a virtual pion generated at the proton vertex.

   - Traditional deep inelastic scattering: It is generated for processes shown in Fig 8.3.1, in which a parton carrying a colour is removed from the proton and a coloured proton remnant is left. This remnant, together with the coloured partons of the hard interaction must form a colour singlet state. This colour string generates a particle flow between the proton remnant and the partons of the hard scattering.
   - The Ingelman and Schlein model: As explained in section [2.3], the photon coupling to the incoming lepton interacts with partons of the pomeron instead of interacting with partons of the proton directly as in the traditional quark parton model of deep inelastic scattering. These processes are shown in Fig. 8.3.2.

     The simulation of the pomeron-proton coupling follows the Regge theory and the photon-pomeron coupling is treated according to whether the partonic constituent of the pomeron is made of gluons or quarks.

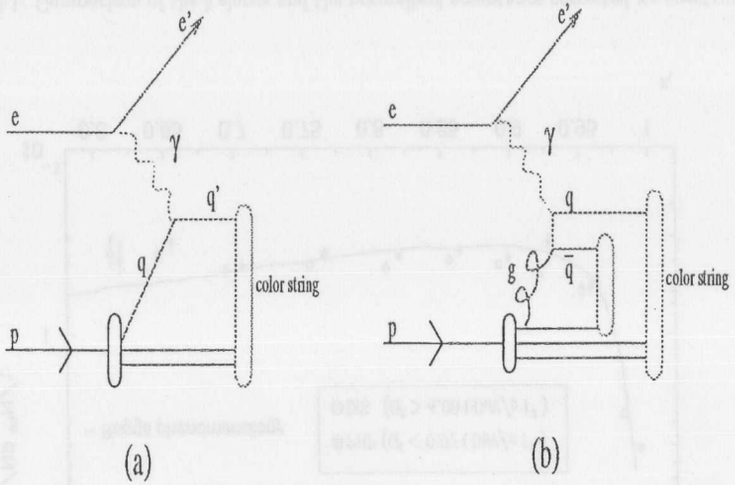

Figure 8.3.1: Basic processes for inelastic lepton nucleon scattering. (a) shows the lowest order process. (b) shows the $O(\alpha_{em}\alpha_s)$ for gamma gluon fusion. It illustrates the colour flow when a coloured parton is scattered off the proton directly.

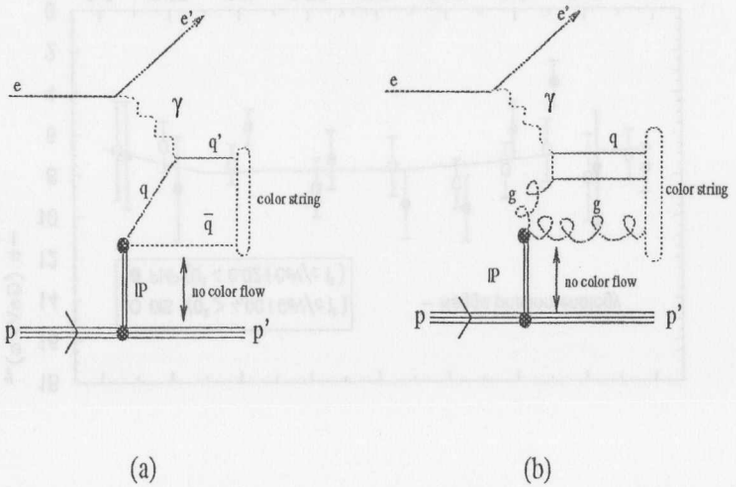

Figure 8.3.2: Basic processes for inelastic lepton scattering on a pomeron. (a) shows the lowest order process. (b) shows the $O(\alpha_{em}\alpha_s)$ for gamma gluon fusion. Since the pomeron is a colour neutral object there is no colour flow between the diffractively scattered proton and the particles of the hard interaction. A gap in rapidity is observed between the fast moving proton and the other particles.

- Pion exchange events: They are simulated similarly as for pomeron exchange with the corresponding modifications for the outgoing particle, which can be p, n, Δ^{++} corresponding to π^0, π^+ or π^- exchange.

In all these processes, higher order gluon emission is simulated using the Colour Dipole Model (ARIADNE) [90] and hadronisation is performed using the LUND string fragmentation model [91].

RAPGAP event samples used in this analysis were generated using the pomeron exchange mechanism in single and double dissociation. Single dissociation indicates the proton's break-up only. Double dissociation indicates both, the proton and pomeron break-up processes. In addition a sample of events with a π^0 exchange mechanism was used.

The prediction of the slope parameter, b, using this Monte Carlo generator, is shown in Fig. 8.3.3 as a continuous line. Single and double dissociation processes tends to be in line with the data. Single dissociation is present at high values of x_L ($x_L > 0.9$) while double dissociation covers the entire x_L region available in our measurement. The pion exchange mechanism, as implemented in this Monte Carlo, does not explain the distribution of the slope parameter, b, as a function of x_L.

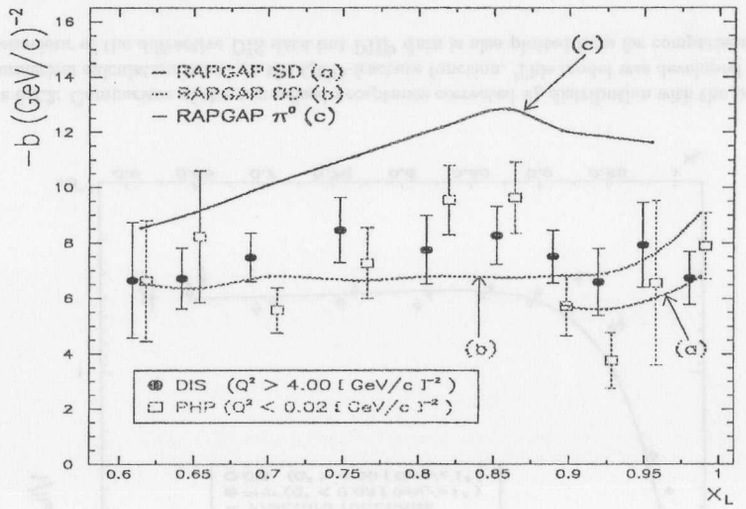

Figure 8.3.3: Comparison of the slope parameter, b, as predicted from RAPGAP Monte Carlo (continuous lines), with our measurements for DIS and PHP data

The comparison of the prediction of the normalised acceptance corrected x_L distribution with our measurement is shown in Fig. 8.3.4. Although the contributions from double and single dissociation processes qualitatively describe the shape of the x_L spectrum, they fail to reproduce the data.

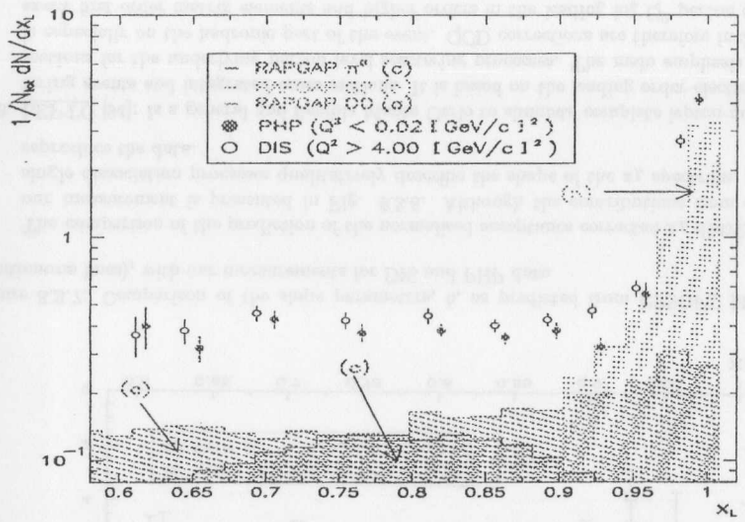

Figure 8.3.4: Comparison of the normalised acceptance corrected x_L distribution,with the predictions from RAPGAP Monte Carlo (hatched histograms). The labels (a), (b) and (c) correspond to the double, single dissociation and π^0-exchange processes implemented in RAPGAP.

2. EPSOFT [92]: Is a Monte Carlo program for simulating diffractive and non-diffractive γp collisions at HERA developed in the framework of HERWIG 5.8 [93]. In this Monte Carlo generator the exchange photon in the ep scattering is assumed to fluctuate into a virtual meson that undergoes a soft collision with the proton. It relies on the Regge type of cross section parametrisations and statistical modelling of the final state particles.

   The treatment of the final state particles assumes that hadrons are very complex clouds of virtual objects and that the collision of two hadrons involves many interactions between their constituents.

   In soft non-diffractive γp interactions each of the constituents are considered to carry only a very small fraction of the hadron energy and hence no high transverse momentum exchange can occur when the two clouds meet. The transverse momentum of the emerging hadrons is assumed to be entirely due to thermal motions. Fig. 8.3.5 shows the soft non-diffractive γp scattering simulated in EPSOFT.

   In soft diffractive γp interactions, the process is modelled as an exchange of a neutral, colourless object, a pomeron. Since the pomeron is assumed to behave as a hadron, the diffractive dissociation is treated as a collision of two hadrons: the dissociating particle and the pomeron. Fig. 8.3.6 shows the diffractive subprocesses generated by EPSOFT corresponding to elastic vector meson production ($\gamma p \to Vp$), photon dissociation ($\gamma p \to Xp$), proton (single) dissociation ($\gamma p \to VN$) and double dissociation ($\gamma p \to XN$).

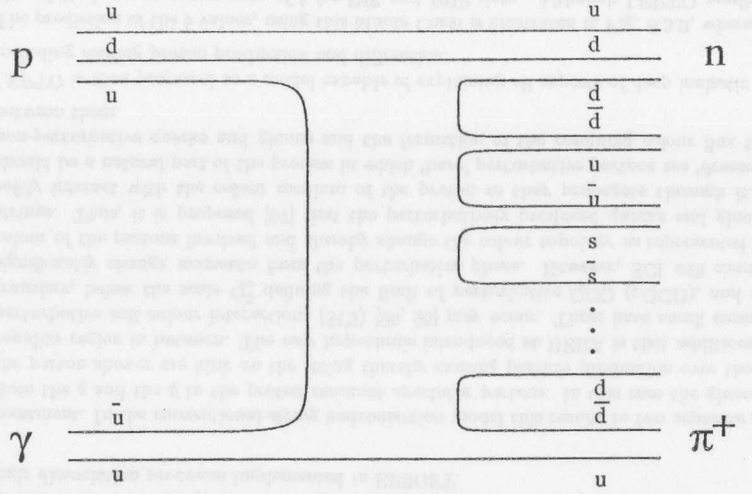

Figure 8.3.5: Soft non diffractive γp scattering showing the valence quark flavour connection between the colliding particles and the hadrons as simulated in EPSOFT

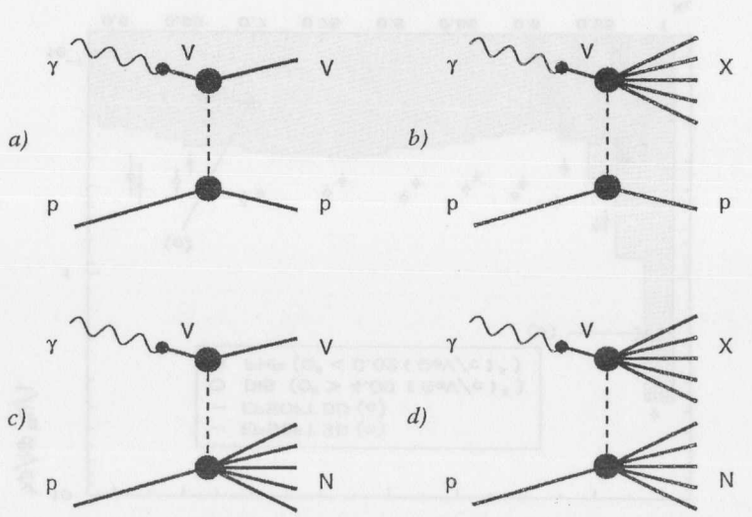

Figure 8.3.6: Diffractive subprocess generated by EPSOFT: (a) elastic vector meson production, (b) photon dissociation, (c) proton (single) dissociation and (d) double dissociation. (The electron vertex is not drawn)

EPSOFT event samples used in this analysis were generated using single and double dissociation processes. The prediction for the slope parameter, b, using this Monte Carlo Generator is illustrated in Fig. 8.3.7. Single dissociation process is present at high x_L values ($x_L > 0.9$) and agrees well with our measurements. Double dissociation covers the whole x_L region available in our measurements but does not reproduce well the data. It predicts higher values of b at low values of x_L ($0.6 < x_L < 0.8$) and reproduces within certain accuracy the data as long as x_L approaches to unity.

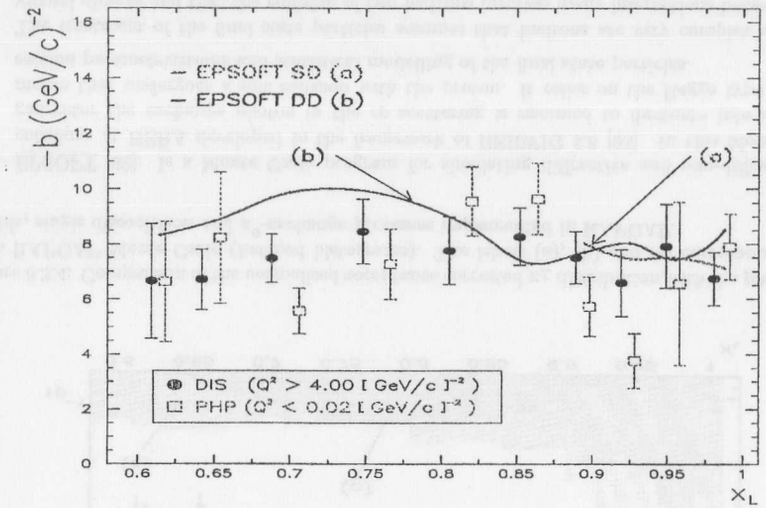

Figure 8.3.7: Comparison of the slope parameters, b, as predicted from EPSOFT Monte Carlo (continuous lines), with our measurements for DIS and PHP data

The comparison of the prediction of the normalised acceptance corrected x_L distribution with our measurement is presented in Fig. 8.3.8. Although the contributions from double and single dissociation processes qualitatively describe the shape of the x_L spectrum, they fail to reproduce the data.

3. LEPTO [94]: Is a general and flexible Monte Carlo to simulate complete lepton-nucleon scattering events and integrated cross sections. It is based on the leading order electroweak cross sections for the underlying parton level scattering processes. The main emphasis of LEPTO is especially on the hadronic part of the event. QCD corrections are therefore included using exact first order matrix elements and higher orders in the leading log Q^2 parton cascade approach. The fragmentation of produced partons into observable hadrons is performed with the Lund string hadronisation model [91].

   At small Bjorken-x (10^{-4} - 10^{-2}), where the rapidity gap events occur, the events are frequently initiated by a gluon from the proton. This can either be directly from the boson gluon fusion matrix element or after the initial state parton shower, including a possible split in the sea quark

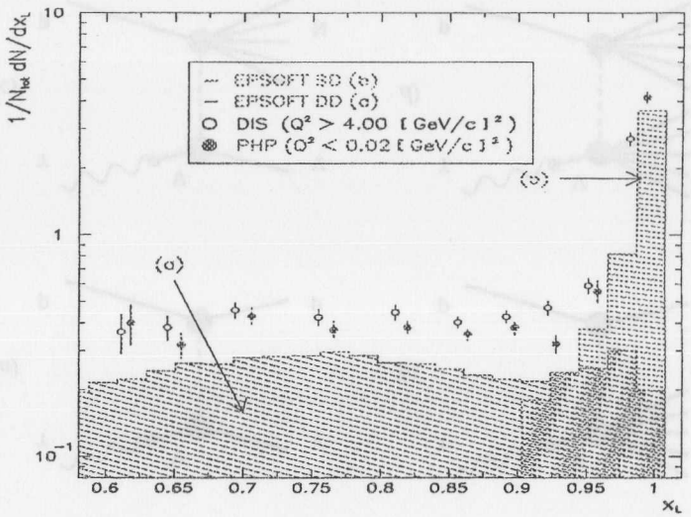

Figure 8.3.8: Comparison of the normalised acceptance corrected x_L distribution,with the predictions from EPSOFT Monte Carlo (hatched histograms). The labels (a) and (b) correspond to the double and single dissociation processes implemented in EPSOFT.

treatment. In the conventional string hadronisation model this results in two separate strings from the q and the $\bar{q}$ to the proton remnant spectator partons. In this case the gluons from the parton shower are kink on the string thereby causing particle production over the whole rapidity region in between. The new hypothesis introduced at HERA is that additional non-perturbative soft colour interactions (SCI) [95, 96] may occur. These have small momentum transfers, below the scale Q_o^2 defining the limit of perturbative QCD (pQCD), and do not significantly change momenta from the perturbative phase. However, SCI will change the colour of the partons involved and thereby change the colour topology as represented by the strings. Thus, it is proposed [97] that the perturbatively produced quarks and gluons can softly interact with the colour medium of the proton as they propagate through it. This should be a natural part of the process in which 'bare' perturbative partons are 'dressed' into non-perturbative quarks and gluons and the formation of the confining colour flux tube in between them.

LEPTO is then proposed as a model capable of explaining all aspects of deep inelastic events including leading proton production and diffraction.

The prediction of the b values, using this Monte Carlo is illustrated in Fig. 8.3.9, where it was also plotted our measurements of b for DIS and PHP data. Although LEPTO predicts the production of leading protons in the whole x_L available region in our measurements, it does not reproduce the slope parameters b of their P_t^2 distributions.

The comparison of the prediction of the normalised acceptance corrected x_L distribution with

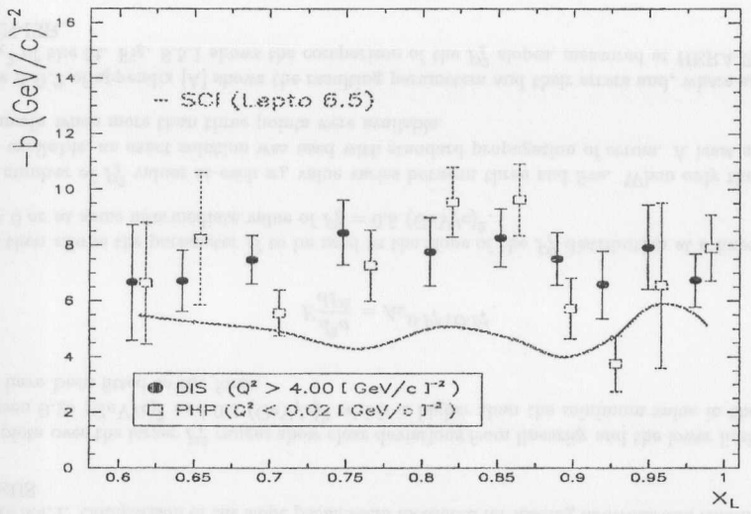

Figure 8.3.9: Comparison of the slope parameters, as predicted from LEPTO Monte Carlo (continuous lines), with our measurements. Although this Monte Carlo is proposed to explain the behaviour of the DIS data, PHP data is also plotted here for comparison.

our measurement is indicated in Fig. 8.3.10. The result of this prediction fails to reproduce the data, but it gives a qualitative description of the peak at values of $x_L > 0.95$.

8.4 Comparison with Forward Neutron Calorimeter data of ZEUS

Since 1994, the ZEUS experiment was also instrumented with a highly segmented high resolution Forward Neutron Calorimeter (FNC) [98] located in the HERA tunnel at $\theta = 0°$, $Z = 106$ m from the interaction point in the proton direction.

With an energy resolution measured in a beam test [98], of $\sigma_E/E = 65\%/\sqrt{(E)}$, it can measure large energy deposits (> 100 GeV) from ep scattering events. These deposits can be attributed to the production of energetic neutrons, photons or protons produced at very small scattering angles with respect to the incoming proton direction. The aperture of the HERA proton beam line elements in front of the FNC limits the geometrical acceptance for neutral particles to angles < 0.6 mr and transverse momenta $P_t < 0.5$ (GeV/c) [99].

The production of leading neutrons have been studied using the FNC in the deep inelastic scattering domain ($Q^2 > 4$ (GeV/c)^2) and with longitudinal momentum fraction with respect to the p-beam momentum $x_L > 0.48$. The acceptance corrected P_t^2 distribution for leading neutrons are fitted with a single exponential function [100] and the slope parameters of these fits, b, extracted.

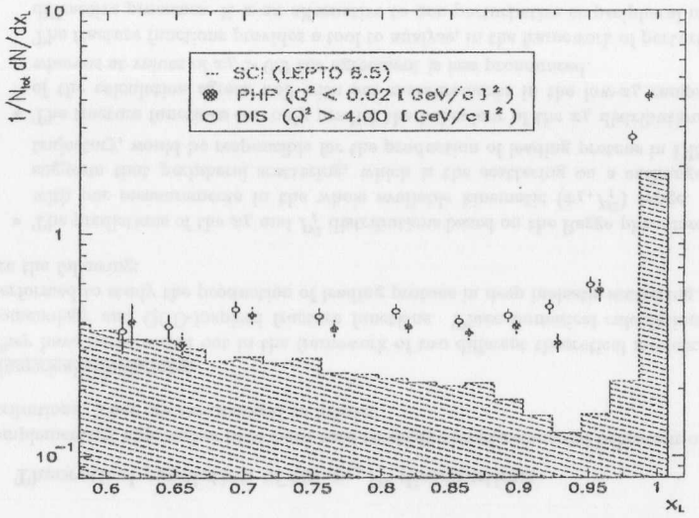

Figure 8.3.10: Comparison of the normalised acceptance corrected x_L distribution, with the predictions from LEPTO Monte Carlo (hatched histogram). Although this Monte Carlo is proposed to explain the behaviour of the DIS data, PHP data is also plotted here for comparison.

The comparison of the slope parameter, b, from the acceptance corrected P_t^2 distributions, for leading protons and leading neutrons are shown in Fig. 8.4.1. The measurements differ at low values of x_L ($0.6 < x_L < 0.75$) and converge within the limits of statistical accuracy at intermediate values of x_L ($0.75 < x_L < 0.93$).

8.5 Comparison with the ISR P_t^2 distributions

A series of careful measurements of the inelastic $\sigma(pp)$ cross section was made at the ISR[1] using a single arm spectrometer set at small angles to one beam, together with veto counters around the other p-beam to exclude elastic events [101].

The emphasis of the analysis in that paper was the variation of the x_L ($x_L = \frac{\text{Scattered proton energy}}{\text{Beam energy}}$) distribution with the transverse momentum (P_t) and also on the distribution of the mass M_X associated with the non-observed proton. Invariant cross sections are tabulated in the paper, and include a certain number of values which are interpolations to particular P_t values. A copy of their data after removing the interpolated points is shown in table A.0.1 of appendix [A]. Plots of invariant cross section as function of P_t^2 are shown for various x_L values in table A.0.2 of appendix [A]. The overall (x_L, P_t^2) range for this data is $0.519 < x_L < 1.005$ and $0.225 < P_t^2 < 1.755$ (GeV/c)^2

[1]Intersecting Storage Ring, facility at CERN during the 1970s where pp interactions were produced at 30 - 50 GeV centre of mass energy

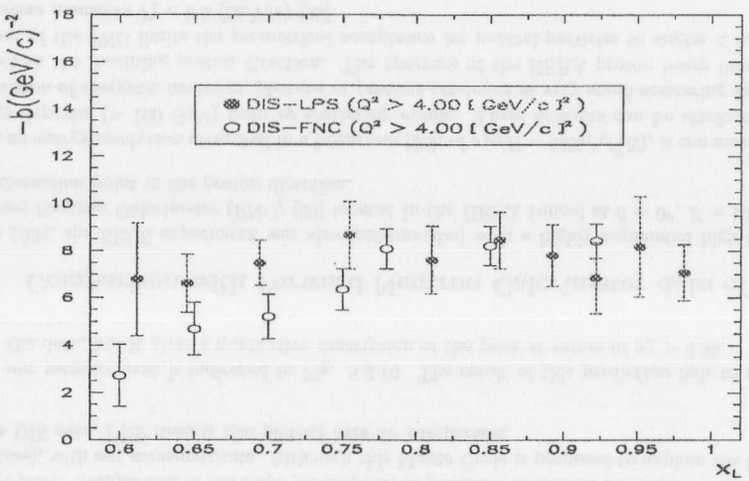

Figure 8.4.1: Comparison of the slope parameters measured for leading neutrons and leading protons at ZEUS

The plots over the larger P_t^2 ranges show clear deviations from linearity and the lower limit of P_t^2 is between 0.25 $(\mathrm{GeV/c})^2$ and 0.4 $(\mathrm{GeV/c})^2$ which is higher than the minimum value in the LPS, so they have been fitted to the form:

$$E\frac{d^3\sigma}{dP^3} = Ae^{B\cdot P_t^2 + C\cdot P_t^4}. \tag{8.1}$$

This then allows the parameter B to be used as the slope of the P_t^2 distribution at a fixed value of $P_t^2 = 0$ or at some intermediate value of $P_t^2 = 0.5$ $(\mathrm{GeV/c})^2$.

The number of P_t^2 values at each x_L value varies between three and five. When only three points were available, an exact solution was used with standard propagation of errors. A least squares fit was made when more than three points were available.

Table A.0.2 of appendix [A] shows the resulting parameters and their errors and, where applicable, the χ^2 of the fit. Fig. 8.5.1 shows the comparison of the P_t^2 slopes, measured at HERA-ZEUS and CERN-ISR.

8.6 Summary of comparisons

In this chapter, a comparison of the x_L and the slopes of the P_t^2 distributions of leading protons, in DIS and PHP data, with different theoretical models have been performed. In addition, the b values obtained from our measurements have also been compared with the ones found from other experiments.

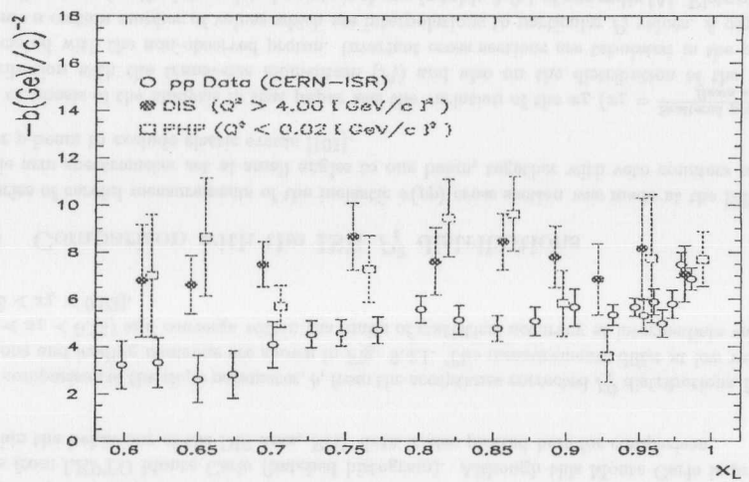

Figure 8.5.1: Comparison of the P_t^2 slopes measured at HERA-ZEUS and CERN-ISR

8.6.1 Theoretical prediction of the x_L, P_t^2 distributions

Two complementary approaches have been used to study the experimental behaviour of the x_L and P_t^2 distributions. They are summarised as follows:

1. Numerical calculations:
   They have been carried out in the framework of two different theoretical models: Regge phenomenology and QCD-inspired fracture functions. These numerical calculations have been performed to study the production of leading protons in deep inelastic scattering. The results are the following:

   - The predictions of the x_L and P_t^2 distributions based on the Regge phenomenology agree with our measurements in the whole available kinematic (x_L, P_t^2) range. This result suggests that peripheral scattering, which is the scattering on a exchange particle or trajectory, would be responsible for the production of leading protons in DIS.
   - The fracture functions can only predict the behaviour of the x_L distribution. The result of the calculation agrees well with our measurements in the low-x_L range ($x_L < 0.9$) whereas at values of $x_L > 0.9$ the agreement is less pronounced.
     The fracture functions provides a tool to analyse, in the framework of perturbative QCD, diffractive processes. It is an alternative to non perturbative or peripheral models.

2. Monte Carlo generated samples:
   Different Monte Carlo generators have been used to simulate real data. As explained in section [8.3], peripheral, diffractive and non diffractive processes are implemented in RAPGAP, EPSOFT and LEPTO. The predictions of the x_L and P_t^2 distributions using these Monte Carlo generators are summarised as follows:

- RAPGAP: In average, the slopes of the P_t^2 distributions are approximatively explained by single and double dissociation processes. Differences of one standard deviation in the measurements the b values are found in some x_L bins.

  Although the contributions from double and single dissociation processes, as implemented in this Monte Carlo generator, do not reproduce the x_L spectrum, the flatness of the normalised acceptance corrected x_L distributions at values of $x_L < 0.9$ and the peak at values of $x_L > 0.9$ are qualitatively described by these processes.

  The π^0-exchange mechanism as implemented in this Monte Carlo disagrees completely with our measurements.

- EPSOFT: The prediction of slopes of the P_t^2 distributions differs between one to three standard deviations from our measurements. However, this Monte Carlo generator gives a qualitative description of the distribution these slopes as a function of x_L.

  The contributions from double and single dissociation processes as implemented in this Monte Carlo generator do not reproduce the x_L spectrum, but it gives a qualitative description of the flatness of the normalised acceptance corrected x_L distributions at values of $x_L < 0.9$ and the peak at values of $x_L > 0.9$.

- LEPTO: The predictions from this Monte Carlo generator fails to reproduce our measurements but tends to give a qualitative description of the slopes of the P_t^2 distributions as well as the normalised acceptance corrected x_L spectrum.

In general, all the above mentioned Monte Carlo generators do not reproduce our measurements. They can only describe, in some cases, qualitatively the shapes of the x_L or b distributions.

8.6.2 Comparison with other experiments

- At HERA, the acceptance corrected P_t^2 distributions for leading neutrons have been fitted with a single exponential and their slope parameters compared with the ones found for leading protons

  The result of this comparison indicate similarities at values of $0.75 < x_L < 0.93$ and differences, of up-to 1.5 standard deviations from the statistical errors, at values of $x_L < 0.75$.

- At CERN-ISR experiment, a series of careful measurements of the inelastic $\sigma(pp)$ cross section was made. In these measurements, the variation of the x_L distribution with the transverse momentum, P_t, was emphasised.

  A rearrangement of their data, in order to have variations of P_t with x_L has been performed and the distributions fitted with a double exponential of the form:

$$E\frac{d^3\sigma}{dP^3} = Ae^{B\cdot P_t^2 + C\cdot P_t^4}$$

  The B parameters can be interpreted as the slope of the P_t^2 distribution at fixed value of $P_t^2 = 0$ or at some intermediate value of $P_t^2 = 0.5$ (GeV/c)^2.

  The comparison of the distribution of this B parameters with our measurements agrees in the diffractive kinematic region ($x_L > 0.97$).

9 Events with a final state Leading Proton

9.1 Introduction

As explained in section [2.3], we have classified the production of leading protons in two kinematic regions, which have apparently nothing or very little in common. However it is assumed that *photo-production* and *deep inelastic scattering* are connected and that there is no discontinuity in the dynamics. This assumption is based on the *correspondence principle* and the *no change hypothesis* introduced by J.D. Bjorken [102] in the early 1970s to explain the scaling behaviour of the dynamics of the final state particles in photo-production at fixed values of the total center of mass energy W and its extrapolation at larger values of Q^2.

Final state particles from both reactions can, in general, be grouped in three regions of the pseudorapidity[1] phase-space, each region characterising a particular process or mechanism by which the hadronic final state is produced. This kind of classification by the spatial topology of the produced events, according to J.D. Bjorken [102], is *model independent* and supported by earlier measurements in hadron-hadron scattering processes during the 1970s in which, *interalia*, a short range correlation between the transverse momenta and the rapidity of the produced hadrons were observed. Fig. 9.1.1 shows the definition of the expected three regions in the pseudorapidity phase-space to classify final state particles in γp interactions.

The similarity between hadron-hadron scattering and γp interactions is due to the fact that at low values of $Q^2 \sim 0$, the photon can be described in a Vector Meson Dominance -like picture [103], where the photon is assumed to fluctuate into a vector meson before interacting with the proton showing in general, features of low-p_T processes as seen in hadronic collisions. Furthermore, at high values of $Q^2 >> 0$, recent measurements at HERA and high precision measurements from fixed target lepto-production experiments have shown that the data in the low Bjorken-x region reveal properties from soft interactions as well.

An overview of the global topology of the produced hadrons in the presence of a produced leading proton will be discussed in the following sections.

9.2 The Deep Inelastic Scattering Regime

In order to study the behaviour of the inclusive particle production in the presence of a final state leading proton in this regime, a binning choice in Q^2 and W according to early measurements [104], [105], [106], has been introduced as shown in Fig. 9.2.1. This binning choice is constrained by the present statistics and resolution measurement of the kinematic variables such as Q^2, W and x_{BJ}. The data sample is selected as described in section [6.2]. In addition a reconstructed vertex is required with a maximum spread along the proton beam direction of $V_z \leq 3\sigma$.

In order to investigate whether the longitudinal momentum spectra (x_L) of the leading protons have any dependence in the above binning choice, the ratios of uncorrected relative x_L spectra and

[1] The pseudorapidity, at HERA, is defined as: $\eta = -\ln(\tan(\theta/2))$, where θ is the polar angle in the direction of the $+z$ axes

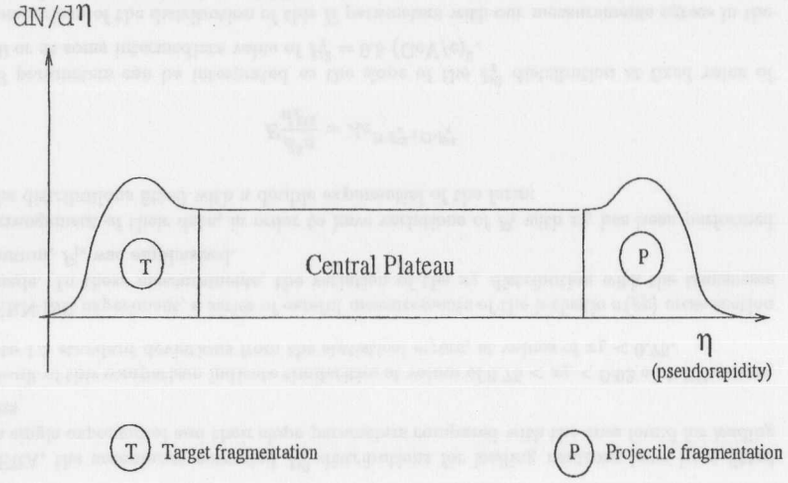

Figure 9.1.1: Definition of the expected three regions in the pseudorapidity phase-space to classify final state particles in $\gamma^* p$ interactions

number of events in every Q^2 and W regions are compared, because of the limited statistics in our sample and the assumption that, acceptance and efficiency corrections will cancel out if the above mentioned ratios are applied.

The ratios of uncorrected x_L spectra in bins of W and Q^2 are shown in Figs. 9.2.2 and Fig. 9.2.3. In average and in light of the limited statistics available, these ratios can be fitted with a constant line, suggesting that the leading proton production might not depend neither on the total center of mass energy W nor on the virtuality of the probe Q^2.

A second step is to investigate the changes in the population of leading protons in every (W,Q^2) cell by calculating the uncorrected fraction of DIS events with a final state leading proton. Due to the small statistics in our sample, to perform this test, two different sets of Q^2 bins are used as follows:

1. The original binning choice is used and the fraction of the total events with a leading proton in the final state is calculated. The results are shown with *open circles* in the histograms of Fig. 9.2.4.

2. The original bins are re-arranged in such a way that they include data at values lower than $W < 90$ GeV^2. The resulting binning is then: $W = (50, 100, 140, 170, 200, 225)$. The fractions of DIS events with a leading proton in the final state using this set of Q^2 bins are calculated and shown with *full circles* in the histograms of Fig. 9.2.4

The use of the above set of Q^2 bins lets us observe a constant behaviour in the production of leading protons at any values of W and Q^2, thus indicating that their production might not depend neither on the virtuality of the probe nor on the available center of mass energy of the $\gamma^* p$ system (W). A least squares linear fit to this ratio (r) for $5 < Q^2 < 40$ GeV^2, gives as a result: $r = 0.025475 \pm 0.000378$, a constant line.

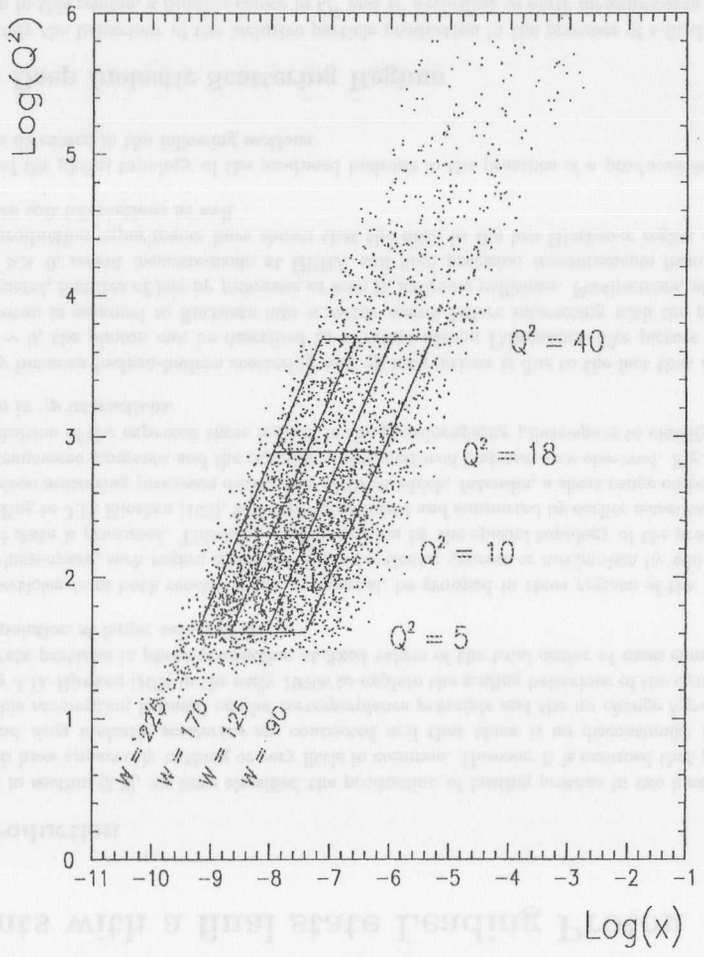

Figure 9.2.1: The LPS-DIS data in the (x, Q^2) plane and the binning selection as a function of W and Q^2

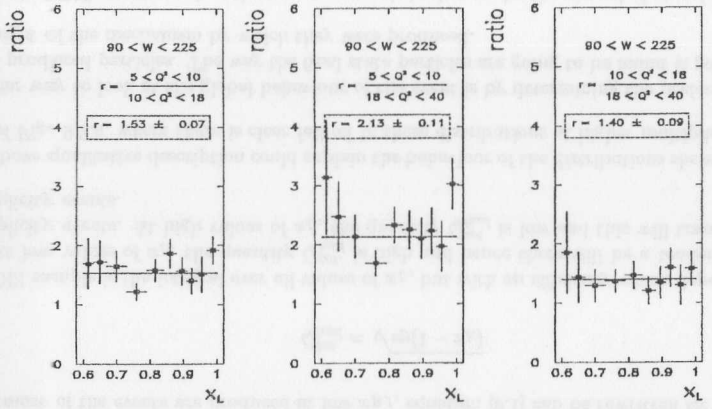

Figure 9.2.2: Ratios of the uncorrected relative x_L spectra in bins of W. In light of the limited statistics available, these ratios can be fitted with a constant line.

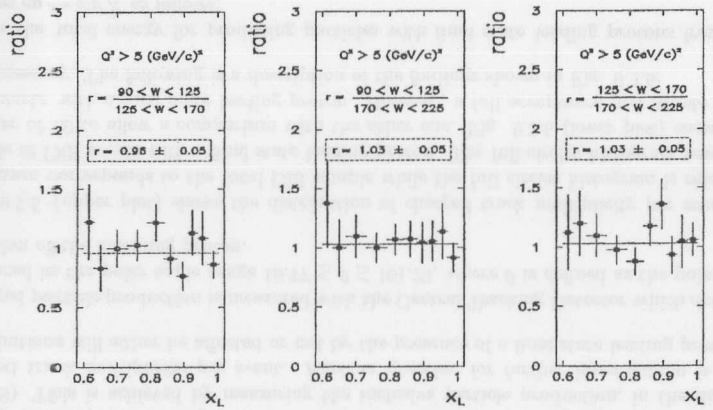

Figure 9.2.3: Ratios of the uncorrected relative x_L spectra in bins of Q^2. In light of the limited statistics available, these ratios can be fitted with a constant line.

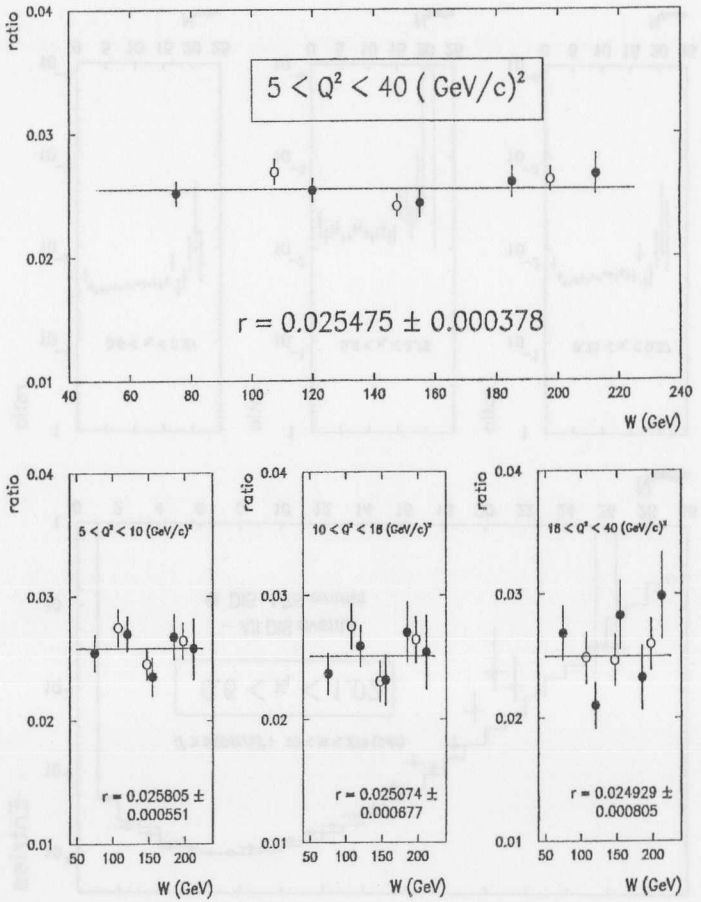

Figure 9.2.4: Calculated fraction of DIS events with a final state leading proton as a function of the available $\gamma^* p$ center of mass energy (W). The open circles correspond to the original W bins shown in Fig. 9.2.1 and the full circles correspond to a re-arrangement of the W binning choice so that it can be examined if any structure is present in the distributions.

A step forward in our analysis is the study of the global event topology in the central detector (ZEUS). This is achieved by measuring the inclusive particle production, in the distributions of charged track multiplicity per event. Another question for further investigation is whether this distributions will either be affected or not by the presence of a final state leading proton.

Charged particle production is measured with the Central Tracking Detector which detects particles produced in the polar angle range $18.77 \leq \theta \leq 161.23$, where θ is defined as the polar angle in the direction of the incoming proton.

Fig. 9.2.5 (upper plot) shows the distribution of charged track multiplicity per event. The solid histogram corresponds to the total DIS sample while the full circles histogram is related to a subsample of DIS events with a final state leading proton. The full circles histogram was scaled-up by a factor of 30 to allow a comparison with the other one. Fig. 9.2.5 (lower plot) shows the ratio of DIS events with a final state leading proton. However, a full acceptance and Monte Carlo studies are necessary. The following is a description of the findings shown in Fig. 9.2.5:

Define the total energy for producing particles with final state leading protons from the general process $ep \rightarrow e'p'X$ as follows:

$$(Q^{tot}_{had})^2 = M^2_X = (e-e')^2 + (p-p')^2 + 2(e-e')\cdot(p-p')$$

where: e, e', p and p' are the four momenta of either the incoming or outgoing electron and proton, and M^2_X the mass of the associated hadrons in the reaction. The result is approximately the following:

$$Q^{tot}_{had} = \sqrt{sy(1-x_{BJ}-x_L)} \tag{9.1}$$

Since most of the events are produced at low x_{BJ}, equation [9.1] can be rewritten as:

$$Q^{tot}_{had} = \sqrt{sy(1-x_L)} \tag{9.2}$$

The DIS sample is the integral over all values of x_L, but with an efficiency which depends on y and x_L. At low values of x_L, the quantity Q^{tot}_{had} is high and hence there will be a tendency for higher multiplicity events. At high values of x_L, the quantity Q^{tot}_{had} is low and this will translate in lower multiplicity events.

The above qualitative description could explain the behaviour of the distributions shown in the lower part of Fig. 9.2.5, where there is clear fall-off in these distributions at higher multiplicities.

Another way to look at the global behaviour of the event is by determining the preferred directions of the produced particles. The way the final state particles are going to be found is going to give us an insight of the mechanism by which they were produced.

In a typical DIS reaction, when the target proton is broken-up by the virtual photon (γ^*), the topology of the produced hadrons, in the framework of the quark parton model, will follow a characteristic spatial distribution which is explained by the materialisation process of the quark-diquark colour string in the direction of the incoming proton. This information can be obtained by measuring the pseudorapidity of the inclusive particle production η

However, since the first evidence at HERA of DIS-like type of events in which a rapidity gap in the final hadronic state was observed [107], [108], a sizeable amount of these kind of events ($\sim$ 10% of the

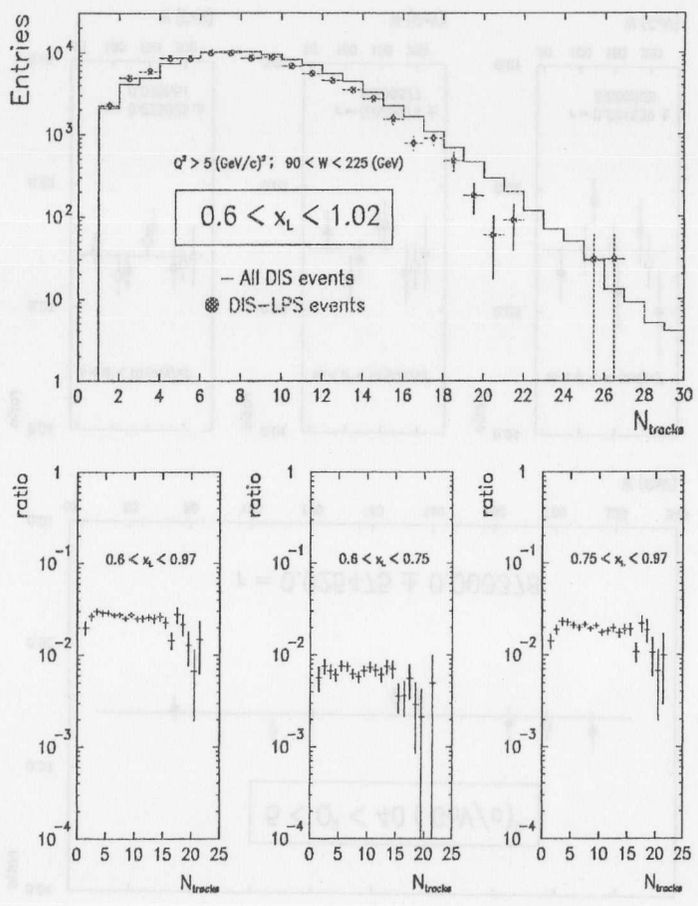

Figure 9.2.5: Upper plot: comparison of total DIS charged track multiplicity per event (solid histogram) with a subsample of DIS events with a final state leading proton (full circles). The data containing a final state leading proton were scale-up by a factor of 30 to compare with the other histogram. Lower plot: ratio of DIS events with a final state leading proton. The distributions are not corrected for acceptance.

total) has been identified that have no colour flow signature in between the place where the particle production populates and the direction of the incoming proton. These events are called Diffractive Deep Inelastic Scattering and the mechanism by which they are thought to be produced are mainly the exchange of a colour neutral object, the pomeron and their signature is a *large rapidity gap* event with values of maximum pseudorapidity per event of $\eta_{max} \leq 1.5$ units.

It is, however, important to find out if the produced leading protons could give us some information about the maximum pseudorapidity of the particle production in the central detector. Fig. 9.2.6 (upper plot) shows a comparison of the maximum pseudorapidity per event in the total DIS sample (solid histogram) with their equivalent found in a DIS subsample having a leading proton in the final state (full circles). The DIS subsample has been scaled up by a factor of 30 to allow a comparison of both histograms. Although a full understanding of the acceptance and efficiency for this class of events is needed, both distributions tend to follow approximatively the same pattern. The contribution from low x_L ($0.6 < x_L < 0.97$) and high x_L ($x_L > 0.97$) leading proton events are shown in the lower part of Fig. 9.2.6. The cut $\eta_{max} = 1.5$ units, is used to separate diffractive and non-diffractive processes.

9.3 The Photo-production regime

As described in section [6.2], photo-production data is selected at very small values of $Q^2 \leq 0.02$ $(\mathrm{GeV/c})^2$ and at γp center of mass energies of $176 \leq W \leq 225$ GeV. Only one bin in Q^2 will be used. The binning choice in W is selected following the statistical population of available data and their boundaries are: $W = (176, 195, 210, 225)$ GeV. In addition a reconstructed vertex is required with a maximum spread along the proton beam direction of $V_z \leq 3\sigma$. We will follow the same procedure as developed in section [9.2] to study the behaviour of the inclusive particle production in a presence of a final state leading proton.

The ratios of uncorrected relative x_L spectra for every bin in W is performed and it showed a similar behaviour as found in DIS. In average and in light of the limited statistics available, these ratios can be fitted with a constant line, suggesting that the leading proton production might not have a W dependence in photo-production. Fig. 9.3.1 shows these ratios per every W bin selected.

A calculation of the fraction of the total events with a final state leading proton is now performed. Due to the limited statistics in our sample, two different sets of W bins are used as follows:

1. The original binning choice is used and the fraction of the total events with a leading proton in the final state is calculated. The results are shown with *open circles* in the histograms of Fig. 9.3.2

2. The original bins are re-arranged in such a way that they use the maximum statistical information but changing its sizes. The resulting binning is then $W = (176, 185, 195, 205, 215, 225)$ GeV, and are almost the same as the ones used in the Measurement of the t-distribution in diffractive photo-production [83]. The fraction of the total events with a leading proton in the final state using this particular set of W bins are shown with *full circles* in Fig. 9.3.2

The flatness of the distribution in Fig. 9.3.2 persists after redefining the binning choice in W, thus indicating that the production of leading protons might not depend on the total γp center of mass energy (W) in photo-production.

To analyse the inclusive particle production in the collision, we proceed by measuring the charged track multiplicities per event. Fig. 9.3.3 (upper plot) shows the distribution of the charged track

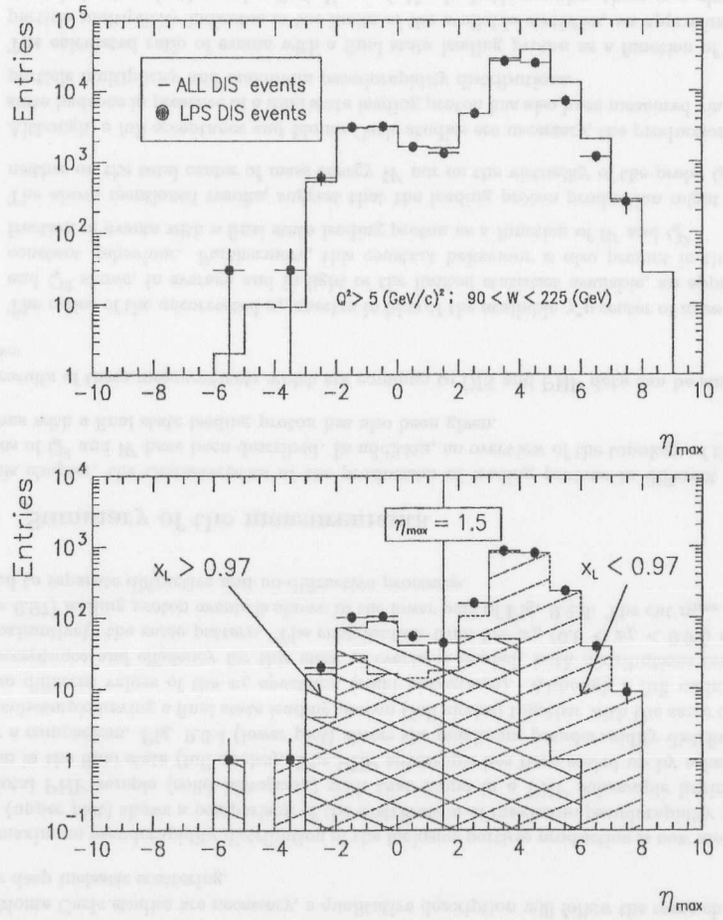

Figure 9.2.6: Upper plot: comparison of total DIS maximum pseudorapidity per event (solid histogram) with a subsample of DIS events with a leading proton in the final state (full circles) which have been scaled up by a factor of 30. Lower plot: contributions from the x_L spectrum to the η_{max} distribution of the DIS subsample having a final state leading proton.

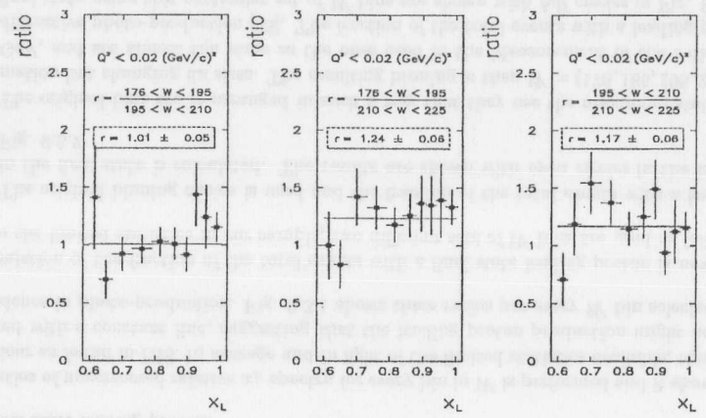

Figure 9.3.1: Ratios of uncorrected relative x_L spectra in bins of W. In light of the limited statistics available, these ratios can be fitted with a constant line.

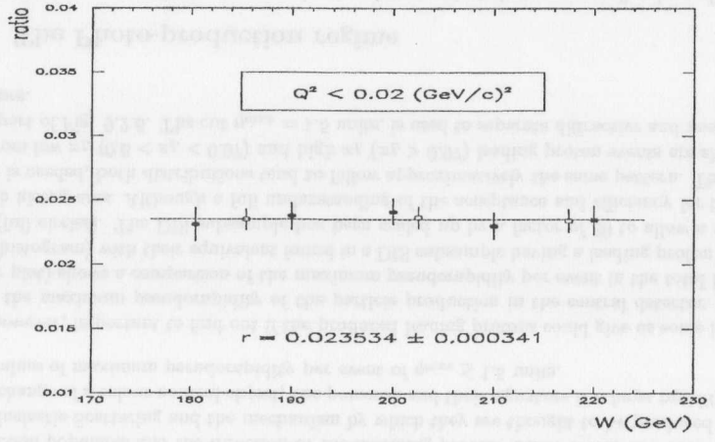

Figure 9.3.2: Calculated fraction of PHP events with a final state leading proton as a function of the available γp center of mass energy (W). The open circles correspond to the original W binning choice and the full circles correspond to a re-arrangement of the W binning choice so that it can be examined if any structure is present in the distributions.

multiplicity per event. The solid histogram corresponds to the total PHP sample while the full circles histogram is related to a subsample of PHP events with a final state leading proton. The full circles histogram was scaled-up by a factor of 30 for ease of comparison. Fig. 9.3.3 (lower plot) show the ratio of PHP events with a leading proton in the final state. Although a full acceptance and Monte Carlo studies are necessary, a qualitative description will follow the same characteristics as for deep inelastic scattering.

The maximum pseudorapidity distribution of the inclusive particle production is now measured. Fig. 9.3.4 (upper plot) shows a comparison of the distribution of maximum pseudorapidity per event in the total PHP sample (solid histogram) with that found in a PHP subsample having a leading proton in the final state (full circles). The PHP subsample has been scaled up by a factor of 30 to allow a comparison. Fig. 9.3.4 (lower plot) shows the maximum pseudorapidity distribution of the SPP subsample having a final state leading proton (full circles) together with the same distributions at two different values of the x_L spectrum (solid histograms). Although a full understanding of the acceptance and efficiency for this class of events is needed, both distributions tend to follow approximatively the same pattern. The contribution from low x_L ($0.6 < x_L < 0.97$) and high x_L ($x_L > 0.97$) leading proton events is shown in the lower part of Fig. 9.2.6. The cut $\eta_{max} = 1.5$ units, is used to separate diffractive and no-diffractive processes.

9.4 Summary of the measurements

In this chapter, the characteristics of the production of leading protons in different kinematical regions of Q^2 and W have been described. In addition, an overview of the topology of the produced hadrons with a final state leading proton has also been given.

The results of these measurements which are common to DIS and PHP data can be summarised as follows:

- The ratios of the uncorrected x_L spectra in bins of the available $\gamma^* p$ center of mass energy (W) and Q^2 shows, in average and in light of the limited statistics available, an approximatively constant behaviour. Furthermore, this constant behaviour is also present in the calculated fraction of events with a final state leading proton as a function of W and Q^2.

  The above mentioned results, suggest that the leading proton production might not depend neither on the total center of mass energy W nor on the virtuality of the probe Q^2.

- Although, a full acceptance and Monte Carlo studies are necessary, the production of the final state hadrons in presence of a final state leading proton has also been measured via the charged particle multiplicity and maximum pseudorapidity distributions.

  The calculated ratio of events with a final state leading proton as a function of the charged particle multiplicity indicates in the limits of the available statistics, an approximatively constant behaviour in the region $3 \leq N_{\text{track}} \leq 15$. In both samples, there is a clear fall-off at higher multiplicities ($N_{\text{track}} > 15$).

  The comparison of the maximum pseudorapidity distribution for all the events in sample, with the ones found with a final state leading proton, shows approximatively the same pattern.

- Final state leading proton events with $x_L > 0.97$ populates most of the large rapidity gap region ($\eta_{\text{max}} < 1.5$) whereas the region ($\eta_{\text{max}} > 1.5$) is mainly populated by final state leading protons with $x_L < 0.97$.

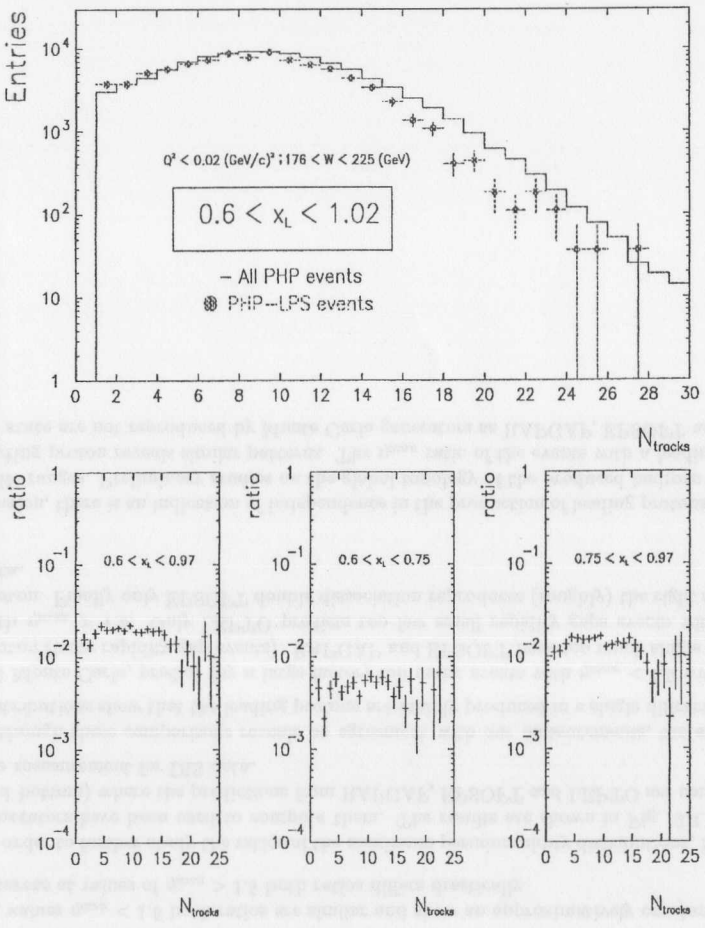

Figure 9.3.3: Upper plot: comparison of total PHP charged track multiplicity per event (solid histogram) with a subsample of PHP events with a leading proton in the final state (full circles) which have been scaled up by a factor of 30. Lower plot: ratio of PHP events with a final state leading proton. The distributions are not corrected for acceptance.

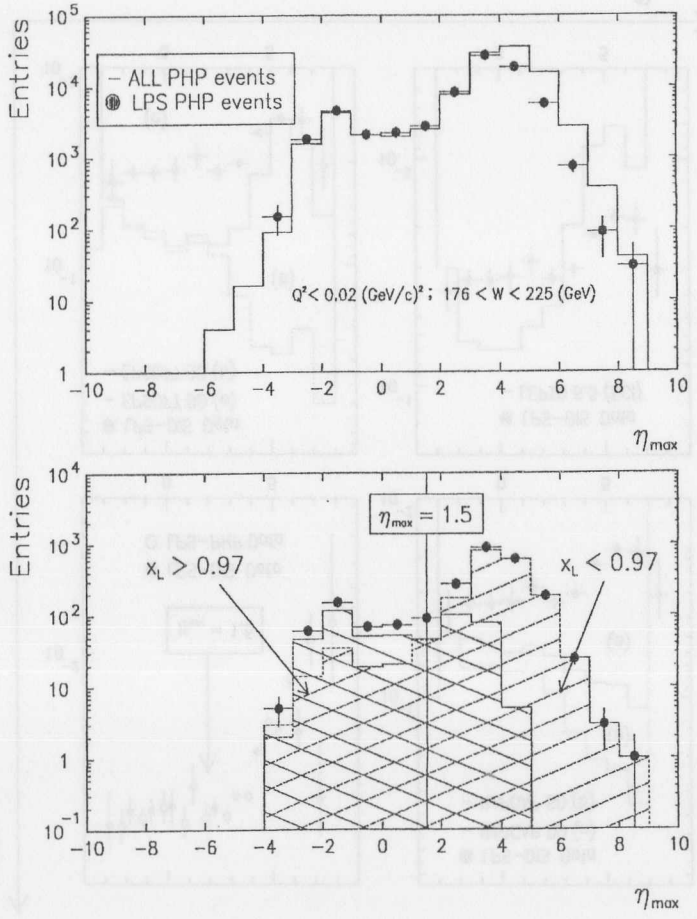

Figure 9.3.4: Upper plot: comparison of total PHP maximum pseudorapidity per event (solid histogram) with a subsample of PHP events with a leading proton in the final state (full circles) which have been scaled up by a factor of 30. Lower plot: contributions from the x_L spectrum to the η_{max} distribution of the PHP subsample having a final state leading proton.

- Similarities in the pattern of the maximum pseudorapidity distributions can better be appreciated by comparing the ratios of the final state leading proton events with the total events in the sample. Fig. 9.4.1 (top-left) shows these ratios for both DIS and PHP data.

  At values $\eta_{\max} < 1.5$ both ratios are similar and show an approximatively constant behaviour whereas at values of $\eta_{\max} > 1.5$ both ratios differs drastically.

- In order to further study the ratios of the maximum pseudorapidity distributions, Monte Carlo generators have been used to compute them. The results are shown in Fig. 9.4.1 (top-right and bottom) where the predictions from RAPGAP, EPSOFT and LEPTO are compared with the measurement for DIS data.

  Although these comparisons reveals no agreement with our measurements, the experimental distributions show that the leading protons are mainly produced in a single diffractive process.

  All Monte Carlo, predict (by a large factor) too many events with $\eta_{max} < 1.5$ with a leading proton (large rapidity gap events). RAPGAP and EPSOFT have too much single dissociation with $\eta_{max} > 1.5$. Only LEPTO predicts too few small rapidity gaps events with a leading proton. Finally only EPSOFT double dissociation reproduces (roughly) the right shape of the data.

In conclusion, there is an indication of independence in the production of leading protons at different Q^2 and W ranges. Preliminary studies on the global topology of the produced hadrons with a final state leading proton reveals similar patterns. The $\eta_{\max}$ ratio of the events with a leading proton in the final state are not reproduced by Monte Carlo generators as RAPGAP, EPSOFT and LEPTO.

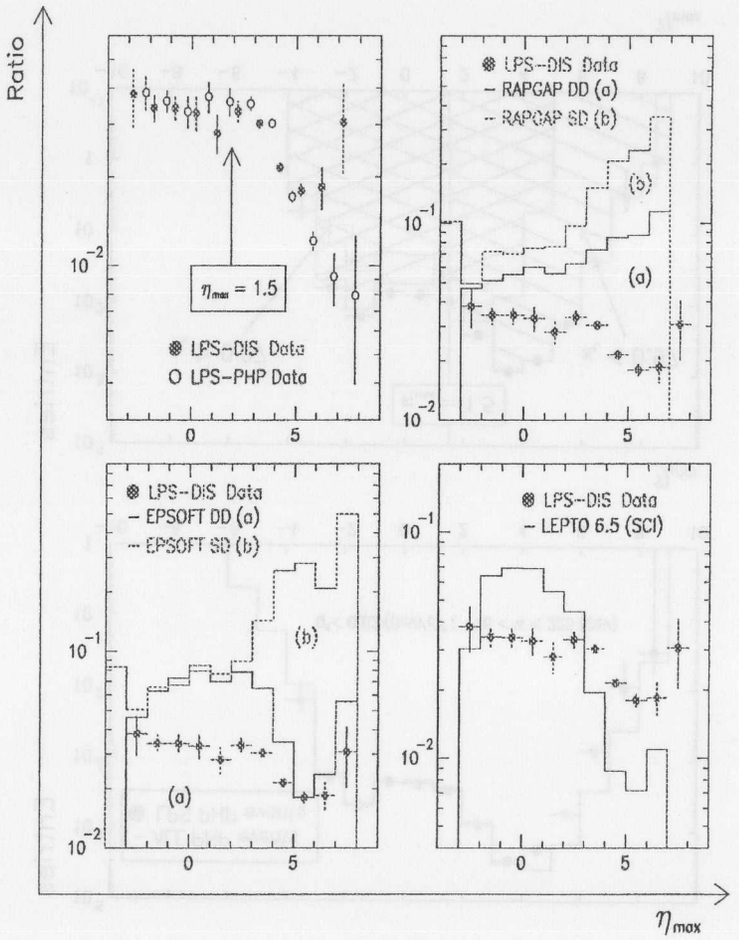

Figure 9.4.1: Upper-left plot: Comparison of the ratios of the maximum pseudorapidity distribution for events with a final state leading proton to all events in DIS and PHP data. Indicating is also a cut in $\eta_{\max} = 1.5$ used to select large rapidity gap events. Upper-right and bottom plots: Comparison of the ratio of the maximum pseudorapidity distribution for events with a final state leading proton in DIS data and the predictions from RAPGAP, EPSOFT and LEPTO Monte Carlo generators.

10 General conclusions

The leading proton spectrometer of ZEUS has been operated at HERA since 1993. It is a single arm spectrometer mounted on the proton beam-pipe and permits, *via* silicon micro-strip detectors, the detection of a fraction of scattered protons which would escape undetected in the beam-pipe. With a longitudinal momentum resolution of $\Delta p_L/p_L \approx \pm 8 \times 10^{-4}$ and a transverse momentum resolution well inside the spread of the incident beam emittance, the LPS allows us a precise measurement of the longitudinal and transverse momentum distributions of the leading proton.

A general summary of the measurements carried out in DIS and PHP follows:

- The acceptance corrected x_L and P_t^2 distributions of the leading proton, for both samples, have been measured. To calculate the acceptance, a two-dimensional fit procedure has been developed and implemented in the analysis to account for migrations and variations in the efficiencies due to detector positioning, reconstruction accuracy and vertex reconstruction.

- Comparisons of the normalised x_L distributions of the leading proton, for both samples, show similar patterns. They show a peak at values of $x_L > 0.9$ and are flat within the experimental errors in the region $0.6 \leq x_L \leq 0.9$. The fraction of events with a leading proton in the region $0.6 \leq x_L \leq 0.9$ is found to be $\approx 13.04\%$ and $\approx 11.77\%$ for DIS and PHP respectively while in the region $x_L > 0.9$ this fraction is $\approx 12.67\%$ and $\approx 17.19\%$ for DIS and PHP respectively.

- The P_t^2 distributions of the leading proton, for both samples, show an experimentally falling behaviour and can be fitted with a simple exponential. Both distributions follow approximately the same pattern. The hypothesis that there is no difference, in the comparison of the b values obtained for both samples, has, on average, a $\chi^2 = 11.72$ for 10 degrees of freedom, corresponding to a confidence level of $\sim 80\%$. This means that there is a probability of ~ 0.6 that shape differences are statistical in origin.

- Two complementary approaches have been used to study the experimental behaviour of the x_L and P_t^2 distributions of the leading proton: numerical calculations and Monte Carlo generated samples.

  While the numerical calculations, based on the Regge phenomenology and QCD fracture functions produce reasonable agreement with our measurements, the Monte Carlo generated samples from RAPGAP, EPSOFT and LEPTO fails to reproduce the data.

- A comparison with the leading neutron data from ZEUS and pp data from the CERN-ISR has been performed. The comparison of the slopes of the P_t^2 distributions for leading neutrons and leading protons shows similarities at values of $0.75 < x_L < 0.93$ while the comparison with the pp CERN-ISR data agrees only in the diffractive kinematic region ($x_L > 0.97$).

- Studies on the production of leading protons in different W and Q^2 regions, indicate probable independence of W and Q^2.

- A preliminary analysis of the event topology of the produced hadrons in a presence of a leading proton, reveals similar patterns. The fraction of DIS and PHP events with a leading proton as a function of $\eta_{\max}$ is approximatively constant and equal for $\eta_{\max} < 1.5$. Although this behaviour is not reproduced by any of the Monte Carlo event generators used in this thesis

the experimental distributions show that the leading protons are mainly produced in a single diffractive process.

All Monte Carlo, predict (by a large factor) too many events with $\eta_{max} < 1.5$ with a leading proton (large rapidity gap events). RAPGAP and EPSOFT have too much single dissociation with $\eta_{max} > 1.5$. Only LEPTO predicts too few small rapidity gaps events with a leading proton. Finally only EPSOFT double dissociation reproduces (roughly) the right shape of the data.

Although using only the limited leading proton statistics in the year 1994, the results presented here show the capabilities of the LPS as an important tool to enhance our knowledge of leading proton production and diffractive ep processes in general.

With the advent of more leading proton statistics, and an improved experimental configuration, these studies will be further pursued towards a better understanding of the leading proton production mechanism.

Appendix A : The CERN ISR data

pp collider: $30 < \sqrt{s} < 50$ GeV
overall x_L range: $0.519 < x_L < 1.005$
overall P_t^2 range: $0.225 < P_t^2 < 1.755$

P_t^2	σ	error	P_t^2	σ	error	P_t^2	σ	error	P_T^2	σ	error
set 1 $x_L = 0.519$			set 2 $x_L = 0.544$			set 3 $x_L = 0.570$			set 4 $x_L = 0.598$		
0.330	3.16	0.32	0.330	3.20	0.32	0.390	2.58	0.26	0.225	4.38	0.44
0.525	1.66	0.17	0.525	1.66	0.17	0.600	1.42	0.14	0.455	2.00	0.20
0.765	0.70	0.07	0.855	0.75	0.08	0.855	0.63	0.60	0.680	1.02	0.10
									0.950	0.41	0.04
set 5 $x_L = 0.623$			set 6 $x_L = 0.650$			set 7 $x_L = 0.674$			set 8 $x_L = 0.701$		
0.275	3.61	0.36	0.275	3.41	0.34	0.330	2.87	0.29	0.330	2.91	0.29
0.455	1.96	0.20	0.525	1.55	0.16	0.600	1.15	0.12	0.600	1.04	0.10
0.680	0.98	0.10	0.765	0.70	0.07	0.855	0.57	0.06	0.855	0.48	0.05
1.050	0.30	0.03	1.050	0.24	0.024	1.155	0.19	0.019	1.155	0.18	0.018
set 9 $x_L = 0.727$			set 10 $x_L = 0.747$			set 11 $x_L = 0.772$			set 12 $x_L = 0.801$		
0.225	4.5	0.4	0.225	3.80	0.57	0.275	2.84	0.42	0.275	2.76	0.42
0.390	2.04	0.20	0.600	0.96	0.15	0.600	0.86	0.12	0.680	0.55	0.09
0.680	0.70	0.07	1.155	0.22	0.033	1.265	0.16	0.03	1.265	0.14	0.02
0.950	0.32	0.03									
1.265	0.11	0.011									
set 13 $x_L = 0.827$			set 14 $x_L = 0.853$			set 15 $x_L = 0.879$			set 16 $x_L = 0.906$		
0.330	2.19	0.33	0.330	2.06	0.31	0.390	1.58	0.24	0.225	4.2	0.6
0.680	0.57	0.09	0.765	0.42	0.06	0.765	0.38	0.06	0.390	1.52	0.22
1.265	0.12	0.018	1.380	0.086	0.015	1.380	0.072	0.010	0.855	0.28	0.04
									1.500	0.048	0.009
set 17 $x_L = 0.932$			set 18 $x_L = 0.947$			set 19 $x_L = 0.953$			set 20 $x_L = 0.960$		
0.225	6.3	0.6	0.275	5.1	0.7	0.275	5.0	0.7	0.275	6.2	0.7
0.455	1.32	0.13	0.950	0.28	0.03	0.525	1.46	0.17	0.525	1.43	0.17
0.950	0.24	0.02	1.755	0.033	0.007	0.950	0.27	0.03	1.050	0.20	0.02
1.625	0.02	0.003				1.625	0.030	0.006	1.755	0.025	0.006
set 21 $x_L = 0.966$			set 22 $x_L = 0.973$			set 23 $x_L = 0.979$			set 24 $x_L = 0.986$		
0.275	7.3	0.9	0.275	8.0	0.9	0.275	10.4	1.0	0.275	20.5	2.0
0.525	1.65	0.18	0.525	1.91	0.22	0.525	2.56	0.28	0.600	2.87	0.29
1.050	0.29	0.03	1.050	0.24	0.03	1.050	0.23	0.03	1.050	0.40	0.04
1.755	0.025	0.006	1.755	0.023	0.005	1.755	0.058	0.007	1.755	0.04	0.007
set 25 $x_L = 0.993$			set 26 $x_L = 0.999$			set 27 $x_L = 1.005$					
0.275	32.5	3.2	0.330	15.3	1.5	0.330	3.1	0.5			
0.600	5.02	0.50	0.600	3.26	0.33	0.600	0.61	0.11			
1.050	0.62	0.06	1.050	0.70	0.07	1.155	0.23	0.03			
1.755	0.059	0.009	1.755	0.042	0.007	1.755	0.005	0.003			

Table A.0.1: Invariant cross section measurements for the reaction $p + p \longrightarrow p' + X$ at CERN ISR

x_L	A	δA	B	δB	C	δC	χ^2	m_o
0.519	2.124	0.349	-2.725	0.695	-0.677	0.664		
0.544	2.589	0.318	-4.925	0.620	1.824	0.571		
0.570	1.884	1.380	-2.112	2.820	-0.739	2.817		
0.598	2.193	0.260	-3.224	1.005	-0.016	0.835	0.177	1
0.623	2.184	0.304	-3.327	1.049	0.097	0.769	0.052	1
0.650	1.989	0.293	-2.615	1.000	-0.605	0.742	0.021	1
0.674	1.992	0.334	-2.802	1.009	-0.300	0.668	0.763	1
0.701	2.344	0.328	-4.070	0.985	0.490	0.651	0.374	1
0.727	2.438	0.174	-4.509	0.574	0.686	0.386	2.019	2
0.747	2.308	0.285	-4.569	0.558	1.091	0.475		
0.772	2.246	0.303	-4.690	0.559	1.158	0.460		
0.801	2.421	0.309	-5.568	0.566	1.660	0.454		
0.827	2.337	0.346	-5.123	0.609	1.265	0.482		
0.853	2.188	0.315	-4.779	0.537	1.026	0.416		
0.879	2.269	0.365	-5.078	0.601	1.106	0.449		
0.906	2.559	0.252	-5.654	0.777	1.291	0.452	1.341	1
0.932	2.847	0.157	-5.343	0.437	0.760	0.247	14.002	1
0.947	3.101	0.227	-5.659	0.374	1.110	0.279		
0.953	2.981	0.262	-5.316	0.663	0.819	0.356	0.183	1
0.960	3.286	0.210	-5.885	0.548	1.113	0.301	2.341	1
0.966	3.149	0.224	-4.972	0.571	0.656	0.308	7.078	1
0.973	3.539	0.220	-5.789	0.587	0.941	0.308	1.650	1
0.979	4.271	0.196	-7.462	0.532	1.939	0.258	0.401	1
0.986	4.773	0.186	-6.861	0.470	1.326	0.244	1.061	1
0.993	5.231	0.185	-6.729	0.455	1.219	0.230	0.063	1
0.999	4.201	0.218	-4.925	0.526	0.437	0.262	7.853	1
1.005	1.619	0.409	-2.083	1.140	-0.666	0.679	21.356	1

Table A.0.2: Fit parameter results to: $E\frac{d^3\sigma}{dP^3} = Ae^{B \cdot P_t^2 + C \cdot P_t^4}$

Bibliography

[1] W. Panofsky, Proceedings of the International Conference in High Energy Physics, Vienna, Austria, (1968).

[2] E. D. Bloom *et al*, Physical Review Letters, 23 (1969) 930.

[3] M. Gell-Mann, Physics Letters 8 (1964) 214.

[4] G. Zweig, Erice lecture 1964, in Symmetries in Elementary Particle Physics.

[5] R. P. Feynman, Physical Review Letters 23 (1969) 1415.

[6] J. D. Bjorken, Physical Review 179 (1969) 1547.

[7] J. D. Bjorken and E. A. Paschos, Physical Review, 185 (1969) 1975.

[8] A. Bodek *et al*, Experimental studies of the neutron and proton electromagnetic structure functions, Physical Review D29 (1979) 1471.

[9] H. Fritzsch *et al*, Physics Letters B 47 (1973) 365.

[10] D. J. Gross and F. Wilczek, Physical Review D 8 (1973) 3633.

[11] S. Weinberg, Physical Review Letters 31 (1973) 494.

[12] J. Kuti and V. F. Weisskopf, Physical Review, D4 (1971) 3418.

[13] H. D. Politzer, Asymptotic Freedom: an Approach to Strong Interactions, Physics Reports C 14 (1974) 129.

[14] Proceeding of the Workshop Physics at HERA, Hamburg, (1991), edited by W. Buchmüller, G. Ingelman.

[15] M. Basile *et al*, The method of removing the Leading Protons in the Study of High-Energy *pp* Reactions, Compared with the Standard Analysis, Il Nuovo Cimento, Vol. 65 A, N. 3, 1981.

[16] M. Basile *et al*, The "Leading Particle" Effect in Hadron Physics, Il Nuovo Cimento, Vol. 66 A, N. 2, 1981.

[17] St. Bentvelsen, J. Engelen, P. Kooijman, Reconstruction of (x,Q^2) and Extraction of Structure functions in Neutral Current Scattering at HERA, Proceedings of the HERA Worshop Physics at HERA, Vol. 1, 23-41, Hamburg, (1991), edited by W. Buchmüller, G. Ingelman.

[18] G. Wolf, HERA Physics, DESY 94-022 (1994).

[19] F. Jacquet and A. Blondel, Proccedings of the Workshop "Study of an *ep* Facility in Europe", 1979, p.391.

[20] F. Halzen, A. D. Martin, Quarks & Leptons: An Introductory Course in Modern Particle Physics, John Wiley & Sons. Inc, ISBN 0-471-88741-2 (1984).

[21] B. Badelek *et al*, Working Group Report on the Structure of the Proton, DESY 96-049 (1996).

[22] A. M. Cooper-Sarkar, R. C. E. Devenish and A. De Roeck, Structure Functions of the Nucleon and their Interpretation, DESY 97-226 (1997).

[23] R. Peschanski, HERA: The Fundamental Strong Interaction Under the Microscope, Europhysics News, Vol. 28 - Nr. 3, (1997).

[24] V. N. Gribov and L. N. Lipatov, Sov. J. Nuclear Physics 15 (1972) 438
G. Altarelli and G. Parisi, Nuclear Physics B126 (1977) 298
Yu. L. Dokshitzer, Sov. Physics JETP 46 (1977) 641

[25] E. A. Kuraev, L. N. Lipatov and V. S. Fadin, Physics Letters B60 (1975) 50; Soviet Physics JETP 44 (1976) 443; Soviet Physics JETP 45 (1977) 199
ya. ya. Balitsky and L. N. Lipatov, Sov. J. Nuclear Physics 28 (1978) 822

[26] G. Ingelman, P. E. Schlein, Jet Structure in High Mass Diffractive Scattering, Physical Review Letters B152 (1985) 256.

[27] R. Bonino *et al*, Evidence for Transverse Jets in High Mass Diffraction. Physics Letters, B21 (1988) 239.

[28] N. N. Nikolaev and B. G. Zakharov, Pomeron Structure Functions and Diffraction Dissociation of Virtual Photons in Perturbative QCD, Z. Physics, C53 1992.

[29] N. N. Nikolaev, B. G. Zakharov and V. R. Zoller, The Spectrum and Solutions of the Generalized BFKL Equation for Total Cross-Section. hp-th/9401052, submitted to Physics Letters B (1994) 23.

[30] Gerhard A. Schuler and Torbjörn Sjöstrand,
The hadronic properties of the photon in γp interactions, CERN-TH 6718 (1992).
Towards a Complete Description of High-Energy Photoproduction, CERN-TH 6796 (1993).

[31] J. J. Sakurai, Ann. Physics, 11 (1960) 1.

[32] T. Regge,Introduction to Complex Orbital Momenta, Nuovo Cimento 14 (1959) 951.

[33] G. F. Chew and S. C. Frautschi, Physical Review Letters 7 (1961) 394).

[34] I. V. Pomeranchuck, Soviet Physics JETP 7 (1958) 499

[35] M. Froissart, Physical Review, 123 (1961) 394.

[36] A. Donnachie and P. V. Landshoff,
Nuclear Physics B 224 (1984) 322;
Nuclear Physics B 267 (1986) 690;
Nuclear Physics B 191 (1987) 309;
Nuclear Physics B 303 (1988) 634;
Nuclear Physics B 296 (1992) 227;
Nuclear Physics C 61 (1994) 139.

[37] B. Burrow, Ph.D. Thesis, Toronto University (1993), DESY F35D-94-01 (1994).

[38] A. Levy, Low-x Physics at HERA, DESY 97-013 (1997).

[39] C. Coldewey, Study of two Jet Photoproduction at HERA, Ph.D. Thesis, DESY F35D-95-16 (1995).

[40] J. Mainusch, Measurement of the Total Photon-Proton Cross-Section at HERA Energies, Ph.D. Thesis (1995).

[41] N. N. Nikolaev *et al*, Leading proton spectrum from DIS at HERA, preprint hep-ph/9712261

[42] L. Trentadue and G. Veneziano, Physics Letters B323, 201 (1993).

[43] L. Trentadue, HEP-PH-9506324, 1995.

[44] E. Berger, Semi-Inclusive Inelastic Electron Scattering from Nuclei, Proceedings of the NPAS Workshop on Electronuclear Physics with Internal Targets, SLAC-report 316, p. 82, 1987.

[45] D. de Florian & R. Sassot, Phenomenology of Forward Hadrons in DIS: Fracture Functions and its Q^2 Evolution, CERN-TH/96-339.

[46] D. de Florian & R. Sassot, QCD Analysis of Diffractive and Leading-Proton DIS Structure Functions in the Framework of Fracture Functions, CERN-TH/98-109, hep-ph/9804240.

[47] HERA, A Proposal for a Large Electron-Proton Colliding Beam Facility at DESY, DESY-HERA Report 81-10.

[48] R. Ayad and C. Nemoz, Background From Synchrotron Radiation For The ZEUS Leading Proton Spectrometer, CERN/LAA/LP/93-24 (1993).

[49] The ZEUS Detector, Status Report, DESY 1993.

[50] The Calculation of the Magnetic Field and Forces in the ZEUS Detector, DESY 92-084, (1992).

[51] ZEUS SRTD Group, The Small Angle Rear Tracking Detector of ZEUS, DESY 97-157 (1997).

[52] J. Straver, Design Construction and Beam Tests of the High Resolution Uranium Scintillator Calorimeter for ZEUS, Phd Thesis (1991).

[53] J. Krüger, The Uranium Scintillator Calorimeter for the ZEUS Detector at the Electron-Proton Collider HERA, DESY-Report, DESY F35-92-02 (1992).

[54] The ZEUS Luminosity Monitor Group, First Measurement of HERA Luminosity by ZEUS Lumi Monitor, DESY 92-066, (1992).

[55] K. Piotrzkowski, Experimental Aspects of the Luminosity Measurement in the ZEUS Experiment, Ph.D. Thesis, DESY F35D-93-06 (1996).

[56] H. Bethe and W. Heitler, Proceedings of the Roy. Soc. A146 (1934) 83.

[57] F. Benotto *et al*, The LPS Trigger System, ZEUS-Note 95-165 & DESY 96-045 (1996).

[58] K. O'Shaughnessy *et al*, Testing and Installation of ZEUS Leading Proton Spectrometer detector planes, Nuclear Inst. and Methods, A 342 (1994) 260-263.

[59] A. Staiano, Silicon Detectors for the Leading Proton Spectrometer of ZEUS, Proceedings of the *Third International Workshop on Vertex Detectors*, IUHEE-95-1.

[60] Peter Ford, A constant tension spring device used for atmospheric force compensation, CERN/LAA/LP/94-08 (1994).

[61] E. Barberis *et al*, A fast Shaping Amplifier-Comparator Integrated Circuit for Silicon Strip Detectors. SCIPP 92/40, 1992.

[62] E. Barberis *et al*, A Low Power Bipolar Amplifier Integrated Circuit for the ZEUS Silicon Strip System. SCIPP 92/35, 1992.

[63] J. De Witt. The Digital Time Slice Chip. University of California, Santa Cruz, June 7, 1991.

[64] H. Larsen, The LPS Readout Controller, CERN-LAA,(1994).

[65] H. Larsen, LPS Fast-Fan-Out. CERN-LAA, (1994).

[66] H. Larsen. The LPS Serial Readout Controller, CERN-LAA, (1994).

[67] T. Massam, Thermal Properties of the Leading Proton Front End Multi-Layer Circuit, ZEUS-Note 90-059.

[68] G. Anzivino *et al*, Thermal properties of the Leading Proton Multi-Layer PCB Prototype, ZEUS-Note 93-028.

[69] Ronald F. Holsinger and Christoph Iselin, The CERN-Poisson Program Package (POISCR) User Guide.

[70] C. Nemoz, The ZEUS Leading Proton Spectrometer Hardware Control System, ZEUS-Note 94-163, (1994).

[71] Roberto Sachhi, Dottorato di Ricerca in Fisica VIII Ciclo, Iniversità degli Studi di Torino (1996). ZEUS-Note 96-024.

[72] T. Massam *et al*, Alignment Optics for the Leading Proton Spectrometer, CERN/LAA/LP/92-002 and ZEUS Note 92-036 (1992).

[73] T. Massam *et al.*, The Leading Proton Spectrometer: High Precision Momentum Calibration, CERN/LAA/LP/94-18 and ZEUS Note 94-075 (1994).

[74] N. Cartiglia *et al*, LPS Alignment, Calibration and Reconstruction for 1994 Data, ZEUS Note 96-059 (1996).

[75] ZEUS Data Acquisition System, ZEUS contribution to the *Real-Time Conference*, Vancouver, Canada, DESY 93-091 (1993)
ZEUS Data Acquisition Group, ZEUS contributed papers of *CHEP 92*, Annecy, FRANCE, DESY 92-150 (1992).

[76] F. Chlebana, Description of the ZEUS Global Second Level Trigger in 1994, ZEUS Note 94-102 (1994).

[77] S.M. Fisher and P. Palazzi, ADAMO Entity-Relationship Programming System, CERN PTG/ECP Division.

[78] R. Sinkus, H. Abramowicz, Electron Identification with Neural Networks at ZEUS, ZEUS Note 93-117 (1993).

[79] LPS Group, On the 1994 LPS Efficiency, ZEUS-Note 94-156.

[80] M. Kasprzak, Ph.D. Thesis, University of Warsaw, (1996), DESY Report F35D-96-16.

[81] B. D. Burow, Ph.D. Thesis, University of Toronto, (1994), DESY Report F35D-94-01.

[82] J. Mainush, Ph.D. Thesis, University of Hamburg, (1995), DESY Report F35D-95-14.

[83] A. Garfagnini and R. Sacchi, A Measurement of the t-slope in diffractive dissociation of real photons with the LPS from 1994 Data, ZEUS Note 97-028 (1997).
J. Breitweg *et al*, Measurement of the t Distribution in Diffractive Photoproduction at HERA, ZEUS Collaboration, DESY 97-238 (1997).

[84] MOZART, Montecarlo for ZEUS analysis, Reconstruction and Trigger. ZEUS collaboration.

[85] F. James, Minuit, Function Minimization and Error Analysis, CERN Program Library Long Writeup D506.

[86] J. Rahn, Reweighting LPS MC for Motor Movements, Private Comunication.

[87] A. Garfagnini, Dottorato di Ricerca in Fisica X Ciclo, Università degli Studi della Clabria (1998), unpublished.

[88] D. de Florian, CERN-TH, Private comunication.

[89] H. Jung, Comput. Phys. Commun., 86 (1995) 147 - 161.

[90] L. Lönnblad, DESY 92-046 (1992) & Comput. Phys. Commun., 15 (1992) 72.

[91] B. Andersson, G. Gustafson, G. Ingelman T. Sjöstrand, Phys. Rep. 97 (1983) 31.

[92] M. Kasprzak, EPSOFT - a Monte Carlo generator of soft photon-proton collisions, ZEUS Note 95-069.

[93] B. R. Webber, Ann. Rev. Nucl. Paret. Sci. 36 (1986) 253
G. Marchesini *et al.*, Comput. Phys. Commun. 67 (1992) 465

[94] G. Ingelman, A. Edin, J. Rathsman, LEPTO 6.5 -A Monte Carlo Generator for Deep Inelastic Lepton-Nucleon Scattering, DESY Report 96-057 (1996).

[95] A. Edin, J. Rathsman and G. Ingelman, Rapidity Gaps in DIS through Soft Colour Interactions, DESY 95-145 (1995).

[96] W. Buchmüller, Soft Colour Interactions and Diffractive DIS, DESY 97-122 (1997).

[97] A. Edin, G. Ingelman, J. Rathsman, Physics Letters B366 (1996) 371.

[98] S. Bhadra *et al*, The Design and Test of a Forward Neutron Calorimeter for the ZEUS Experiment at HERA, preprint hep-ex/9701015.

[99] M. Derrik *et al*, Physics Letters B384 (1996) 388.

[100] B. Schmidke, ZEUS-FNC group, Private comunication.

[101] M.G. Albrow *et al*, The spectrum of protons produced in pp collisions at 31 GeV total energy, Nuclear Physics B54 (1973) 6-16.

[102] J. D. Bjorken, SLAC Summer School SLAC-167 (1973) 1.
J. D. Bjorken, Symposium on Electron and Photon Interactions at High energies, Cornell 1971.

[103] J. J. Sakurai, Physical Review Letters, 22 (1969) 981.

[104] I. Gialas and T. Massam, DIS Events with Leading Protons of $x_L < 0.9$ detected in the LPS of ZEUS, ZEUS-Note 96-062 (1996)

[105] I. Gialas and T. Massam, Description of the Analysis of DIS Events with a Leading Proton, Zeus-Note, 96-063 (1996).

[106] N. Cartiglia, Properties of Events with a Leading Proton in DIS and Photoproduction at HERA, International Europhysics Conference on High Energy Physics, August 1997.

[107] M. Derrick *et al*, Observation of events with a large rapidity gap in deep inelastic scattering at HERA, Physics Letters B 315 (1993) 481-193.

[108] T. Ahmed *et al*, Deep Inelastic Scattering Events with a Large Rapidity Gap at HERA, DESY 94-133 (1994)